# UNDERSTANDING MAGNETIC FIELD EVOLUTION FROM THE SOLAR INTERIOR TO THE HELIOSPHERE



**Shaonwita Pal**

**(19RS038)**

Supervisor: Prof. Dibyendu Nandi

Center of Excellence in Space Sciences India

Indian Institute of Science Education and Research Kolkata

This dissertation is submitted for the degree of

***Doctor of Philosophy in Science***

November 2025

"সঙ্কোচের বিহ্বলতা নিজেরে অপমান,
সঙ্কটের কল্পনাতে হোয়ো না ম্রিয়মাণ।
মুক্ত করো ভয়, আপনা-মাঝে শক্তি ধরো, নিজেরে করো জয়।"

Do not let hesitation make you weak.
Do not fear what only exists in your mind.
Free yourself from fear — find your strength within and overcome yourself.

— রবীন্দ্রনাথ ঠাকুর (Rabindranath Tagore)

*To Ma, Baba, and Didi*

*My guiding lights and my forever safe place.*

&

*To those who have been knocked down but never stopped,*

*who have faced failures yet never lost hope — this is for you.*

# Declaration

Date: 04 November 2025

I, Miss. Shaonwita Pal, Registration No. 19RS038 dated 26$^{th}$ July 2019, a student of Center of Excellence in Space Sciences India of the PhD Program of IISER Kolkata, hereby declare that this thesis is my own work and, to the best of my knowledge, it neither contains materials, previously published or written by any other person, nor it has been submitted for any degree/diploma or any other academic award anywhere before, unless explicitly stated. I have used the originality checking service to prevent inappropriate copying.

I also declare that all copyrighted material incorporated into this thesis is in compliance with the Indian Copyright Act, 1957 (amended in 2012) and that I have received written permission from the copyright owners for my use of their work.

I hereby grant permission to IISER Kolkata to store the thesis in a database which can be accessed by others.

Shaonwita Pal
Center of Excellence in Space Sciences India
Indian Institute of Science Education and Research Kolkata
Mohanpur 741246, West Bengal, India

# Certificate from the Supervisor

Date: 04 November 2025

This is to certify that the thesis entitled **"Understanding Magnetic Field Evolution from the Solar Interior to the Heliosphere"** submitted by Shaonwita Pal, Registration No. 19RS038 dated 26$^{th}$ July 2019, a student of Center of Excellence in Space Sciences India of the PhD Program of IISER Kolkata, is based upon her own research work under my supervision. I also certify, to the best of my knowledge, that neither the thesis nor any part of it has been submitted for any degree/diploma or any other academic award anywhere before. In my opinion, the thesis fulfils the requirement for the award of the degree of Doctor of Philosophy.

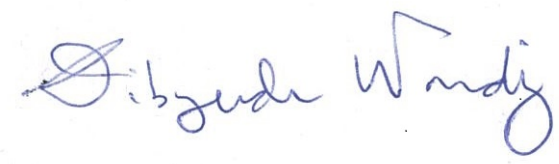

Dr. Dibyendu Nandi
Professor
Department of Physical Sciences
Center of Excellence in Space Sciences India
Indian Institute of Science Education and Research Kolkata
Mohanpur 741246, West Bengal, India

# Acknowledgments

In July 2019, on a rainy day, I first met Prof. Dibyendu Nandy, marking the beginning of my PhD journey. I am grateful to him for his supervision and support throughout this journey, especially in helping me navigate the challenges of balancing my research with my job responsibilities and other commitments. His guidance has been invaluable and will always remain with me. My interest in physics began long before my PhD, and for that, I must express my heartfelt gratitude to Nirmal Sir, who first sparked my curiosity during my eleventh-grade years. This passion grew stronger during my five years at the 'University of Calcutta', where I was fortunate to be mentored by inspiring professors. Stepping into Rajabazar Science College was a fulfilling experience, where I had the privilege of learning from Prof. Amitabha Rai Choudhury, Prof. Anindya Dutta, Prof. Abhijit Bhattacharya, Prof. Amitabha Dutta, Prof. Dipankar Das, and all other esteemed faculty members of the Department of Physics. These people's teachings, encouragement and mental support have played a crucial role in shaping not only my academic journey, but also life's journey.

Before I begin reflecting on my PhD journey, I would like to thank Bibekanjan Sir and Jethima because they hold a special place in my heart. There are also people from my school to M.Sc. days whom I may not be regularly in touch with anymore, but who were once an important part of my life: Pratip, Suchismita, Arko, and Sudip da. When I first joined IISER-K, I didn't have any close friends until I met Ananyapam, who helped me navigate those early days. The memories of hostel life at IISER – roaming around the campus and endless topic-less chattering – would be incomplete without Sumana and Annyasa. I still fondly miss our long dinner sessions that started at 8 p.m. and stretched until the last canteen batch had left. I also want to cherish the beautiful moments I spent chatting, laughing, and sharing stories with Samiksha, Debu da, Nivedita, Anand, Anita, Suchismita, Souradeep, Anisha, Arpita, Gopi, Shreyan, Suvam, Soumyadeep, and Viswa-

jit, there at IISER Kolkata.

As a member of CESSI, I would like to express my heartfelt gratitude to all past and present lab members — Prasenjit da, Lekshmi di, Maitrayo da, Arghya da, Arnab da, Subhadip da, Souvik da, Sakshi, Poulomi di, Sanchita di, Utkarsh, and Pradipto — each of whom has, at some point, stood beside me in this journey. I am deeply thankful to Prantika di and Soumya da, my first mentors in the PhD journey, for guiding me through every step with patience and encouragement. Beyond research, Prantika di has been like an elder sister — someone I can always rely on for advice and support in life. I also extend my thanks to Soumitra da, the first senior of CESSI, from whom I learned many valuable lessons. I would also like to remember Priyansh and Chitradeep – my juniors, yet dear friends – for their constant support and for the wonderful trips and memories we created together. I hope there are many more trips awaited together! I enjoyed working with Sanghita, Sneh, and Sushant during my PhD. I shouldn't forget about some people whom I met at Solar Physics conferences and were involved in scientific discussions, including Anshu di, Kristof, Paul, Nick, Rajaguru, Dipu da, Bibhuti da, Dibya and Nitin. I would also like to express my gratitude to Sujoy da, Raveena, Harsh, Ritam, Rajyashree, and Ketan for being part of my journey and offering support in their own ways. I am thankful to Piklu – someone with whom I shared long conversations, unexpected laughter, and those childish fights that meant so much to me.

In December 2021, I joined as a Lecturer in Physics under WBTET in the West Bengal Government, while continuing my PhD journey in parallel. Balancing both was never easy, and I owe it to Abhik da and the JCGP students, who supported me immensely in those initial days. My students have been a source of light for me – they reminded me how much I matter in their lives. Without the joy of teaching them, this PhD journey would have felt incomplete. I am also grateful to my other colleagues, with whom I've shared many joyful moments. In this phase of my life, I found two especially important friends – Sudipa di and Sudip– whose thoughtful conversations and comforting presence brought warmth and clarity during uncertain times. Sudipa di has been a compassionate listener, always there to hear out my worries from both personal and academic fronts, and held my hand.

Now, as I reach the end of this section, it feels only right to acknowledge those who have been an inseparable part of my journey — because, as the saying goes, 'old is gold'.

I am deeply grateful to Sayantan, who has been by my side through every high and low, offering unwavering support. He is someone I could trust completely; his encouragement, understanding, and faith in me helped me overcome moments of self-doubt and exhaustion. My heartfelt thanks also go to Kaku and Kakima for their warm care and for cooking my favorite dishes that made me feel at home. I want to thank my school friend Shraboni, my closest companion from school days, with whom reconnecting after years brought back fond memories that always lift my spirits. My gratitude also goes to Anol, whose constant support and decade-long friendship have been a steady source of strength and comfort throughout this journey. To Yoshita and Brinda, two of my most cherished friends – thank you for inspiring me with your resilience and for standing beside me during my toughest times and constantly encouraged me to rise above them. I extend my sincere thanks to Susmita and Tanmoy da, who were always there to listen, understand, and guide me in their own caring ways.

Lastly, I believe family members can not be acknowledged formally, I cannot help but express how fortunate I am to have Sukhomoy da, Masimoni, Mesomoni, Tinku dada, Boudi, Bubli, and Dodo in my life – each of them has supported me in their own loving way. Most importantly, **Ma, Baba, and Didi** are my world. Whatever I have achieved, or will achieve in the future, is rooted in their unconditional love, countless sacrifices, and unwavering support in me. Being the youngest in the family, I have always been surrounded by their affection, care, and gentle pampering – which has been both my comfort and my strength. Every milestone in this journey carries a part of them – their faith, their blessings, and their love. They are my safe place, my greatest strength, and my forever home. I owe every success, every step forward, to them – and I love them to infinity and beyond.

Before I close, I want to say that these memories continue to warm my heart and remind me how truly fortunate I've been to have such wonderful people walk beside me through this journey. Each of them has touched my life in ways words can hardly capture! I hope that, in some way, I too have been a meaningful part of their lives by offering them same kindness, strength, and support they have shown me. I wish that our bonds remain unbroken and that all these people stay with me through every step ahead – for there are still **"miles to go before I sleep."**

# Abstract

In the modern era, our understanding of solar and stellar physics has evolved dramatically, driven by both observational advances and sophisticated modelling techniques. One of the most dynamic and consequential aspects of solar and stellar behavior is their magnetic activity, which manifests through various energetic phenomena such as flares, coronal mass ejections (CMEs), and high-speed solar wind streams. These events have a profound impact on the upper atmospheres of planets, including Earth, and shape the radiation environment of the heliosphere. Collectively, their influence is recognized as space weather, which can disrupt satellite operations, navigation systems, communication infrastructure, and even power grids on Earth. Therefore, understanding the solar cycle is essential for anticipating space weather risks. Understanding the underlying mechanisms that govern solar magnetic activity also offer fundamental insights on the behaviour of the magnetized plasma in cosmos.

The Sun, being the nearest star to Earth, serves as an exceptional laboratory for investigating the detailed physics of magnetic cycles that are believed to operate in other solar-like stars. Solar magnetic activity is intimately linked to the approximately 11-year sunspot cycle, a visible manifestation of the Sun's internal magnetic dynamo. For example, solar energetic events are far more frequent and intense during solar maximum, when the Sun's magnetic field is most dynamic and complex, and sunspot numbers peak. During this phase, the increased number of active regions and magnetic field reconfigurations enhances the likelihood of explosive energy release through reconnection processes. Conversely, during solar minimum, such energetic events become rare due to the Sun's relatively stable and weaker magnetic configuration. Since the number of sunspots varies cyclically, accurately predicting the strength and timing of future solar cycles is crucial, as the amplitude of the sunspot cycle changes from one cycle to the next. However, despite

significant progress, reliable prediction of solar cycle strength remains a long-standing challenge in solar physics. The challenge arises due to the nonlinear and stochastic nature of the solar dynamo process, which operates within the Sun's interior and on its surface. This brings forward a fundamental question: What drives the irregularities and variability observed in the solar cycle? Understanding this would not only aid in predicting solar activity but may also shed light on how magnetic variability influences the structure and dynamics of the heliosphere – the vast bubble carved out by the solar wind in the interstellar medium. It is to be noted that variability in the solar magnetic field affects the total and open solar magnetic flux, which in turn modulates cosmic ray fluxes reaching Earth and influences long-term space weather conditions.

Another important aspect of understanding the Sun's dynamics is that the generation and evolution of the Sun's magnetic fields are governed by complex interactions between plasma flows and magnetic fields within its convective zone and across the solar surface. Key processes such as differential rotation, meridional flow, and turbulent convective motions redistribute magnetic flux on the surface, leading to observable large-scale patterns such as the emergence of bipolar magnetic regions (BMRs) and polar field reversals. Studying these surface processes and their coupling with the solar atmosphere is critical to decoding the observed behavior of the Sun.

This doctoral research focuses on understanding these magnetic processes through a combination of observational data analysis, analytical theory, and advanced numerical modelling techniques. In particular, we have developed and employed a data-driven Surface Flux Transport (SFT) model, named SPhoTraM, to simulate the long-term evolution of the solar surface magnetic field. This model helps in probing the origin of solar cycle variability, predicting polar field buildup, and evaluating solar cycle precursors. Furthermore, by coupling SFT simulations with the coronal magnetic field model, such as the full Magnetohydrodynamic (MHD) model or the Potential Field Source Surface (PFSS) extrapolation technique, we have investigated how photospheric field distributions affect the global coronal structure and the heliospheric magnetic field.

We begin this thesis with **Chapter 1**, which provides a brief introduction connecting the Sun's interior to the outer heliosphere, highlighting the physical processes behind the Sun's variability as reflected in observations.

In **Chapter 2**, we present the numerical models employed to address the various scientific questions explored in this thesis. The chapter primarily focuses on the development of the data-driven surface flux transport model, SPhoTraM, along with an extensive parameter space study to investigate the underlying physics captured by the SFT framework. Additionally, we provide an overview of coronal magnetic field extrapolation techniques, including the Potential Field Source Surface (PFSS) model and the Alfvén Wave Solar Model (AWSoM), as well as a brief introduction to solar dynamo models, discussing key parameters and boundary condition implementations. These models are important tools for studying the Sun's interior, surface and atmosphere as well.

**Chapter 3** introduces an algebraic method for estimating the Sun's axial dipole moment using historical sunspot observations. Using this approach, we reconstruct the dipole moment over the past century and demonstrate its potential for forecasting future solar cycle strength, which we apply in the case of Solar Cycle 25. Notably, this simplified analytic framework reinforces the significance of the Babcock–Leighton mechanism, offering a more efficient and less parameter-dependent alternative to complex numerical simulations.

In **Chapter 4**, we demonstrate that even a small fraction of anomalous sunspots – particularly anti-Hale regions, which exhibit polarity orientations opposite to the standard Hale's law, and anti-Joy regions, which possess abnormal tilt angles – can significantly influence the evolution of the polar flux and the solar axial dipole moment, thereby affecting the amplitude of the subsequent solar cycle. We also investigate various emergence statistics by altering the spatio-temporal distribution of these anomalous active regions to identify which types exert the greatest impact on solar cycle variability.

**Chapter 5** investigates the physical basis behind the sharp fall from Solar Cycle 19 to 20 and finds that stochastic variations in tilt and polarity of sunspot emergences can fully explain extreme solar variability. It also establishes that the stochasticity is the primary driver of solar cycle irregularities over the centennial timescales.

In **Chapter 6**, we address the question, which polar precursor – hemispheric polar flux or the global axial dipole moment – better predicts the solar cycle. Using century-scale solar cycle simulations and observational data, we find that the axial dipole moment consistently serves as a more reliable candidate for solar cycle forecasting (both in amplitude

and peak timing) over the polar flux.

**Chapter 7** demonstrates that polar filaments, which trace the evolution of the Sun's large-scale magnetic field, can serve as reliable precursors to polar flux and thereby the strength of future solar cycles. This study also establishes a clear connection between the temporal variations of polar filaments and the Babcock–Leighton (BL) process, highlighting their role in the surface field evolution that governs solar cycle modulation.

**Chapter 8** investigates whether the large-scale coronal magnetic field retains memory during the period of solar maximum, when solar activity is at its peak. To examine this, we utilize the event of the total solar eclipse on April 8, 2024, to validate our magnetic field predictions obtained from the Surface Flux Transport Model (SPhoTraM) coupled with the coronal magnetic field model (AWSoM). The comparison reveals that the large-scale coronal structure preserves its magnetic memory even near the solar maximum.

Finally, in **Chapter 9**, we reconstruct a century-long time series of the open solar flux by coupling SPhoTraM with the PFSS extrapolation model and dynamically adjusting the source surface height to optimize the interplanetary magnetic field variations with in situ data. This work addresses the open solar flux problem directly and reveals the decline of open flux after Cycle 21 and the end of the Modern Grand Maximum.

In a nutshell, in this thesis, we primarily explore the physical basis of the variations in the Sun's magnetic output and how these variations influence interplanetary space. Together, these efforts contribute to the development of tools for solar cycle prediction, deepen our understanding of the physical processes driving the solar dynamo, improve our ability to model and understand the Sun's corona, improve the reconstruction of open solar flux, and ultimately strengthen our capacity to forecast space weather events.

**It is noted that Chapters 3 through 9 (except Chapter 7) of this thesis present the primary outcomes of the research work and are directly adapted from the author's published and submitted research manuscripts. Chapter 7 is based on collaborative research, and only the portions corresponding to the author's specific contributions are included in this thesis.**

## List of Publications

The following peer-reviewed publications have been produced as part of the research pre-

sented in this thesis:

1. **Pal, Shaonwita**, Bhowmik, Prantika, Mahajan, S. Sushant and Nandy, Dibyendu, "Impact of Anomalous Active Regions on the Large-scale Magnetic Field of the Sun", 2023, *Astrophysical Journal*, 953 (1), 13. DOI

2. **Pal Shaonwita** and Nandy Dibyendu, "Algebraic quantification of the contribution of active regions to the Sun's dipole moment: applications to century-scale polar field estimates and solar cycle forecasting", 2024, *Monthly Notices of the Royal Astronomical Society*, Volume(Issue), 531 (1), 1546-1553. DOI

3. **Pal Shaonwita** and Nandy Dibyendu, "Extreme Fluctuations in the Sun's Activity over the Modern Maximum: Understanding the Enigmatic Solar Cycles 19-20", 2025, *Astronomy & Astrophysics Letters*. DOI

4. **Pal Shaonwita**, "Which Polar Precursor Better Predicts Solar Cycles: Global Dipole Moment or Hemispheric Polar Flux of the Sun?", 2025, *Submitted*.

5. Routh Srinjana, **Pal Shaonwita**, Chatterjee Subhamoy, Nandy Dibyendu, Banerjee Dipankar and Khan Saleem Md, "Polar Filaments Capture High Latitude Solar Poloidal Field Interactions and can Foretell the Future Sunspot Cycle Amplitude before Polar Field Precursors", 2025, *Accepted to Astrophysical Journal Letters*. DOI

6. **Pal Shaonwita**, Dash Soumyaranjan, Hazra, Soumitra and Nandy Dibyendu, "The Sun's corona has a memory of large-scale magnetism", 2025, *Submitted*.

7. **Pal Shaonwita** and Nandy Dibyendu, "Reconstruction of Century-scale Open Solar Flux utilizing Physics-based Data-driven Models", 2025, *In preparation*.

Additional publications by the author, not directly included in this thesis, are listed here:

8. Nandy, Dibyendu, Baruah, Yoshita, Bhowmik, Prantika, Dash Soumyaranjan, Gupta Sakshi, Hazra Soumitra, Lekshmi B, Pal Sanchita, **Pal Shaonwita**, Roy Souvik, Saha Chitradeep and Sinha Suvadip, "Causality in heliophysics: Magnetic fields

as a bridge between the Sun's interior and the Earth's space environment", 2023, *Journal of Atmospheric and Solar-Terrestrial Physics*, 106081. DOI

**9**. Tripathi, Durgesh et al. (including **Pal Shaonwita**), "Critical Science Plan of SUIT", 2025, *Submitted to Solar Physics*.

# Contents

# List of Figures

# List of Tables

# Chapter 1

# Introduction

Figure 1.1: This image represents a 10th-century basalt sculpture of Surya, the Hindu Sun God, crafted in Bihar. Now it is displayed at the Indian Museum, Kolkata, India. Credit: Wikipedia

"Om Jaba Kusuma Sankaasham Kashyapeyam Mahadyutim,

Tamorim Sarva Paapagnam Pranatosmi Divakaram."

This mantra is the ancient *Surya Pranam*, a salutation to the Sun which says – "*I bow to the Sun, who is radiant like the hibiscus flower, full of great light and energy, the destroyer of darkness and the remover of all sins – the divine maker of the day.*" Since ancient times, people across different cultures — Indians, Greeks, Egyptians, and Romans — have worshipped the Sun as a powerful life-giving force, long before science could explain

why. Figure 1.1 shows a historical 10th-century statue of the Sun, revered as a deity, now preserved and displayed at the Indian Museum in Kolkata. In Vedic philosophy, the Sun has been worshipped as the dispeller of darkness (*tamaso ma jyotir gamaya*), symbolizing both physical light and the illumination of knowledge. Based on modern science, today we understand that the Sun is indeed the ultimate source of light and energy, sustaining all forms of life on Earth, that the Sun is not just a symbol of divinity, but a real powerhouse in the sky. It is a G-type main-sequence magnetic star — a giant glowing ball of hot plasma held together by gravity, where nuclear fusion in its core produces the energy that lights and warms our planet. Despite being just an ordinary star among billions in the galaxy, the Sun plays an extraordinary role in sustaining life on Earth and driving the dynamics of our solar system. To truly understand how the Sun functions — from the energy produced deep in its core to the solar wind that blows past Earth — we must explore its internal and external structure and the physical processes within. In this Chapter we summarize phenomenological aspects of diverse domains of the Sun which sustain a range of dynamic activity explored in this thesis.

Particularly in this thesis, we explore the origin of solar magnetic variability in the Sun's near-surface layers and its interior, its influence on solar coronal structure, to its modulation of the heliospheric open flux. Since these phenomena span multiple layers and physical domains of the Sun, the following sections of this introduction provide a concise synopsis of the relevant background necessary to appreciate the context and motivation of the work presented in this thesis.

## 1.1 The Sun: Understanding its Structure and Plasma Flows

### 1.1.1 Internal and External Structure of the Sun

The Sun's structure is broadly divided into two main domains: the internal (or interior) structure and the external (or atmospheric) structure. The layers of the Sun are depicted in Figure 1.2. Internally, the Sun consists of four primary layers: the core, the radiative zone, the tachocline, and the convective zone. The **core** ($0 - 0.25\ R_\odot$) is the site of thermonuclear

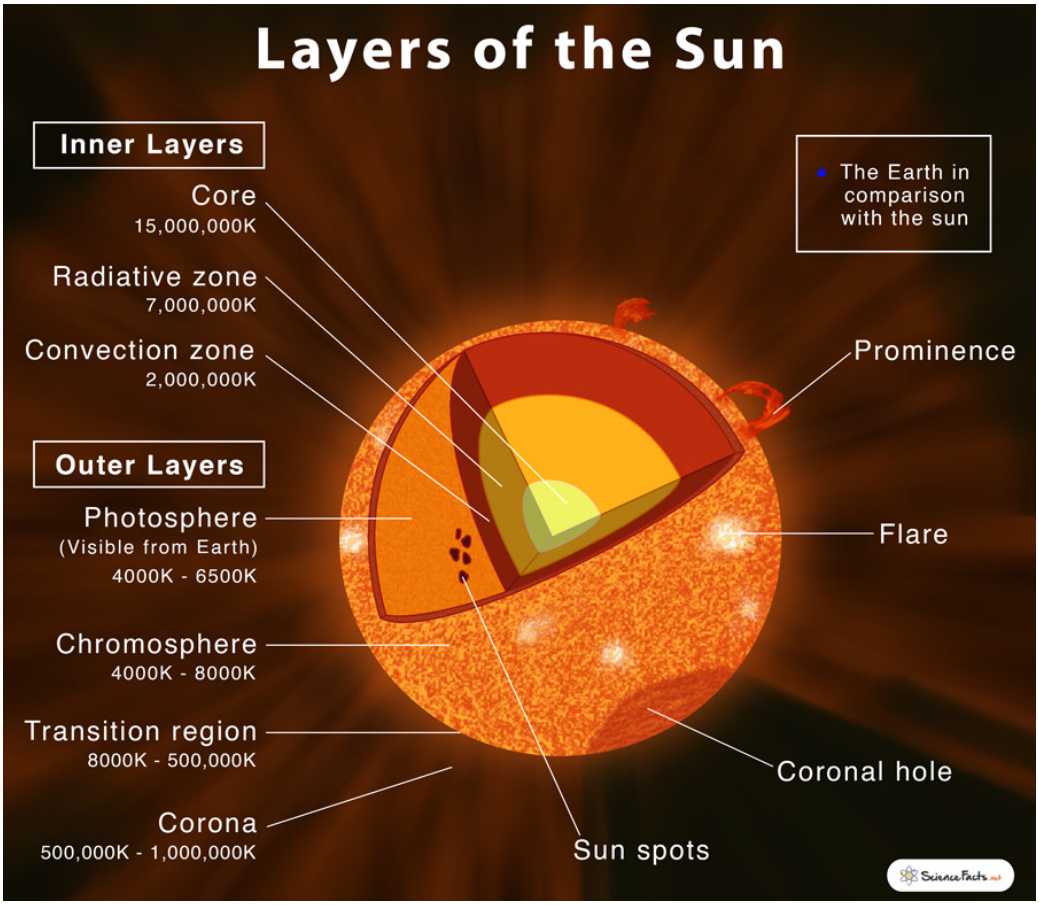


Figure 1.2: A cartoon image of the internal and external structure of the Sun. Credit: Science-facts.net

fusion where hydrogen nuclei combine to form helium, releasing enormous amounts of energy primarily in the form of gamma-ray photons, neutrinos, and the kinetic energy of helium nuclei and positrons.

Surrounding the core is the **radiative zone** (0.25 – 0.70 $R_\odot$), where energy is transported outward via radiative diffusion. Photons in this region scatter countless times, taking thousands to millions of years to escape. Beyond this lies the **convective zone** (0.70 – 1.0 $R_\odot$), extending up to the visible surface (the photosphere). Here, energy is carried outward by convective motions of hot plasma, forming dynamic structures like granules and supergranules. In the interface between the radiative and convection zone there is a thin, shear layer, known as the **tachocline** ($\sim 0.695R_\odot - 0.725R_\odot$). Here, the transition from rigid-body rotation in the radiative zone to latitudinal differential rotation in the convection zone results in strong shear, believed to amplify toroidal magnetic fields, critical in the solar dynamo process.

Externally, the Sun's structure includes the photosphere, chromosphere, transition region, and corona. The **photosphere** is the visible surface of the Sun, from which most of the Sun's light is emitted. Above this layer lies the **chromosphere**, a region of increasing temperature that emits strongly in certain spectral lines, such as H$\alpha$. The outermost layer, the **solar corona**, extends millions of kilometers into space and is characterized by its extremely high temperatures (several million Kelvin), although it is much less dense. The corona is the source of the solar wind and is strongly structured by the Sun's magnetic field, giving rise to features such as coronal loops and helmet streamers. Together, the internal and external layers of the Sun form a complex, dynamic system governed by the interplay of plasma physics, thermodynamics, and magnetohydrodynamics, which ultimately drive solar variability and impact the entire heliosphere.

### 1.1.2 Plasma Flows in the Solar Interior

The solar interior is a dynamic environment filled with highly ionized plasma. Unlike the solid or liquid interiors of terrestrial planets, the Sun's interior is composed of an electrically conducting fluid medium, which supports complex and large-scale flow patterns. These plasma flows play a fundamental role in the transport of energy and magnetic flux, as well as in the operation of the solar dynamo – the process that sustains the Sun's mag-

netic activity cycle. There are three main types of plasma flows that dominate the solar interior: differential rotation, meridional circulation, and convective turbulence.

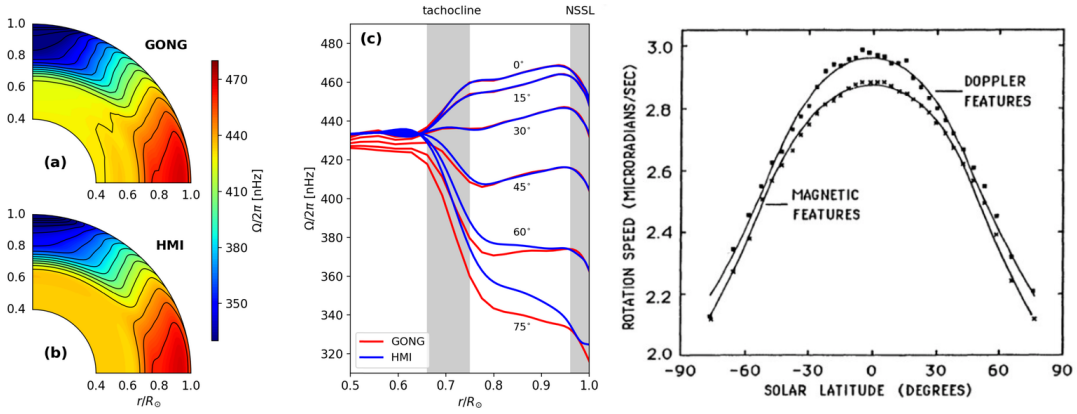


Figure 1.3: Differential rotation profile of the Sun. The first panel shows the mean solar rotation profile obtained from (a) GONG and (b) HMI data, where the overlaid contours represent lines of constant angular velocity. The middle panel displays radial cuts of rotation rate at fixed latitudes, highlighting how rotation varies with depth. Credit: Kichatinov (1990). The third panel presents the surface differential rotation profile measured using feature tracking techniques, based on data from Snodgrass and Ulrich (1990).

**Differential rotation** refers to the variation in the angular velocity of the solar plasma with latitude and depth. Helioseismic observations have revealed that the equatorial regions of the Sun rotate faster (∼25 days) than the poles (∼35 days), and that this latitudinal rotational shear persists into the convection zone (Schou et al., 1998; Paternò, 2010; Kitchatinov, 2011; Kosovichev and Korzennik, 2023; Mahajan et al., 2024). This radial and latitudinal shear is most pronounced at the base of the convection zone in a region known as the tachocline – a thin, shear layer. The toroidal component of the magnetic field generation is thought to take place throughout the solar convection zone, and then it amplifies and stores this field in the tachocline region (Nandy, 2002; Rempel, 2005; Miesch et al., 2006; Muñoz-Jaramillo et al., 2009; Balbus and Latter, 2010; Charbonneau, 2020). The differential rotation profile and its latitudinal variation inside the convection zone and solar surface are depicted in Figure 1.3.

**Meridional circulation** is a large-scale flow pattern in which plasma moves poleward near the solar surface ($\sim$ 10–20 m s$^{-1}$) and equatorward at the base of the convection zone. It was first observed in the late 1970s by Howard (1979) and Duvall (1979) using feature

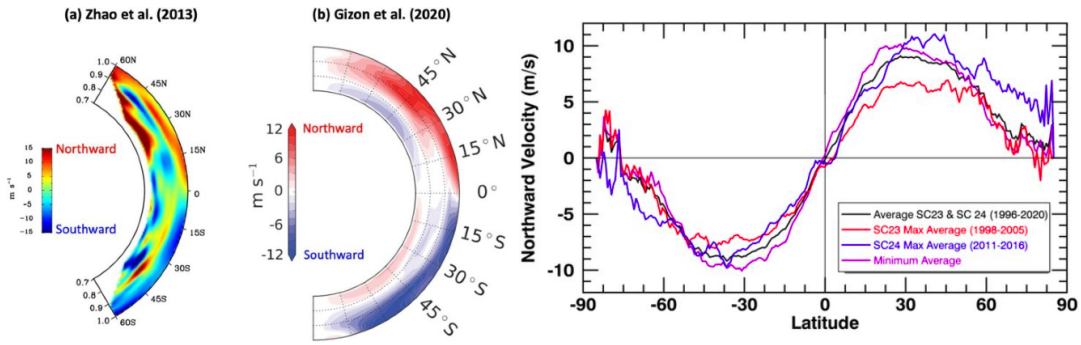


Figure 1.4: Meridional flow profile of the Sun. The first and second panels show the latitudinal component of the meridional flow inferred from time-distance local helioseismology. These measurements were obtained by Zhao et al. (2013) using SDO/HMI data (2010–2012) and by Gizon et al. (2020) using GONG data (2008–2019), respectively. Red and blue shades indicate northward and southward flows. The third panel presents average meridional flow profiles derived from magnetic feature tracking using MDI and HMI data across different time periods. The red and blue curves correspond to flow during the maxima of Solar Cycles 23 and 24, respectively. The purple line represents the cycle minimum, and the black curve shows the average over both cycles. Image credit: Norton et al. (2023).

tracking, decades after it was theoretically proposed by Vogt and Eddington (Eddington, 1925). Later studies and local helioseismology confirmed its peak near 30° latitude (Chen and Zhao, 2017; Rajaguru and Antia, 2020; Gizon et al., 2020; Hanasoge, 2022). Though its exact profile and subsurface return flow remain debated, it is widely accepted that the flow vanishes at the equator and poles, peaking at mid-latitudes (see third panel of Figure 1.4). The circulation likely arises from a combination of Reynolds stresses, Coriolis forces, and anisotropic convective transport, with the return flow depth estimated between 0.7 and 0.87$R_\odot$ (Hathaway, 2012; Zhao et al., 2013). Although much slower than differential rotational flows, meridional circulation is thought to be essential for transporting magnetic flux across latitudes and redistributing it over the solar surface. It helps in the reversal and build-up of the Sun's polar magnetic fields and modulates the solar cycle period in flux-transport dynamo models. The meridional circulation profile and it's latitudinal variation inside the convection zone and solar surface is depicted in Figure 1.4.

**Convective turbulence**, which dominates the outer third of the solar radius, arises from the unstable temperature gradient in the convection zone. At the solar surface, the smallest observable scale of convection is the **granular flow**, consisting of cells approximately 1,000 km in diameter with lifetimes of 5–10 minutes. Each granule represents a convective cell where hot plasma rises at the center and cooler plasma sinks along the edges, giving

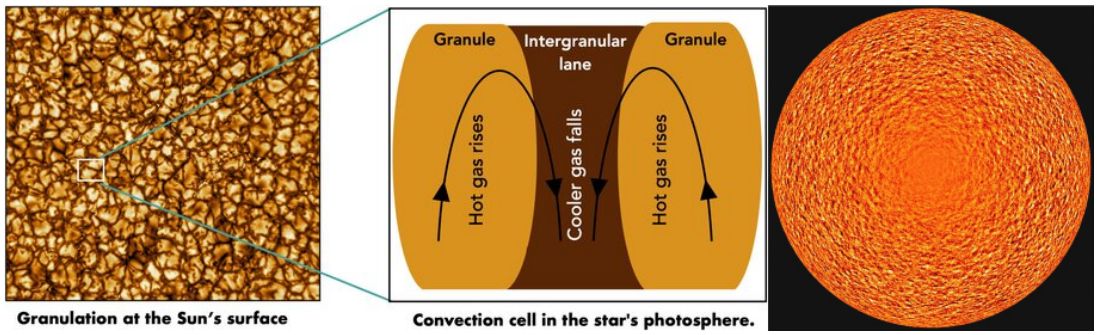


Figure 1.5: Solar granulation and supergranulation. The first panel shows a high-resolution image of the Sun's surface taken at a wavelength of 789 nm using the Daniel K. Inouye Solar Telescope (NSO/AURA/NSF). The image reveals the granulation pattern—cell-like structures known as granules, ranging in size from approximately 30 to 1500 km. The second panel presents a schematic cross-section of a granule, illustrating the convective motion: hot plasma rises at the center of granules (orange region) and cools as it sinks down along the darker intergranular lanes (brown region). Credit: Dalal et al. (2023). The third panel displays a Dopplergram revealing the supergranulation pattern on the solar surface, captured by SOHO/MDI (ESA/NASA). Supergranules are larger convective cells, typically around 30,000 km in diameter, and are visible through horizontal flow patterns in Doppler velocity maps.

rise to the characteristic mottled appearance of the photosphere (Dalal et al., 2023). A larger convective pattern known as **supergranulation** spans 20,000–30,000 km and persists for about 1–2 days. These flows are predominantly horizontal and help organize magnetic fields into the network patterns observed on the Sun (Rieutord and Rincon, 2010; Hanasoge and Sreenivasan, 2014). These convective motions are not only responsible for transporting energy outward but also generate the small-scale magnetic fields observed in the quiet Sun. Additionally, turbulent convection contributes to the $\alpha$-effect in mean-field dynamo theory, wherein helical flows twist and regenerate poloidal magnetic fields from toroidal ones. Figure 1.5 denotes such granular and supergranular convective flows on the solar surface.

Apart from the large-scale meridional circulation and differential rotation, **turbulent pumping** in the solar convection zone acts as an additional mechanism of magnetic field transport. It arises due to the interaction between small-scale convective turbulence and the large-scale magnetic field, effectively producing a net advective transport of magnetic flux. Turbulent pumping can have radial and latitudinal components. The radial (downward) pumping tends to confine magnetic flux toward deeper layers of the convection zone, thereby reducing magnetic diffusion losses at the surface. Meanwhile, the latitudinal pumping can influence the migration of magnetic flux toward the equator or poles,

depending on the convective structure.

### 1.1.3 Helioseismic Probes of the Solar Interior

Helioseismology is the study of pressure-driven acoustic oscillations (commonly called *p*-modes) on the Sun's surface, which are generated by turbulent convection beneath the photosphere (Christensen-Dalsgaard, 2002; Basu and Antia, 2008). These oscillations propagate as acoustic waves through the solar interior and are sensitive to the Sun's internal structure and dynamics. By measuring the frequencies and spatial distribution of these waves, scientists can infer properties of the solar interior – similar to how seismology reveals Earth's internal structure through the study of earthquakes (Libbrecht and Woodard, 1991).

Observationally, helioseismology involves monitoring Doppler shifts and brightness variations on the solar surface, typically using instruments aboard space missions like Solar and Heliospheric Observatory / Michelson Doppler Imager (SOHO/MDI) or Solar Dynamics Observatory / Helioseismic and Magnetic Imager (SDO/HMI), or ground-based networks like Global Oscillation Network Group (GONG). These observations reveal standing wave patterns that form due to constructive interference of sound waves trapped within the solar interior. Helioseismology has led to major breakthroughs in our understanding of the Sun's interior, including: 1) Determining the depth of the convection zone (approximately $0.71R_{\odot}$) (Zhao et al., 2009), 2) Mapping the solar internal rotation profile, which reveals differential rotation in the convection zone and nearly uniform rotation in the radiative zone (Charbonneau et al., 1999; Gizon et al., 2020; Mahajan et al., 2024), and 3) Identifying the tachocline region (Zhao et al., 2009) e.t.c.

## 1.2 Solar Magnetism: Sunspots and the Solar Cycle

Sunspots have been observed since antiquity, with early records from Chinese and Korean astronomers noting dark blemishes on the Sun visible to the naked eye. A significant turning point came in the early 17th century, shortly after the invention of the telescope. In 1611, several European astronomers – including Galileo Galilei, Christoph Scheiner, and Thomas Harriot – began detailed telescopic observations of sunspots. Initially, some

astronomers believed these dark spots were planets transiting the Sun, such as Mercury. Johannes Fabricius and Galileo Galilei are the first to publish observations of sunspots, clarified that these features moved across the solar disk in a way inconsistent with planetary orbits, establishing their solar origin. These early studies not only confirmed that sunspots were features on the Sun itself but also provided the first evidence of solar rotation.

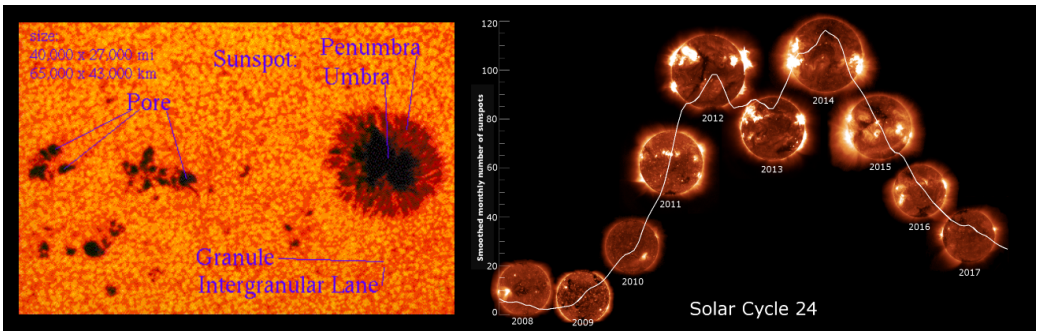


Figure 1.6: Sunspot structure and solar activity over Solar Cycle 24. The left panel illustrates the internal structure of a sunspot, highlighting features such as the dark umbra, the surrounding penumbra, granule and intergranular lane. Credit: NASA. The right panel shows the evolution of solar activity throughout Solar Cycle 24, composed of a series of X-ray Telescope (XRT) images taken annually since 2008. This sequence, captured by the Hinode Observatory, reveals changes in coronal brightness and complexity as the cycle progresses.

Sunspots are dark, magnetically active regions on the solar photosphere that appear darker than their surroundings due to being cooler by about 1500 K, as seen in the first panel of Figure 1.6. Sun's magnetism was first discovered by Hale (1908). Sunspots typically appear in bipolar pairs with opposite magnetic polarities and are manifestations of concentrated magnetic flux tubes emerging through the convective layer to the surface. Modern magnetograms reveal that sunspots are intensely magnetized regions, with field strengths of up to several thousand gauss, much stronger than the quiet photosphere. Figure 1.7 shows the sunspots as bipolar magnetic regions (BMRs) on the solar surface observed from HMI magnetogram.

Systematic sunspot observations began in the 19th century, with a major breakthrough by Samuel Schwabe (1844), who, after nearly two decades of visual tracking, discovered the number and distribution of sunspots vary over time in a quasi-periodic fashion, known as the *solar cycle*, which lasts approximately 11 years (Hathaway, 2010a; Cliver, 2014). This cycle is characterized by the gradual rise and fall of sunspot numbers, starting from a minimum phase with few sunspots, building up to a maximum with many active regions, and then declining again (see the second panel of Figure 1.6). Historical reconstruction

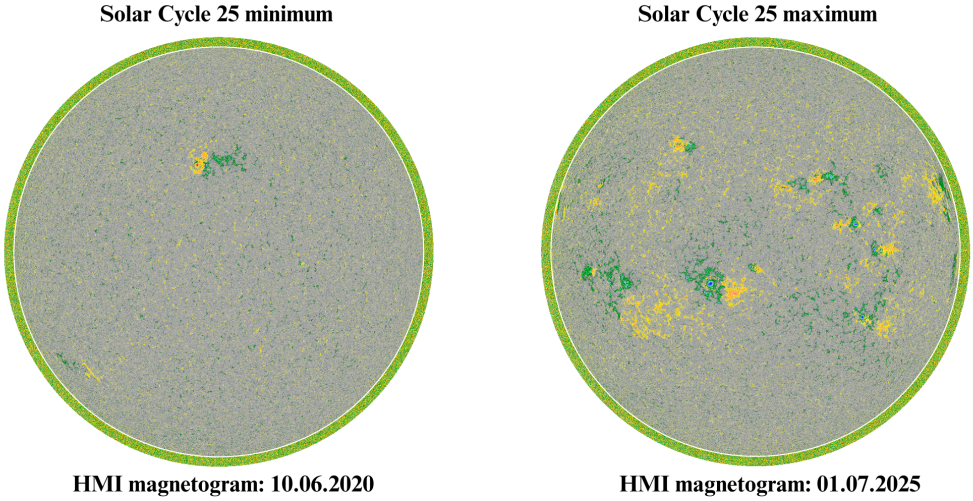


Figure 1.7: Magnetic field associated with sunspots. The first panel shows an HMI magnetogram of the solar surface during the minimum of Solar Cycle 25, observed on June 10, 2020. The second panel presents a magnetogram from the maximum phase of Cycle 25, taken on July 1, 2025. In both panels, red–yellow colors indicate regions of negative magnetic polarity, while blue–green colors represent positive magnetic polarity.

by Wolf identified Cycle 1 (which is named arbitarily) as beginning in 1755. With time, the scope of observations expanded to include sunspot positions, areas and numbers, now compiled in modern datasets like RGO/USAF/NOAA Data Centre (2023), SILSO World Data Center (2019) etc (see sunspot time serie in Figure 1.8). Beyond the regularly observed sunspot databases, considerable effort has been made to reconstruct earlier solar cycles, as illustrated in Figure 1.8. These datasets reveal variations in cycle strength and support the identification of sunspot patterns such as the butterfly diagram, first introduced by Edward and Annie Maunder in 1904. Observationally, the sunspots tend to emerge at higher latitudes early in the cycle and migrate equatorward as the cycle progresses. This is known as **Sporer's law** (Ivanov and Miletsky, 2014). This equatorward migration pattern appears as a a butterfly wing-like structure and is hence named the *sunspot butterfly diagram*. Figure 1.9 reveals the magnetic butterfly diagram, which plots sunspot latitudes over time. This diagram illustrates that the magnetic polarity of sunspots follows well-defined patterns: in each hemisphere, the leading sunspot (in the direction of solar rotation) in a bipolar pair typically maintains the same polarity throughout a cycle, with this polarity reversing from one cycle to the next. Moreover, the polarity pattern of sunspots exhibits hemispheric asymmetry: for a given solar cycle, if the leading sunspots in the Northern Hemisphere possess positive magnetic polarity, those in the Southern Hemisphere will

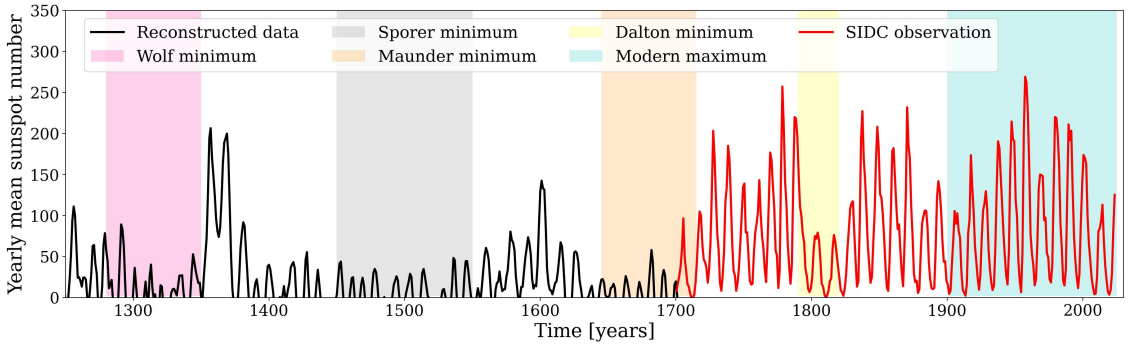


Figure 1.8: Sunspot time series. The black curve represents the reconstructed sunspot number (Usoskin, 2023) over the past several centuries, while the red curve shows the observed sunspot number from the SIDC/SILSO database. The shaded regions in different colors indicate historical grand minima—periods when solar activity was significantly reduced, such as the Maunder Minimum and Dalton Minimum. The current period is identified as the Modern Maximum, a time of relatively high solar activity.

exhibit negative polarity. This configuration reverses in the subsequent cycle, contributing to the 22-year magnetic (Hale) cycle. This polarity orientation, described by **Hale's law**, implies a magnetic cycle of about 22 years (Muñoz-Jaramillo et al., 2021). Additionally, **Joy's law** describes the systematic tilt of bipolar sunspot pairs with respect to the solar equator, such that the leading spot lies closer to the equator than the following one (positive tilt in the Northern Hemisphere and negative tilt in the Southern Hemisphere) (McClintock and Norton, 2013). A cartoon image illustrating the Hale's law and Joy's law is depicted in Figure 1.10.

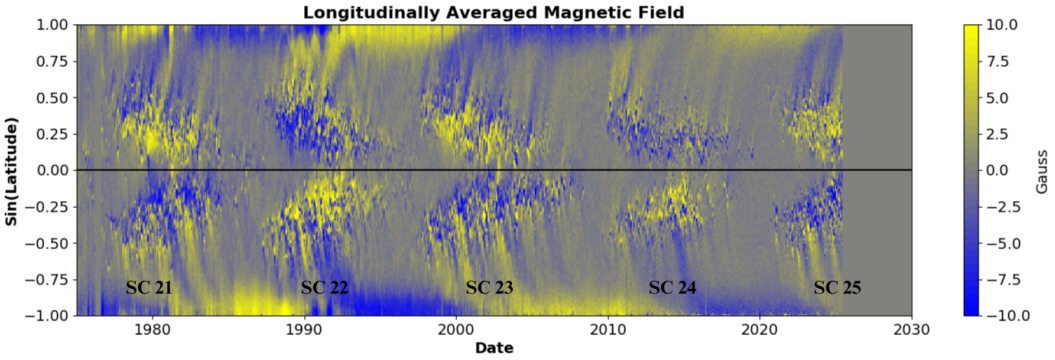


Figure 1.9: Magnetic Butterfly Diagram. This diagram shows the latitudinal distribution of the longitudinally averaged solar surface magnetic field over the past five solar cycles. This average is taken over each Carrington Rotation using data from SOLIS/MDI/HMI. The polar regions exhibit opposite magnetic polarities that reverse around the time of each solar maximum, illustrating the cyclic nature of the Sun's magnetic field evolution. Credit: Hathaway 2025.

Figure 1.9 vividly illustrates the equatorward drift of active region belts with opposite

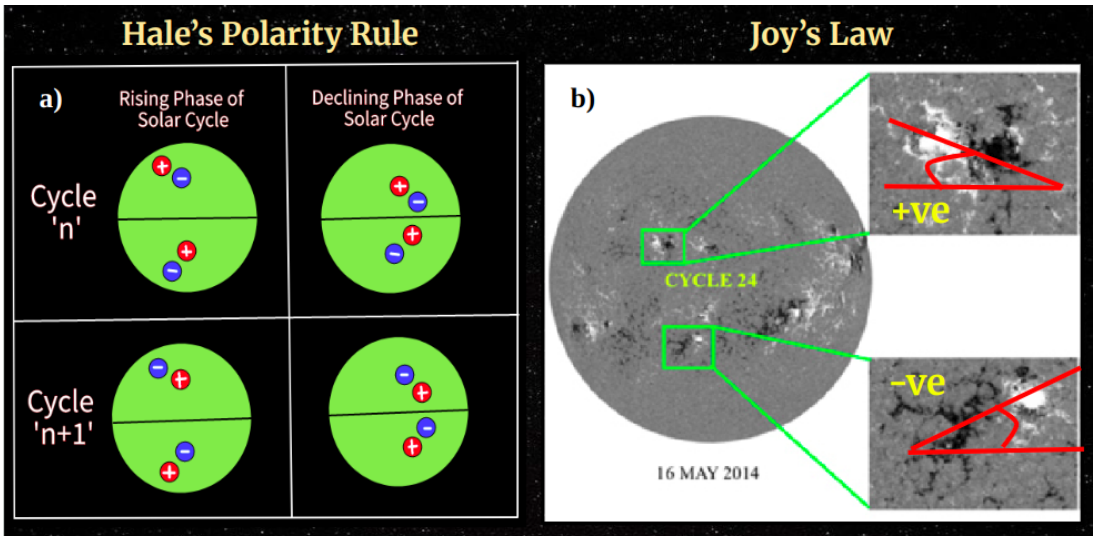


Figure 1.10: Illustration of Hale's Polarity Rule and Joy's Law. This cartoon depicts two fundamental observational laws of solar active regions. Hale's polarity rule states that the leading and trailing sunspots in a bipolar magnetic region (BMR) have opposite magnetic polarities, and that this polarity orientation reverses from one solar cycle to the next and between hemispheres. Joy's Law describes the systematic tilt of BMRs, where the leading polarity lies closer to the equator than the trailing polarity, with the average tilt angle increasing with latitude.

magnetic polarities during each solar cycle (blue and yellow alternately in both hemispheres). As sunspots emerge and decay, the flux of the leading polarity spots from both hemispheres tend to migrate toward the equator (for example, yellow depicts leading polarity in the Northern Hemisphere in Solar Cycle 21), where they almost entirely cancel out through cross-equatorial interaction. Meanwhile, the trailing polarity flux (blue depicts following polarity in the Northern Hemisphere in solar cycle 21) is transported poleward by surface flows. This high-latitude transport leads to the gradual weakening and eventual reversal of the existing polar magnetic fields. During the first half of a cycle, the polar field maintains the same polarity (yellow in the northern hemisphere in solar cycle 21) as the dominant leading spot polarity, while its strength steadily decreases. Around the time of solar maximum, the polar field reverses, and in the declining phase of the cycle, the new polarity begins to strengthen. By solar minimum, the Sun once again attains a well-defined dipolar magnetic configuration, but with reversed polarity compared to the previous cycle (blue in the northern hemisphere in solar cycle 21). This cyclical process of polar field reversal and regeneration is the hallmark of the Babcock–Leighton mechanism (Babcock, 1961; Leighton, 1969), a surface-driven dynamo process that plays a central role in the solar magnetic cycle (Babcock, 1961; Leighton, 1969; Charbonneau and Dikpati, 2000;

Hazra et al., 2023). The individual contributions of surface flows and active region properties in this mechanism are described in detail in later chapters.

The solar cycle is not strictly periodic; variations in amplitude and duration are evident across centuries of sunspot records. For instance, cycle 19 (1954–1964) was among the strongest recorded, while cycle 24 (2008–2019) was one of the weakest cycles. Extended periods of low activity, such as the Maunder Minimum (1645–1715), as seen in Figure 1.8, are also captured in historical sunspot archives and remain a topic of ongoing scientific investigation.

## 1.3 Application of Magnetohydrodynamics to Understand the Solar Magnetism

The Sun is made up of plasma, the fourth state of matter. What makes plasma special? It consists of freely moving positive and negative charges, unlike a neutral gas, where the charges are bound within atoms. Now, one might wonder: if the number of positive and negative charges in a small volume of plasma is equal, is it not just like a non-ionized gas? The answer is – no. Despite being quasi-neutral (overall charge-balanced), plasma behaves very differently. In a non-ionized gas, there are no free charges, and hence no electric currents. But in plasma, the free charges can move collectively, producing electric currents and where there are currents, there are magnetic fields. So even though a plasma element doesn't build up large electric fields due to its neutrality, it can – and does – generate large-scale magnetic fields, provided there are plasma motions.

### 1.3.1 Basic Equations and Physical Principles

In a plasma system, a strong magnetic field can confine charged particles within localized regions for a sufficiently long time. This confinement allows the plasma to behave like a continuous fluid on macroscopic scales. With this fluid-like behavior in mind, we can couple the equations of fluid dynamics with Maxwell's equations, giving rise to the framework known as magnetohydrodynamics (MHD) (Choudhuri, 1998). But when is the MHD approximation valid? Let's break it down:

(a) The plasma must behave like a single fluid, meaning charge separation is negligible.

This condition holds when the characteristic length scale of the system is much larger than the Debye length – the scale over which electric fields are shielded.

(b) The plasma should be non-relativistic and slowly varying in time, remaining close to thermal equilibrium. In simpler terms, the typical timescales of the system must be much longer than the inverse of the plasma frequency.

(c) The plasma must be globally neutral, though locally it can support currents, following the relation J = $\sigma$E, where J is the current density, $\sigma$ is the conductivity, and E is the electric field.

So, at its core, MHD is the study of the interaction between plasma and magnetic fields, and this interaction is precisely what governs much of the Sun's dynamic behavior – from solar cycle to the solar corona.

One of the primary components of the MHD framework is the well-known Navier–Stokes equation (NSE), which describes the motion of a fluid under the influence of body forces, pressure gradients, Lorentz forces, and viscous forces.

$$\frac{\partial \mathbf{v}}{\partial t} + (\mathbf{v}\cdot\nabla)\mathbf{v} = \mathbf{F} - \frac{1}{\rho}\nabla p + \frac{1}{\rho c}\mathbf{j}\times\mathbf{B} + \nu\nabla^2\mathbf{v} \tag{1.1}$$

For non-relativistic plasmas, we can express Ampère's law (neglecting the displacement current) as $\nabla\times\mathbf{B} = \frac{4\pi}{c}\mathbf{j}$ which allows the magnetic force term (the third term on the right-hand side of the velocity equation) to be written as $\frac{1}{4\pi\rho}(\nabla\times\mathbf{B})\times\mathbf{B}$. After expanding this term, the velocity equation takes the following modified form:

$$\frac{\partial \mathbf{v}}{\partial t} + (\mathbf{v}\cdot\nabla)\mathbf{v} = \mathbf{F} - \frac{1}{\rho}\nabla\left(p + \frac{B^2}{8\pi}\right) + \frac{(\mathbf{B}\cdot\nabla)\mathbf{B}}{4\pi\rho} + \nu\nabla^2\mathbf{v} \tag{1.2}$$

This equation indicates that the magnetic force (Lorentz force) can be decomposed into two components: the magnetic pressure, represented by the term $\frac{\mathbf{B}^2}{8\pi}$ and the magnetic tension force, given by $(\mathbf{B}.\nabla)\mathbf{B}$. The tension term represents a restoring force that acts to straighten curved or bent magnetic field lines, much like tension in an elastic string.

Another important equation in the MHD framework is the magnetic induction equation, which governs the evolution and transport of the magnetic field in the presence of plasma flows. This equation is derived by combining Faraday's law, Ohm's law, and Ampère's law

(neglecting the displacement current).

$$\frac{\partial \mathbf{B}}{\partial t} = \nabla \times (\mathbf{v} \times \mathbf{B}) + \eta \nabla^2 \mathbf{B} \tag{1.3}$$

The magnetic induction equation consists of two key terms, each representing distinct physical processes. The first term $\nabla \times (\mathbf{v} \times \mathbf{B})$ acts as the **source term** and is primarily responsible for the generation and evolution of the magnetic field, along with how they are advected by the plasma flow and how they are stretched, compressed, or twisted due to velocity gradients and plasma motions. The second term $\eta \nabla^2 \mathbf{B}$ is the **diffusion term**, which leads to the decay and diffusive mixing of the magnetic field, typically due to turbulent or resistive dissipation in strongly convective systems.

### 1.3.2 Magnetic Field Line Freezing: Alfvén's Theorem

The relative importance of these two terms is quantified by the dimensionless magnetic Reynolds number, defined as $R_m = \frac{VL}{\eta}$, where $V$ is a characteristic velocity, $L$ is a typical length scale of the system, and $\eta$ is the magnetic diffusivity. In astrophysical systems such as the Sun, both $V$ and $L$ are very large, resulting in $R_m \gg 1$. This implies that the advection (source) term dominates over the diffusion (decay) term. Under this condition, the induction equation simplifies to ideal MHD: $\frac{\partial \mathbf{B}}{\partial t} = \nabla \times (\mathbf{v} \times \mathbf{B})$. It means that in astrophysical systems, it is easier to sustain magnetic fields. This leads to the well-known **flux-freezing theorem**, or **Alfvén's theorem**, proposed by the physicist Hannes Olof Gösta Alfvén. The theorem states that for any magnetic loop moving with the plasma flow, the magnetic flux through the surface bounded by the loop remains constant in time: $\frac{\partial}{\partial t} \int \mathbf{B} \cdot \mathbf{dS} = 0$

This implies that magnetic field lines are frozen into the plasma – they just move with it. So, if a plasma column is twisted or bent, the magnetic field lines will be twisted or bent in the same way. For his foundational contribution to MHD, Alfvén was awarded the Nobel Prize in Physics in 1970.

In regions of low diffusivity (high $R_m$), the field lines are "frozen" into the plasma and move with the flow. In contrast, diffusion dominates in high-diffusivity zones, allowing reconnection and field annihilation. Therefore, to study a system – particularly to understand the self-consistent generation, dissipation, transport, and evolution of magnetic fields due to plasma motion – we must solve the full MHD equations, specifically Equations (1.2)

and (1.3), in conjunction with three additional equations: the equation of state, the energy equation, and the equation of continuity.

### 1.3.3 The Plasma-$\beta$ Parameter

It is evident that the MHD system is inherently dynamic. However, in a state of static equilibrium, when all forces are balanced, the left-hand side of Equation (1.2), as well as the viscous term $\nu\nabla^2\mathbf{v}$, vanish. Neglecting body forces for simplicity and substituting Ampère's law in the form $\nabla \times \mathbf{B} = \frac{4\pi}{c}\mathbf{j}$, the momentum equation reduces to: $\nabla p = \frac{1}{4\pi}(\nabla \times \mathbf{B}) \times \mathbf{B}$. This equation describes a balance between the thermal pressure and the magnetic stress in a static plasma. In this context, a key dimensionless parameter is defined as the **plasma** $\beta$ parameter,

$$\beta = \frac{\text{gas pressure}}{\text{magnetic pressure}} = \frac{p}{\frac{B^2}{8\pi}}$$

This parameter helps determine which type of pressure dominates in a given astrophysical environment. For example, consider a magnetic flux tube embedded in a plasma. If there is no confining force, the tube will tend to expand due to the excess internal pressure. To maintain equilibrium, this expansion must be counteracted by the surrounding gas pressure. In the solar interior, where both temperature and plasma density are high, the gas pressure significantly exceeds the magnetic pressure — i.e., $\beta \gg 1$. In this regime, the flux tube remains unstable to buoyancy. In contrast, in the solar atmosphere (e.g., the corona), the density and gas pressure are much lower, and the magnetic pressure dominates — i.e., $\beta \ll 1$. As a result, flux tubes in these regions may not be confined and tend to expand or diffuse. The variations of plasma-$\beta$ parameter in the solar interior and atmosphere are shown in Figure 1.11.

### 1.3.4 Dynamics of Magnetic Flux Tube

Inside the convection zone, at some localized regions, we find some magnetic fields are concentrated, which are often assumed to be in a cylindrical shape and called magnetic flux tubes. Inside this flux tube, two types of pressure exist: 1) internal gas pressure $p_i$, 2) internal magnetic pressure $p_m$. To be in pressure balance condition across the bounding surface of the flux tube, these two pressures should be balanced by the external gas pressure

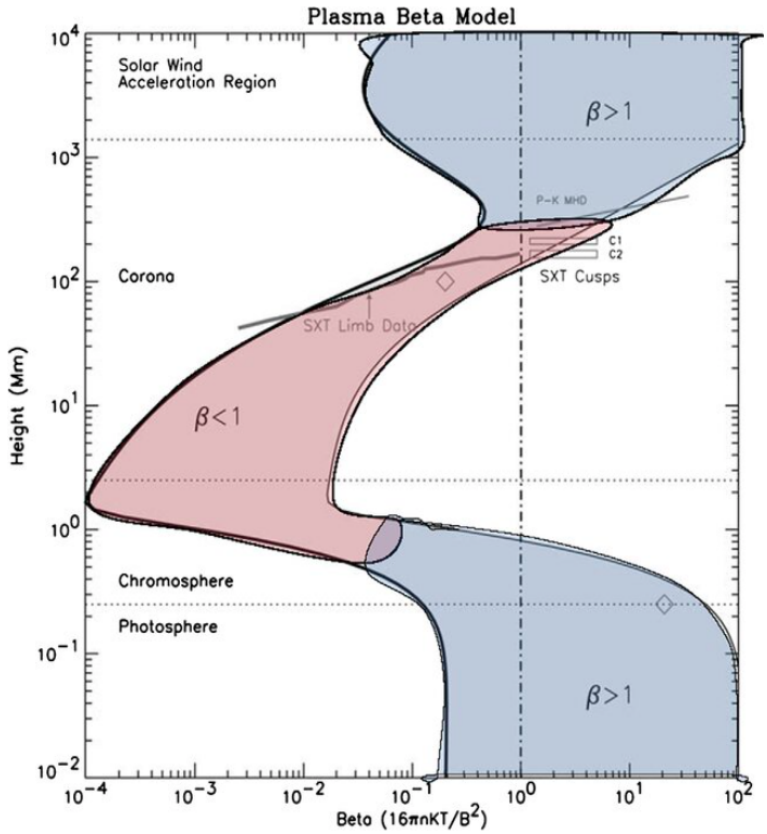


Figure 1.11: Plasma-$\beta$ value in the solar interior and atmosphere. This figure is taken from Wiegelmann et al. (2017), which is modified from Gary (2001), Fig. 3.

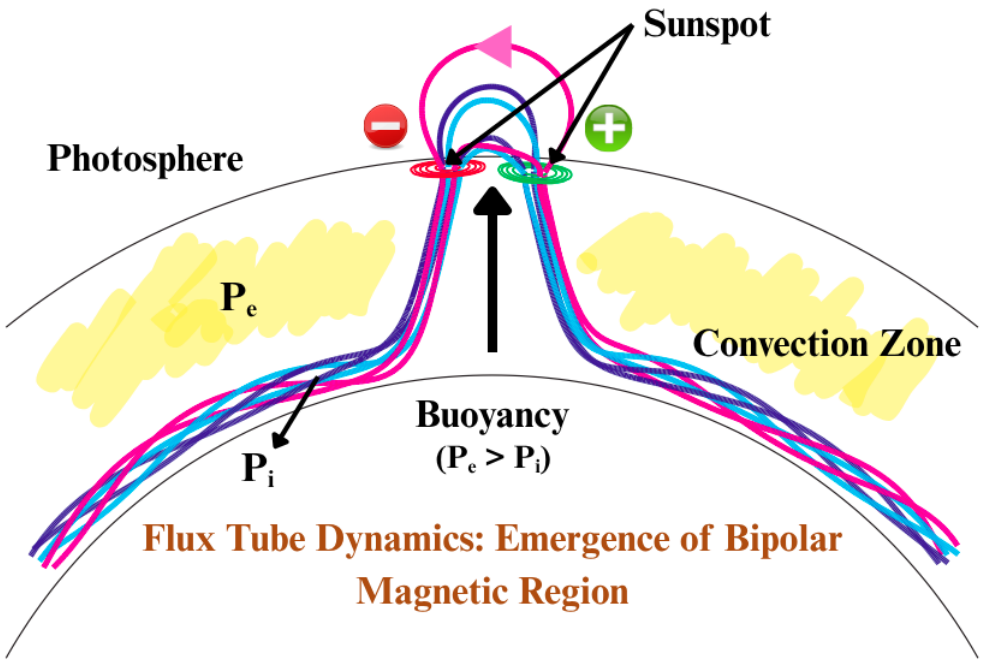


Figure 1.12: Magnetic flux tube dynamics. A magnetic flux tube rises through the solar convection zone due to magnetic buoyancy and emerges at the photosphere as a bipolar pair of sunspots. Image is modified from van Ballegooijen and Mackay (2007) for better illustration.

$p_e$.

This demands that $p_i > p_e$. If we consider ideal gas conditions, then $p_i = \rho RT$ and $p_e = \rho_e RT$, assuming the temperature both inside and outside the flux tube is T. From this, we can see that if the fluid inside the flux tube is lighter, it becomes buoyant. Now, in high Reynolds number systems, such as inside the sun, the flux freezing theorem holds, meaning that magnetic field lines move along with the fluid. As the lighter fluid rises, the magnetic flux tube, as a whole entity, becomes buoyant and rises against gravity. This phenomenon is depicted in Figure 1.12. During the rise of the flux tube, the Coriolis force imparts a tilt to the apex of the flux tube, and the tube can be unstable to ideal instabilities, such as the kink instability (D'Silva and Choudhuri, 1993; Nandy, 2006).

## 1.4 Solar Interior and Photosphere

The first scientific mention of Earth's magnetism came from William Gilbert in 1600, who proposed in his seminal work De Magnete that the Earth itself behaves like a giant magnet. However, until the early twentieth century, it was not known whether other astronomical objects might also possess magnetic fields similar to Earth. A major breakthrough came in 1908, when American astronomer George Ellery Hale applied the Zeeman effect to light from sunspots using a spectroheliograph at the Mount Wilson Observatory (Hale, 1908). He discovered that sunspots are regions of intense magnetic fields. This marked the first detection of a magnetic field beyond Earth, representing a milestone in the development of modern astrophysics.

While Earth's magnetic field is relatively stable and evolves slowly – changing polarity only over geological timescales – the Sun's magnetic field exhibits far more dynamic and periodic behavior. It varies in a cyclic fashion creating the sunspot cycle, as discussed in section 1.2. In the following section, we describe the physics of how the solar magnetic field is generated and sustained in the Sun's interior, and how sunspots emerge and evolve on the photosphere as a manifestation of this deep-seated magnetic dynamics.

### 1.4.1 Solar Dynamo Theory

As discussed in subsection 1.3.1, the Sun satisfies the conditions under which the magnetohydrodynamic (MHD) approximation is valid. Whether plasma flows within the Sun can sustain its magnetic field can be investigated by solving the MHD equations (Equation 1.2 and Equation 1.3), in conjunction with appropriate transport coefficients and an equation of state. To address this problem, two main approaches can be employed: 1) the kinematic approach, and 2) the fully dynamical approach. In the kinematic approach, the velocity field is assumed to be prescribed or externally specified, and only the magnetic induction equation is solved. This method offers significant practical advantages. For a broader discussion on these two approaches the interested readers may refer to Charbonneau (2020); Hazra et al. (2023).

In this section, we will focus on understanding the basic physics of the kinematic dynamo theory, which provides insight into how magnetic fields can be amplified and sustained by plasma flows without solving the full set of MHD equations (Roberts, 1972; MacGregor and Charbonneau, 1997; Choudhuri, 2000; Karak et al., 2014).

Let us begin by considering the solar magnetic field as a combination of two distinct components: 1) A poloidal component, which lies in the meridional plane (the r - $\theta$ plane), and 2) A toroidal component, which lies in the azimuthal direction ($\phi$) around the Sun's rotation axis (Parker, 1955). We start with the Sun at sunspot minimum where the global solar magnetic field is predominantly dipolar, representing the poloidal field configuration. According to the Alfvén flux-freezing theorem, magnetic field lines are "frozen" into the highly conductive solar plasma and thus move with the plasma flow. Due to the Sun's differential rotation, which is faster at the equator than at the poles, the poloidal field lines are gradually sheared and stretched in the azimuthal direction. This process generates a new large-scale toroidal magnetic field from the existing poloidal component. This generation mechanism is known as the $\Omega$-effect (see figure for illustration Figure 1.13). Once the toroidal magnetic field is built up, magnetoconvection consideration suggests that it does not remain uniformly distributed but rather becomes concentrated into magnetic flux tubes within the solar convection zone. When these flux tubes become magnetically buoyant and unstable, they begin to rise through the convection zone, opposing gravitational forces. As the flux tubes ascend and emerge through the photosphere, they do so in the form of

Ω-shaped loops. These emergent structures appear on the solar surface as bipolar sunspot pairs, where the two spots typically show opposite magnetic polarities and are located in opposite hemispheres, consistent with Hale's polarity law.

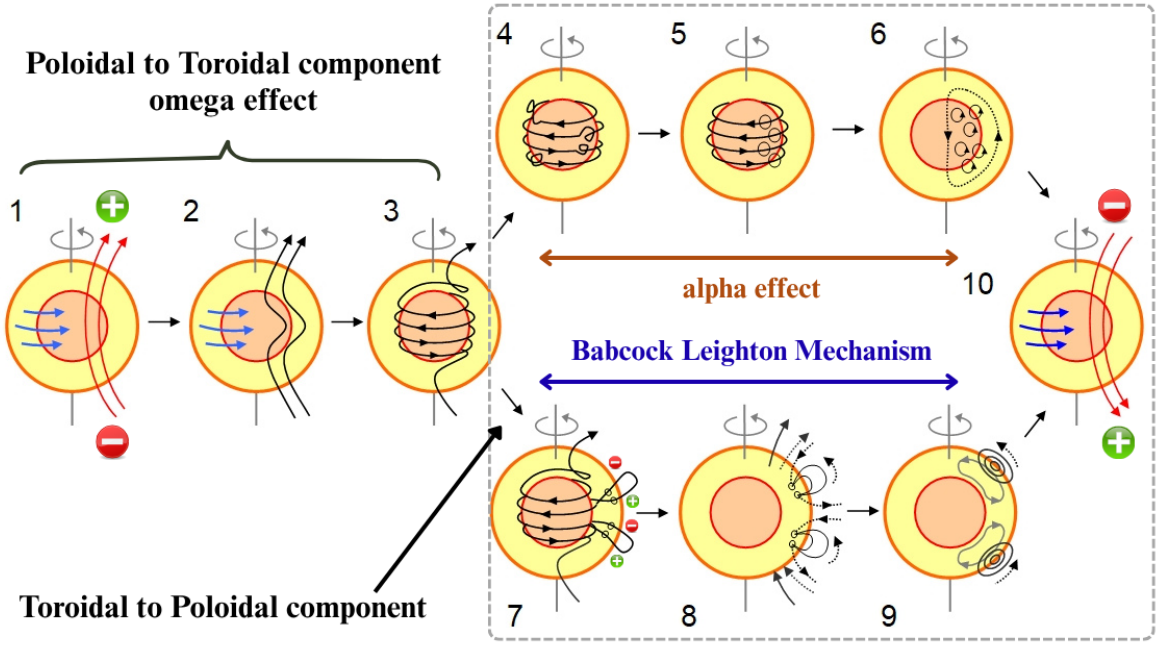


Figure 1.13: Cartoon illustrating the solar dynamo process. The diagram shows the conversion between poloidal and toroidal components of the Sun's magnetic field. The differential rotation stretches poloidal field lines into the toroidal direction. In the reverse direction, the regeneration of the poloidal field from the toroidal component occurs through two mechanisms: the $\alpha$-effect in the convection zone and the Babcock–Leighton (BL) mechanism near the surface. This image is modified from Sanchez et al. (2014) for better illustration.

To regenerate the poloidal magnetic field from the existing toroidal field, the Coriolis force plays a key role. As magnetically buoyant plasma blobs rise through the solar convection zone, they are twisted by helical turbulent convective motion. These helically rising plasma elements impart a twist to the frozen-in toroidal magnetic field lines, generating magnetic loops oriented in the meridional plane. Through magnetic diffusion and reconnection, these loops contribute to the formation of a new global dipolar field – but with a reversed polarity compared to the original poloidal field. This regeneration mechanism is referred to as the mean $\alpha$-effect, and it is fundamental to many solar dynamo models (see Choudhuri (1998) for more details). In summary, the solar magnetic cycle begins with a poloidal field, which is stretched into a toroidal field by the Ω-effect. Part of this toroidal field emerges as bipolar sunspots, while the remaining toroidal field is twisted by

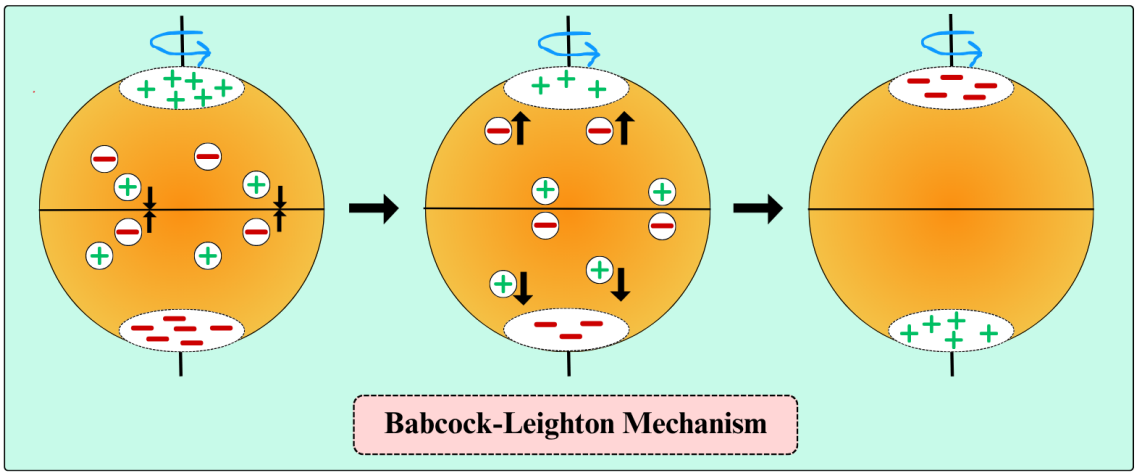


Figure 1.14: Cartoon illustrating the Babcock–Leighton mechanism. Initially, BMRs emerge following Hale's and Joy's laws. Over time, the leading polarity cancels across the equator, while the trailing polarity is transported poleward by surface flows. This process reverses the existing polar field and builds a new dipole.

the $\alpha$-effect to regenerate the poloidal component with opposite polarity, thus completing the magnetic cycle. $\Omega$-effect and $\alpha$-effect is shown in the flow-digram in Figure 1.13.

### 1.4.2 Flux Transport Dynamo Mechanism

Flux tube simulations by Choudhuri and Gilman (1987), as well as by D'Silva and Choudhuri (1993), demonstrated that the strength of the toroidal magnetic field at the base of the convection zone must be of the order of $10^5$ G – almost an order of magnitude greater than the local equipartition field strength in the convection zone. At such high field strengths, helical turbulence is insufficient to twist the toroidal field lines, rendering the traditional $\alpha$-effect ineffective. This limitation necessitates an alternative mechanism, known as the **Babcock–Leighton (BL) mechanism**, to generate the poloidal field (Babcock, 1961; Leighton, 1964, 1969). The cartoon of BL mechanism is depicted in Figure 1.14.

According to this mechanism, when a BMR forms on the solar surface, the leading polarity is oriented ahead in the direction of solar rotation, while the trailing polarity lags behind. Based on Joy's law and Hale's polarity rule, these bipolar regions are tilted and exhibit opposite polarities in the northern and southern hemispheres (as discussed in section 1.2). The surface differential rotation increases the longitudinal separation between the opposite polarities of an active region. Simultaneously, magnetic diffusion causes the leading polarity flux from opposite hemispheres to cancel out near the equator, while the

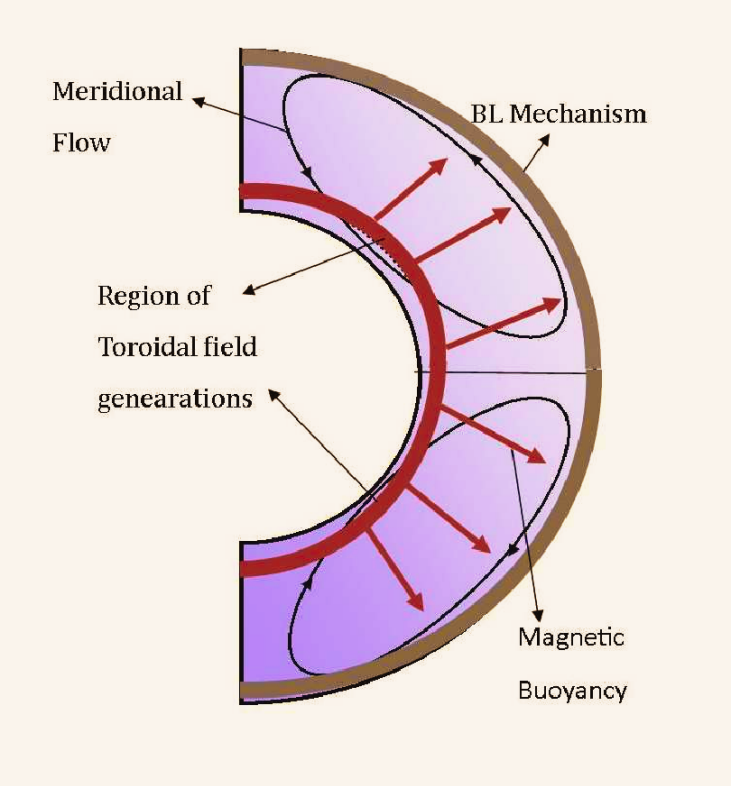


Figure 1.15: Cartoon illustrating the flux transport dynamo model.

trailing polarity flux – largely unipolar – migrates poleward, driven by a combination of meridional circulation and diffusion. This poleward transport alters the Sun's global dipolar field, reversing its polarity compared to the previous cycle. A return flow within the meridional circulation carries magnetic flux back toward the base of the convection zone, where the poloidal field transports through the solar convection zone, the differential rotation shears it to produce a new toroidal field. This toroidal field subsequently becomes unstable, rises due to magnetic buoyancy, and forms new tilted bipolar sunspots of opposite orientation. This triggers the BL mechanism again to regenerate the poloidal field that reverses the existing old polar field. This polar field subsequently generates the toroidal field of opposite sign and completes the cycles.

The resulting poloidal field is once again transported poleward and then downward to the tachocline, thereby completing the cycle. This self-sustaining loop is the foundation of the 'flux transport dynamo', a model that explains the generation and maintenance of the Sun's magnetic field across both its interior and photosphere (Hazra et al., 2023). The mechanism is portrayed in Figure 1.15. The Babcock-Leighton flux transport dynamo has received both theoretical and observational support, and it is considered the primary driver

of the sunspot cycle.

## 1.5 The Sun's Corona

The solar corona is the outermost layer of the Sun's atmosphere, extending millions of kilometers into space. Despite its tenuous nature, the corona exhibits extremely high temperatures, typically on the order of $10^6$ K, significantly hotter than the underlying photosphere, which maintains a temperature of approximately 5800 K. This counterintuitive temperature inversion is known as the *coronal heating problem* (Aschwanden et al., 2007). To explain this phenomenon, two broad physical mechanisms have been proposed. In *wave-based heating models*, energy is transported from the solar interior via magnetohydrodynamic (MHD) waves and dissipates in the corona, heating the plasma (De Moortel and Browning, 2015). In contrast, *reconnection-based models* attribute the heating to small-scale, impulsive magnetic reconnection events—often referred to as *nanoflares*—that are driven by the continual stressing and braiding of magnetic field lines due to convective motions at the solar surface (Parker, 1988; Klimchuk, 2006).

The coronal plasma is fully ionized and exhibits low particle densities, typically ranging from $10^8$ to $10^{10}$ cm$^{-3}$. Due to the overwhelming brightness of the photosphere and low density of the corona, the solar corona is not usually visible from Earth. However, during total solar eclipses, when the Moon completely obscures the solar disk, the faint and structured outer atmosphere becomes clearly visible as a luminous halo surrounding the Sun.

### 1.5.1 Observation of the Solar Corona

The coronal plasma is fully ionized and exhibits low particle densities, typically ranging from $10^8$ to $10^{10}$ cm$^{-3}$. Due to the high temperature and low density of the solar corona, it emits primarily in extreme ultraviolet (EUV) and soft X-ray wavelengths, requiring space-based instrumentation for regular observations (Golub and Pasachoff, 2009; Antonucci et al., 2020). Ground-based observations are limited to rare total solar eclipses or specialized coronagraphs that block the solar disk and observe the white light corona. Historically, the corona was first studied during total solar eclipses, when the bright solar

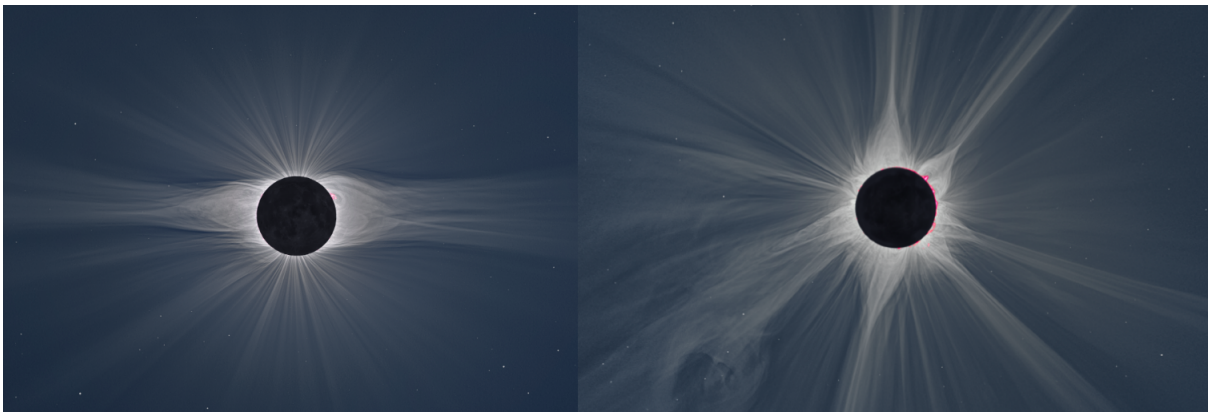

Figure 1.16: Left panel denotes complex structure of the solar corona seen during a total solar eclipse at solar maximum on July 2, 2019, from Chile. The right panel denotes the complex structure of the solar corona seen during a total solar eclipse at solar maximum on April 20, 2023, from Australia. These images are captured and processed by Prof. Miloslav Druckmüller.

disk is obscured by the Moon, revealing the faint, extended outer atmosphere as a glowing halo. Figure 1.16 represents solar eclipses during minimum and maximum. These early observations revealed large-scale features such as *streamers*, *plumes*, and *coronal holes*.

Modern observations of the corona rely on a variety of advanced instruments, both space- and ground-based. Notable space-based missions include: 1) The Solar and Heliospheric Observatory (SOHO) provides EUV images with the Extreme-ultraviolet Imaging Telescope (EIT) (Domingo et al., 1995), and white-light images of the extended corona with the Large Angle and Spectrometric Coronagraph (LASCO) (Brueckner et al., 1995), 2) The Atmospheric Imaging Assembly (AIA) on the Solar Dynamics Observatory (SDO) offers high-resolution, multi-wavelength imaging of the corona with a cadence of 12 seconds (Pesnell et al., 2012), 3) Hinode's X-ray Telescope (XRT) and EUV Imaging Spectrometer (EIS) allow detailed imaging and spectroscopy of coronal plasma (Kosugi et al., 2007), 4) ESA's Solar Orbiter mission provides both close-up and out-of-ecliptic views of the corona, 5) Polarimeter to UNify the Corona and Heliosphere (PUNCH) images the corona–solar wind transition using wide-field polarimetric imaging (Deforest et al., 2022), 6) PRoject for OnBoard Autonomy-3 (Proba-3) — formation-flying coronagraph for imaging the inner corona under eclipse-like conditions (Llorente et al., 2013). Figure 1.17(a), (b) show the extent of the solar corona in white light from LASCO C2 and C3 space based instrument. In the same figure, panel (c) presents a complex coronal structure captured in the EUV 171 Å channel by SDO/AIA.

Besides these space-based instruments, Ground-based coronagraphs such as the Mauna

Loa Solar Observatory (MLSO) or the Daniel K. Inouye Solar Telescope (DKIST) offer complementary observations (Rimmele et al., 2020), especially in white light and near-infrared. Figure 1.17(d) shows the extent of the solar corona in white light from MLSO observatory using K-Cor instrument. These observations have revealed that the corona is

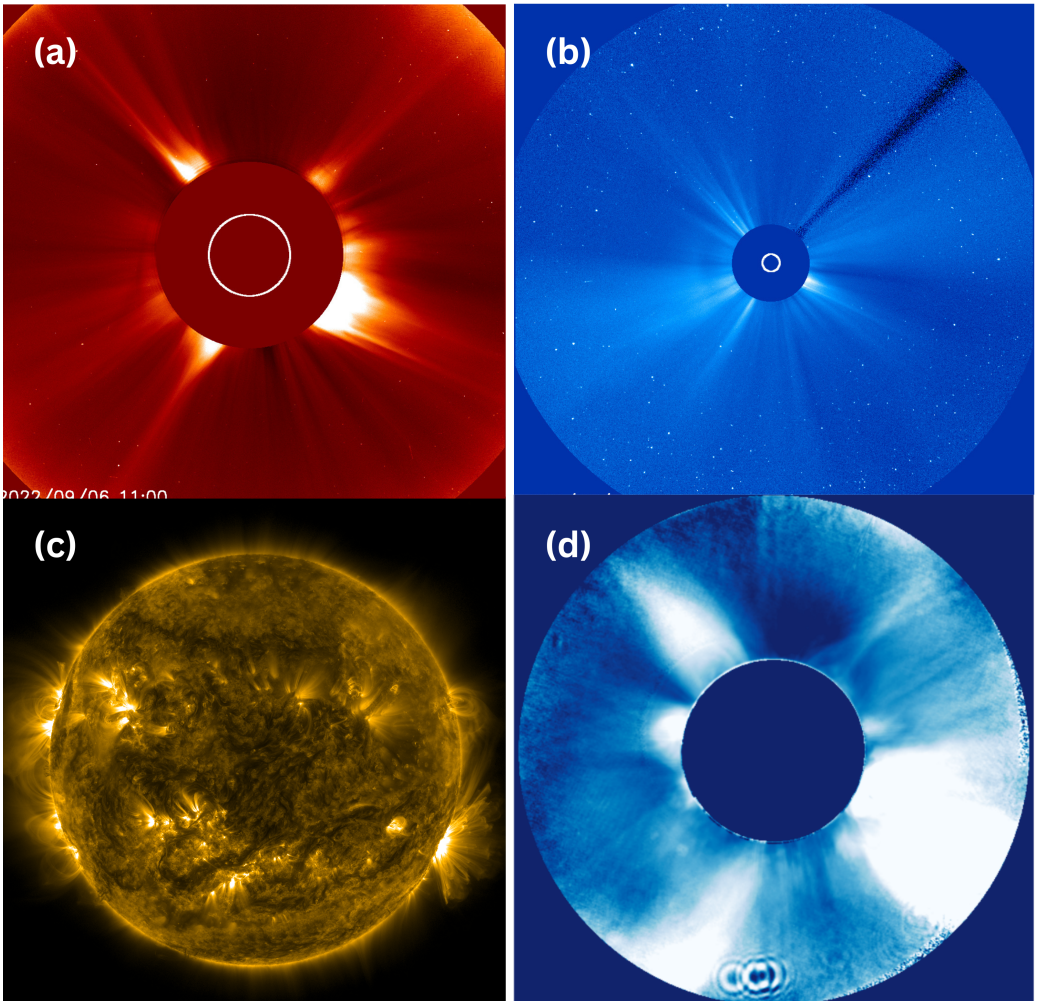


Figure 1.17: Panel (a) and (b) show observations of the solar corona from the space-based coronagraphs onboard SOHO. Panel (a) is from LASCO-C2, which observes the corona in the field of view from 2.5 $R_\odot$ to 6 $R_\odot$, while Panel (b) is from LASCO-C3, covering a wider range from 3.5 $R_\odot$ to 30 $R_\odot$. Panel (c) presents a complex coronal structure captured in the EUV 171 Å channel by SDO/AIA. Panel (d) displays the white-light observation of the corona extending up to $\sim$2.5 $R_\odot$, taken from the ground-based Mauna Loa Solar Observatory (MLSO) using the K-Cor instrument. All four observations correspond to September 6, 2022.

highly dynamic, structured by the solar magnetic field, and exhibits phenomena such as coronal loops, prominences, jets, waves, and eruptions.

### 1.5.2 Physics of Solar Coronal magnetic field

The corona is shaped by the Sun's magnetic field, which originates from the dynamo action in the solar interior and emerges through the photosphere in the form of sunspots and active regions. In the previous section, we have noted that the plasma-$\beta$ in the solar corona is very low, meaning that magnetic pressure dominates over plasma (thermal) pressure. In such low-$\beta$ conditions, the motion of plasma is strongly constrained along magnetic field lines, and the Lorentz force becomes the dominant force governing equilibrium. Under the low-$\beta$ approximation, the plasma pressure gradient $\nabla p$ can be neglected, i.e., $\nabla p \approx 0$. The equilibrium condition from the momentum equation then reduces to:$(\nabla \times \mathbf{B}) \times \mathbf{B} = 0$, or equivalently, $\mathbf{j} \times \mathbf{B} = 0$. This approximation implies that the magnetic field is in a force-free configuration, and it allows two possibilities: 1) $\mathbf{j} = 0$: the current vanishes, allowing the application of a **potential field source surface (PFSS)** model, which corresponds to the minimum energy configuration. 2) $\mathbf{j} \parallel \mathbf{B}$: the current density is aligned with the magnetic field, implying that $\nabla \times \mathbf{B} \propto \mathbf{B}$. This is known as a **force-free magnetic field**, commonly used to model coronal magnetic structures (Low and Lou, 1990). In this force-free condition:

$$\nabla \times \mathbf{B} = \alpha \mathbf{B}, \quad \nabla \cdot \mathbf{B} = 0 \quad --> \quad \mathbf{B} \cdot \nabla \alpha(r) = 0 \tag{1.4}$$

where $\alpha$ is a scalar function, varies in space. In PFSS model, $\alpha = 0$, implying current-free fields. Other physical models exist beyond force-free fields, which consider pressure gradients and gravity, such as **Magnetohydrostatic (MHS)** model (Riley et al., 2006). The coronal equilibrium in this model is governed by the equation:

$$-\nabla p + (\mathbf{j} \times \mathbf{B}) + \rho \mathbf{g} = 0 \tag{1.5}$$

MHS models are more suitable for large-scale structures like streamers or prominences where plasma forces cannot be neglected. Another successfull model to study solar corona is **Magnetofrictional (MF) Models** (Mackay et al., 2010; Yeates et al., 2010; Guo et al., 2016). These models are designed to simulate the slow, quasi-static evolution of the coronal magnetic field under the assumption that the field evolves through a series of force-free states. Instead of solving full MHD, the magnetic field evolves via the induction equation

with an artificial frictional velocity:

$$\mathbf{v} = \frac{1}{\nu}\frac{\mathbf{j}\times\mathbf{B}}{B^2}, \tag{1.6}$$

which drives the system toward a force-free state. Magnetofrictional models are ideal for studying long-term evolution, helicity transport, and flux rope formation. They balance computational efficiency with more realism than PFSS or static extrapolations. Lastly, the more complex, computer-intensive direct approach to study solar corona is the **Full MHD Models** (Riley et al., 2006). Time-dependent MHD simulations solve the full set of governing equations and are capable of modeling dynamic phenomena such as solar wind generation, flares, and coronal mass ejections (CMEs). These include models like MAS, ENLIL and AWSoM, which are often driven by photospheric magnetic data and can couple the corona with the heliosphere.

The coronal magnetic field can be open or closed. Closed field lines trap hot plasma and form loops, while open field lines extend into the heliosphere, allowing plasma to escape as the solar wind. The transition from closed to open field typically occurs at the *source surface*, placed at $r = 2.5R_\odot$ in PFSS models.

### 1.5.3 Coronal Magnetic Field Structures

The corona is dominated by the Sun's magnetic field, which structures the plasma into various features such as loops, arcades, plumes, and helmet streamers. These features are manifestations of the complex interaction between the magnetic field and the ionized plasma, a state of matter governed by magnetohydrodynamic (MHD) equations. The structure of the corona is largely shaped and maintained by the solar magnetic field. As such, it exhibits a wide variety of magnetic configurations:

**Coronal Holes:**

Coronal holes are regions of the solar corona characterized by reduced emission in ultraviolet (UV) and extreme ultraviolet (EUV) wavelengths, as observed by instruments such as Solar and Heliospheric Observatory / Extreme Ultraviolet Imaging Telescope (SOHO/EIT), Solar Dynamics Observatory / Atmospheric Imaging Assembly (SDO/AIA) and

Hinode / Extreme-ultraviolet Imaging Spectrometer (Hinode/EIS) (Harvey and Sheeley, 1979; Cranmer, 2009). These dark areas in coronal images indicate lower-density and temperature plasma compared to the surrounding quiet Sun. Physically, coronal holes are

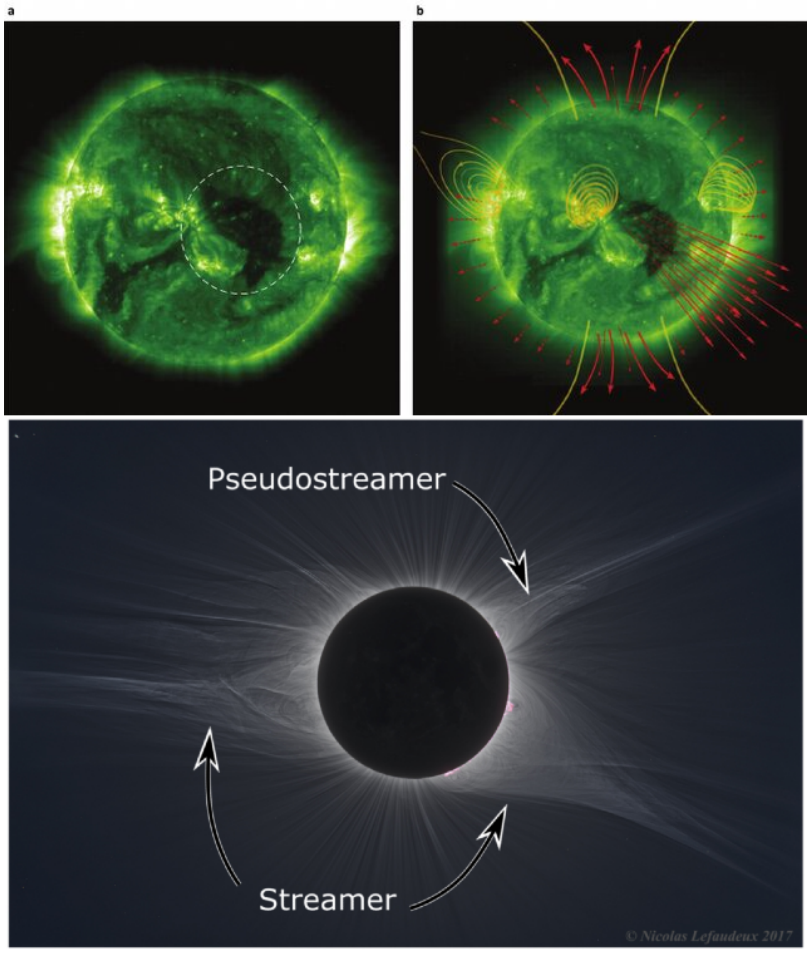


Figure 1.18: Panel (a) highlights a coronal hole located at the center of the solar disk, marked by a dashed circle. Panel (b) illustrates a model of the Sun's magnetic field, including open magnetic field lines emanating from the coronal hole region (Image courtesy: SOHO, ESA and NASA; Credit: Ciecholewski (2015)). The bottom panel shows the structure of coronal streamers and pseudostreamers, depicting the large-scale magnetic topology of the solar corona. Credit: Scott et al. (2021)

associated with **open magnetic field lines** that extend radially outward into the heliosphere (Levine, 1982). The open magnetic topology allows plasma to escape more freely, making coronal holes the primary source regions of the *fast solar wind*, with typical outflow speeds ranging from 600–800 km/s.

Coronal holes occur in various locations and configurations: 1) **Polar coronal holes** are prevalent during solar minimum and can persist for many solar rotations, 2) **Equatorial or mid-latitude holes** are more transient and often associated with decaying active regions or

magnetic field reconfiguration during solar maximum. In Figure 1.18, panel (a) highlights an equatorial coronal hole marked by a dashed circle, while panel (b) shows open magnetic field lines emanating from this region.

In Potential Field Source Surface (PFSS) extrapolations, these regions correspond to footpoints of field lines that reach the source surface and remain open, connecting to the heliosphere. The magnetic flux from coronal holes contributes to the Sun's **open magnetic flux**, which influences heliospheric conditions and modulates galactic cosmic ray access to the inner solar system. Coronal holes also play an important role in space weather forecasting. As high-speed streams from coronal holes interact with slower solar wind streams, they form **co-rotating interaction regions (CIRs)**, which can drive geomagnetic disturbances upon encountering Earth's magnetosphere (Broiles et al., 2012).

**Coronal Streamers:**

Coronal streamers are large-scale structures in the solar corona, prominently visible during total solar eclipses as bright, helmet-shaped features extending outward from the Sun (Koutchmy and Livshits, 1992). These structures form above **regions of closed magnetic field lines**, typically located near the heliospheric current sheet (HCS) and often associated with active regions or the boundary between opposite magnetic polarities on the solar surface.

Physically, coronal streamers are composed of dense, relatively cool plasma confined by the Sun's magnetic field. The magnetic topology in streamer regions is typically a *closed-loop arcade* at low heights, transitioning to *open field lines* at greater altitudes, separated by a *magnetic cusp*. This cusp region marks the boundary where magnetic reconnection can occur, allowing some plasma to escape along open field lines into the heliosphere.

Beyond helmet streamers, there are pseudostreamers, which are large-scale structures in the solar corona that resemble classical streamers in appearance but differ fundamentally in their magnetic topology. Unlike traditional streamers, which lie above polarity inversion lines (PILs) and separate regions of opposite magnetic polarity on the solar surface, pseudostreamers separate like-polarity regions. This means that the magnetic field lines on both sides of a pseudostreamer connect to regions with the same magnetic polarity. As a

result, pseudostreamers do not form a current sheet in the heliosphere like helmet streamers do. These structures are often observed during solar minimum when large unipolar regions dominate the solar surface, and they play a key role in shaping the heliospheric magnetic field. The bottom panel of Figure 1.18 illustrates the structure of streamers and pseudostreamers in the coronal magnetic field.

Coronal streamers are key sources of the *slow solar wind*, which has typical velocities of 300–500 km/s. Unlike the fast solar wind from coronal holes, the slow wind emanates from the top of streamers or from adjacent open-field corridors. The density, temperature, and variability of the slow solar wind are linked to the dynamic processes in the streamer belt, including magnetic reconnection and plasma outflows.

## 1.6 Solar Wind and the Heliosphere

The Sun is not only a source of light and heat, but also sustains a continuous flow of supersonic plasma and magnetic fields into interplanetary space, known as the *solar wind* (Axford, 1985; Vidotto, 2021). This supersonic outflow of charged particles, primarily electrons, protons and ions escapes the Sun's gravitational field and carries with it the embedded solar magnetic field, forming a large-scale structure called the *heliosphere* (Owens and Forsyth, 2013; Kleimann et al., 2022). The study of the solar wind and its interaction with planetary environments is crucial to understanding space weather phenomena and the Sun-Earth connection.

### 1.6.1 Solar Wind: Origin and Properties

The solar wind originates in the outermost layer of the solar atmosphere – the corona – where temperatures exceed $10^6$ K (Fisk and Schwadron, 2001; Panasenco et al., 2020). At such high temperatures, the thermal energy of charged particles is sufficient to overcome the Sun's gravitational potential and escape the solar corona. The solar wind starts subsonic, accelerates due to pressure gradients and gravity, and becomes supersonic beyond a certain critical point (like how gas flows through a nozzle). The first simplified, spherically symmetric hydrodynamic model of solar wind expansion is given by the Parker solar wind solution (Parker, 1959, 1965).

**Parker's Hydrodynamic Model:**

In 1958, Eugene Parker proposed that the solar corona cannot remain in hydrostatic equilibrium at large radial distances but must instead undergo a continuous and accelerating expansion (Parker, 1959). This led to the concept of the solar wind – a steady, supersonic outflow of plasma from the Sun. Parker's model is based on several simplifying assumptions: the flow is steady-state, spherically symmetric, radially outward, isothermal, and composed of an ideal gas (Parker, 1958). By applying the principles of mass conservation and momentum conservation under these assumptions, one can derive an equation that describes how the velocity of the solar wind varies with heliocentric distance:

$$\left(v - \frac{a^2}{v}\right)\frac{dv}{dr} = \frac{2a^2}{r} - \frac{GM_\odot}{r^2} \tag{1.7}$$

where $a = \sqrt{\frac{2K_BT}{m_p}}$ is isothermal sound speed, v is outflow velocity, r is the radial distance, $K_B$ is the Boltzmann constant, T is temperature, $m_p$ is the proton mass, G is the gravitational constant, and $M_\odot$ is the mass of the Sun. Now, the right-hand side and the coefficient of $dv/dr$ must vanish simultaneously for a smooth solution: $v = a, \quad r_c = \frac{GM_\odot}{2a^2}$. Thus, at this critical radius ($r_c$) the outward pressure gradient becomes dominance over the gravitational forces. This is the location where the solar wind transitions from subsonic to supersonic flow. One can derive the famous Parker solution:

$$\left(\frac{v}{a}\right)^2 - \ln\left(\frac{v}{a}\right)^2 = 4\ln\left(\frac{r}{r_c}\right) + 4\frac{r_c}{r} - 3 \tag{1.8}$$

Parker's solar wind model yields five classes of solutions, as illustrated in Figure 1.19, each corresponding to different flow regimes of the solar plasma: 1) **Solution AC** is physically implausible as it remains confined to low radial distances. This implies that the solar wind does not escape into the heliosphere, contradicting observations, 2) **Solution BD** describes a flow that exists only at large distances, failing to connect with the solar corona. 3) **Solution BC** implies that the solar wind is already supersonic at the base of the corona. However, spectroscopic and in-situ measurements indicate that the solar wind starts as a subsonic flow and transitions to supersonic speeds only beyond a certain critical radius. 4) **Solutions AD and AB** both begin with subsonic outflows near the solar sur-

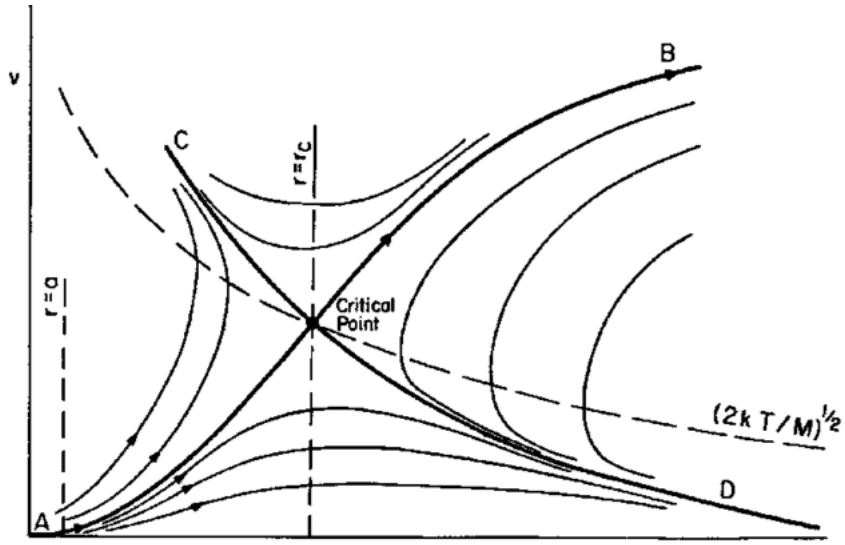


Figure 1.19: Solutions to Parker's solar wind equation. Figure adapted from Parker (1965), showing solar wind velocity as a function of radial distance from the Sun. The plot illustrates five possible solutions to the solar wind equation, with only the transonic solution (passing smoothly from subsonic to supersonic speeds) representing the physically realistic solar wind outflow.

face, consistent with observational data. The distinction lies in their asymptotic behavior at large radial distances. Solution AD levels off to a finite velocity, which corresponds to a non-zero pressure at infinity, which is unphysical.

Parker identified **Solution AB** as the only physically viable scenario. This transonic solution begins subsonically near the solar surface, passes smoothly through a critical point where the flow speed equals the local sound speed, and continues to accelerate into the supersonic regime at large distances.

**Solar Wind Observation:**

Observations from spacecraft (e.g., Ulysses, WIND, Advanced Composition Explorer (ACE), Parker Solar Probe) have shown that the solar wind is not uniform and can be broadly classified into: 1) **Fast Solar Wind:** Originating from coronal holes, it has a typical speed of $\sim$ 700 km s$^{-1}$, low density, and lower variability (Kojima et al., 2004). It is more prominent during solar minimum and flows along open magnetic field lines, 2) **Slow Solar Wind:** Emanating from regions near the heliospheric current sheet and streamer belt, it has a speed of $\sim$ 300–500 km s$^{-1}$, is denser, and more variable (Feldman et al., 2005; Abbo et al., 2016). Its origin is less well understood and may involve interchange reconnection and closed field expansion. Interaction of high-speed solar wind streams with the

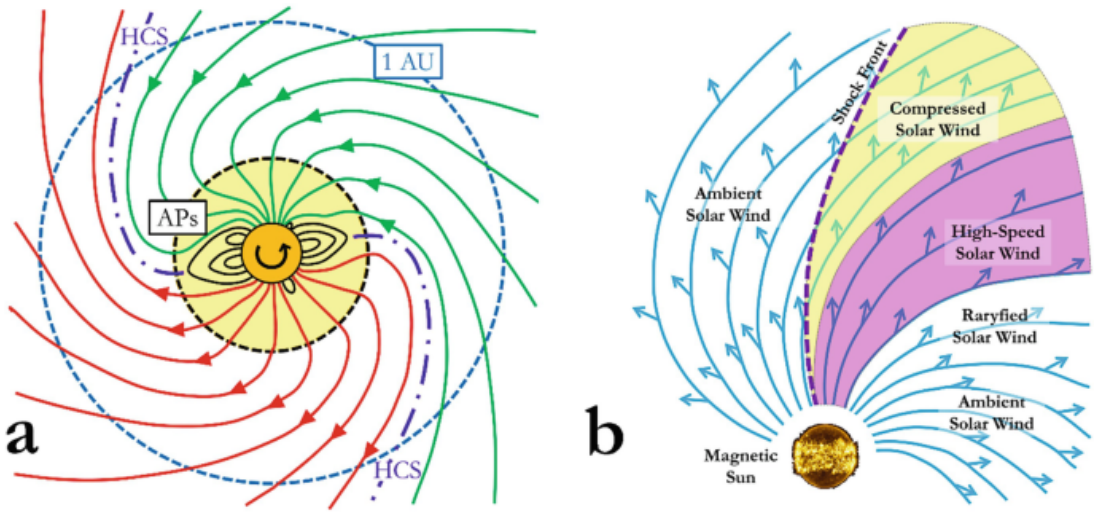


Figure 1.20: Large-scale structure of the heliospheric magnetic field and solar wind dynamics. (a) Schematic of the Parker spiral magnetic field structure in the heliosphere. The red and blue lines are magnetic field lines of opposite polarity. The Sun's rotation causes magnetic field lines to spiral outward, forming the Archimedean (Parker) spiral. The heliospheric current sheet (HCS) is shown as a wavy surface (dotted dashed blue line) dividing regions of opposite magnetic polarity. The dashed blue circle marks the location of 1 AU (Earth's orbit). (b) Interaction of high-speed solar wind streams with the surrounding ambient solar wind. The image is taken from von Kusserow and Marsch (2025).

surrounding ambient solar wind is presented in Figure 1.20(b).

### 1.6.2 The Heliosphere

The heliosphere is a plasma bubble forced by the Sun, within which all planets of the solar system reside. The outer boundary of the heliosphere is determined by its interaction with the **very local interstellar medium (VLISM)**, which contains interstellar plasma, magnetic fields, and neutral gas. As the solar wind travels outward, it remains supersonic until it reaches a critical distance where it begins to interact with the pressure of the surrounding VLISM. At this point, the solar wind undergoes a sudden deceleration at a shock front known as the **termination shock**. Here, the solar wind transitions from supersonic to subsonic speeds, resulting in compression, heating, and increased turbulence of the plasma and magnetic fields. This region beyond the termination shock but inside the heliopause is called the **heliosheath**.

The **heliopause** marks the outermost boundary of the heliosphere, where the outward thermal and magnetic pressure of the solar wind balances the inward pressure of the VLISM. At this boundary, the heliospheric magnetic field becomes distorted and com-

pressed, and the previously well-ordered spiral structure breaks down, giving way to a turbulent and tangled magnetic environment. The interaction between the solar and interstellar plasma and magnetic fields at the heliopause may lead to turbulence, magnetic reconnection and other dynamic processes.

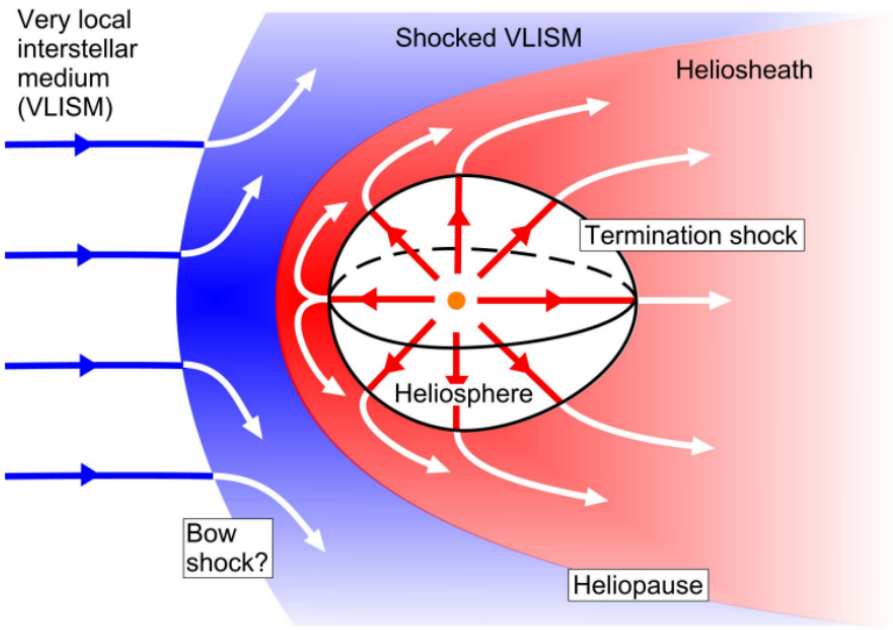


Figure 1.21: A cartoon illustration of the heliosphere adapted from Owens and Forsyth (2013). The figure shows the solar wind flowing outward from the Sun, forming distinct regions such as the termination shock, the heliosheath, and the heliopause – the boundary where the solar wind pressure balances with the interstellar medium.

Beyond the heliopause, the VLISM flows around the heliosphere. Depending on the relative speed and magnetic field orientation of the Sun's motion through the interstellar medium, a **bow shock** may form – similar to the shockwave in front of a supersonic aircraft. However, whether a well-defined bow shock exists remains still an open question. Observations from the *Voyager 1* and *Voyager 2* spacecraft have provided direct evidence of the termination shock (crossed in 2004 and 2007, respectively), the heliosheath, and the heliopause. A detailed structure of the outer heliosphere is illustrated in Figure 1.21.

### 1.6.3 Interplanetary Magnetic Field, Heliospheric Current Sheet and Open Solar Flux:

The Sun's magnetic field does not end at the photosphere but is carried outward by the solar wind into interpanetary space, forming the **Heliospheric Magnetic Field (HMF)** (Owens and Forsyth, 2013). This frozen-in magnetic field pervades the entire heliosphere — the bubble-like region of space influenced by the Sun — and governs the transport of solar energetic particles, the structure of the solar wind, and the coupling between solar and planetary magnetospheres. The **Interplanetary Magnetic Field (IMF)** is the local manifestation of the HMF, typically measured *in situ* by spacecraft near Earth or elsewhere in the heliosphere (Levy, 1976; Thomson et al., 2001). Assuming that magnetic field lines are rooted in the solar photosphere and co-rotate with the Sun, the continuous outflow of the solar wind stretches these field lines outward. Due to the Sun's rotation, the outward-moving plasma imparts a spiral shape to the large-scale HMF. This results in an Archimedean spiral structure, commonly known as the Parker spiral (Parker, 1958), governed by:

$$B_\phi(r) = -\frac{\Omega r \sin\theta}{v} B_r(r) \tag{1.9}$$

where $\Omega$ is the angular rotation rate of the Sun, $r$ is the radial distance, $v$ is the solar wind speed, and $B_r$ is the radial magnetic field component. The tightness of the Parker spiral depends on several factors. The spiral becomes more tightly wound with increasing radial distance from the Sun and with decreasing solar wind speed $v_r$. Additionally, it tends to be more tightly wound closer to the solar equatorial plane, where rotational effects are strongest. Figure 1.20(a) iuulstrates such Parker spiral structure of HMF.

At 1$\sim$AU, where the typical solar wind speed is approximately $v_r \approx 450\,\mathrm{km/s}$, the ratio of the azimuthal to radial magnetic field components is $B_\phi/B_r \approx -1$. This implies that the magnetic field vector forms an angle of approximately 45° with respect to the radial direction, consistent with the classic Parker spiral geometry. The IMF is characterized by its strength and orientation (e.g., components $B_r, B_t, B_n$), and exhibits variability on timescales from minutes to solar cycles. The IMF generally exhibits a large-scale magnetic structure with alternating polarities. The **Heliospheric Current Sheet (HCS)** is a vast, wavy surface extending throughout the heliosphere (see blue dotted-dashed line in Figure 1.20(b)),

that separates regions of these oppositely directed magnetic fields (Smith, 2001; Lavraud et al., 2020; Szabo et al., 2022). The HCS is formed due to the Sun's tilted magnetic dipole and varies with solar activity. During solar minimum, the HCS is nearly flat, while at solar maximum the HCS becomes highly warped and distorted due to complex magnetic field configurations. It plays a crucial role in modulating galactic cosmic rays and influences solar-terrestrial interactions.

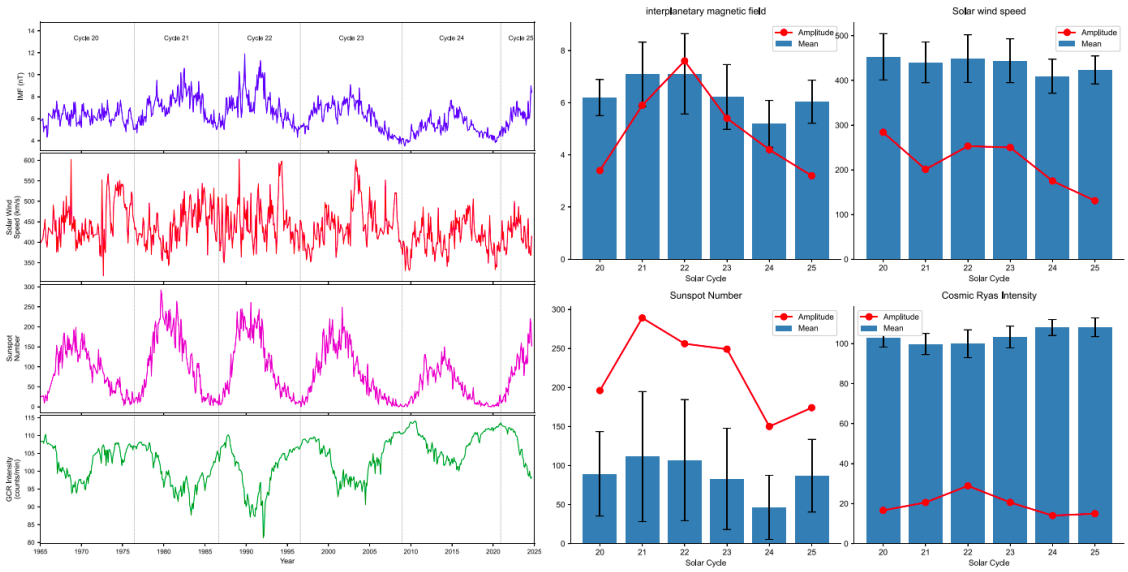


Figure 1.22: Long-term trends and solar cycle–averaged behavior of heliospheric parameters (1964–2024). The left panels illustrate the time series of several key parameters over six solar cycles: the interplanetary magnetic field (IMF) strength in nanotesla (blue), solar wind speed in $\mathrm{kms}^{-1}$ (red), monthly averaged sunspot number (magenta), and cosmic ray intensity measured in $\mathrm{countss}^{-1}$ (green). The right panels summarize cycle-by-cycle statistics. Here, blue bars indicate the average value for each parameter during individual solar cycles, with error bars representing one standard deviation from the mean. Red lines highlight the peak-to-valley amplitude within each cycle. The sunspot number time series is taken from the SIDC/SILSO database, while solar wind and IMF data are obtained from the OMNI2 dataset.

Another key component of the HMF is the **Open Solar Flux (OSF)**, which refers to the magnetic flux originating in the solar corona that is connected to the heliosphere via field lines that are not closed back onto the Sun (Lockwood et al., 2009b). These open field lines extend indefinitely into interplanetary space and are rooted in coronal holes, particularly during solar minimum (Lowder et al., 2017; Higginson et al., 2017). Unlike closed field lines that form magnetic loops, open field lines allow plasma and magnetic flux to escape into the heliosphere, thereby contributing to the structure of the solar wind and IMF. Quantitatively, the OSF is typically estimated from the radial component of the IMF

measured near Earth, assuming spherical symmetry and conservation of magnetic flux. Variations in OSF reflect changes in solar activity, including flux emergence, interchange reconnection, and coronal mass ejections, and are thus intimately tied to the solar dynamo and the magnetic flux budget of the Sun (Pal et al., 2020). Such variations of the IMF, Solar wind, and Cosmic ray intensity with the solar cycle are plotted in Figure 1.22 (read the caption for details).

## 1.7 From Sun to Earth: The Science of Space Weather

Space weather refers to the dynamic conditions in the near-Earth space environment that arise from solar activity and its interaction with the Earth's magnetosphere, ionosphere, and thermosphere. The Sun's corona, being the origin of the solar wind and interplanetary magnetic field (IMF), plays a crucial role in modulating space weather. High-speed solar wind streams, coronal mass ejections (CMEs), solar flares, and solar energetic particles (SEPs) are the primary solar drivers. Flares release bursts of electromagnetic radiation that can immediately impact Earth's ionosphere, while CMEs and high-speed streams, upon interacting with Earth's magnetic field, lead to geomagnetic storms, auroras, and disturbances in satellite and navigation systems. The large-scale structure of the corona and the heliospheric magnetic field also modulate cosmic ray fluxes and determine the strength of space weather impacts. The southward (negative Bz) orientation of the IMF is especially geoeffective as it reconnects efficiently with Earth's northward magnetic field, injecting energy into the magnetosphere.

To monitor and predict such events, both ground-based and space-based assets are employed. Missions such as ACE, WIND, SDO, SOHO, STEREO, Parker Solar Probe, and Solar Orbiter provide real-time data on solar and interplanetary conditions. Ground networks like magnetometers, ionosondes, neutron monitors, and radio telescopes complement these observations. Forecasting models such as ENLIL, WSA, and D-RAP utilize these data to predict solar wind conditions and radiation hazards. A shift toward physics-based modeling—employing dynamo theory, coronal magnetic field extrapolation, and MHD simulations—is underway to improve predictive accuracy, particularly for CME initiation and the critical southward IMF component. As humanity becomes increasingly reliant on space-borne technologies, the societal importance of robust space weather fore-

casting grows. International collaborations, including efforts by NASA, ESA, ISRO, and the World Meteorological Organization, aim to enhance global preparedness and resilience against space weather threats.

In this thesis, we explore solar magnetic field dynamics, from its origin and fluctuations through solar cycle models, to its manifestation in the solar corona and heliospheric open flux. Our exploration, therefore, is relevant for timescales that encompass space weather to space climate.

In the following chapter (Chapter 2), we discuss the technical details of the various physical models that have been utilized in this thesis. This is followed by the presentation of scientific investigations based on these numerical models and observational data. In Chapter 3, we employ a simple algebraic reconstruction approach – rather than complex numerical modeling – to derive the century-scale evolution of the solar axial dipole moment and use it to predict Solar Cycle 25. Chapter 4 focuses on the impact of anomalous active regions (those with opposite polarity or non-Joy's law tilts) on the evolution of large-scale magnetic fields and their role in regulating solar cycle amplitudes. In Chapter 5, we address the long-standing question of the physical origin of the strongest solar cycle ever observed directly (solar cycle 19) and the weak following Cycle 20. Chapter 6 examines which polar precursor – axial dipole moment or hemispheric polar flux – serves as a more reliable predictor of future solar cycle amplitudes. In Chapter 7, we investigate how the Babcock–Leighton mechanism explains the formation of polar filaments and how these may serve as a potential new solar cycle precursor. In Chapter 8 we demonstrate that the corona has a long-term ''memory' of large-scale magnetism – revealed through data driven coronal modelling and eclipse observations. In Chapter 9, we address the long-standing solar open flux problem by reconstructing the century-scale evolution of the heliospheric open flux and show how source surface variations may explain it. Finally, Chapter 10 concludes this thesis with a summary of major findings and an outlook on future research directions arising from this work.

# Chapter 2

# First-principle based Numerical Models

A first-principles approach to studying solar magnetic fields relies on fundamental physical laws, such as the Magnetohydrodynamic (MHD) equations to simulate plasma dynamics (rather than depending on empirical fits to solar cycle time series or purely statistical methods). In this thesis, we employ three primary computational models to investigate the dynamics of the solar magnetic field: (1) a data-driven Surface Flux Transport (SFT) model, (2) coronal magnetic field models, and (3) a two-dimensional axisymmetric kinematic solar dynamo model.

The most significant contribution of this thesis lies in the development of a new SFT model based on a finite difference numerical scheme. We refer to this model as the Solar Photospheric flux Transport Model, abbreviated as 'SPhoTraM'. The other two models – coronal field models and solar dynamo model – are established frameworks developed by other research groups, which we have utilized and modified accordingly to address specific scientific questions discussed in the subsequent chapters. This chapter begins with a detailed description of the development of the SPhoTraM model, which forms the core of this chapter (**section 2.1**). Then we briefly review the Potential Field Source Surface (PFSS) and full Magnetohydrodynamic (MHD) coronal magnetic field models (section 2.2). Finally, we conclude with a concise discussion of the kinematic solar dynamo model which is used to elucidate the dynamics of magnetic fields in the Sun's interior (section 2.3).

## 2.1 Magnetic Flux Transport on the Sun's Surface: SFT Model

The Sun's photosphere is directly observable, and both ground-based and space-based observatories routinely monitor it since $19^{th}$ century. Ground-based facilities such as the Royal Greenwich Observatory (RGO), Global Oscillation Network Group (GONG) and the Daniel K. Inouye Solar Telescope (DKIST), along with space missions like the Solar Dynamics Observatory (SDO) and the Solar and Heliospheric Observatory (SOHO), regularly capture white-light images and magnetograms that provide critical information about the Sun's surface magnetic field. Since direct probing of the Sun's interior is challenging, the photosphere serves as a valuable observational layer to study the transport of magnetic flux on the solar surface. This is effectively modeled using the Surface Flux Transport (SFT) model, which captures the essence of the BL mechanism described in subsection 1.4.2. In this framework, surface plasma flows (such as meridional circulation, differential rotation and turbulent diffusion) transport the magnetic flux of tilted active regions from low latitudes toward the poles. As the leading polarity flux from opposite hemispheres migrates poleward, it cancels the existing polar fields during solar maximum, leading to the formation of a new poloidal field with reversed polarity. This process – sunspot decay followed by polar field regeneration – forms the core of the SFT model and underpins the large-scale solar magnetic cycle.

### 2.1.1 SPhoTraM: A Newly Developed Data-Driven Numerical Modeling of Surface Flux Transport Mechanism

**Fundamental equations:**

Observational evidence suggests that the magnetic field in the Sun's photosphere is predominantly radial in nature (Solanki, 1993). Consequently, the SFT model focuses on solving the radial component of the magnetic induction equation (i.e $B_r$), incorporating various large-scale transport mechanisms such as differential rotation, meridional circulation, and turbulent diffusion, which represents the effect of supergranular convective flows on the solar surface (Hotta et al., 2023). The fundamental dynamical equation governing

the SFT model is given by:

$$\frac{\partial B_r(\theta,\phi,t)}{\partial t} = -\omega(\theta)\frac{\partial B_r}{\partial \phi} - \frac{1}{R_\odot \sin\theta}\frac{\partial}{\partial \theta}\Big(v(\theta)B_r \sin\theta\Big) + \frac{\eta}{R_\odot^2}\left[\frac{1}{\sin\theta}\frac{\partial}{\partial\theta}\left(\sin\theta\frac{\partial B_r}{\partial\theta}\right) + \frac{1}{\sin^2\theta}\frac{\partial^2 B_r}{\partial\phi^2}\right] + S(\theta,\phi,t) \tag{2.1}$$

Here, $B_r(\theta,\phi,t)$ represents the radial component of the photospheric magnetic field. The symbols, $R_\odot$, $\theta$ and $\phi$ denote the solar radius, heliographic co-latitude and heliographic longitude, respectively. The term $v(\theta)$ and $\omega(\theta)$ dictates the advective meridional circulation and differential rotation, respectively. The parameter $\eta$ is the turbulent diffusivity. Lastly, the source term, $S(\theta,\phi,t)$ in this equation imitates the emergence of new sunspots on the solar surface.

To solve this equation numerically, first we decompose the right-hand side of the equation into three distinct terms (primarily the first three terms), each representing a different physical transport mechanism. Then the spatial derivatives involved are numerically solved using appropriate finite difference schemes, as described below.

- **First Term:** $\omega(\theta)\frac{\partial B_r}{\partial \phi}$

  This term accounts for the differential rotation of the Sun. The partial derivative $\frac{\partial B_r}{\partial \phi}$ represents the longitudinal advection of the radial magnetic field $B_r$ due to this rotation $\omega(\theta)$. The rotational velocity $v_\phi$ varies on the order of 33 m/s to 1800 m/s, which poses numerical challenges for finite difference schemes and can lead to instabilities. If we utilize low-order numerical schemes such as the upwind method, the code remains stable and monotonic; however, it suffers significantly from *numerical diffusion* (Karadimou and Markatos, 2018). This artificial diffusion smears out sharp gradients in the solution and leads to unphysical flux loss, particularly in problems involving steep transitions or discontinuities. On the other hand, employing high-order schemes like the Lax–Wendroff method enhances accuracy in smooth regions but can introduce *spurious oscillations* near discontinuities (e.g., the Gibbs phenomenon), potentially leading to numerical instability (Lax, 2006).

  To balance these competing issues – numerical diffusion in low-order methods and oscillatory behavior in high-order methods – we employ *Total Variation Diminishing* (TVD) schemes (Darwish and Moukalled, 2003; Zhang et al., 2015). A scheme is

said to be TVD if it ensures that the total variation of the numerical solution does not increase with time.

TVD schemes are typically constructed in the framework of Godunov-type methods, where the numerical flux is adaptively modified using *flux limiters*. These limiters blend high-order and low-order schemes: in regions where the solution is smooth, the limiter allows the use of a higher-order accurate method; near sharp gradients or discontinuities, it reverts to a more diffusive, low-order scheme such as upwind. As a result, TVD schemes maintain both the stability and monotonicity of the numerical solution, while reducing numerical diffusion and avoiding unphysical oscillations.

- **Second Term:** $\frac{1}{\mathrm{R}_\odot \sin\theta}\frac{\partial}{\partial\theta}\left(v(\theta)B_r\sin\theta\right)$

  This term represents how the radial field is transported along the meridional (north-south) direction, modulated by the poleward meridional circulation flow speed $v(\theta)$. The amplitude of the meridional flow is significantly smaller than that of the Sun's differential rotation amplitude — typically by a factor of 100. As a result, this term poses minimal stability issues for the numerical scheme, and we employ a first-order upwind method (Press et al., 1992; Blazek, 2005) to handle it. This scheme is directionally dependent and relies on the sign of the velocity to determine the appropriate differencing approach. In the case of a northward flow (i.e., positive velocity), the numerical flux is computed using a *backward difference* scheme. Conversely, for a southward flow (i.e., negative velocity), a *forward difference* method is employed. It is important to note that this method is only first-order accurate in space.

- **Third Term:** $\frac{\eta}{\mathrm{R}_\odot{}^2}\left[\frac{1}{\sin\theta}\frac{\partial}{\partial\theta}\left(\sin\theta\frac{\partial B_r}{\partial\theta}\right)+\frac{1}{\sin^2\theta}\frac{\partial^2 B_r}{\partial\phi^2}\right]$

  This term represents the turbulent diffusion of the radial magnetic field on the solar surface, caused by small-scale convective motions like supergranulation. The first part inside the brackets corresponds to latitudinal diffusion, while the second part corresponds to longitudinal diffusion. Together, they form the Laplacian operator in spherical coordinates applied to $B_r$. To solve this term we employ central difference numerical scheme from finite difference (FD) family (Press et al., 1992; Blazek, 2005). This scheme utilizes function values on both sides of a given grid point, hence it is referred to as a "central" scheme. This method has second-order accuracy

in spatial direction.

In this code we perform time integration using the forward Euler method (Press et al., 1992). The major constraint in solving the SFT equation in finite difference methods is the presence of $\frac{1}{\sin\theta}$ term in the equation. This produces singularity in the poles (as $\frac{1}{\sin 0^\circ}$ / $\frac{1}{\sin 180^\circ}$ term will give infinity at poles), to avoid this we bound our code domain within $-88.5^\circ$ to $88.5^\circ$ in the latitudinal direction. The advantage of the finite difference technique is that any sharp change in amplitude distribution is better tackled than the spherical harmonic techniques, which suffer from the ringing effect (Brett, 1988).

**Surface Flow Parameters:**

In Surface Flux Transport (SFT) models, the evolution of the photospheric magnetic field is governed by large-scale plasma flows on the solar surface. These flows include: 1) **Differential rotation** $\omega(\theta)$, 2) **Meridional circulation** $v(\theta)$, and 3) **Turbulent diffusion** $\eta$. *Differential Rotation:* The Sun exhibits differential rotation, where the angular velocity $\omega(\theta)$ varies with latitude $\theta$. This shears the magnetic field in the longitudinal (east-west) direction, redistributing flux along lines of constant latitude, where the strongest shear occurs at mid-latitudes. As the leading and trailing spots of a tilted active region reside at different latitudes, differential rotation primarily acts to increase their longitudinal separation over time, thereby enhancing the contribution of the active region to the Sun's axial dipole moment. In our model SPhoTraM, the rotation rate is typically modeled as:

$$\omega(\theta) = 13.38 - 2.30\,cos^2\theta - 1.62\,cos^4\theta \quad \text{degrees day}^{-1}. \tag{2.2}$$

This empirical profile is inspired from the helioseismic observation (Snodgrass, 1983; Mahajan et al., 2024). This profile leads to equatorial regions rotating faster than the poles, with a typical equator-to-pole rotation time difference of about 7 days. On the Sun, the characteristic timescale for differential rotation is $\tau_{\rm dr} = 2\pi/[\Omega(90^\circ) - \Omega(0^\circ)] \approx 0.25$ year, using the empirical profile Equation 2.2.

*Meridional Circulation:* The meridional flow is a weaker, poleward-directed flow that transports magnetic flux from active latitudes (low/mid-latitudes) toward the poles. It is typically antisymmetric about the equator: positive (northward) in the northern hemisphere

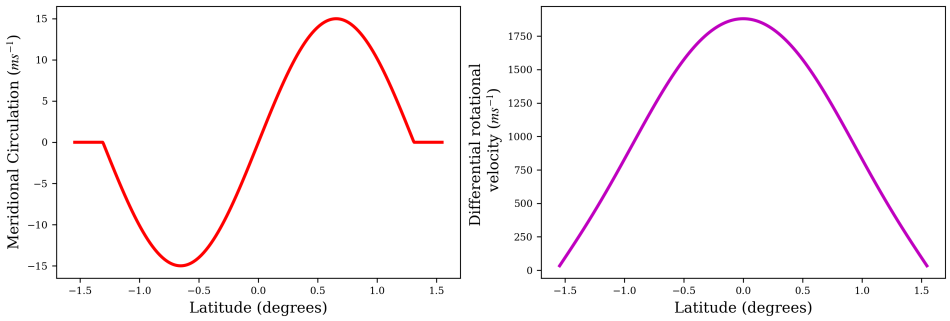


Figure 2.1: Plasm flows profile in SPhoTraM simulation. The left panel denotes the meridional circulation profile varies along latitude, peaked at 15 $\mathrm{m\,s^{-1}}$. The right panel denotes the differential rotational velcoity varies along latitude with peak rotation 13.38 deg/day.

and negative (southward) in the southern. The flow speed peaks around mid-latitudes ($\sim$35°) and drops to nearly zero near the poles and equator. A commonly used parametrization is:$v(\theta) = v_0 \sin(2\theta)^p$, where $v_0$ is the peak flow speed (typically 10–20 m $\mathrm{s^{-1}}$), and $p$ controls the latitude of the peak. The timescale for meridional circulation from equator to pole can be estimated as: $\tau_{\mathrm{mf}} \sim \frac{R_\odot}{v_0} \approx \frac{7\times10^8 \text{ m}}{15 \text{ m/s}} \approx 1.5$ years. In our SPhoTraM simulation, we use the mathematical profile for meridional circulation taken from van Ballegooijen et al. (1998):

$$v(\lambda) = \begin{cases} -v_0 \sin\left(\dfrac{\pi\lambda}{\lambda_0}\right), & \text{if } |\lambda| < \lambda_0, \\ 0, & \text{otherwise,} \end{cases} \tag{2.3}$$

where $\lambda$ is the latitude in degrees ($\lambda = \pi/2 - \theta$), and $\lambda_0$ is the latitude beyond which the meridional circulation speed drops to zero. In our model, we adopt $\lambda_0 = 75°$ and $v_0 = 15$ $\mathrm{m\,s^{-1}}$ for the majority of the SFT simulations. This empirical profile is also inspired from the helioseismic observation (Mahajan et al., 2024).

*Turbulent Diffusion:* In addition to advective transport, small-scale convective motions (e.g., granulation and supergranulation) are modeled as an effective turbulent diffusivity, typically denoted by $\eta$. This process helps in the dispersal and cancellation of opposite-polarity magnetic flux, also helps in flux transport across solar surface. Typical values of surface magnetic diffusivity used in SFT models are in the range: $\eta = 250 - 800$ $\mathrm{km^2\ s^{-1}}$ (Wang et al., 1989; Schrijver and Zwaan, 2000). We set it at 250 $\mathrm{km^2\ s^{-1}}$ in our model. The characteristic diffusion timescale over a length scale $L$ is: $\tau_{\mathrm{diff}} \sim \frac{R_\odot^2}{\eta}$. For a pole-to-

equator length scale and $\eta \sim 250$ km$^2$ s$^{-1}$, $\tau_{\rm diff}$ is: $\tau_{\rm diff} \sim \frac{(7\times10^8)^2}{2.5\times10^8} \approx 62$ years. This shows that turbulent diffusion acts over much longer timescales compared to meridional flow, but is critical in shaping the large-scale field structure. However, on AR length scales, the diffusion timescale is significantly shorter. Instead of using a constant diffusivity, some models implement a discrete random walk process as a proxy for turbulent dispersion (Wang and Sheeley, 1994; Schrijver and Title, 2001), while others incorporate convective flows directly into the velocity profile in purely advective flux transport models (Upton and Hathaway, 2014).

In SFT models, differential rotation redistributes flux azimuthally, meridional circulation transports flux poleward, and turbulent diffusion facilitates flux dispersal and cancellation as well as transport of magnetic flux. The interplay among these processes determines the surface evolution of the solar magnetic field and the reversal of the polar field over the solar cycle.

### Model Set-up

The spatial resolution of SPhoTraM code is 0.5° in both latitudinal and longitudinal directions (i.e. 500 × 1000 grid resolution). Physically, it can resolve a maximum of 4.3 megameters (Mm) at the solar surface (whereas the diameters of super-granules and granules are 30 Mm and 1 Mm, respectively). In terms of longitudinal spatial resolution, this code's grid does indeed resolve much more finely near the poles than at the equator. Overall resolution 4.3 Mm on the solar surface, whilst near the pole this is finer, 0.11 Mm. Our code solves SFT equation in Earth's reference frame, i.e. taking the exact value of Sun's rotation 13.38 deg/day, following Equation 2.2.

### Modelling the Active Region Source Term

The source term in Surface Flux Transport (SFT) models represents the emergence of new bipolar magnetic regions (BMRs) on the solar surface. These regions inject magnetic flux into the photosphere. In this model, each sunspot or AR is represented as an idealized bipolar magnetic region (BMR) – a pair of opposite-polarity magnetic patches on the solar surface, mimicking the magnetic structure of a sunspot group. In this study, the emergence of BMRs is modeled using a data-driven insertion routine, in which magnetic bipoles are

introduced based on sunspot properties such as latitude, longitude, tilt angle, flux, separation between poles and spot size.

Each BMR is constructed as a pair of oppositely signed magnetic patches, separated in latitude and longitude according to the observed Joy's law tilt and sunspot area. The following and leading polarity spots are located at angular distances symmetric around the central emergence position, defined by the sunspot latitude $\theta_0$ and longitude $\phi_0$, and are offset using the tilt angle $\gamma$ and a separation distance $d$ given by: $\theta_\pm = \theta_0 \mp \frac{d\cdot\sin\gamma}{2}$ and $\phi_\pm = \phi_0 \mp \frac{d\cdot\cos\gamma}{2}$, where $d = 3R_{\text{spot}}$ is proportional to the spot radius. The radial magnetic field from each polarity is modeled using a Gaussian distribution over the spherical surface of the Sun followed from van Ballegooijen et al. (1998). At any point $(\theta,\phi)$, the contribution from a polarity located at $(\theta^*,\phi^*)$ (where $*$ denotes either $+$ or $-$) is given by:

$$B_r^{(*)}(\theta,\phi) = B_{\max}\cdot\exp\left(\frac{-2+2\cos\Delta\Psi}{0.16\,w^2}\right), \tag{2.4}$$

where $\Delta\Psi$ is the angular distance between $(\theta,\phi)$ and $(\theta^*,\phi^*)$, computed as:$\cos(\Delta\Psi) = \sin\theta\sin\theta^* + \cos\theta\cos\theta^*\cos(\phi-\phi^*)$. The width $w$ of the Gaussian is determined by the spot radius and the grid resolution: $w = R_{\text{spot}}\cdot\frac{d\theta+d\phi}{2}$. To ensure flux conservation, the amplitude $B_{\max}$ is normalized such that the total unsigned flux from each polarity integrates to half of the total flux $\Phi$:

$$B_{\max} = \frac{\Phi}{\iint \sin\theta\,\exp\left(\frac{-2+2\cos\Delta\Psi}{0.16\,w^2}\right)\,d\theta\,d\phi}. \tag{2.5}$$

The full BMR field is then the superposition of both polarities, inserted additively into the radial magnetic field grid:

$$B_r^{\text{BMR}}(\theta,\phi) = B_r^{(+)}(\theta,\phi) + B_r^{(-)}(\theta,\phi). \tag{2.6}$$

This physically motivated formulation ensures that each BMR adheres to observational constraints and contributes correctly to the surface magnetic flux budget. The location, orientation, and flux content of each BMR are typically sourced from sunspot databases such as RGO/USAF/NOAA database. The total unsigned magnetic flux $\Phi$ of the BMR is usually related to the sunspot area $A$ by an empirical conversion $\Phi = k\times A$, where

$k \sim 7 \times 10^{19}\,\mathrm{Mx}/\mu\mathrm{Hem}$ is a proportionality constant derived from observations (Dikpati et al., 2006). The tilt angle $\gamma$ of the BMR with respect to the local east–west direction follows Joy's Law, i.e. proportional to latitude (Jiang et al., 2014).

Lastly, the source term, S($\theta$,$\phi$,t) in this SFT model equation imitates the emergence of the sunspots on the surface that can be constructed in two ways: 1) Using data-driven mathematical modeling of the ideal bipolar magnetic region (Jiang et al., 2011, 2013), 2) Direct data assimilation of synoptic maps or SHARP data series (Worden and Harvey, 2000; Durrant et al., 2004; Yeates et al., 2015).

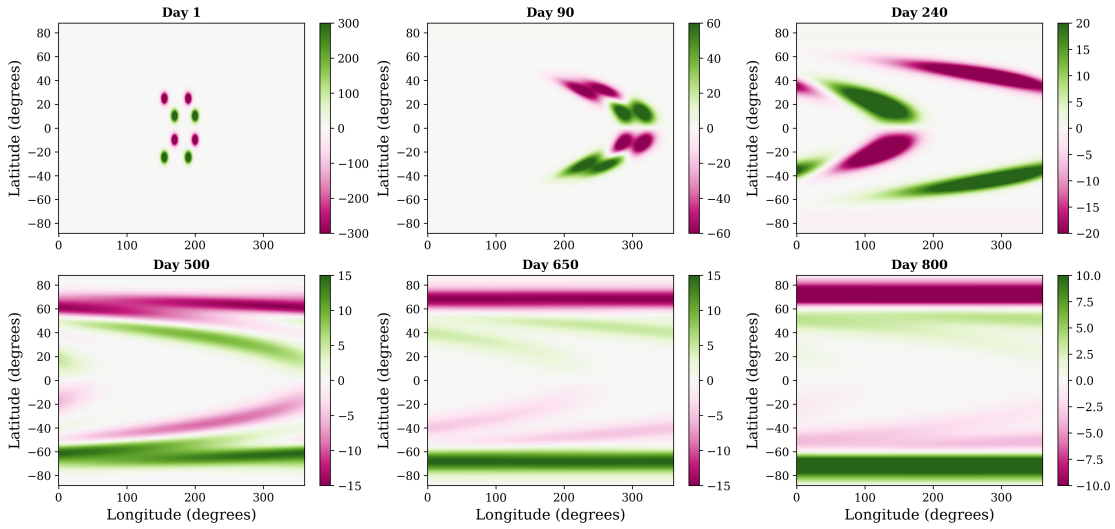


Figure 2.2: SFT simulation. The top panels show the surface magnetic field evolution on days 1, 90, and 240, where the bottom panel depicts the evolution on days 500, 650, and 800, respectively, starting from an initial configuration consisting of four BMRs, two in each hemisphere.

### 2.1.2 Parameter Space Study in SPhoTraM

We consider four BMRs – two in each hemisphere, containing an equal amount of flux – as the initial condition of the SFT model (SPhoTraM). Additionally, positive and negative magnetic fields are placed in the northern and southern polar regions, respectively (see first panel of Figure 2.2, day 1). As time progresses, the combined effects of differential rotation, meridional circulation, and turbulent diffusion act on the BMRs. The latitudinal shear from differential rotation stretches the BMRs in the toroidal (longitudinal) direction, meridional circulation advects them poleward, and diffusion aids both the equatorward cancellation of the leading polarity and the overall redistribution of magnetic flux. These

effects are clearly visible in other panels of Figure 2.2 (Day 90 to 800).

In the bottom panels of the same figure, the cumulative effect of the Babcock–Leighton (BL) mechanism becomes apparent. The initially positive polar field in the northern hemisphere reverses its sign and becomes negative after some time. The timing and efficiency of this reversal depend on the strength of the transport profiles, BMR properties as well as the amplitude of the initial magnetic field. In the next section, we perform a detailed parameter-space study to examine how the transport mechanisms and active region properties influence magnetic flux evolution in the SFT model.

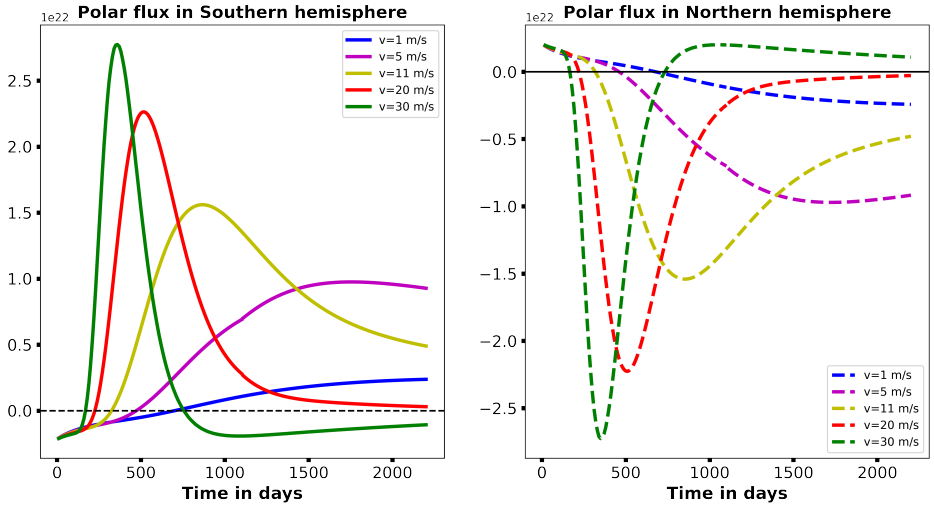


Figure 2.3: Evolution of the hemispheric polar magnetic flux for different values of the meridional circulation amplitude, with the diffusivity held fixed at 250 $km^2 s^{-1}$. The left panel and the right panel show the time variation of the northern and southern polar regions, respectively.

### Variations in Flow Parameters

**Case 1: Meridional circulation amplitude variations:** At first, we set diffusivity at 250 $km^2 s^{-1}$ and vary the meridional circulation from 1 m $s^{-1}$ to 30 m $s^{-1}$. In Figure 2.3, blue, magenta, yellow, red, and green curves denote v = 1, 5, 11, 20, and 30 m $s^{-1}$ respectively. The solid lines and dashed lines represent the time evolution of Southern and Northern Polar flux, respectively. Let us consider the right plot of Figure 2.3 (Polar flux evolution in the Northern hemisphere) for detailed analysis. The plot shows that the reversal time will decrease with increasing meridional flow, i.e., higher meridional flow velocity will take the following polarity quickly towards the pole, and the reversal of polarity happens faster.

Polar flux maxima will decrease with decreasing flow velocity. Due to slower flow velocity, diffusion will play a dominant role in the system, thus flux cancellation will happen more, and a lower amount of flux will be able to reach the pole. Also, while a slower velocity will take longer to transport flux towards the pole, most of the magnetic field will diffuse away and will result in a smaller amount of flux inside the polar region.

An interesting change can be noted in the magenta (v = 5 m $s^{-1}$), yellow (v = 11 m $s^{-1}$), and red (v = 20 m $s^{-1}$) curves. If the flow velocity rises to a very high value, then the polar flux accumulation will end up with a lesser flux (see the red curve). High velocity will pull the leading flux (+ve) along with the following (-ve) one towards the north pole, and taking part in the cancellation of negative flux will cause the lower flux value at the end. The opposite scenario will happen for the low velocity profile (see magenta curve). But, for very small velocities, this phenomenon will not take place due to more diffusion of the magnetic field (see blue curve).

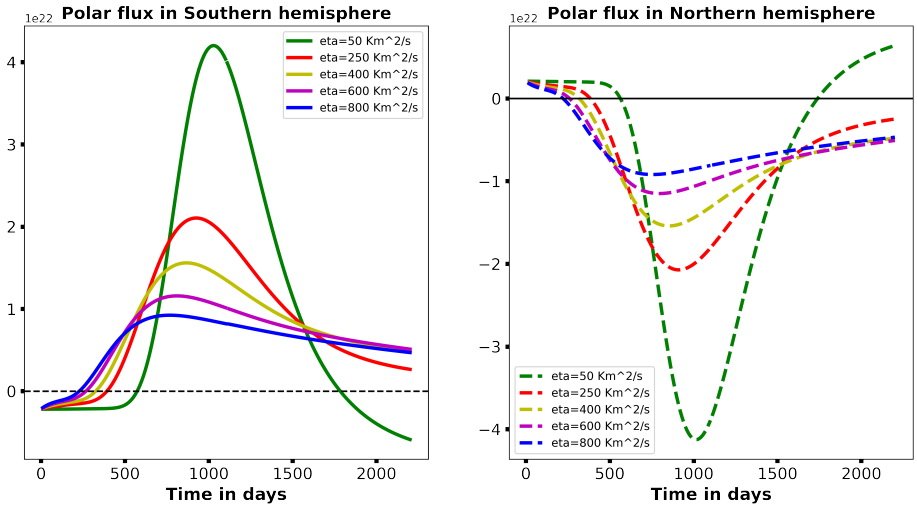


Figure 2.4: Evolution of the northern hemispheric polar magnetic flux for different values of the diffusion coefficient, with the meridional circulation speed amplitude held fixed at 11 m $s^{-1}$. The left panel and the right panel show the time variation of the northern and southern polar regions, respectively.

**Case 2: Diffusivity variations:** Here we set the meridional flow velocity at 11 m $s^{-1}$ and vary the diffusivity from 50 $Km^2sec-1$ to 800 $Km^2sec-1$. In Figure 2.4, green, red, yellow, magenta, and blue curves denote the results with diffusivity 50, 250, 400, 600, and 800 $Km^2sec-1$, respectively. The solid lines and dashed lines represent the time evolution of Southern and Northern Polar flux, respectively. Let us consider the right plot

of Figure 2.4 (Polar flux evolution in the Northern hemisphere) for detailed analysis. The plot shows that the reversal time will decrease with increasing diffusivity, i.e., diffusion will also play an important role in the poleward advection process.

Polar flux maxima will decrease with increasing diffusivity. Due to higher values of diffusivity, flux cancellation will happen more, and a lower amount of flux will be able to reach the pole. Also, when meridional flow takes the flux to the pole, most of the magnetic field will diffuse away and will result in a smaller amount of flux inside the polar region.

An interesting change can be noted in the magenta ($\eta$ = 600 $Km^2sec-1$) and red ($\eta$ = 250 $Km^2sec-1$) curves. If the diffusivity rises to a very high value, then the polar flux accumulation will end up with a higher flux (see the magenta curve), although the maxima are lower. This is because lower diffusivity will not reduce the leading polarity magnetic field, and a leading polarity with a sufficient amount will also advect towards the pole and cancel the remaining polarity there.

**Case 3: Differential rotation amplitude variations:** In our simulations, we set the meridional flow speed to 11 m $s^{-1}$ and the surface magnetic diffusivity to 250 $km^2$ $s^{-1}$. We systematically varied the amplitude of the differential rotation from 0.5 to 2 times its standard value to assess its influence on polar flux evolution. Our results indicate that changes in the differential rotation amplitude have minimal impact on the polar flux dynamics. This outcome is expected, as SFT models are axisymmetric and primarily sensitive to flows in the meridional (latitudinal) direction; the differential rotation, acting longitudinally, plays a limited role in the accumulation of magnetic flux at the poles.

### Variations in AR properties

Here, we first introduce a single BMR on the solar surface, positioned at a longitude of 180°, latitude of 20°, with a tilt angle of 4.47°, a magnetic flux of $5.1 \times 10^6$ Mx, and a polarity separation of 17.3°. We note that the leading polarity is negative and the following polarity is positive. We also keep the flow parameters at a fixed value for all cases.

**Case 1: Latitudinal position variations:** Here, the latitudinal position is varied from 5° to 40° in the northern hemisphere only, keeping other AR properties fixed. We find that as the emergence latitude increases, the magnetic flux from the BMR reaches the pole more quickly. However, both polarities (positive and negative) are advected toward the

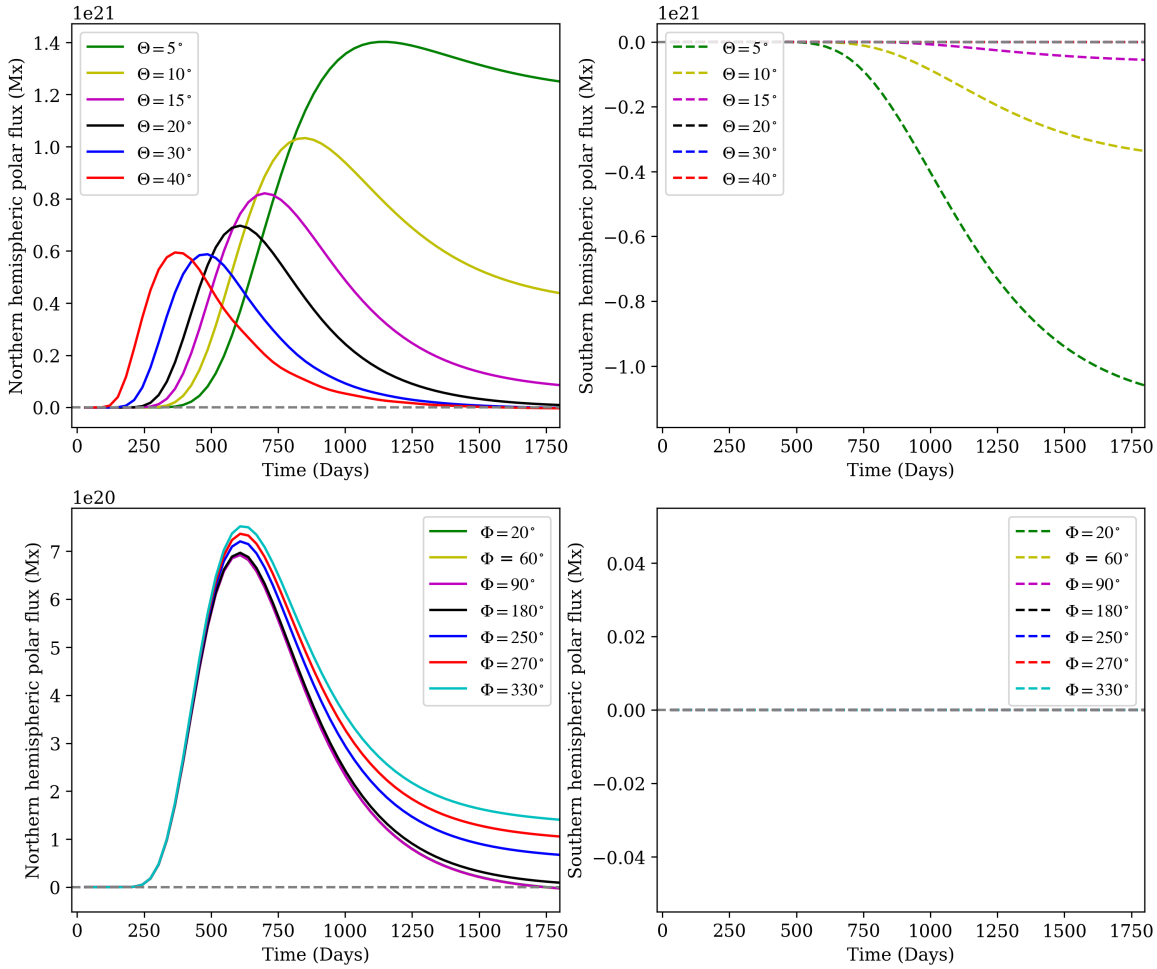


Figure 2.5: Polar flux evolution due to variations in the emergence latitude and longitude of a single BMR. Panel (a) shows the evolution of northern polar flux for emergence latitudes ($\Theta$) ranging from 5° to 40°. Panel (b) presents the corresponding evolution for the southern hemisphere. Panel (c) depicts the time evolution of northern polar flux for different emergence longitudes ($\Phi$), varying from 20° to 330°. (d) shows the same for the southern hemisphere.

pole, leading to intra-active-region cancellation. As a result, a smaller net flux reaches the pole, and the peak amplitude of polar flux decreases with increasing emergence latitude. Additionally, the time required to diffuse the accumulated polar flux is shorter at higher latitudes. These results are depicted in Figure 2.5a.

In contrast, when the BMR emerges at lower latitudes, the trailing polarity takes longer to reach the pole, but a larger fraction of the flux is transported poleward. This occurs because the leading polarity has more time to cancel and diffuse across the equator. Cross-equatorial flux transport is enhanced in such cases. As shown in Figure 2.5b (green dashed line), a significant amount of negative flux from the leading polarity crosses the equator and contributes to the build-up of the southern polar field.

**Case 2: Longitudinal position variations:** Here, the longitudinal position is varied from 20° to 330°, keeping other AR properties fixed. We find that in the Northern Hemisphere, there is only a slight variation in the polar flux as the longitudinal position increases from 180° to 330°, indicating that longitudinal variations do not significantly affect magnetic flux transport as shown in Figure 2.5c. In the Southern Hemisphere, no flux reaches the pole when the BMR appears at 20°, due to the absence of cross-equatorial flux transport (seeFigure 2.5d).

**Case 3: Tilt angle variations:** Here, the tilt angle is varied from −45° to 60°, while keeping other AR properties fixed. As the tilt angle increases (from 0° to 60°), the trailing polarity moves closer to the pole more rapidly, reducing the chance of intra-active-region cancellation. Consequently, the northern hemispheric polar flux (positive) increases and has a higher peak value as shown in Figure 2.6a. In all cases, the timing of the peak polar flux is nearly identical. However, although a larger tilt angle facilitates faster transport of the trailing polarity flux to the pole, this early accumulation does not persist. Over time, a portion of the leading polarity flux also migrates poleward due to increased latitudinal separation, leading to partial cancellation at the poles. As a result, the final polar flux levels converge across different tilt angles (see Figure 2.6a). Additionally, the increased latitudinal separation causes a fraction of the following polarity flux ($\sim$10 times lesser) to cross the equator and accumulate in the southern hemisphere (see Figure 2.6b).

On the other hand, for tilt angles opposite to Joy's law (e.g., −20° and −45°), the leading polarity shifts to higher latitudes while the trailing polarity moves closer to the equator.

In this scenario, negative polarity flux is transported to the northern pole, reversing the expected sign of the polar flux, as reflected in Figure 2.6a and b.

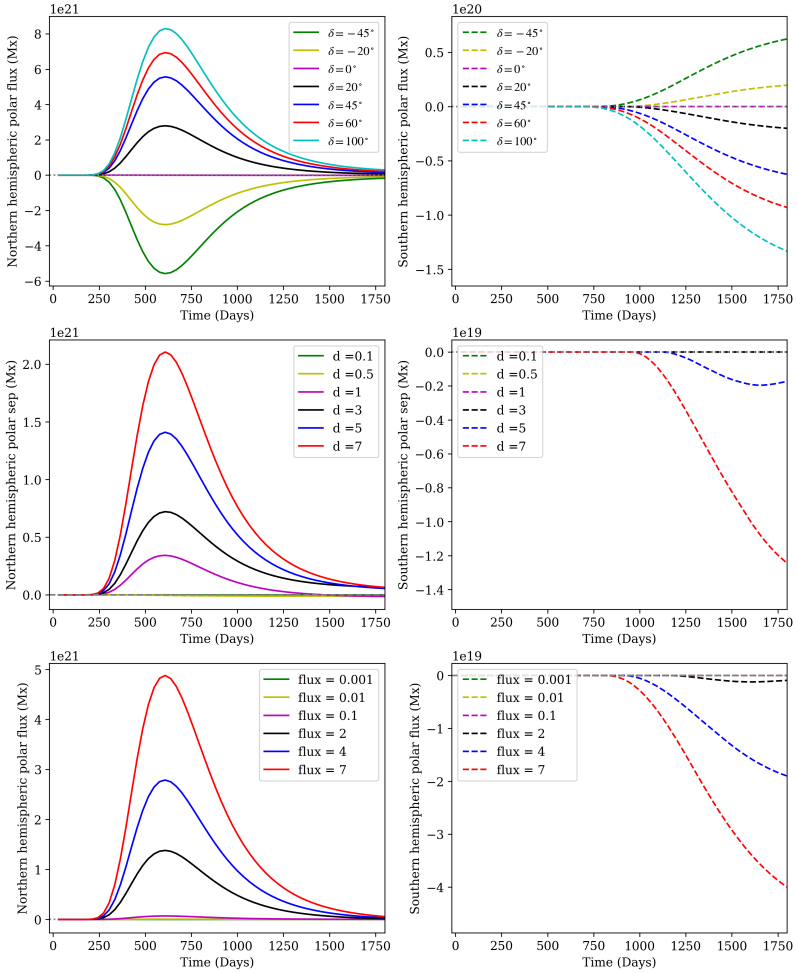


Figure 2.6: Polar flux evolution due to variations in the tilt angle, separation, and flux content of a single BMR. Panel (a) shows the evolution of northern polar flux for tilt angle ($\delta$) ranging from -45° to 100°. Panel (b) presents the corresponding evolution for the southern hemisphere. Panel (c) depicts the time evolution of northern polar flux for different polarity separation values, varying from 0.1× original separation to 7× original separation of the BMR. Panel (d) shows the same for the southern hemisphere. Panel (e) depicts the time evolution of northern polar flux for different flux content, varying from 0.001× original flux to 7× original flux of the BMR. Panel (f) shows the same for the southern hemisphere.

**Case 4: Separation variations:** Here, we vary the separation between the two polarities of the BMR from $0.1 \times d$ to $7 \times d$, where $d$ is the original separation, keeping all other AR properties fixed. The resulting evolution exhibits a trend similar to that observed for increasing tilt angles. As the separation increases, the latitudinal distance between polarities grows, which enables more trailing polarity flux to reach the northern pole early. However, much of this flux gradually diffuses over time (see Figure 2.6c).

Furthermore, larger separations bring the leading polarity closer to the equator, allowing a small amount of negative flux to cross into the southern hemisphere. Although this cross-equatorial transport is about two orders of magnitude weaker than in the northern hemisphere, it still results in a detectable buildup of polar flux in the south (see Figure 2.6d).

**Case 5: Flux variations:** Here, the magnetic flux content of the BMR is varied from $0.001, \Phi$ to $7, \Phi$, where $\Phi$ is the reference flux, while keeping other active region (AR) properties fixed. The evolution shows similar characteristics to the cases of increasing tilt angle or polarity separation. As the total flux increases, a greater amount of trailing polarity flux is transported to the northern hemisphere, leading to a higher peak in polar flux, which then gradually diffuses over time (see Figure 2.6e). Additionally, larger flux content delays the diffusion of the leading polarity, allowing a small portion to cross the equator. Although this cross-equatorial transport is about two orders of magnitude smaller, it contributes weakly to the buildup of southern polar flux (see Figure 2.6f).

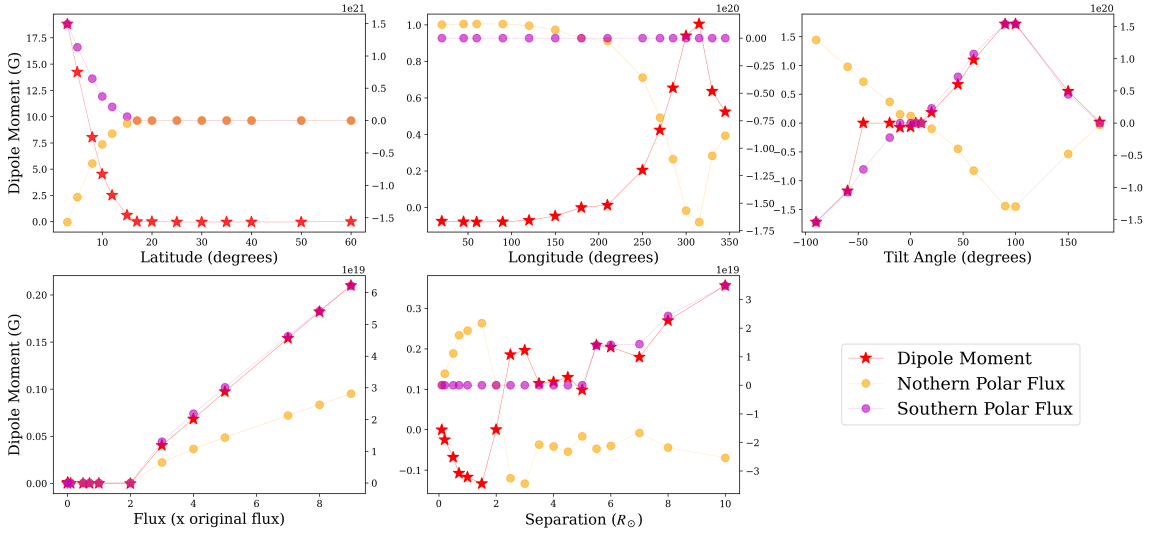


Figure 2.7: Variation of dipole moment and hemispheric polar flux at the end of the cycle as a function of different BMR properties. The parameters varied include emergence latitude, emergence longitude, tilt angle, magnetic flux content, and polarity separation. These results help assess the relative influence of each parameter on the buildup of the large-scale solar magnetic field.

To assess which active region (AR) property has the most significant influence on the Surface Flux Transport (SFT) mechanism, we compute the dipole moment (DM) and hemispheric polar flux at the end of each simulation, and plot their dependence on key AR parameters: latitude, longitude, tilt angle, magnetic flux, and polarity separation (see Fig-

ure 2.7). The results show that latitude has the strongest impact on large-scale magnetic field evolution. Specifically, we find that as the emergence latitude increases, the resulting DM decreases. This implies that in stronger solar cycles, where BMRs tend to emerge at higher latitudes, the effective polar field generation is suppressed – an effect known as latitudinal quenching (Jiang, 2020; Yeates et al., 2025). This phenomenon serves as a natural regulator, preventing unlimited amplification of solar cycle strength.

It is important to note that this analysis is based on simulations involving a single BMR. In reality, the solar surface hosts a multitude of emerging sunspots throughout the cycle. In such cases, tilt angle, flux content, and separation also play critical roles alongside latitude, influencing the balance between flux cancellation and accumulation (for reference see Baumann et al. (2004)). Additionally, because the SFT model is axisymmetric, the longitudinal position of BMRs has a negligible effect on the net flux transport, justifying its weak influence in the simulations.

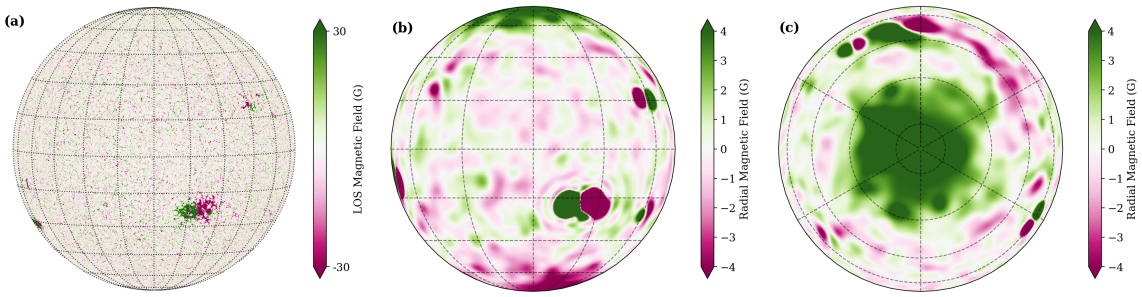


Figure 2.8: Panel (a) shows the line-of-sight magnetic field distribution from an HMI magnetogram. Panel (b) presents a simulated surface magnetic field map from a solar surface flux transport (SFT) model, viewed from the plane of the ecliptic, mimicking the Earth-based perspective. Panel (c) displays the same simulation from a top-down (north pole) view, revealing details of the polar cap that are not visible from the low-latitude perspective, highlighting the advantage of SFT modeling in capturing the full-Sun magnetic structure.

### 2.1.3 Key Insights from the SFT Model

One of the main strengths of Surface Flux Transport (SFT) models is their ability to explain the physical processes behind the observed changes in the Sun's magnetic field. These models not only reproduce what we see in observations but can also reveal magnetic features that are not directly visible in solar magnetograms. For example, Figure 2.8 shows a comparison between an observed full-disk magnetogram and one produced by the SFT

model using the SPhoTraM code. The model clearly captures the formation of the polar fields, showing how useful it is in understanding solar magnetic evolution.

A key advantage of using SFT models is that they can generate magnetic maps of the full Sun. This is something that observations alone cannot do accurately, due to several limitations: 1) We can only observe one side of the Sun at a time, so sunspots that appear and disappear on the far side go unnoticed, 2) Data near the edges (limbs) of the solar disk are often affected by projection errors 3) It is difficult to directly observe the magnetic fields at the solar poles. Because of these challenges, observed magnetograms can have missing or incorrect magnetic flux. This missing information can affect how we understand and model the Sun's magnetic field. SFT models help fill in these gaps by simulating how magnetic flux is transported across the solar surface over time.

In summary, SFT models are powerful tools for studying how the Sun's large-scale magnetic field, especially the polar fields, changes over time. They are also very useful for predicting the solar cycle, modeling solar eclipses, and estimating the Sun's open magnetic flux and solar wind—topics that are discussed in the next chapters.

## 2.2 Coronal Magnetic Field Models

### 2.2.1 Potential Field Source Surface (PFSS) Model

As discussed in section 1.5, one of the most intriguing and long-standing questions in solar physics concerns the extraordinarily high temperature of the solar corona, referred to as the coronal heating problem, has driven decades of research to identify the mechanisms that transfer and dissipate energy from the solar interior into the tenuous upper atmosphere. Central to this puzzle is the role of the Sun's magnetic field, which dominates the dynamics of the low $\beta$ coronal plasma. Understanding the structure and evolution of coronal magnetic fields is therefore crucial to unraveling the physical processes that heat the corona.

However, due to the low plasma density and optically thin nature of the corona, routine direct measurements of magnetic field strengths are not feasible. Despite this challenge, modern instrumentation is making significant progress as mentioned in subsection 1.5.1. Nevertheless, observational limitations still necessitate the use of computational models –

such as Potential Field Source Surface (PFSS), magneto-frictional, and full magnetohydrodynamic (MHD) simulations – to extrapolate the magnetic field from the photosphere into the corona. Most global coronal magnetic field evolution models are quasi-static in nature,

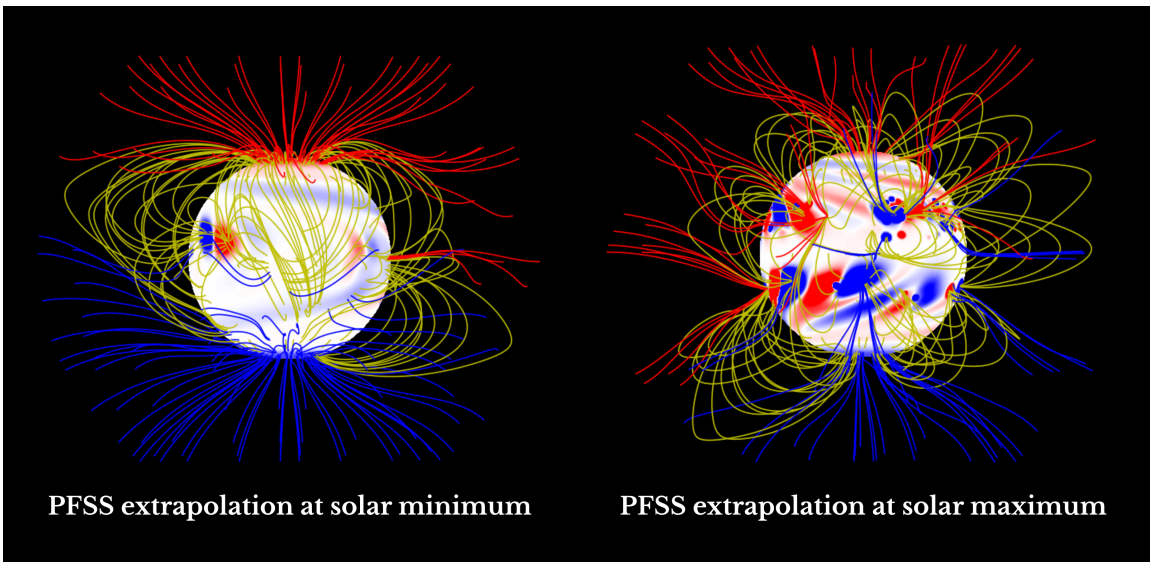


Figure 2.9: PFSS extrapolation of the solar magnetic field during solar cycle minimum (left panel) and maximum (right panel), using the SFT-simulated photospheric magnetic field as the lower boundary condition.

as the large-scale evolution of the coronal field typically occurs on timescales much longer than the dynamic relaxation timescale of the system (Mackay and Yeates, 2012). That is, magnetic forces act quickly to restore equilibrium following perturbations, allowing the field to be modeled as evolving through a sequence of force-free or current-free configurations. One of the simplest and most widely used models in this category is the Potential Field Source Surface (PFSS) model (Hoeksema, 1984; Schatten et al., 1969; Schrijver and De Rosa, 2003; Wiegelmann et al., 2017), which has proven effective in capturing the large-scale structure of the solar corona.

The PFSS model assumes that the region between the solar surface ($R_\odot$) and a spherical outer boundary called the source surface $R_{ss}$ (typically set at $2.5, R_\odot$) is current-free (i.e. $\nabla \times \mathbf{B} = 0$), meaning the magnetic field $\mathbf{B}$ satisfies Laplace's equation (Wang et al., 1996; Schrijver and De Rosa, 2003):

$$\nabla \times \mathbf{B} = 0 \quad \Rightarrow \quad \mathbf{B} = -\nabla \Phi, \tag{2.7}$$

where $\Phi$ is the scalar magnetic potential. Substituting into Maxwell's equation $\nabla \cdot \mathbf{B} = 0$

gives Laplace's equation for $\Phi$:

$$\nabla^2 \Phi = 0. \tag{2.8}$$

To solve for $\Phi$, we impose the following boundary conditions: **1. At the photosphere** ($r = R_\odot$), the radial field must match observations:

$$B_r(R_\odot, \theta, \phi) = -\left.\frac{\partial \Phi}{\partial r}\right|_{r=R_\odot} = B_r^{\mathrm{obs/SFT}}(\theta, \phi) \tag{2.9}$$

**2. At the source surface** ($r = R_{\mathrm{ss}}$), the magnetic field is assumed to be purely radial, so the transverse components vanish:

$$B_\theta(R_{\mathrm{ss}}, \theta, \phi) = -\frac{1}{r}\left.\frac{\partial \Phi}{\partial \theta}\right|_{r=R_{\mathrm{ss}}} = 0 \tag{2.10}$$

$$B_\phi(R_{\mathrm{ss}}, \theta, \phi) = -\frac{1}{r\sin\theta}\left.\frac{\partial \Phi}{\partial \phi}\right|_{r=R_{\mathrm{ss}}} = 0 \tag{2.11}$$

These boundary conditions ensure that the magnetic field becomes radial at the source surface and conforms to photospheric magnetogram data at the solar surface. Given these conditions, $\Phi$ is typically expanded in spherical harmonics, and the magnetic field components are derived accordingly:

$$\Phi(r, \theta, \phi) = \sum_{\ell=1}^{\ell_{\max}} \sum_{m=-\ell}^{\ell} \left[a_{\ell m} r^{\ell} + b_{\ell m} r^{-(\ell+1)}\right] Y_{\ell m}(\theta, \phi), \tag{2.12}$$

where $Y_{\ell m}(\theta, \phi)$ are the spherical harmonics, and the coefficients $a_{\ell m}$ and $b_{\ell m}$ are determined using the boundary conditions and solved using finite difference schemes. In this thesis work, we have used the PFSS code developed by Dr. Anthony Yeates, which can be found at https://github.com/antyeates1983/pfss.

The PFSS model employs the observed photospheric magnetic field as the lower boundary condition to extrapolate the coronal magnetic field structure. These photospheric maps are obtained from full-disk synoptic observations provided by instruments such as the Helioseismic and Magnetic Imager (HMI), the Global Oscillation Network Group (GONG), and the Wilcox Solar Observatory (WSO), or from surface magnetic field reconstructions generated by SFT models, denoted as $B_r^{\mathrm{obs/SFT}}$. In Figure 2.9, we employ SFT-generated magnetic maps corresponding to solar minimum (left panel) and solar maximum (right

panel) epochs to compare the global coronal magnetic field structure using the PFSS model. These simulations reveal prominent closed-loop field line structures that characterize the helmet streamers – elongated features formed by magnetic loops that trap dense, hot plasma in the corona, making them appear bright in white-light observations. At solar maximum, a more complex and multipolar magnetic field topology emerges due to the frequent and widespread emergence of active regions. In contrast, the magnetic structure during solar minimum is relatively simple and dipole-like, dominated by large-scale, ordered field configurations.

The Potential Field Source Surface (PFSS) model provides a good first approximation of the large-scale coronal magnetic field because, for much of the time, the coronal field is nearly force-free – that is, the magnetic field does not exert a net Lorentz force at the coronal base, satisfying a Maxwell stress-free condition. However, the PFSS model has important limitations. One key drawback is that in reality, the coronal magnetic field does not become perfectly radial within the region where electric currents are negligible. As a result, some coronal features are not accurately represented. For instance, observed polar plumes often bend more toward the equator than predicted by the PFSS model. Similarly, helmet streamers tend to bend more equatorward during solar minimum and more poleward during solar maximum – features that the PFSS model cannot fully capture due to its simplified assumptions. Moreover, accurately generating the polar flux in the surface magnetic map is crucial, as it serves as the lower boundary input to the PFSS model and significantly influences the extrapolated coronal magnetic field structure. A stronger polar flux tends to bend the large-scale streamer structures more equatorward, as typically observed during solar minimum. In contrast, a weaker polar flux allows streamers to extend more poleward, as is characteristic during solar maximum.

### 2.2.2 Alfvén Wave Solar-atmosphere Model (AWSoM)

The *Alfvén Wave Solar-atmosphere Model* (AWSoM) is a physics-based model designed to simulate the solar corona and solar wind, extending from the solar surface out to Earth and beyond. It is part of NASA's Space Weather Modeling Framework (SWMF) and is often run using the BATS-R-US MHD solver (Gombosi et al., 2021). Unlike empirical models that use artificial heating terms, AWSoM relies on physically motivated processes

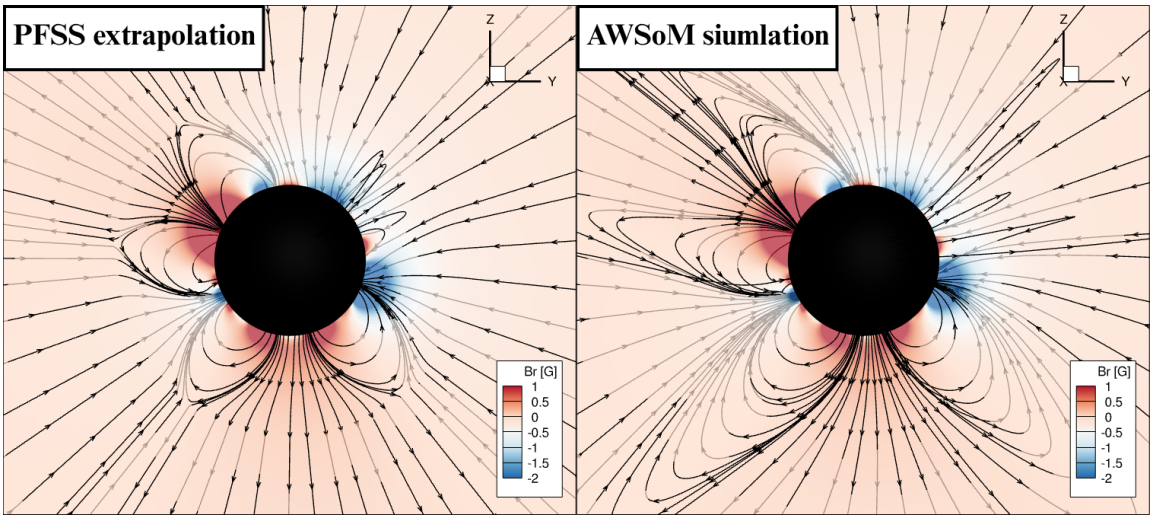


Figure 2.10: Coronal magnetic field extrapolation using two different models: the left panel shows the PFSS (Potential Field Source Surface) extrapolation, while the right panel displays the full MHD-based extrapolation using the Alfvén Wave Solar Model (AWSoM).

– primarily *Alfvén wave turbulence* – to explain the heating of the solar atmosphere and the acceleration of the solar wind.

In AWSoM, Alfvén waves are launched from the lower solar atmosphere and propagate outward along magnetic field lines. Due to variations in plasma density and magnetic field strength, a portion of these waves reflects back, and the counter-propagating waves interact to generate turbulence. This turbulence leads to energy dissipation, which heats the coronal plasma and accelerates it outward, forming the solar wind. Thus, a key advantage of AWSoM is that it does not prescribe coronal heating in an ad hoc manner; instead, the heating and acceleration arise naturally from the dynamics of wave–plasma interaction. This full MHD model also offers other physics-based improvements over PFSS models, including the consideration of electric currents in the solar corona and radiative plasma cooling.

The model solves the full set of MHD equations, plus wave transport and thermodynamics: 1) Mass conservation, 2) Momentum conservation (including wave pressure), 3) Energy equations (electron + ion), 4) Magnetic induction equation, 5) Alfvén wave energy transport equations. Input: Photospheric magnetic field (from magnetograms). At the inner boundary (approximately 1 $R_\odot$), the model is prescribed with specific values of plasma density and temperature. Alfvén wave energy flux is launched from this boundary based on the local magnetic field strength. The simulation domain typically extends up to 30 $R_\odot$

or beyond.

To capture the steep transition between the chromosphere and corona, AWSoM employs a special numerical method called the *field-line-threaded* approach. This allows it to handle sharp gradients without needing extremely fine spatial resolution, making the model efficient and suitable for near-real-time simulations. AWSoM has successfully reproduced many observed features of the solar corona and solar wind, such as: the bimodal structure of the solar wind (fast and slow streams), realistic shapes of the heliospheric current sheet, the formation of polar plumes and streamers, and temperature and density profiles consistent with EUV and X-ray observations etc (Szente et al., 2019; Sachdeva et al., 2019; van der Holst et al., 2022; Huang et al., 2023; Shi et al., 2024). Due to its realistic physics and reliable performance, AWSoM is now widely used in both solar research and operational space weather forecasting.

**Advantages of full MHD models over PFSS model:**

There are several advantages to using a full MHD model instead of potential field models to construct the coronal magnetic field structure. In Figure 2.10, we compare the coronal magnetic field structure obtained from the final steady-state solution of the 3D time-independent MHD model with that derived using the PFSS extrapolation method. We find PFSS models fail to reproduce the cusp-like elongated features of the streamer belt as observed (see the left panel of Figure 2.10). To accurately model the large-scale corona, it is necessary to consider the coupled interaction of magnetic plasma and solar gravity forces, including the effects of solar wind. Clearly, when time-dependent phenomena are important, MHD models are essential.

With the MHD model, we can obtain plasma density and temperature profiles along with magnetic field distributions, which can be directly used to estimate the shape of the white light image of the corona, rather than relying on synthetic white light images. PFSS models also struggle to capture sheared field lines near Active Regions, which is particularly important during solar maximum when more active regions are present and temporal variations significantly impact the large-scale coronal structure. Another important application of the MHD model is in comparing observed Faraday rotation values with those extracted from MHD steady-state simulations of the solar corona. When a linearly polar-

ized radio wave propagates through a magnetized plasma, such as the corona, its plane of polarization rotates—this rotation angle is called Faraday rotation. Since Faraday rotation is proportional to the product of the electron density and the component of the magnetic field along the observer's line of sight, an MHD model is crucial for interpreting these observations and inferring coronal structures.

## 2.3 Solar Dynamo Model

The solar magnetic field exhibits an approximately 11-year cycle during which the number of sunspots waxes and wanes, and the Sun's magnetic polarity reverses. This global cyclic behavior is attributed to an MHD dynamo mechanism operating within the solar convection zone as mentioned in the introduction. In the current understanding, this dynamo results from the interplay between large-scale plasma flows – namely, differential rotation and meridional circulation – and the evolution of magnetic fields through induction, diffusion, and buoyant eruption. A particularly successful framework for modeling the solar magnetic cycle is the BL-type flux transport dynamo model, which assumes that the poloidal magnetic field is regenerated near the solar surface through the decay and dispersal of tilted bipolar sunspot regions. The physical details of this dynamo action have already been discussed in the introduction.

Here, we briefly discuss the SURYA code developed by Choudhuri and collaborators (Choudhuri et al., 1995; Nandy, 2002; Chatterjee et al., 2004; Jiang et al., 2007), which is utilized in this thesis to address scientific problems. This numerical code is a numerical realization of the $\alpha - \Omega$ dynamo model in axisymmetric two-dimensional spherical geometry. It evolves the large-scale axisymmetric magnetic field under the influence of kinematic velocity flow fields and parametrized source terms. Mathematically, the axisymmetric magnetic field in the convection zone can be decomposed in terms of a toroidal component $B_\phi$ and a vector potential $A_\phi$ for the poloidal component, such that the full magnetic field is expressed as:

$$\mathbf{B} = B_\phi(r,\theta)\,\hat{e}_\phi + \nabla \times \left[A_\phi(r,\theta)\,\hat{e}_\phi\right]. \tag{2.13}$$

The time evolution of the poloidal and toroidal components is governed by the following

coupled partial differential equations derived from the magnetic induction equation:

$$\begin{aligned} \frac{\partial A_\phi}{\partial t} + \frac{1}{s}\left[\mathbf{v_p}\cdot\nabla(sA_\phi)\right] &= \eta_p\left(\nabla^2 - \frac{1}{s^2}\right)A_\phi + \alpha B_\phi \\ \frac{\partial B_\phi}{\partial t} + s\left[\mathbf{v_p}\cdot\nabla\left(\frac{B_\phi}{s}\right)\right] + (\nabla\cdot\mathbf{v_p})B_\phi &= \eta_t\left(\nabla^2 - \frac{1}{s^2}\right)B_\phi + s\left(\left[\nabla\times(A_\phi\hat{\mathbf{e}}_\phi)\right]\cdot\nabla\Omega\right) \\ &\quad + \frac{1}{s}\frac{\partial(sB_\phi)}{\partial r}\frac{\partial\eta_t}{\partial r} \end{aligned} \tag{2.14}$$

where $s = r\sin\theta$, $\mathbf{v_p} = (v_r, v_\theta)$ is the meridional circulation, $\Omega$ is the angular velocity profile of differential rotation, $\alpha$ is the source term representing poloidal field generation from toroidal component, and $\eta_p$, $\eta_t$ are the magnetic diffusivities for the poloidal and toroidal components, respectively.

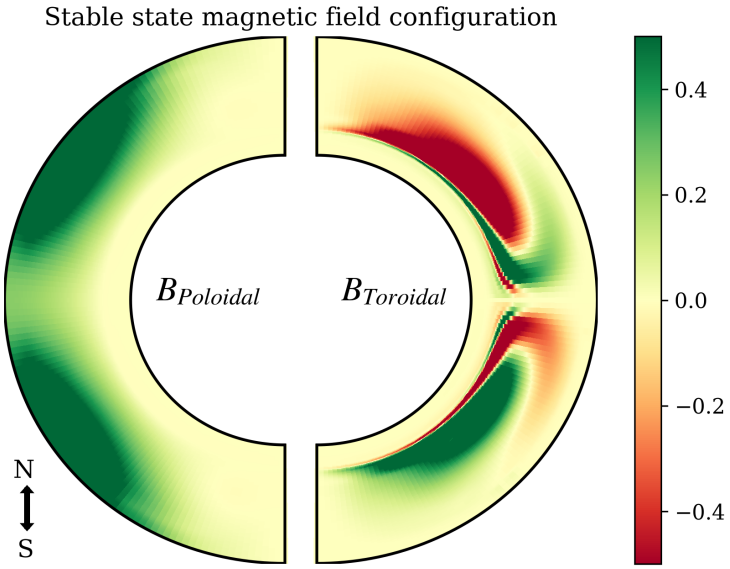


Figure 2.11: Solar dynamo simulation using the SURYA code. This meridional cut illustrates the final state of the dynamo simulation. The left panel shows the poloidal magnetic field, while the right panel depicts the toroidal field strength, typically concentrated near the base of the convection zone.

We now discuss how all the terms in this model are mathematically framed and how the model parameters are set for stable dynamo action. This dynamo model operates in a kinematic regime, which means the magnetic field dynamics does not produce any changes in the velocity fields. In this model, the velocity field is assumed to be time-independent and consists of two components: the internal solar differential rotation ($\Omega$) and the meridional circulation ($\mathbf{v_p}$). The rotation profile is modeled based on helioseismic inversion data and

features radial shear in the tachocline and latitudinal shear (equator rotates faster than high latitudes) throughout the convection zone. The analytic profile used in SURYA is:

$$\Omega(r,\theta) = \Omega_c + \frac{1}{2}\left[1 + \mathrm{erf}\left(\frac{r - r_c}{d_c}\right)\right](\Omega_s(\theta) - \Omega_c), \tag{2.15}$$

where $\Omega_s(\theta) = \Omega_0 + \Omega_1 \cos^2\theta + \Omega_2 \cos^4\theta$ represents the surface differential rotation, $\Omega_c$ is the uniform rotation rate of the radiative core, $r_c$ is the location of the tachocline, and $d_c$ sets the thickness of the transition (see Chatterjee et al. (2004) for details).

The meridional circulation, critical for flux transport, is poleward near the surface and equatorward at the base of the convection zone. In this model, the return flow penetrates slightly below the base of the convection zone (r = $0.65R_\odot$), an important feature required to reproduce the observed equatorward migration of sunspot emergence in the butterfly diagram (see Nandy (2002) for details). The meridional circulation is typically modeled using a stream function $\psi$:

$$\mathbf{v}_p = \nabla \times (\psi(r,\theta)\mathbf{e}\phi), \tag{2.16}$$

where $\psi$ is chosen such that the flow is confined within the convection zone and satisfies the mass conservation condition $\nabla \cdot (\rho \mathbf{v}_p) = 0$. A typical form used is:

$$\psi(r,\theta) = \psi_0 (r - r_b)^2 (R - r) \sin^3\theta, \tag{2.17}$$

where $r_b$ is the bottom of the convection zone and $R$ is the solar radius. Turbulent magnetic diffusivity is modeled differently for poloidal and toroidal fields. The poloidal field is allowed to diffuse freely with a high diffusivity value, reflecting the open, weak-field nature of the large-scale surface field.

In contrast, the toroidal field is assumed to be stored in the relatively laminar tachocline, with a lower diffusivity in the deep interior. This difference in diffusivity is also key to preserving the antisymmetric (dipolar) parity across the equator, as symmetric solutions can arise if turbulent diffusivity is not high enough in the bulk of the convection zone.

$$\eta(r) = \eta_c + \frac{\eta_s - \eta_c}{2}\left[1 + \mathrm{erf}\left(\frac{r - r_d}{d_d}\right)\right], \tag{2.18}$$

where $\eta_s$ is the surface diffusivity, $\eta_c$ is the diffusivity in the deeper layers, and $r_d$ and $d_d$

define the location and thickness of the transition.

In this model, the source term $\alpha$ includes both the B-L mechanism and mean field $\alpha$-effect and can be divided as $\alpha = \alpha_{BL} + \alpha_{MF}$. Here, $\alpha_{BL}$ is considered to be spatially confined to near-surface layers and often modeled with a radial profile peaking around r = $0.95R_{\odot}$, with an angular dependence such as $\alpha$ to capture observed hemispheric preferences. A typical profile used for the $\alpha$-effect in SURYA is:

$$\alpha(r,\theta) = \alpha_0 \frac{\cos\theta}{4}\left[1+\text{erf}\left(\frac{r-r_1}{d_1}\right)\right]\left[1-\text{erf}\left(\frac{r-r_2}{d_2}\right)\right], \tag{2.19}$$

where $\alpha_0$ is the amplitude of the $\alpha$-effect, $r_1$ and $r_2$ define the radial extent of the $\alpha$-layer, and $d_1$ and $d_2$ control the thickness of the transition.

In this code, boundary conditions are chosen to match the magnetic field at the upper boundary to a potential field, assuming no currents above the surface. At the lower radial boundary and along the polar axis, the field is set to zero, assuming a perfectly conducting boundary. Importantly, the SURYA code also implements magnetic buoyancy as a non-local algorithm where the toroidal field exceeding a critical threshold (typically $10^5$G) is made to erupt through the surface, simulating sunspot emergence. An example of a solar dynamo simulation using the SURYA code is illustrated in Figure 2.11 and Figure 2.12. Figure 2.11 presents the meridional structure of the magnetic field, showing the poloidal field concentrated near the solar surface and the toroidal field confined to the base of the convection zone, with opposite polarity in the two hemispheres. Figure 2.12 provides a detailed temporal evolution: the top panel demonstrates the characteristic out-of-phase behavior between the toroidal and poloidal components, indicating the mutual regeneration process fundamental to the solar dynamo. The middle panel shows the periodic magnetic polarity reversals on the solar surface, a hallmark of solar cycles. The bottom panel exhibits the toroidal field strength at the bottom of the convection zone, revealing a clear butterfly diagram pattern. Overall, the simulation reproduces key observational features of the solar magnetic cycle, such as the 11-year periodicity, dipolar symmetry, equatorward migration of sunspot-forming toroidal fields, and robust cycle stability – demonstrating the efficacy of the SURYA dynamo model in capturing the essential physics of solar magnetism.

In previous research works, the model successfully reproduces several key features of the solar cycle, including the correct phase relationship between polar fields and sunspots,

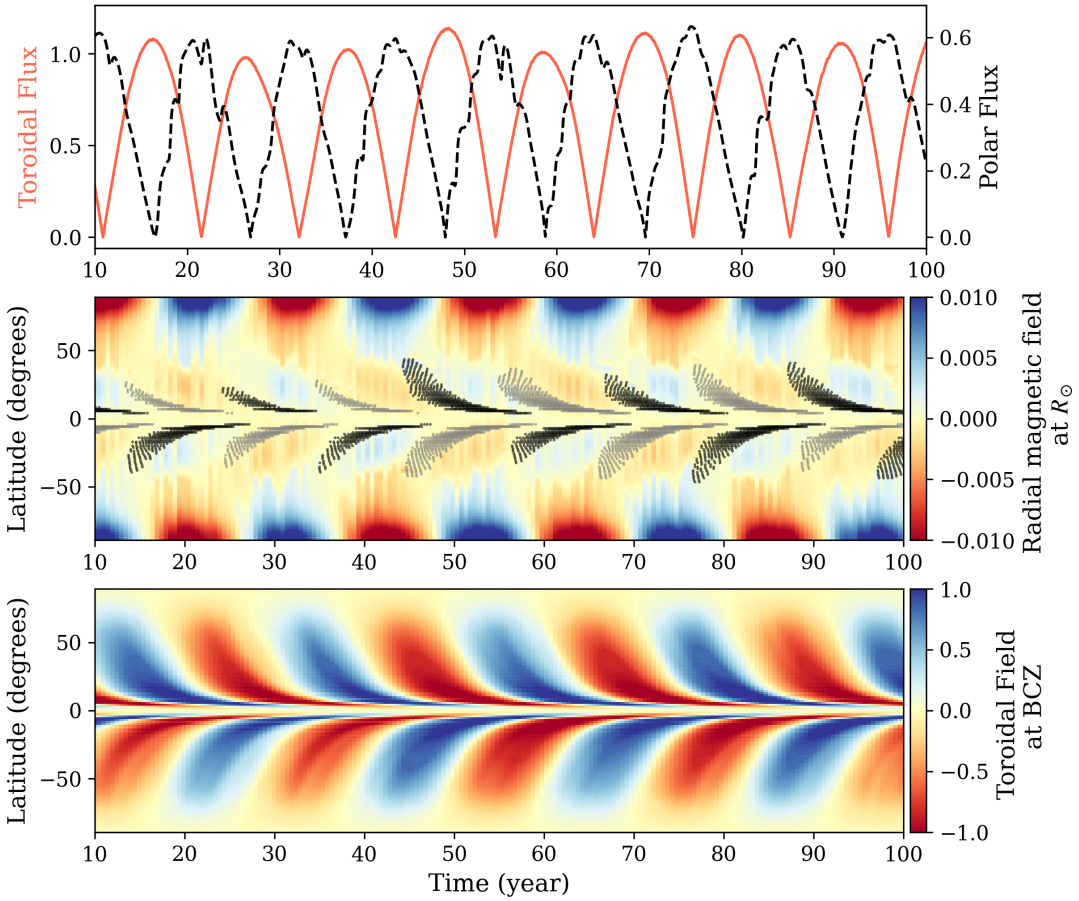


Figure 2.12: Long-term solar dynamo simulation using the SURYA code. The top panel shows the temporal evolution of the toroidal flux (red solid line) and poloidal flux (black dashed line) near the base of the convection zone. The middle panel displays the radial magnetic field ($B_r$) at the solar surface, with black and grey indicating proxies for sunspot emergence of positive and negative polarities, respectively. The bottom panel illustrates the spatiotemporal evolution of the toroidal magnetic field at the bottom of the convection zone (BCZ), forming a solar butterfly diagram. Red and blue indicate negative and positive magnetic polarities, respectively, in the middle and bottom panels. It is noted that toroidal flux and polar flux values are in code units.

equatorward migration of toroidal field belts, poleward migration of surface radial fields, and the roughly 11-year periodicity of sunspot cycles (Choudhuri et al., 1995; Nandy, 2002; Karak and Choudhuri, 2011; Karak et al., 2014). The introduction of deep meridional circulation was crucial for matching the observed butterfly diagram. Additionally, the inclusion of realistic buoyancy and a spatially confined $\alpha$-effect helped align the timing of the polar field reversals with observations. Thus, the SURYA model provides a robust numerical framework for exploring the dynamics of solar magnetic field generation. Variants of this model have been used to study the effects of stochastic forcing, grand minima, and parity transitions, offering deep insight into the nonlinear and memory-bearing behavior of the solar dynamo system (Passos et al., 2014; Hazra et al., 2014; Hazra and Nandy, 2016; Hazra and Choudhuri, 2017; Hazra and Nandy, 2019; Saha et al., 2022; Saha et al., 2025).

# Chapter 3

# Algebraic Quantification of the Sun's Dipole Moment

*"The solar cycle is generated by a magnetohydrodynamic dynamo mechanism which involves the induction and recycling of the toroidal and poloidal components of the Sun's magnetic field. Recent observations indicate that the Babcock-Leighton mechanism – mediated via the emergence and evolution of tilted bipolar active regions – is the primary contributor to the Sun's large-scale dipolar field. Surface flux transport models and dynamo models have been employed to simulate this mechanism, which also allows for physics-based solar cycle forecasts. Recently, an alternative analytic method has been proposed to quantify the contribution of individual active regions to the Sun's dipole moment. Utilizing solar cycle observations spanning a century, here, we test the efficacy of this algebraic approach. Our results demonstrate that the algebraic quantification approach is reasonably successful in estimating dipole moments at solar minima over the past century – providing a verification of the Babcock-Leighton mechanism as the primary contributor to the Sun's dipole field variations. We highlight that this algebraic methodology serves as an independent approach for estimating dipole moments at the minima of solar cycles, relying on characteristics of bipolar solar active regions. We also show how this method may be utilized for solar cycle predictions; our estimate of the Sun's dipole field at the end of cycle 24 using this approach indicates that solar cycle 25 would be a moderately weak cycle, ranging between solar cycle 20 and cycle 24.* [1] *"*

## 3.1 Introduction

Our home star, the Sun, is a gigantic hot ball of plasma with inherent magnetic activity. Sunspots, strongly magnetized dark regions on the solar surface (Hale, 1908), serve as reliable indicators of this magnetic activity. Observations show that sunspot numbers undergo

[1] This chapter is based on Pal and Nandy (2024a).

quasi-periodic variations following an approximately 11-year recurring cycle, known as the solar cycle (Clark and Stephenson, 1978; Schwabe, 1844; Schatten, 2003; Hathaway, 2015). Halfway through the solar cycle, the Sun's activity reaches its peak, or the solar maximum, with the highest number of sunspot emergences. During this maximum phase, its magnetic north and south poles flip, after which the Sun calms down until it reaches a solar minimum, indicating the beginning of a new sunspot cycle. During solar maximum, a more magnetically active Sun leads to frequent occurrences of magnetic outbursts and plasma outflows, such as solar flares and coronal mass ejections(CMEs). These phenomena significantly impact satellite operations, space-based technologies and the Earth's upper atmosphere (Kutiev, Ivan et al., 2013; Solanki, 2002). Therefore, understanding the dynamics of the solar cycle is crucial to be able to predict the Sun's magnetic activity and its consequences on space weather and planetary environments (Petrovay, 2020; Nandy, 2021; Bhowmik et al., 2023; Nandy et al., 2023).

The magnetic cycle of the Sun can be explained through the Babcock-Leighton (BL) Solar Dynamo theory, which primarily establishes the interplay between the global poloidal field and the toroidal field in the presence of various plasma flows within the solar convection zone (Wang et al., 1991; Leighton, 1964; Charbonneau, 2020). During the initial phase of the solar cycle, the global magnetic field is primarily dominated by the poloidal field component. The Sun's differential rotation stretches this poloidal field in the longitudinal direction, leading to the formation of the toroidal field in the tachocline region (Snodgrass, 1987). Subsequently, these toroidal flux ropes are unstable within the convection zone, and due to magnetic buoyancy, they emerge on the solar surface as dark sunspots. Once the tilted bipolar active regions (BMRs) appear on the solar surface, their evolution and the regeneration of the toroidal field are primarily governed by the Babcock-Leighton (BL) mechanism (Babcock, 1961). The BL mechanism constitutes two processes: one is the annihilation of the leading polarities across two hemispheres, and the second one is the drift and diffusion of the following polarity towards the pole. These unipolar magnetic regions cancel the existing poloidal field at the pole and generate the poloidal field with opposite signs for the new solar cycle. Altogether, the BL-type Solar Dynamo model effectively captures the key aspects of the decay and dispersal of sunspots, polar field reversal, and the new polar field buildup (Charbonneau, 2007; Kitchatinov and Olemskoy, 2011;

Cameron and Schüssler, 2017; Bhowmik and Nandy, 2018; Kumar et al., 2019; Pal et al., 2023).

It is well-established that during a solar activity minimum, the poloidal magnetic field, often referred to as polar field, and other polar field proxies (for example, axial dipole moment, A-t index, Geomagnetic aa-index etc.) strongly correlates with the amplitude of the succeeding cycle (Schatten et al., 1978; Yeates et al., 2008; Muñoz-Jaramillo et al., 2012). Utilizing polar field proxies as a seed for predicting the amplitude of the next solar cycle is known as the 'precursor method', which has evolved as one of the most successful techniques of sunspot cycle prediction (Nandy, 2021; Petrovay, 2020). However, selecting an appropriate precursor for solar cycle forecasts relies on substantial physical insight and aids in accurate cycle predictions. In the context of the dynamo mechanism, the dipole moment (DM) closely relates to the poloidal field at the end of a solar cycle. Analysis of the observed photospheric magnetic field over the past four solar cycles suggests that the reversal of the dipole moment epoch aligns better with the cycle maximum than the average timing of polar field reversal (Upton and Hathaway, 2013; Iijima et al., 2017; Virtanen et al., 2019). Moreover, the dipole moment contains information from the entire photosphere, mitigating the effects of a hemispherically asymmetric magnetic field distribution. Hence, during the solar minimum, the axial dipole moment component acts as a seed for the toroidal component of the next cycle (Upton and Hathaway, 2018; Charbonneau, 2020; Nandy et al., 2023).

Predicting the dipole moment at the end of the solar cycle minimum is a feasible approach to estimate the strength of the next cycle. This task can be achieved through various methods, including observations and physics-based numerical models (Upton and Hathaway, 2013; Virtanen et al., 2019; Jaswal et al., 2024). However, determining the dipole moment through magnetogram analysis is limited to a few past solar cycles and thus relies on physical models. One commonly used physics-based model for predicting the dipole moment is the Surface Flux Transport (SFT) model based on the BL mechanism (Upton and Hathaway, 2013; Bhowmik and Nandy, 2018; Pal et al., 2023; Yeates et al., 2023). However, calibrating such numerical models sometimes becomes challenging and time-consuming. What if we explore an alternative to numerical methods, moving away from complex computer-intensive modelling and adopting a simplified approach?

The first attempt in this direction was made by Jiang et al. (2019); Petrovay et al. (2020). They introduced a mathematical framework aimed at calculating the distinct contributions of each emerging active region that collectively generate the ultimate global dipole moment during the cycle minimum. In their work, synthetic active region data was utilized to compute the ultimate dipole moment, and the results were compared with those derived from the 2 $\times$ 2D dynamo model (Lemerle and Charbonneau, 2017) simulations. Subsequently, Pal et al. (2023) adopted a similar approach to investigate the impact of anomalous active regions, specifically the combinations of synthetic Anti-Hale and Anti-Joy regions, on the solar cycle.

In this study, we employ the modified analytical approach to calculate the ultimate dipole moment at the end of a solar cycle, using the observational properties of bipolar active regions emerging throughout the declining phase of the sunspot cycle. Initially, we validate our method by estimating the dipole moment at the minima of solar cycles 14 to 23 and comparing it with observations. Subsequently, based on the algebraically derived dipole moment for solar cycle 24, we predict the peak amplitude of the ongoing solar cycle, *i.e.* solar cycle 25, along with the associated uncertainties. We have also discussed the advantages, limitations and future possibilities of our methodology using observational insights.

## 3.2 Methods

Here, we discuss the method of quantifying the ultimate axial dipole moment of a solar cycle mathematically, which was first adopted by Petrovay et al. (2020). A spatially two-dimensional Surface Flux Transport model can be simplified to an azimuthally averaged 1D SFT model (Petrovay et al., 2020; Pal et al., 2023). In this model, tilted sunspots transform into a bipolar flux ring with a finite latitudinal separation. Now, the 'initial unsigned dipole moment' of any i$^{\text{th}}$ active region can be expressed as,

$$\delta D_{1,i} = \frac{3}{4\pi R_{\odot}^2} \Phi_i \, d_{\lambda_i} \cos\lambda_i. \tag{3.1}$$

Here, $\lambda_i$ is the latitudinal position of the i$^{\text{th}}$ sunspot and $R_{\odot}$ is the solar radius. The term $d_{\lambda_i}$ denotes the latitudinal separation of the leading and following polarities of the

$i^{th}$ sunspot, $\Phi_i$ represents the magnetic flux content in the concerned sunspot. We take $d_{\lambda_i} = d_i \times \sin\alpha_i$, where $d_i$ represents the full angular polarity separation and $\alpha_i$ is the tilt angle of the sunspot relative to the east–west direction. In this study, we assume the tilt angle $\alpha_i$ to be proportional to the latitude expressed as $\alpha_i = 0.5 \times \lambda_i$ following Lemerle et al. (2015). Additionally, we consider $d_i$ be proportional to the radius of the sunspot (Bhowmik and Nandy, 2018). Therefore, $d_{\lambda_i}$ is not constant for all sunspots and varies with the sizes and tilt angles of the active regions.

The evolution of the dipole moment involves additional physical factors that govern the regular dipole moment reversal and its accumulation. The dipole moment build-up may be influenced by the radial diffusion of the photospheric magnetic field. This radial diffusion term is expressed as $e^{-t/\tau}$, where $\tau$ represents the exponential decay term. This expression indicates that the dipole moment gradually diminishes over time due to the radial outflows.

Another asymptotic dependency of the dipole moment is linked to the latitudinal position of sunspots. Jiang et al. (2014) demonstrated, through SFT simulations, that the amplitude of the dipole moment decreases with increasing latitude. This asymptotic dipole moment contribution factor, denoted as $f_\infty$, can be modeled as a Gaussian function of latitude:

$$f_\infty = C\, e^{-\frac{\lambda^2}{2\lambda_R^2}} \tag{3.2}$$

This expression eventually takes care of the latitudinal quenching effect, indicating that low-latitude sunspots have a more significant impact on the ultimate dipole moment, while high-latitude active regions contribute less to its buildup. The dynamo effectivity range $\lambda_R$ and $C$ $(= A/\lambda_R)$ can be taken as constant, which are determined by specific flux transport profiles, such as meridional circulation and turbulent diffusion assumed in different surface flux transport models (Petrovay et al., 2020; Nagy et al., 2020; Wang et al., 2021). However, approximate analytic estimates of these constants are also possible based on first principles, observations and certain assumptions. Following Petrovay et al. (2020), $\lambda_R$ in the low-latitude limit can be expressed as,

$$\lambda_R = \left[\sigma^2 + \frac{\eta}{R_\odot^2 \Delta_v}\right]^{1/2}, \text{where } \Delta_v = \left(\frac{1}{R_\odot}\frac{dv}{d\lambda}\right)\Bigg|_{\lambda=0} \tag{3.3}$$

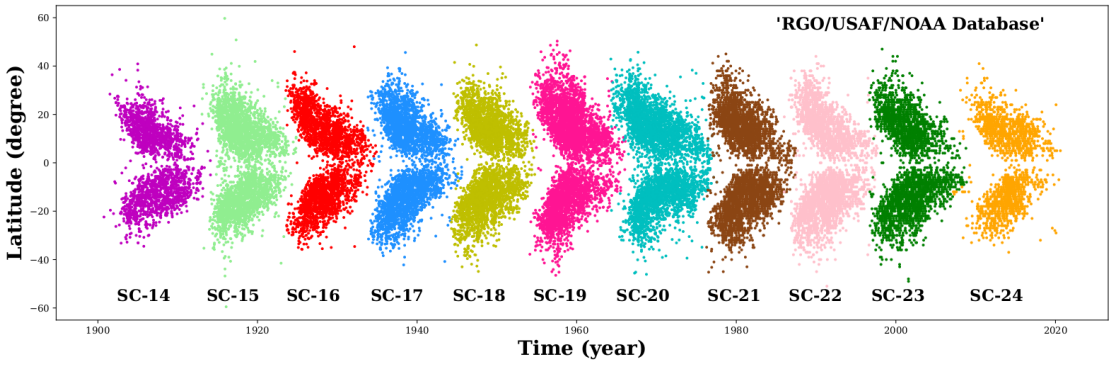


Figure 3.1: The butterfly diagram depicts the spatiotemporal changes spanning Solar Cycles 14 to 24. This figure illustrates the evolution of sunspots across the last 11 solar cycles, using time and latitudinal position data sourced from the RGO/USAF/NOAA Data Centre (2023). Distinct colours are used to differentiate between the various solar cycles.

Here, $\sigma$ represents the half-width of a Gaussian sunspot, $\Delta_v$ is the divergence of the meridional flow at the equator, and $\eta$ is the magnetic diffusivity. Following helioseismic observations, we consider a sinusoidal profile for the meridional circulation peaking at mid-latitude (Jiang et al., 2014; Petrovay et al., 2020). Thus, the meridional circulation velocity profile can be expressed as, $v = v_0 \sin 2\lambda$. The half-width of a sunspot is assumed to be proportional to its radius, which is determined from the mean of the distribution of the observed sunspot radii. We find $\sigma = 0.56^\circ$ (the maximum half-width can go up to $4^\circ$). The transport parameters, including diffusivity ($\eta$) and peak amplitude of meridional circulation ($v_0$), were constrained within observational ranges (Jiang et al., 2014). Specifically, we take $\eta = 700\,\mathrm{km^2 s^{-1}}$ and $v_0 = 10\,\mathrm{ms^{-1}}$ which results in $\lambda_R = 12.86^\circ$. We emphasize that changing $\sigma$ from $0.56^\circ$ to $4^\circ$ does not change $\lambda_R$ much ($\pm 1^\circ$). We assume that these transport profiles act similarly for individual active regions and will not vary from one solar cycle to another, therefore, $\lambda_R$ is constant throughout our analysis. Additionally, we utilize the observational polar field data (WSO Data Centre, 2023) to determine the constant $C$. We find $C$ = 5.48. The method of calibrating $C$ is described in subsection 4.3.1.

Thus, if an i$^{\text{th}}$ active region emerges at time $t_i$, then the ultimate dipole moment contribution from that active region at the end of cycle n at time $t_{n+1}$ becomes:

$$\delta D_{\mathrm{U},i} = f_{\infty,i}\, \delta D_{1,i}\, \mathrm{e}^{\frac{(t_i - t_{n+1})}{\tau}}. \tag{3.4}$$

The initial dipole moment contribution from i$^{\text{th}}$ sunspot ($\delta D_{1,i}$) will be positive or

negative depending on the polarity of the sunspot that is closest to the equator. In general, one expects a positive contribution for Hale-Joy sunspots and a negative contribution for anomalous sunspots towards the ultimate dipole moment. In our recent study of anomalous active regions, we utilized this sign convention of dipole moment, revealing that the dipole moment decreases at solar minima when multiple anomalous active regions appear in a solar cycle (Pal et al., 2023). Here, for simplicity, we do not consider anomalous sunspots and confine ourselves to Hale-Joys active regions.

According to the BL mechanism, the sunspots of the current cycle decay and disperse due to plasma flows, cancelling the old cycle's dipole moment. Hence, the dipole moment at the end of a solar cycle is the combined result of the cancellation of the preceding cycle's dipole moment and the subsequent build-up of the new cycle's dipole moment. For brevity, in our study, we limit ourselves to active regions appearing after the reversal of the old cycle dipole moment to estimate the strength of the ultimate dipole moment of the cycle under consideration. In essence, therefore, we calculate the dipole moment contribution relative to its zero value (the latter happens approximately at solar maximum). The advantage of this methodology is that the calculation can be achieved even when the dipole moment at the end of the previous cycle is unknown.

Thus, the net contribution into the dipole moment at the end of $n^{th}$ cycle from the active regions emerged during the $n^{th}$ cycle can be expressed as the sum of the dipole moment contributions from individual sunspots that appeared after reversal time of that cycle. The analytic approach confirming this methodology is implemented as follows. The dipole moment at the end of cycle n is denoted by $\Delta$DM which is given by

$$\begin{aligned}
\Delta\mathrm{DM} &= \sum_i \delta D_{\mathrm{U},i} \\
&= \sum_i f_{\infty,i}\, \delta D_{1,i}\, \mathrm{e}^{\frac{(t_i - t_{n+1})}{\tau}} \\
&= \frac{3}{4\pi R_\odot^2} \sum_i \Phi_i\, d_{\lambda_i} \cos\lambda_i\, C \mathrm{e}^{-\frac{\lambda_i^2}{2\lambda_R^2}} \\
&= \frac{3}{4\pi R_\odot^2} \sum_i \Phi_i\, d_i \sin\alpha_i \cos\lambda_i\, C \mathrm{e}^{-\frac{\lambda_i^2}{2\lambda_R^2}}\,. \qquad (3.5)
\end{aligned}$$

Here, 'i' takes care of all active regions that emerge after the reversal of the dipole moment. We assume there are no radial outflows, *i.e.* $\tau$ is infinity.

We compute the dipole moment at solar cycle minima for solar cycles 14 to cycle 24, utilizing the observed characteristics of the sunspots and the observed time reversal epoch of the dipole moment. We use the RGO/USAF/NOAA Data Centre (2023) database to extract information on the latitudinal position and area of the bipolar active regions ranging from solar cycle 14 to cycle 24. In this study, we specifically focus on the statistics of active regions when they reach their maximum size. Figure 3.1 illustrates the butterfly diagram, spanning the last century, with time and latitude information obtained from the RGO/USAF/NOAA database. We use the dipole moment reversal timing epoch from the WSO average polar field, available only for solar cycle 21 to cycle 24 (WSO Data Centre, 2023). For the rest of the solar cycles (*i.e.* solar cycle 14 to cycle 20), we opt for the sunspot cycle peak time because the Sun's global dipole magnetic field generally flips its polarity around the maximum phase of the solar cycle. We extract the solar cycle maximum epoch from SILSO World Data Center (2019) time series. Our analysis considers these dipole moment reversal timings as the standard reversal epoch.

## 3.3 Results and Discussions

### 3.3.1 Dipole moment comparison for past solar cycles spanning a century

Utilizing the observational sunspot characteristics in the aforementioned analytical model, we estimate the century-scale calibrated global axial dipole moment at each solar minimum, spanning from solar cycle 14 to cycle 23. These algebraically derived dipole moments can be compared with observational dipole moment proxies, considering that the Sun's global magnetic field is primarily dipolar during the solar minimum. For this purpose, we use three observational time series: 1) Polar flux obtained from MWO polar faculae count (Muñoz-Jaramillo et al., 2012), 2) Makarov's A-t index (Makarov et al., 2001), and 3) WSO polar field (WSO Data Centre, 2023). We consider the average northern and southern hemispheric polar flux or polar field as a proxy for the dipole moment.

Our mathematical approach focuses on determining the dipole moment's value at the end of the solar cycle rather than explaining its time evolution. Thus, we utilize the average polar field ($P_{av}$) obtained from the WSO Data Centre from 1976 onwards to calibrate the

computed ultimate dipole moment for the last three solar cycles. We multiply all algebraic dipole moment (DM) values corresponding to each solar cycle minimum by the same constant factor $C$ and vary it until the DM versus $P_{av}$ is characterized by a line with a unit slope and zero intercept (i.e. we optimize the constant $C$ such that $P_{av} = C \times \mathrm{DM}$). This results in $C = 5.48$. We select this particular constant as the calibration factor.

In Figure 3.2, red stars denote the estimated calibrated dipole moment compared with MWO polar flux, Makarov's A-t index and WSO polar field marked with magenta, green and orange. We calculate the potential error in the dipole moment computation by choosing the accurate dipole moment reversal time. The dipole moment reversal epoch may not always align with the solar cycle maxima; it can lead or lag the sunspot maximum epoch. If the dipole moment reversal timing lags the solar maximum epoch, then the total sunspots contribution towards the dipole moment will decrease, which in turn dampens the ultimate dipole moment. At the same time, the dipole moment will increase if the reversal time leads to the solar maximum epoch. Therefore, we assume that the dipole moment reversal time varies within a two-year interval around the standard reversal epoch, encompassing one year before and one year after the standard reversal epoch. Following that, we compute the contribution to the dipole moment at the endpoints of specified reversal time intervals. Based on this, we introduce an error bar on the derived dipole moment (see Figure 3.2). The algebraically derived dipole moments from solar cycle 14 to cycle 24 are tabulated in Table 3.1.

To check the efficacy of our methodology, we conduct a correlation analysis between the analytically calculated dipole moment and the observed polar field proxies at the solar minima. The results are depicted in Figure 3.3. The correlation analysis demonstrates a reasonably good match between the algebraically derived dipole moment and the observed data, with one notable exception - solar cycle 19. The computed dipole moment for solar cycle 19, deviates significantly from the observational polar field proxies. Given this, we consider solar cycle 19 an outlier and exclude it from the correlation analysis.

After omitting solar cycle 19, we find a statistically significant correlation coefficient between the mathematically computed dipole moment and the observed polar field proxies, as mentioned in Figure 3.3. In Section 3.3.3, we discuss potential factors contributing to our inability to retrieve the ultimate dipole moment of solar cycle 19. This study reveals

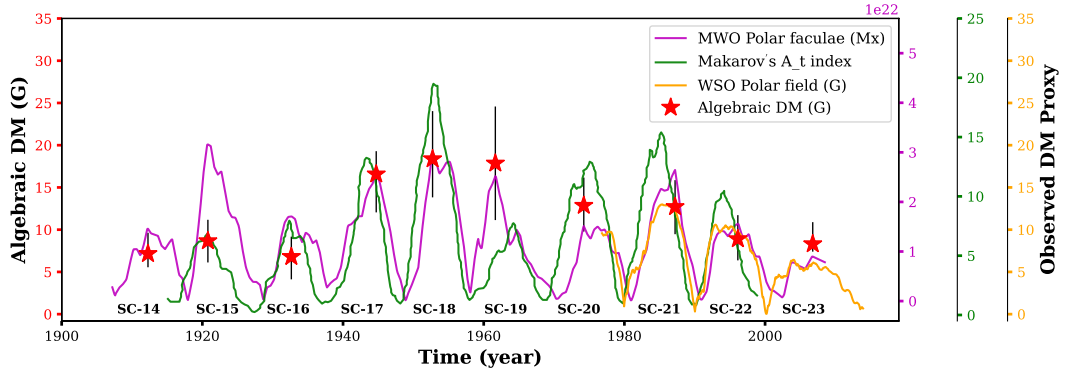


Figure 3.2: Time series of Dipole moment (DM) proxies ranging from solar cycle 14 to 24. In this representation, the MWO polar faculae data is depicted in magenta (Muñoz-Jaramillo et al., 2012), Makarov's A-t index (Makarov et al., 2001) is shown in green, and the WSO polar field data (WSO Data Centre, 2023) is represented in orange. All polar field data is averaged from the northern and southern hemispheres to facilitate comparison with the dipole moment. Additionally, red stars indicate the algebraically computed ultimate dipole moment at the end of each cycle spanning solar cycle 14 to solar cycle 23.

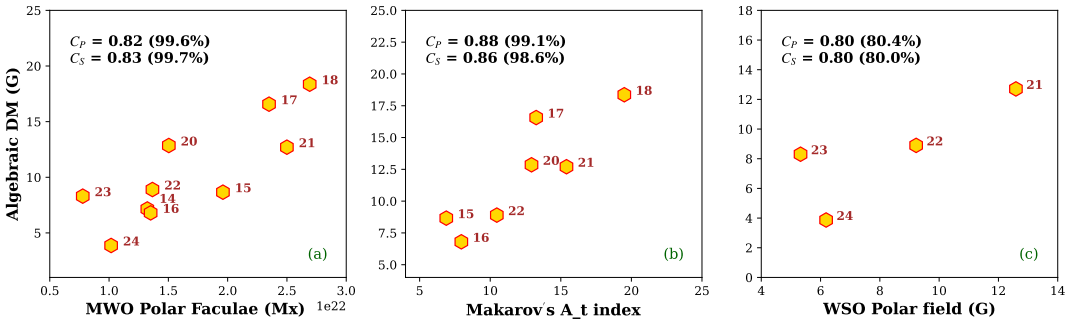


Figure 3.3: Statistical correlation analysis between observational dipole moment proxies and algebraic dipole moment. In Panel (a), (b), and (c), three different databases have been considered as the observed DM proxies: MWO polar faculae data (Muñoz-Jaramillo et al., 2012), Makarov's A-t index (Makarov et al., 2001), and WSO polar field (WSO Data Centre, 2023). $C_P$ and $C_S$ denote Pearson and Spearman rank correlation coefficients, respectively.

that the analytically estimated dipole moment for the past ten solar cycles aligns with the observed polar flux. This alignment underscores the physics of decay and dispersal of sunspots, contributing to the ultimate build-up of the dipole moment from a mathematical perspective.

### 3.3.2 Prediction of solar cycle 25

In this study, we find a significant deviation in the dipole moment of sunspot cycle 19. This deviation influences the peak amplitude of solar cycle 20, given the causal connection between the dipole moment at the solar minimum and the subsequent solar cycle strength. Hence, we exclude the dipole moment of solar cycle 19 and the peak amplitude of sunspot cycle 20 from our current analysis.

Table 3.1: Analytically derived dipole moment (DM) at the end of the solar cycle and predicted sunspot numbers, spanning last century (from solar cycle 14 to cycle 25).

| **Solar cycle #** | **DM at solar minima (G)** | **Peak sunspot #** |
|---|---|---|
| SC-14 | 7.05 [+2.6,-1.6] | - |
| SC-15 | 8.44 [+2.6,-2.6] | 156 [+25,-21] |
| SC-16 | 6.78 [+2.5,-2.8] | 169 [+27,-23] |
| SC-17 | 16.67 [+2.7,-4.4] | 153 [+24,-21] |
| SC-18 | 18.60 [+5.3,-4.6] | 246 [+40,-31] |
| SC-19 | 17.24 [+6.2,-6.4] | 264 [+43,-33] |
| SC-20 | 13.11 [+3.4,-3.2] | 251 [+41,-31] |
| SC-21 | 12.87 [+3.0,-3.3] | 213 [+35,-27] |
| SC-22 | 8.65 [+2.7,-2.4] | 211 [+34,-27] |
| SC-23 | 8.20 [+2.6,-0.9] | 171 [+27,-23] |
| SC-24 | 3.98 [+1.1,-1.5] | 169 [+27,-22] |
| SC-25 | - | 127 [+20,-18] |

We integrate the SIDC SILSO yearly averaged sunspot numbers dataset (SILSO World Data Center, 2019) into our analysis to empirically predict ongoing solar cycle 25. First, we perform a correlation analysis between the analytically derived dipole moment at the end of a cycle [n-1] and the yearly mean sunspot number (SSN) of the consequent cycle [n]. The scatter plot in Figure 3.4 illustrates a strong positive correlation (with 99% confidence level) between these two quantities. This correlation suggests a potential empirical avenue

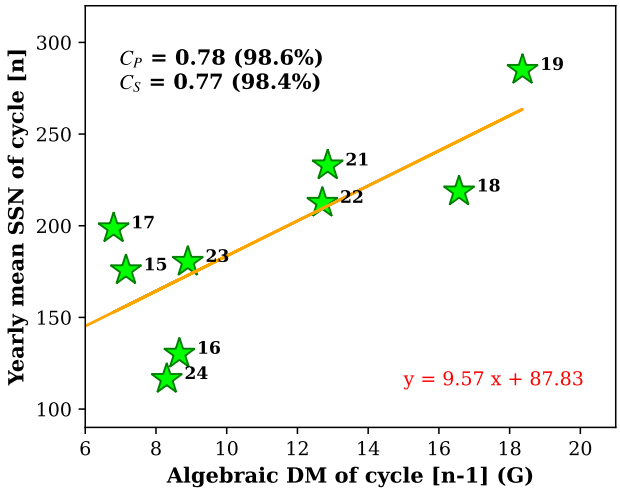


Figure 3.4: Statistical correlation analysis between analytically computed dipole moment of the cycle [n-1], denoted by 'DM' and the yearly averaged sunspot number of the cycle [n] obtained from SILSO World Data Center (2019), denoted by 'N'. The scattered data points have been fitted with a linear regression model, visually represented by the orange line. The established relationship is expressed as follows: N = 9.36 × DM + 90.07.

for forecasting future cycles. Also, for the first time, we reconstruct the dipole moment spanning a century (from 1902 onwards) and utilize it for solar cycle prediction.

We fit this scatter plot in Figure 3.4 with a linear regression model and find a relationship between the analytically derived dipole moment (DM) and the sunspot number (N). The relationship is: N = 9.36 × DM + 90.07. Utilizing the ultimate analytic dipole moment at solar minimum (DM), we calculate the yearly average sunspot number (N) for solar cycle 14 to solar cycle 24. This method effectively reconstructs the past cycles, except solar cycle 20. Figure 3.5 shows that the empirically derived sunspot number at solar cycle maxima (red stars) is overplotted with the SIDC/SILSO sunspot numbers. This result is also tabulated in Table 3.1. The deviation in cycle 20 is understandable, as our inability to accurately determine the cycle 19 dipole moment affects the subsequent cycle.

Finally, by inputting the analytically computed ultimate dipole moment for solar cycle 24 into our fitted linear relationship, our prediction suggests that solar cycle 25 will be stronger than its predecessor, solar cycle 24. To be precise, we anticipate that solar cycle 25 will reach a yearly average peak sunspot number of 127, ranging between solar cycle 20 and cycle 24 (see Figure 3.5). The reasonably good match of derived sunspot cycle

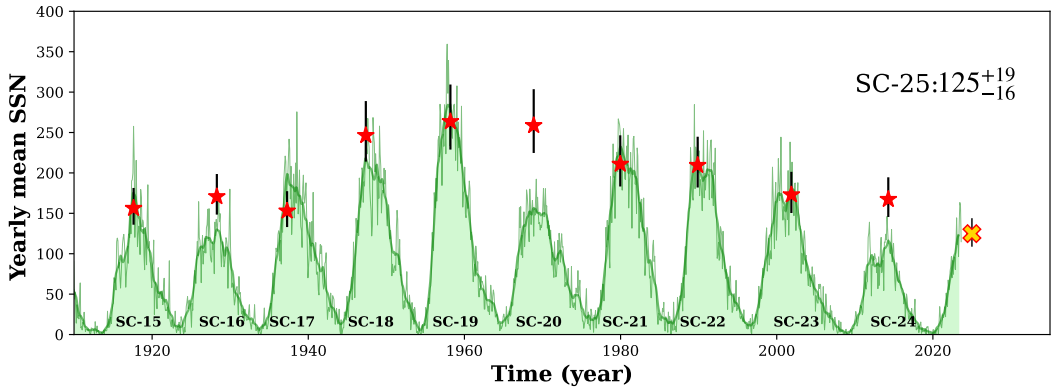


Figure 3.5: Solar Cycle 25 Prediction. The peak sunspot number for the last ten cycles is calculated and depicted as red stars. This is overlaid with the yearly averaged sunspot number time-series from SILSO World Data Center (2019). Utilizing the ultimate dipole moment of cycle 24, the predicted amplitude of solar cycle 25 is $127^{+20}_{-18}$, denoted by the yellow cross.

maxima with the observed sunspot number over the last centuries also suggests that the dipole moment precursor is a promising candidate for solar cycle forecasts.

### 3.3.3 Dependency of Algebraic Method on bipolar active region (BMR) characteristics

In this analytic model, the dipole moment at the solar cycle minima is sensitive to the quantity and flux content of active regions that emerge after the reversal of dipole moment polarity. To compare how this manifests in observation, we conduct a correlation analysis between the total number of active regions that appear after the time reversal and the 1) observed polar flux and 2) algebraic dipole moment at the end of the sunspot cycle. We find a high correlation between the total number of active regions and the ultimate algebraic dipole moments with a trend that is almost linear. This result is depicted in panel (b) of Figure 3.6. Our finding indicates that as the number of sunspots increases, there is a monotonic rise in the ultimate dipole moment. However, this relationship is not as strong in observations which are indicative of a more non-linear relationship with the Spearman's rank correlation coefficient exceeding the Pearson's linear correlation coefficient (see Panel (a) in Figure 3.6). Particularly during solar cycle 19, the highest number of sunspots appeared, but its dipole moment at the end of the cycle was notably small as illustrated in the same panel.

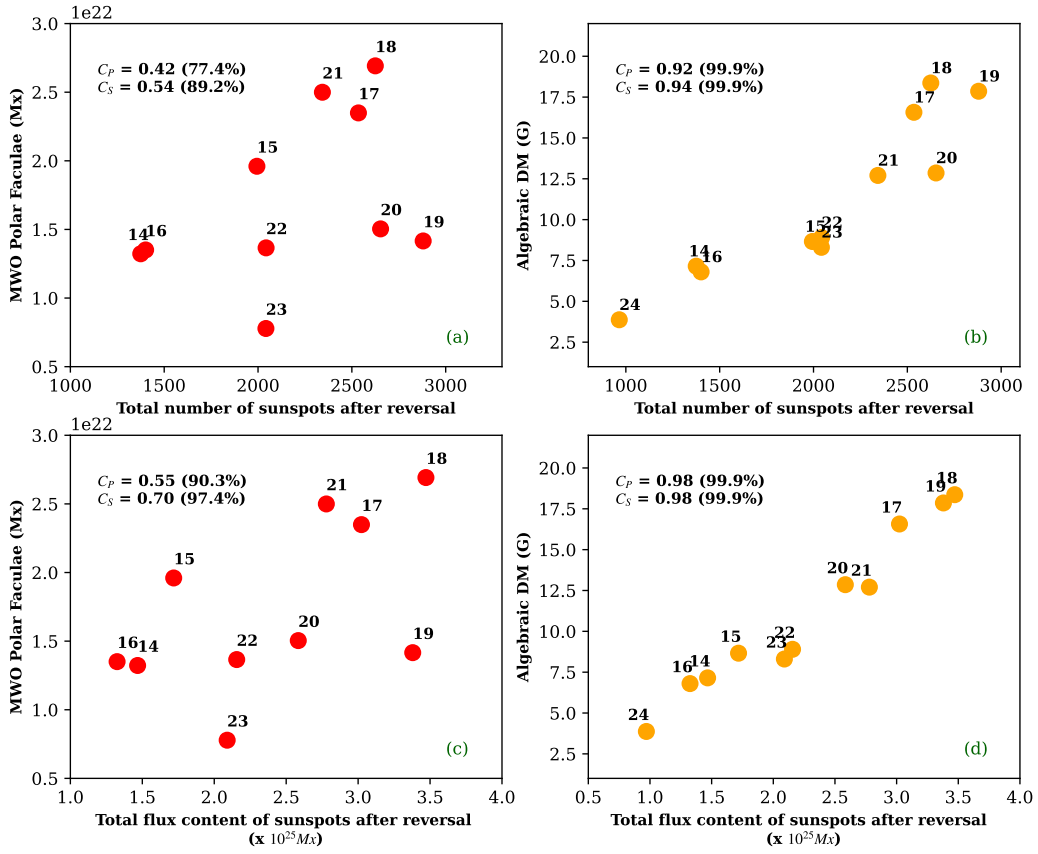


Figure 3.6: The correlation between the algebraic dipole moment (DM) and various properties of the Bipolar Magnetic Regions (BMRs). In Panels (a) and (b), the correlation is observed between the total number of sunspots appearing after the dipole moment reversal and the observational average polar flux (Panel (a)) and algebraic dipole moment (Panel (b)). Similarly, panels (c) and (d) illustrate the correlation between the total flux content of all sunspots emerging after the reversal of the dipole moment and the observational average polar (Panel (c)) and algebraic dipole moment (Panel (d)).

Similarly, we observe a strong correlation between the total flux content of the sunspots emerging after dipole moment reversal and the ultimate algebraic dipole moment estimated from our analytic method as depicted in Panel (d) of Figure 3.6. However, the correlation with the observations depicted in Panel (c) is not as strong and is indicative of non-linearity.

The strong correlation between the number of sunspots and their magnetic flux content can significantly impact our algebraic calculations, occasionally yielding a dipole moment value much higher than expected. Due to this fact, we are unable to estimate the ultimate dipole moment of solar cycle 19 using algebraic techniques. Consequently, we cannot predict the yearly averaged sunspot number for solar cycle 20 very well.

Our analysis suggests that variations in BMR properties are not the sole factors contributing to the irregularities observed in the solar cycle. Other sources, such as nonlinear effects arising from fluctuations in meridional flows across cycles, plasma inflows, tilt quenching and anomalous active regions etc., which are not captured by the analytic method, may also play a significant role in accounting for the variability observed in the buildup of the ultimate dipole moment and, consequently, in modulating the solar cycle. Attempts to imbibe these nonlinear effects into the algebraic technique may lead to further improvements of dipole moment calculations and solar cycle predictions. These will be explored in the future.

## 3.4 Conclusion

In summary, we employ a simplified analytic technique, following the suggestion by Petrovay et al. (2020) to calculate the Sun's dipole moment at the end of a solar cycle. We assess the effectiveness of algebraically derived dipole moments by comparing them with diverse observational data sets from solar cycle 14 to solar cycle 23. This analytic method reasonably estimates the observed dipole moment of solar cycles spanning a century. However, solar cycle 19 is an exception, being the strongest and most extreme cycle in the observation.

Notably, for the first time, our method has allowed reconstruction of the dipole moment at solar minimum spanning a century – allowing a robust test of its value as a precursor for predicting solar cycle amplitudes. We obtain a strong relationship between the dipole moment of the preceding cycle and the sunspot number of the subsequent solar cycle. Using this empirical relationship, we compute the yearly averaged sunspot number from solar cycle 14 to cycle 24. These estimates match the observations well. This is taken advantage of to predict the peak amplitude of sunspot cycle 25. We utilize the algebraically derived dipole moment of solar cycle 24 as a precursor to forecast the strength of solar cycle 25. The predicted amplitude is 128, with a range which places cycle 25 between sunspot cycle 20 and cycle 24.

Our work provides strong support to the idea that the emergence and evolution of tilted bipolar sunspot pairs are the primary contributors to the Sun's dipole field – the so-called Babcock-Leighton mechanism. Surface flux transport models rely on this idea, and numerous dynamo models have been developed based on this idea, which reproduce diverse

characteristics of the sunspot cycles. (Jiang et al., 2014; Cameron and Schüssler, 2015; Hazra and Nandy, 2016; Hazra and Nandy, 2019; Saha et al., 2022; Dash et al., 2023; Karak, 2023; Pal et al., 2023; Hazra et al., 2023)

This analytic method for estimating the Sun's dipole moment relies on diverse properties of sunspots, including their latitudinal position, flux content, separation between two polarities and the total number of active regions that appear in a solar cycle. This method's dependency on BMR characteristics can sometimes lead to deviation from observations in the theoretical dipole moment calculation. For example, in our analysis, we observe a deviation in the dipole moment of solar cycle 19, which in turn impacts the reconstructed amplitude of solar cycle 20. This occurs because the direct dependency on the total number of sunspots and the flux content can weaken the accuracy of dipole moment estimates at the end of the cycle, which is not always seen in the observation. Nevertheless, such deviations are not always significant, and the dipole moment at solar minima derived from this analytic method closely matches the observational proxy based on polar flux. Notably, the sunspot amplitudes of past cycles empirically derived from the analytically estimated dipole moment match sunspot cycle amplitudes spanning the last century. Taken together, these corroborate our algebraic approach for dipole moment estimations.

We emphasize that our methodology is an independent means to estimate the dipole moment at the minima of solar cycles based on characteristics of the sunspot time series. Therefore, this provides a straightforward theoretical tool to reconstruct the dipole moment at the minima of past sunspot cycles. We want to highlight that our method doesn't rely on solving numerical equations like those used in surface flux transport models.

There are certain shortcomings in such an approach, which relies on a 1D analytical model. For example, detailed studies of inter-active region interactions, exploration of non-axisymmetric phenomenon and influence of non-linearities can not be addressed. For these aspects, one must still rely on numerical simulations of spatially extended time-dependent magnetic field evolution models. However, when it comes to estimating the solar dipole moment and making predictions for the solar cycle, the algebraic method explored here appears to be a useful, independent tool.

# Chapter 4

# Solar Cycle Fluctuations: Impact of Anomalous Active Regions

*"One of the major sources of perturbation in the solar cycle amplitude is believed to be the emergence of anomalous active regions that do not obey Hale's polarity law and Joy's law of tilt angles. Anomalous regions containing high magnetic flux that disproportionately impact the polar field are sometimes referred to as "rogue regions." In this study, utilizing a surface flux transport model, we analyze the large-scale dipole moment buildup due to the emergence of anomalous active regions on the solar surface. Although these active regions comprise a small fraction of the total sunspot number, they can substantially influence the magnetic dipole moment buildup and subsequent solar cycle amplitude. Our numerical simulations demonstrate that the impact of "anti-Joy" regions on the solar cycle is similar to those of "anti-Hale" regions. We also find that the emergence time, emergence latitude, relative number, and flux distribution of anomalous regions influence the large-scale magnetic field dynamics in diverse ways. We establish that the results of our numerical study are consistent with the algebraic (analytic) approach to explaining the Sun's dipole moment evolution. Our results are relevant for understanding how anomalous active regions modulate the Sun's large-scale dipole moment buildup and its reversal timing within the framework of the Babcock–Leighton dynamo mechanism—now believed to be the primary source of solar cycle variations.* [1] "

## 4.1 Introduction

Active regions emerging on the solar surface have long been considered the primary element through which the solar cycle manifests itself (Schwabe, 1844). Short and long-term evolution of the magnetic field associated with active regions drives solar magnetic events

[1] This chapter is based on Pal et al. (2023).

such as flares, coronal mass ejections, energetic particle releases, etc., besides controlling the Sun's total electromagnetic output. These activities subsequently affect the Earth and its vicinity, specifically satellite operations, telecommunications, and contribute to various aspects of space weather (Nandy, 2004; Nandy and Martens, 2007; Schrijver et al., 2015). Since surface magnetic field distribution and its evolution play crucial roles in governing the short and long-term changes in space weather and space climate, respectively, it is vital to study the large-scale surface magnetic field during a solar cycle as well as its cycle to cycle irregularities (Bhowmik and Nandy, 2018; Petrovay, 2020; Nandy, 2021; Bhowmik et al., 2023). The magnetic cycle of the Sun can be explained using the Babcock-Leighton (B-L) Solar Dynamo theory (Leighton, 1964; Piddington, 1972; Wang et al., 1991; Hazra and Nandy, 2016; Charbonneau, 2020; Fan, 2021; Hazra et al., 2023). At the solar activity minimum, the global magnetic field is primarily dominated by the poloidal field component, which is predominantly dipolar. The solar differential rotation stretches this poloidal field longitudinally to generate the toroidal field component in the tachocline region. Amplified toroidal flux ropes eventually encounter magnetic buoyancy in the convection zone and emerge primarily as Bipolar Magnetic Regions (BMRs) (Nandy, 2002; Gilman, 2018; Fan, 2021). Near the Sun's equator, the leading sunspot polarities of two opposite hemispheres annihilate each other, and the remaining trailing spot (mainly of uni-polar magnetic fields) drifts towards the respective poles via large-scale meridional flow and diffusion. During the first half of the solar cycle, many such trailing polarities reaching the polar region eventually cancel the existing large-scale polar field and create a new one with the opposite sign. This reversal of the global dipolar field happens during the solar cycle maximum, and the new polar field keeps growing till the end of the cycle. This whole process of redistribution of active region-associated magnetic flux on the solar surface is known as the B-L mechanism (Babcock, 1961; Leighton, 1964; Mackay and Yeates, 2012; Jiang et al., 2014). One of the existing hypotheses explaining the dynamo cycle involves meridional circulation advecting the poloidal field down to the tachocline region from the solar photosphere followed by the generation and enhancement of toroidal field via Parker's Ω-effect (Parker, 1955) - thus completing the full solar cycle. Therefore, the B-L mechanism is the primary means for evolving the polar field and also a crucial component controlling variability in the amplitude of sunspot cycles over decadal to century-scales (Nandy and

Choudhuri, 2001; Dasi-Espuig et al., 2010; Muñoz-Jaramillo et al., 2010; Bhowmik and Nandy, 2018; Kumar et al., 2019; Dash et al., 2020; Nandy et al., 2023).

Active regions associated with a solar cycle have their own characteristics and largely follow specific patterns. They emerge closer to the equator as the cycle progresses. This latitudinal variation of active regions in both hemispheres primarily follows Spörer's Law (Carrington, 1858). Hale's polarity law (Hale et al., 1919; Hale and Nicholson, 1925) determines the sign of magnetic polarities (positive/negative) of active regions also known as Bipolar Magnetic Regions (BMRs) in each hemisphere. According to Hale's law, the relative order of magnetic polarities of the leading and trailing spots remains the same in a particular hemisphere, but it's the opposite between the northern and southern hemispheres. To elaborate, if, during a particular cycle, the leading spots of BMRs emerging in the northern hemisphere have positive polarity, the trailing spots will be of negative polarity. The pattern would be opposite for the southern hemispheric BMRs with negative leading spots and positive trailing spots. This polarity order also reverses every solar cycle. Observations suggest that for most sunspot groups, their leading and following spots are seated close to the equator and the pole, respectively. Thus, the magnetic axis joining the centers of the two spots (leader and follower) has a weak statistical tendency to have a slight positive (negative) tilt angle with the axis parallel to the solar equator in the northern (southern) hemisphere. The amplitude of tilt angles generally increases with increasing latitude. This relation between active regions' emergence latitudes and tilts is well known as Joy's tilt Law (Hale et al., 1919). Coriolis force, responsible for twisting the toroidal flux tube during the time of emergence is believed to cause this tilt angle (Choudhuri and Gilman, 1987; Fisher et al., 1995; Kleeorin et al., 2020).

Spörer's law, Joy's tilt law, and Hale's polarity law - these three well-observed laws that describe the location and orientation of sunspot pairs on the solar surface, play a key role in understanding the solar magnetic cycle and its variations through B-L mechanism. The emerging sunspots which do not obey these laws can significantly impact the long-term behaviour of the large-scale solar magnetic field. We have termed these spots 'anomalous regions'. Rogue region is also one category of anomalous regions whose flux and tilt angle is very high (Nagy et al., 2017, 2019). In short, 'anomalous' classification introduced in this manuscript corresponds to all categories of Anti-hale and Anti-joy regions (or combi-

nations of both) irrespective of the amount of flux and degree of tilt angle. We investigate the strength of impact on the solar cycle for these different categories of anomalous regions due to their diversity of tilt characteristics, flux content and spatio-temporal distribution.

There are several theories on the generation of such anomalous regions. Anti-Joy regions (with tilt angles opposite from what should be according to their latitudinal positions) emerge due to two reasons primarily: (1) randomness in Coriolis force (Schmidt, 1968), (2) convective buffeting of flux tubes (Weber et al., 2013). For the Anti-Hale regions (regions with opposite polarity orientation), studies suggest that they can be formed due to (1) kink instability in highly twisted magnetic flux tube (Nandy, 2006; Knizhnik et al., 2018), (2) oppositely oriented toroidal flux-tubes within the convection zone (Stenflo and Kosovichev, 2012), (3) transport of Hale regions from opposite hemisphere (McClintock et al., 2014), and (4) small-scale dynamo action creating sunspots at the end of the cycle (Sokoloff et al., 2015).

Past studies suggest that tilt quenching and variation in the meridional circulation are vital factors causing cycle irregularities (Wang et al., 2002; Dasi-Espuig et al., 2010; Upton and Hathaway, 2014). Additionally, the scattering in active regions' tilt angles and Anti-Joy regions produce significant changes in large-scale polar field build-up and open magnetic flux dynamics during a solar cycle (Cameron et al., 2010; Jiang et al., 2014). Besides, the appearance of a single large Anti-Joy and Anti-Hale region can have a substantial effect on cycle amplitude, which was argued by past studies (Yeates et al., 2015; Jiang et al., 2015) as a probable cause of weaker peaks during solar cycles 23 and 24. A large rogue region emerging at different cycle phases and latitudes with varying fluxes also affects the subsequent sunspot cycle peak activity (Nagy et al., 2017, 2019). Previous observation-based studies claimed that the Anti-Hale or Anti-Joy spots appearing on the solar surface constitute a certain percentage of the total number of sunspots in a cycle, varying from 3% to 10% (McClintock et al., 2014; Li, 2018; Zhukova et al., 2020; Muñoz-Jaramillo et al., 2021). Thus, it is essential to explore the effect of a group of these anomalous regions on the large-scale surface magnetic field distribution and the overall polar magnetic field variability - which we investigate in this present work. Our detailed quantitative analyses are based on multiple numerical simulations using a data-driven surface flux transport model (Bhowmik and Nandy, 2018). In these simulations, we consider

three classes of anomalous regions based on the orientations and polarities of the two spots within the active regions and study the consequences individually. We also investigate how their effects vary depending on the following factors: their latitudinal position, emergence timing relative to the cycle phase, associated magnetic flux and abundance compared to remaining standard Hale-Joy regions.

The presented work is assembled as follows: in section 4.2, we describe the computational model used in our study, section 4.3 summarizes the results we obtain from our simulations. In section 4.4, we validate the results using algebraic approximation and finally, we present our conclusions with relevant discussion in section 4.5.

## 4.2 Simulation Set-up

### 4.2.1 Surface Flux Transport Model

Surface Flux Transport (SFT) models are utilized to demonstrate the time evolution of the large-scale photospheric magnetic field distribution according to the Babcock-Leighton mechanism. This model includes the effects of supergranular turbulent diffusion ($\eta$) and advective transport through large-scale plasma flows like differential rotation [$\omega(\theta)$] & meridional circulation [v($\theta$)] and particularly solves the radial part of the magnetic induction equation which is given by,

$$\frac{\partial B_r}{\partial t} = -\omega(\theta)\frac{\partial B_r}{\partial \phi} - \frac{1}{R_\odot \sin\theta}\frac{\partial}{\partial \theta}\left(v(\theta)B_r \sin\theta\right) + \frac{\eta}{{R_\odot}^2}\left[\frac{1}{\sin\theta}\frac{\partial}{\partial\theta}\left(\sin\theta\frac{\partial B_r}{\partial\theta}\right) + \frac{1}{\sin^2\theta}\frac{\partial^2 B_r}{\partial\phi^2}\right] + S(\theta,\phi,t). \quad (4.1)$$

Where $B_r$ denotes the radial component of the magnetic field, $\theta$ and $\phi$ are colatitude and longitude, respectively. We choose a constant turbulent magnetic diffusivity of $\eta$ = 250 $km^2 s^{-1}$ for our model (the same value was used in calibrated century-scale observational data-driven SFT simulations by Bhowmik and Nandy, 2018). The source term, S($\theta$,$\phi$,t), mimics the emergence of new active regions on the solar surface. $R_\odot$ is the solar radius. The Equation 4.1 is solved in a domain, $\theta$ : 0 to $\pi$ and $\phi$ : 0 to $2\pi$ radians, i.e., covering the whole photosphere. The same SFT code based on spherical harmonics expansions (with

degrees, $l$: 1 to 63) has been used in many past studies (Nandy et al., 2018; Bhowmik and Nandy, 2018; Bhowmik, 2019).

To include the observed large-scale axisymmetric plasma flow in the toroidal direction, known as differential rotation, $\omega(\theta)$, we rely on the following mathematical expression, provided by Snodgrass (1983),

$$\omega(\theta) = 13.38 - 2.30\,cos^2\theta - 1.62\,cos^4\theta \text{ degrees day}^{-1}. \tag{4.2}$$

This profile is in accordance with the helioseismic observation (Durney, 1974; Schou et al., 1998). In addition, there is another observed weak large-scale plasma flow named meridional circulation (Hathaway, 1993; Komm et al., 1993; Mahajan et al., 2021; Hanasoge, 2022), which helps in transporting magnetized plasma from the equatorial region to the poles in respective hemispheres. In our simulation set-up, this flow is bounded within 0° to ±75° in each hemisphere, attains the peak amplitude in the mid-latitudes and becomes zero at the equator. We choose a time-independent meridional velocity profile similar to van Ballegooijen et al. (1998),

$$v(\lambda) = -v_0 \sin(\pi\lambda/\lambda_0) \qquad \text{if } |\lambda| < \lambda_0 \tag{4.3}$$

$$v(\lambda) = 0 \qquad \text{if } |\lambda| > \lambda_0 \tag{4.4}$$

Where, $\lambda$ is latitude and $\lambda_0$ is the limiting latitude ($\lambda_0$ = 75°) beyond which meridional flow vanishes. The amplitude of the meridional flow ($v_0$) is set at 15 m/s. We initialize our simulation with a dipolar configuration of surface magnetic field concentrated primarily near the 20° broad polar cap region (±70° to ±90°) in both hemispheres. The unsigned strength of the initial polar flux in one hemisphere is nearly about 2 x $10^{22}$ Mx which is consistent with observations.

### 4.2.2 Synthetic Sunspot Cycle Profile

Modeling the source term $[S(\theta,\phi,t)]$ in Equation 4.1 in SFT simulations requires information on emergence latitude, longitude, tilt angle and area of each region which can be constrained by observed properties of active regions. For our study, we use the synthetic solar cycle data which is prepared utilizing mathematical relations based on general prop-

erties of observed solar cycles and their associated active regions. First, we consider a time-dependent Gaussian curve to reproduce the sunspot number time series following Hathaway (2010b). The time-latitude distribution band of active regions is inspired by Jiang et al. (2011). We use the following square root relation, $\alpha = C\sqrt{|\lambda|}$ to incorporate Joy's tilt law in our synthetic data set. Here, $\alpha$ is the tilt angle and $\lambda$ is the latitudinal position of the centroid of the BMR. The tilt angle of BMRs can be constrained with the variation of cycle strength and the localized inflows, incorporated in the constant factor "C" (Jiang et al., 2014). We consider a uniform distribution of active regions over the longitudinal domain of the solar photosphere.

Since large sunspots rarely emerge during the initial and declining phase of a cycle, it is preferable to use a polynomial distribution fitted to sunspot observations to model their area distribution (Jiang et al., 2011; Muñoz-Jaramillo et al., 2015). In order to prescribe the associated magnetic flux, we follow the relationship: $\Phi(A) = 7.0 \times 10^{19}$ A (Maxwell), where A represents the area of the whole active region in micro-hemispheres (Dikpati et al., 2006).

We assume that all active regions are typical $\beta$-spots having equal flux in two polarities. We model each BMR with a Gaussian profile prescribed by van Ballegooijen et al. (1998).

### 4.2.3 Preparation of Anomalous Active Regions

As discussed earlier, a few emerging active regions may have different orientations and polarities in contrast to the standard Joy's tilt law and Hale's polarity law. We categorize four possible combinations in which three are considered (see the last three cases in Figure 4.1a) as candidates of anomalous regions.

- Configuration 1 (H-J): the standard Hale-Joy BMRs (non-anomalous) with negative leading polarity and positive following polarity in the northern hemisphere and the opposite pattern in the southern hemisphere (see first case in Figure 4.1a). These strictly follow Joy's tilt law and are the "ideal" spots (denoted by H-J hereafter).

- Configuration 2 (AH-J): BMR that does not follow Hale's polarity law but follow Joy's tilt law. These configurations are also known as Anti Hale-Joy BMRs (AH-J hereafter).

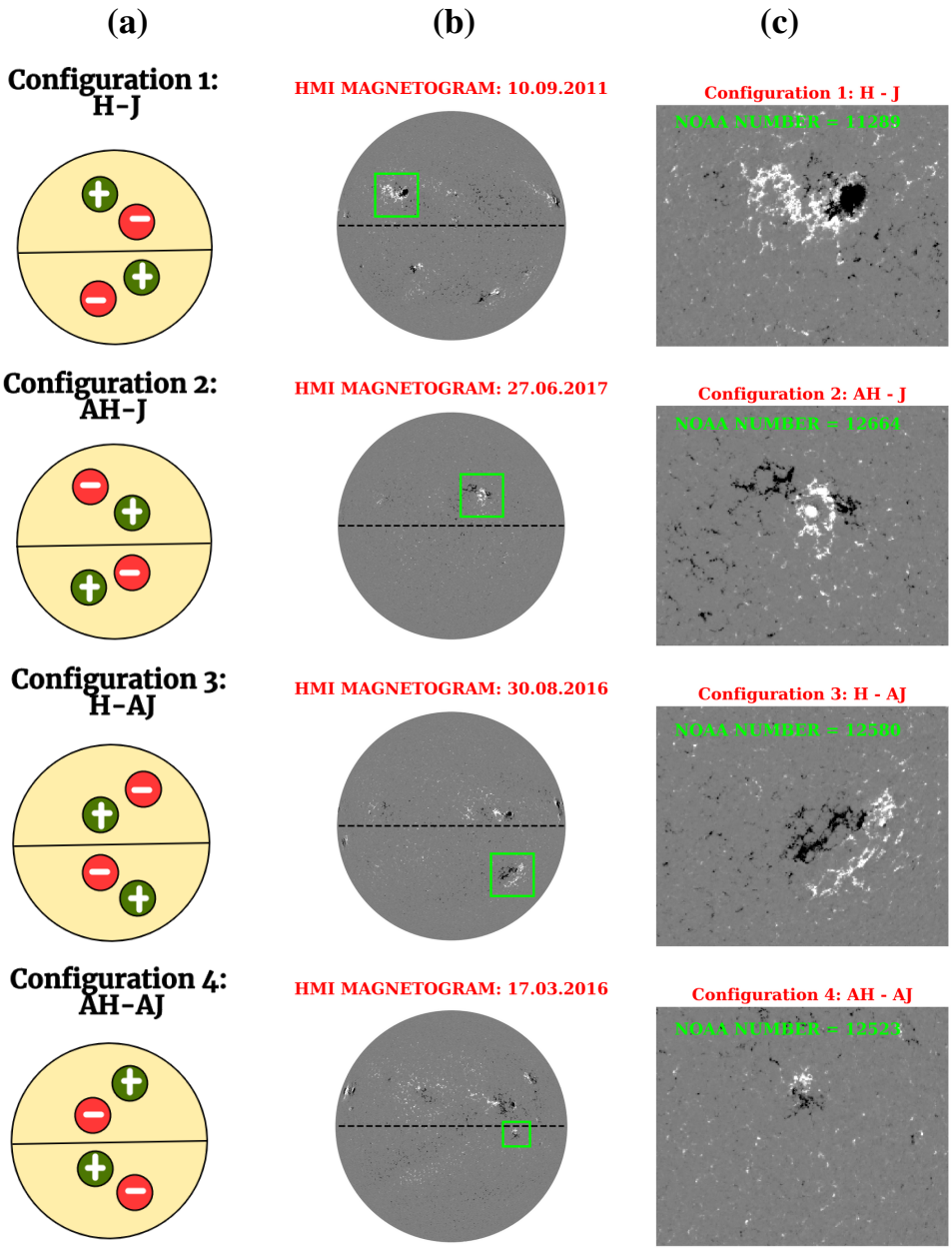


Figure 4.1: *Panel (a):* cartoon of bipolar magnetic region (BMR) with different orientations and polarities in each hemisphere. Here BMR of configuration 1 follows both Hale's and Joy's law (H-J region); configuration 2 represents regions which follow Joy's law but violate Hale's polarity law (AH-J region); configuration 3 does not follow Joy's tilt law but obeys Hale's law (H-AJ region) and lastly, configuration 4 disobeys both Hale's and Joy's law (AH-AJ region). *Panel (b):* surface magnetic field distribution observed in line-of-sight magnetogram from the Helioseismic Magnetic Imager (HMI) instrument on board the Solar Dynamics Observatory (SDO). It denotes four full disk HMI magnetograms observed in Solar Cycle 24. *Panel (c):* cut outs of the green box (in panel b) that serve as examples of the four configurations (H-J, AH-J, H-AJ and AH-AJ regions).

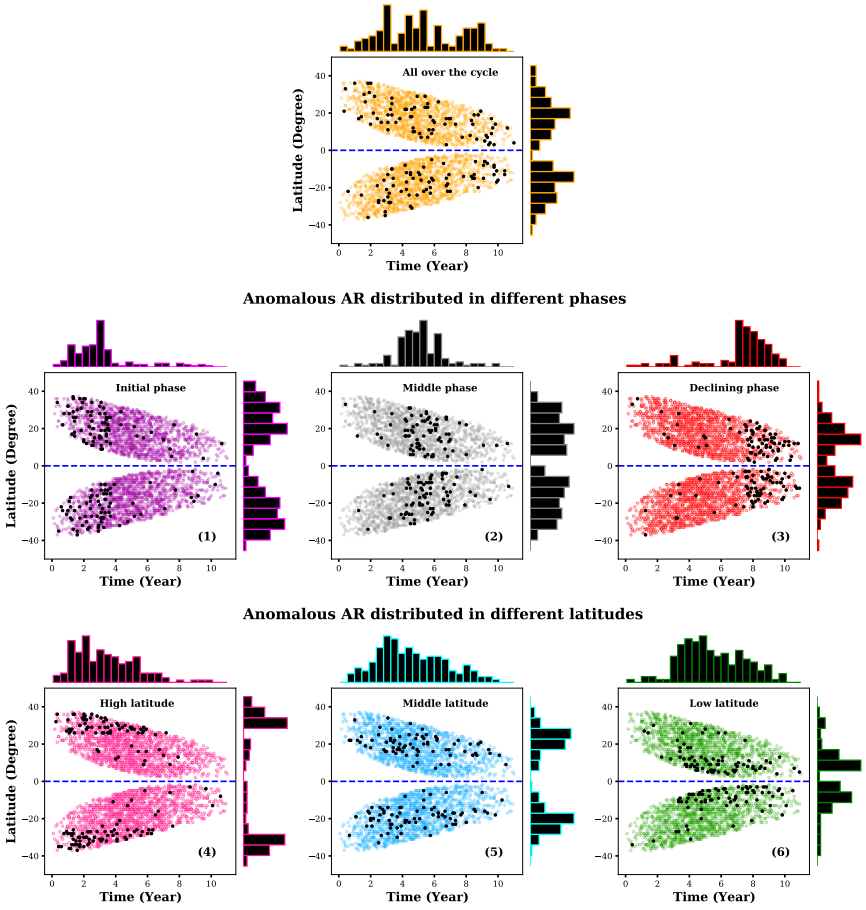


Figure 4.2: Butterfly diagrams reflecting the spatio-temporal variability of the distribution of anomalous regions. Histograms of phase distributions and latitude distributions are plotted on the top axis and right axis respectively in each subplot. Top panel reflects the distribution where 5% anomalous regions are spread all over the cycle. The next panel constitutes the diversity in emergence phase of the anomalous active regions – (1), (2) and (3) dictate population dispersed at initial phase, middle phase and the declining phase, respectively. Third panel denotes the high, mid and low latitude distributions (4, 5 and 6, respectively).

- Configuration 3 (H-AJ): BMR that follows Hale's polarity law but have an opposite tilt, unlike H-J, thus, violating Joy's tilt law. As an example, consider the expected positive tilt angle of a BMR in the northern hemisphere to be negative instead. Such a BMR is categorized as a Hale-Anti Joy BMR (H-AJ hereafter).

- Configuration 4 (AH-AJ): this is the rarest one where the BMR neither follows Hale's polarity law nor Joy's tilt law. It is then an Anti Hale-Anti Joy BMR (AH-AJ hereafter).

The middle and last columns of Figure 4.1 show observational evidence of the above configurations of active regions appearing during Solar Cycle 24.

In most of our simulations, we consider 5% anomalous regions of any kind (AH-J, H-AJ or AH-AJ) comprising 5% of the total unsigned flux associated with the active regions of the whole cycle. We place anomalous regions over the time-latitude domain using a random number generator (see the 1st row in Figure 4.2; the black dots represent anomalous regions). In addition, we also prepare six separate cases by varying emergence latitudes and phases associated with AH-J BMRs. The butterfly diagrams corresponding to these cases are shown in the middle and last panel of Figure 4.2. With each of these different synthetic sunspot series, we perform disparate SFT simulations as described in the following section 4.3.

## 4.3 Results

In order to understand the effect of anomalous active regions on the surface magnetic field we primarily focus on large-scale magnetic field distributions. Especially, it is well-established that the polar field and the axial dipole moment at the end of the solar cycle, which closely reflect the large-scale field distribution, strongly correlate with the succeeding cycle amplitude (Yeates et al., 2008; Muñoz-Jaramillo et al., 2013; Bhowmik and Nandy, 2018). We calculate the dipole moment in the following way,

$$\mathrm{DM}(t) = \frac{3}{4\pi R_\odot^2} \int_{\phi=0}^{2\pi} \int_{\lambda} B_r(\lambda,\phi,t)\, \sin\lambda\, \cos\lambda\, d\lambda\, d\phi, \tag{4.5}$$

where $\lambda$ and $\phi$ represent latitude and longitude, respectively. $R_\odot$ is the solar radius. DM(t) denotes the global axial dipole moment. The dipole moment calculation involves the whole latitudinal and longitudinal domain *i.e.* the entire photospheric radial magnetic field.

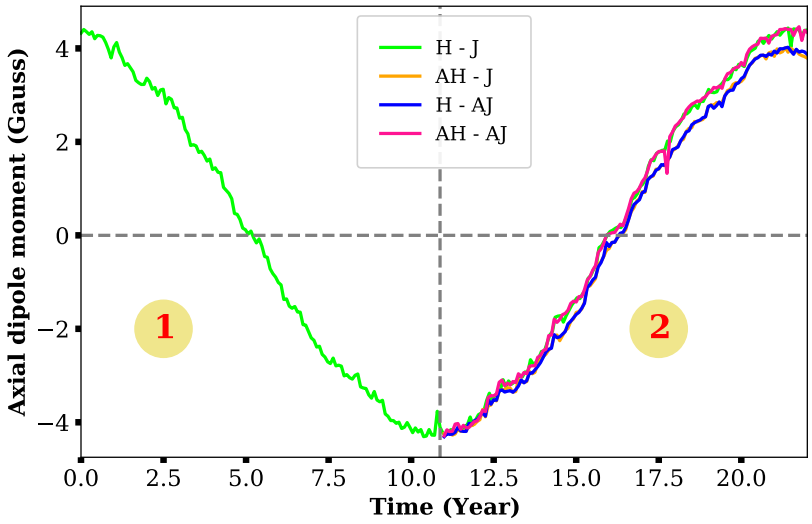


Figure 4.3: Time variation of axial dipole moment over two solar cycles including 5 % of four differently configured BMRs. Green and pink curves denote the axial dipole moment evolution of configuration 1 and configuration 4 (AH-AJ), respectively. Orange and blue curves represent the time evolution of dipole moment for configuration 2 (AH-J) and 3 (H-AJ) respectively.

### 4.3.1 The Effect of Anomalous Regions on Axial Dipole Moment

We initially perform four SFT simulations (duration: 22 years each). One simulation with all H-J spots and the other three simulations are with 5 % anomalous regions in configurations AH-J, H-AJ, and AH-AJ respectively, while the remaining 95 % are H-J regions. It is noted that the spatio-temporal distribution of anomalous regions is kept the same as sunspots in these cases. Figure 4.3 depicts the evolution of the dipole moments associated with each of these four simulations, where the anomalous regions were introduced beyond year 11, *i.e.* in the second cycle. We notice that there is no significant difference in the dipole moment variation for H-J and AH-AJ BMR distribution while AH-J and H-AJ both behave similar to each other, yet significantly different from H-J and AH-AJ. Quantitative details of the dipole moment amplitude for these four configurations are provided in Table 4.1 (see Sl No. 1 to 4).

Table 4.1: A list of quantitative results: Anomalous active regions (AARs) coming from distinct distributions

| **Sl No.** | **Type of AAR distribution** | **Decrease in Dipole Moment** | **Delay in time reversal** |
|---|---|---|---|
| 1) | 5 % AH-J all over the cycle (5% flux) | 13.7 % | 2.61 % |
| 2) | 10 % AH-J all over the cycle (10% flux) | 48.17 % | 7.85 % |
| 3) | 5 % AH-J appearing more at the initial phase | 3.99 % | 3.14 % |
| 4) | 5 % AH-J appearing more at the middle phase | 11.04 % | 5.75 % |
| 5) | 5 % AH-J appearing more at the end phase | 26.17 % | 1.57 % |
| 6) | 5 % AH-J appearing more at the upper latitude | 3.73 % | 3.14 % |
| 7) | 5 % AH-J appearing more at the middle latitude | 9.75 % | 3.14 % |
| 8) | 5 % AH-J appearing more near the equator | 40.64 % | 4.71 % |

In order to understand what leads to these similar outcomes from apparently different BMR configurations, we investigate the temporal evolution of a single BMR each having $\sim 60^{\circ}$ tilt angle corresponding to the four configurations individually (see Figure 4.4). Due to differential rotation, the large-scale surface plasma flow in the azimuthal direction is faster near the equator than at higher latitudes. Consequently, the following spot of an H-AJ region nearer to the equator will advect more towards the right than the leading spot and eventually will attain a configuration similar to that of AH-J. After a short period of evolution ($\sim$ 50 days in our simulations), the only difference remaining between an H-AJ and an AH-J region is that H-AJ region has a higher tilt angle and lower separation between its two polarities than AH-J (see the middle two rows in Figure 4.4). The differential rotation has a similar effect on an AH-AJ region, as it evolves to converge toward the standard H-J configuration with a lower latitudinal separation and a higher tilt angle (see the top and bottom rows in Figure 4.4). Now, the timescale of convergence between the two sets of configurations (H-J & AH-AJ, AH-J & H-AJ) depends on the initial tilt and emergence latitude, which primarily decide the angular separation between the two spots of

the BMR (given that their sizes are similar). In the case of a typical observed active region, its tilt and, thus, the latitudinal separation are much smaller. This makes the timescale of

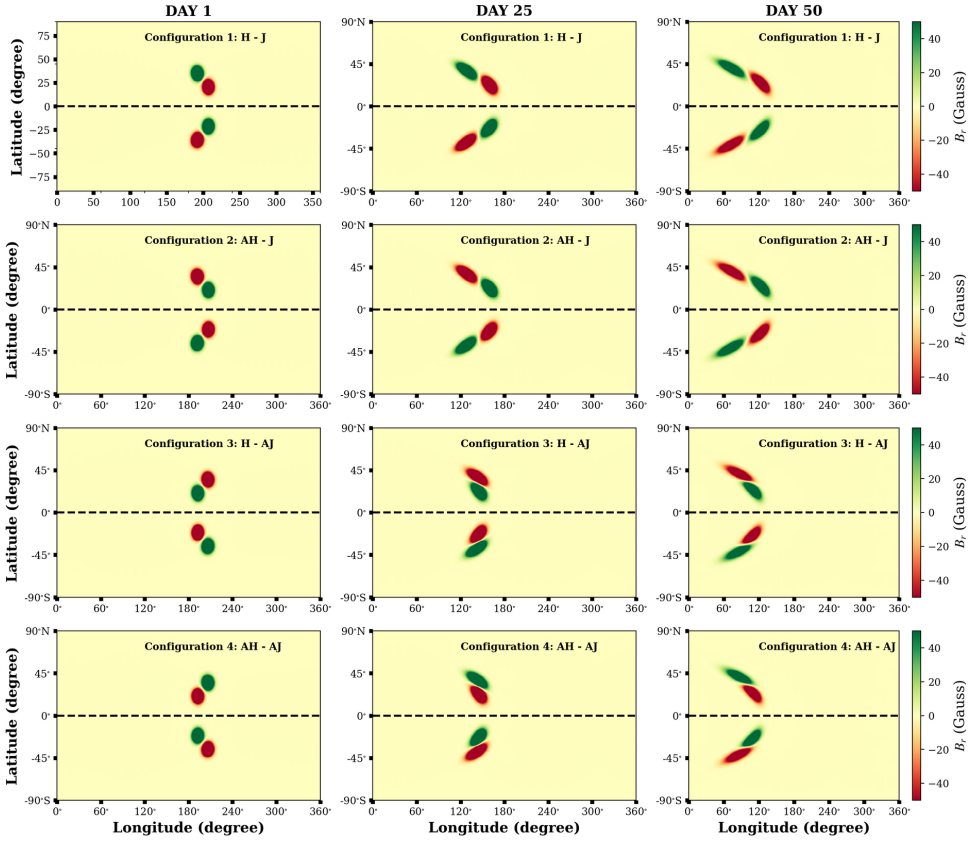


Figure 4.4: Time evolution of the surface magnetic field ($B_r$) for different configurations. Here configuration 1 stands for H-J bipolar magnetic region (BMR), and configurations 2, 3, and 4 indicates the anomalous regions (mentioned in Figure 4.1). SFT simulations are performed for these four initial configurations, and the evolved magnetic field configuration on day 1, 25 and 50 are shown in the left, middle and right panels, respectively.

convergence for the two sets of configurations longer. However, the time scale of empirical sunspot evolution is short compared to long-term behaviour and can be considered transient to the entire solar cycle progression. This explains the similar temporal evolution and the final amplitude of the dipole moments at the end of the 22-year-long SFT simulations (H-J – AH-AJ and AH-J – AH-AJ), even with apparently different classes of anomalous regions. Increasing the percentage of anomalous regions to as high as 25 % does not alter this generic behavior, indicating that the effect of the differential rotation on active regions is quite robust and swift.

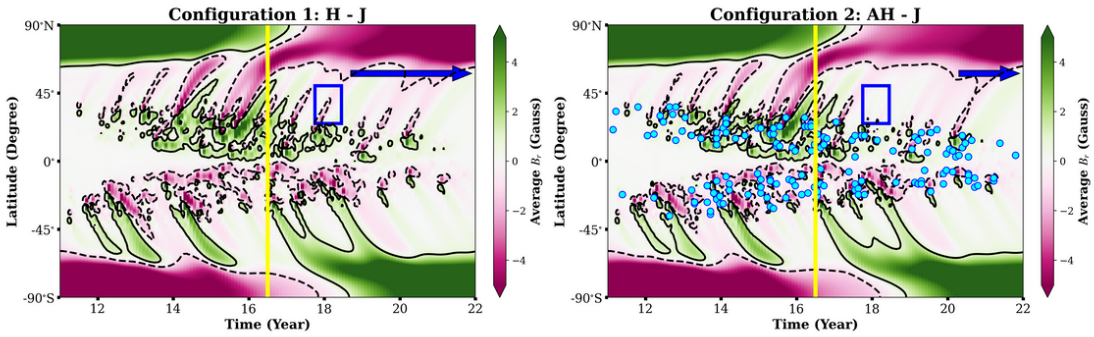


Figure 4.5: Butterfly diagram of the surface magnetic field ($B_r$) for configuration 1 and configuration 2. *Panel (a):* represents the butterfly diagram of H-J regions. *Panel (b):* shows the butterfly diagram of 95 % H-J regions with 5 % AH-J regions. Cyan circles represents the AH-J regions distributed all over the solar cycle. Yellow line in both plots depict the reversal timing of the polar field. Black solid and black dashed lines represent positive and negative polarities respectively. Blue arrow in *Panel (a)* denotes the newly built up polar field region, whereas blue box indicates the opposite polarity surges for H-J BMRs. On the other hand shorter blue arrow in *Panel (b):* reflects the accumulation of lesser amount of negative flux during the end phase of the cycle. Blue box indicates the missing opposite polarity surges in the same panel.

### 4.3.2 Effect on the Succeeding Cycle Amplitude and Time Period

The previous section demonstrates how the AH-J and H-AJ BMRs effectively cause the same variation in the large-scale dipole moment build-up dynamics. Hereafter we limit our analyses only to AH-J regions for simplicity. In the context of solar cycle predictions using either dipole moment or polar flux, we quantitatively evaluate the effect of AH-J regions on the final dipole moment amplitude at the cycle minimum and speculate its implications on the following cycle amplitude.

We utilize magnetic butterfly diagrams (Figure 4.5) depicting the spatio-temporal evolution of the longitudinally averaged $B_r$ on the solar surface to compare two SFT simulations: one with all H-J regions and another one with 5 % AH-J regions (remaining 95 % are H-J regions). We notice two significant differences.

Firstly, in both hemispheres, magnetic fluxes predominantly from the following spots migrate towards the poles as an effect of the B-L mechanism. The amount of these unipolar surges, negative in the northern hemisphere (positive in the southern hemisphere), is relatively higher in H-J configuration than in AH-J.

Secondly, in the second SFT simulation that contains AH-J regions, some negative (in the northern hemisphere) polar surges are suppressed by the magnetic flux associated with

the positive following polarities of AH-J regions (see within the blue rectangle in Figure 4.5). A similar scenario is observed in the southern hemisphere with opposite polarity surges. The overall effect on the evolution and build-up of the large-scale polar magnetic field is manifested in two ways: delay in its polarity reversal and weaker final amplitude at the end of the cycle in the second simulation with AH-J regions compared to purely H-J simulation. Consequently, the succeeding solar cycle is expected to be weaker and have a relatively extended cycle duration (Waldmeier, 1935; Dikpati et al., 2008; Karak and Choudhuri, 2011).

Such changes should be more profound with more AH-J spots, which we verify by performing several SFT simulations with increasing percentages of AH-J regions. Statistical correlation analysis of the decrement of dipole moment amplitude at the solar minimum with the increasing percentage of AH-J regions shows a strong positive correlation with 99.9 % confidence (Spearman coefficient is 0.963) in our SFT simulations. Subsequently, the delay in dipole moment reversal compared to H-J regions bears a positive correlation with the increasing number of AH-J regions (Spearman coefficient is 0.97 with 99.9 % confidence).

### 4.3.3 Relative Effectivity between the Number and Magnetic Flux of Anomalous Regions

According to the basic features of the B-L mechanism, which dictates the evolution of the large-scale magnetic field on the solar surface, the total amount of magnetic flux associated with active regions should have more significance than the total number of regions itself. Although past observational studies (McClintock et al., 2014; Li, 2018; Muñoz-Jaramillo et al., 2021) provide an estimate of the number of AH-J regions (3 % to 10 %), there is scanty information about the total flux contained by these anomalous regions. Thus we perform additional SFT simulations with the aim of determining which one is more important: the number of AH-J regions (relative to H-J regions) or the amount of AH-J region-associated magnetic flux (relative to H-J flux). Thus we consider four distributions and compare the corresponding dipole moment evolution (Figure 4.6).

(a) AH-J regions constituting 5 % of the total number of active regions and 5 % of the total active region-associated magnetic flux. Here the variation in number and flux

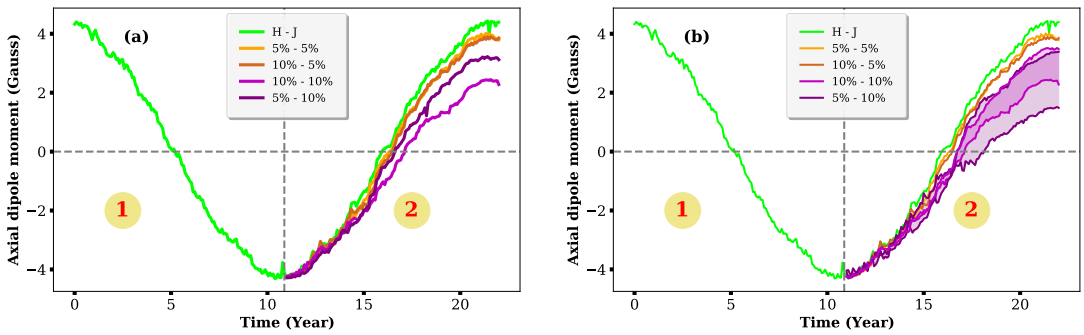


Figure 4.6: Time evolution of axial dipole moment over 22 years incorporating a variation in the number and flux content of the AH-J regions only in the second cycle. Here the variation in number and flux is mentioned as %number-%flux. Orange (5 %-5 %) and dark-orange (10 %-5 %) curves depict the time evolution of dipole moment with AH-J regions having 5 % flux but 5 % and 10 % in number respectively. Violet (10 %-10 %) and dark-violet (5 %-10 %) curves represent AH-J regions having 10% flux but 5 % and 10 % in number respectively. Green curve denotes the corresponding result for 100% H-J regions. *Panel (a):* represents the simulation with single realization. *Panel (b):* depicts the simulations with 20 random realizations for 10 %-10 % and 5 %-10 % cases.

is mentioned as % number-% flux (thus, 5 % - 5 % hereafter).

(b) AH-J regions constituting 10 % of the total active regions and 5 % of the total flux (10 % - 5 % hereafter).

(c) AH-J regions constituting 5 % of the total active regions but 10 % of the total flux (5 % - 10 % hereafter).

(d) AH-J regions constituting 10 % of the total active regions and 10 % of the total flux (10 % - 10 % hereafter).

In Figure 4.6a, we first observe a close resemblance between the dipole moment evolution in cases with fixed flux but different numbers of AH-J regions: 5 % - 5 % (orange curve) and 10 % - 5 % (dark-orange curve). Whereas changing the flux from 5 % to 10 % while keeping the number of AH-J regions fixed to 5 % shows a more profound impact on the reversal timing and final amplitude of the dipole moment at the end of the cycle (see the orange and dark-orange curve in Figure 4.6a). This difference in the large-scale magnetic field evolution becomes increasingly apparent in the later half of the cycle. However, the importance of the number density of AJ-H regions cannot be entirely disregarded. The same amount of magnetic flux (for example, 10 %) can be distributed in one or many AH-J regions randomly positioned in the activity belt. Depending on their emergence timing and

latitude (and tilt angle), additional variations will appear in the dipole moment evolution. We test it by performing additional twenty SFT simulations with different realizations of the time-latitudinal distribution of AH-J regions. The corresponding dipole moment evolution is depicted in Figure 4.6b. The outer curves encompassing the shaded area denote the dipole moment evolution with maximum and minimum amplitudes for cases: 5 % - 10 % (dark-magenta) and 10 % - 10 % (magenta). The width and significant overlap of these two regions indicate that the relative importance between the number and magnetic flux is subjected to the particular distribution of the associated emergence timing, location and latitude-based tilt angles of anomalous spots. The details of these variations are discussed in the next section.

### 4.3.4 Effect of Spatio-temporal Variability of the Anomalous Active Region Distribution

So far, in our SFT simulations, we randomly distribute the anomalous regions over the activity belt of the entire solar cycle. However, results from the previous subsection 4.3.3 indicate that emergence timing and latitude of such regions could introduce more variability in the large-scale magnetic field evolution. Moreover, earlier studies on observed sunspots (Sokoloff et al., 2015; Li, 2018) claim preferential spatio-temporal distribution of anomalous regions which differs from cycle to cycle. Thus, we perform six more SFT simulations to address variations of AH-J region distribution as follows.

We consider that AH-J regions emerging during the: (1) initial phase of the cycle, (2) middle phase i.e. around the cycle maximum, and (3) declining phase of the cycle. Furthermore, we consider other cases with AH-J regions concentrated (4) at higher latitudes, (5) at mid-latitudes and (6) near the equatorial region (low latitudes). The corresponding activity belts are shown in Figure 4.2 and the dipole moment evolution is depicted in Figure 4.7.

For the case with AH-J regions emerging predominantly in the initial phase (simulation 1) of the cycle, we notice a slightly delayed reversal (Figure 4.7a) of the dipole moment caused by unipolar surges from the following spots of AH-J regions which have the same polarity as the existing polar field. However, in the later stage of the cycle, the surface field is dictated by mostly H-J regions, which facilitate a faster increase of the dipole moment,

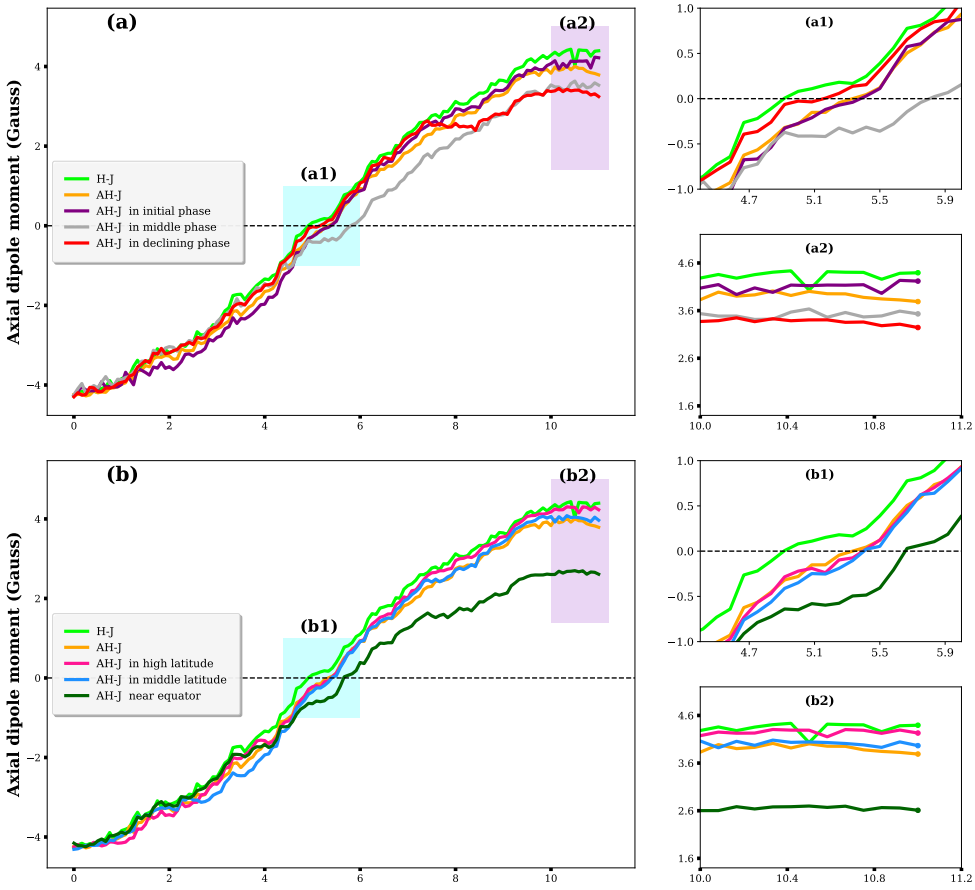


Figure 4.7: Variation in the time series of the dipole moment (only for the second cycle in the simulation) with different distribution of anomalous (AH-J) regions shown in 4.2. *Panel (a):* represents the dipole moment evolution of different phase distributions. The effect of AH-J regions having more density near the starting of the cycle, middle of the cycle and the end of the cycle on the dipole moment is denoted by violet, grey and red curves, respectively. *Panel (b):* pink, light blue and dark green curves depict the dipole moment evolution for AH-J regions emerging in high, mid and low latitudinal positions, respectively. In all of these plots, green and orange curves represent H-J and AH-J, respectively. Panel a1, b1 and a2, b2 are the cut out regions of panels a, b highlighted in cyan and violet, respectively. These sub-panels portray the delay in time-reversal near the cycle maximum and the decrement of dipole moment/polar flux at the minimum of the same cycle.

thereby resulting in a final amplitude similar to the standard randomly distributed AH-J regions all over the activity belt (see orange and violet curve in Figure 4.7a). The impact of AH-J regions appearing around the cycle maximum (simulation 2) is reflected in the significant delay in the reversal of dipole moment (see the grey curve in Figure 4.7a). Note that the bulk of AH-J regions are introduced from year 4 onwards, and the dipole moment almost immediately starts deviating from the H-J case showing a rather sharp deviation in year 5. The effect persists until the cycle minimum with a weaker final dipole moment. Finally, in the case of AH-J regions emerging during the declining phase of the cycle (simulation 3), the dipole moment reversal epoch is similar to the H-J simulation (see the green and red curves in Figure 4.7a). However, the final dipole moment strength is the weakest among all three cases mentioned so far. It is caused by the magnetic flux contribution from the following spots of AH-J regions (having opposite polarity compared to the newly-built polar field) appearing mostly at the end of the activity cycle.

The dipole moment evolution for the three simulations with AH-J regions preferentially emerging in the high (simulation 4), mid (simulation 5), and low latitudes (simulation 6) are depicted in Figure 4.7b. We notice that the high-latitude distribution has minimal effect on the dipole moment (pink curve in Figure 4.7b), resulting in a similar evolution as in all H-J regions case, also concurring with the findings of Yeates et al. (2015). However, the dipole moment corresponding to the simulation with mid-latitude emergences of AH-J regions is almost equivalent to the standard case (where AH-J regions are distributed all over the cycle). The maximum impact on the dipole moment is caused by the AH-J regions emerging at low latitudes (dark green curve in Figure 4.7b), which is directly related to their negative contribution (higher than the other cases) to the dipole moment build-up (explained in more detail in the following sections). Quantitative details on how the dipole moment evolution is affected in these six cases are provided in Table 4.1 (see Sl No. 5 to 10).

## 4.4 Effectivity of Anomalous Regions on Global Dipole Moment: A Theoretical Perspective

In our analyses so far, we have considered the large-scale magnetic field evolution on the solar surface, primarily the dipole moment and polar flux, both of which are longitudinally invariant by definition. While focusing only on these two measures, our spatially two-dimensional SFT simulation (function of latitude, longitude and time) can be reduced to only one spatial dimension with surface magnetic field dependent on latitude and time (Petrovay et al., 2020). Under such simplification, each tilted BMR, after averaging azimuthally, will appear as a pair of flux rings of opposite polarity with a bipole source having a finite latitudinal separation. This methodology has been utilized earlier (Petrovay et al., 2020; Nagy et al., 2020; Yeates, 2020) to propose a mathematical perspective of calculating the individual contribution of each active region emerging during a solar cycle to the final global dipole moment generation at the cycle minimum.

As demonstrated by Petrovay et al. (2020) and Nagy et al. (2020), the change in the global dipole moment during the n$^{\text{th}}$ cycle can be expressed as the sum of the contributions from individual active region dipole moments as follows,

$$\mathrm{DM}_{n+1} - \mathrm{DM}_n = \Delta\mathrm{DM} = \sum_{i=1}^{N_{\text{total}}} \delta D_{\mathrm{U},i} \tag{4.6}$$

where $\delta D_{\mathrm{U},i}$ corresponds to the 'ultimate' dipole moment contribution from the $i^{\text{th}}$ active region during n$^{\text{th}}$ cycle and assuming there are $N_{\text{total}}$ regions in that cycle. Now, the final contribution, $\delta D_{\mathrm{U},i} = f_{\infty,i}\,\delta D_{1,i}$, where $f_{\infty,i}$ is the asymptotic factor (Petrovay et al., 2020). The initial unsigned dipole moment of any active region can be expressed as $\delta D_1 = \frac{3}{4\pi R^2}\Phi d_\lambda \cos\lambda$, where $\lambda$ is the emergence latitude and $d_\lambda$ is the latitudinal separation of the two polarities of the sunspot. $\Phi$ represents the magnetic flux in the BMR's leading (or following) spot. The polarity of the spots closest to the equator determines whether $\delta D_1$ will positively or negatively contribute to the global dipole moment.

The asymptotic factor is a Gaussian function of latitude, $f_\infty = \mathrm{C}\exp(-\lambda^2/2\,\lambda_R^2)$, such that its amplitude decreases with increasing latitude. $\lambda_R$ and C are dependent only on the transport parameters used in the SFT model, which are fixed in all our simulations. Thus,

in summary, the latitude dependency of the ultimate dipole moment contribution from an individual region can be expressed as,

$$\delta D_{\mathrm{U}} \propto d_\lambda \cos\lambda \, \mathrm{e}^{-\lambda^2}. \tag{4.7}$$

The function, $\delta D_{\mathrm{U}}$ has decaying amplitude with increasing latitude, provided $d_\lambda$ is constant for a 1D system (see Figure 4.8a). This theoretical aspect delineated above can be utilized to explain the variations seen in the dipole moment evolution in multiple SFT simulations presented in section 4.3. Firstly, under this one-dimensional formulation, active regions (in Figure 4.2) are reduced to the bipole sources with finite latitudinal separation, whereas the longitudinal separation between the leading and following spots becomes irrelevant. Thus we find pair-wise similarities of dipole moment evolution for the cases: H-J and AH-AJ, and AH-J and H-AJ (provided all emerge at the same latitude, $\lambda$ with the same separation, $d_\lambda$). Secondly, any AH-J (or H-AJ) region will contribute negatively to the dipole moment as its relative polarity configuration is the exact opposite of an H-J (or AH-AJ) region, thus diminishing the global dipole moment as found in subsection 4.3.1 and subsection 4.3.2. These findings are reflected in Figure 4.8b where we carry out a qualitative comparison between the net change in solar dipole moment in SFT simulations with the mathematical approximations.

The latitude dependency shown in equation 4.7 also supports our findings in section 4.3.4. In the first three SFT simulations with the varying spatio-temporal distribution of AH-J regions on the activity belts, we see notable changes in global dipole moment in cases with the anomalous regions emerging during either middle or declining phases of the cycle (see Figure 4.7a). A careful inspection of the latitudinal distribution of these spots on the activity belt (see the second row in Figure 4.2) suggests that more spots emerging in mid-to-low latitudes (in contrast to more high latitude emergences) are responsible for this. Similarly, for cases with AH-J regions appearing in different latitudinal belts (see the third row in Figure 4.2), preferential emergence in low latitudes (smaller $\lambda$) will increase the negative contribution according to equation 4.7. Therefore, it will cause the maximum reduction of the final global dipole moment (see the pink curve in Figure 4.7b). Figure 4.8b shows the qualitative comparison between these results (high/mid/low latitudinal emergence impacts) from our SFT simulations and aforementioned algebraic prescription.

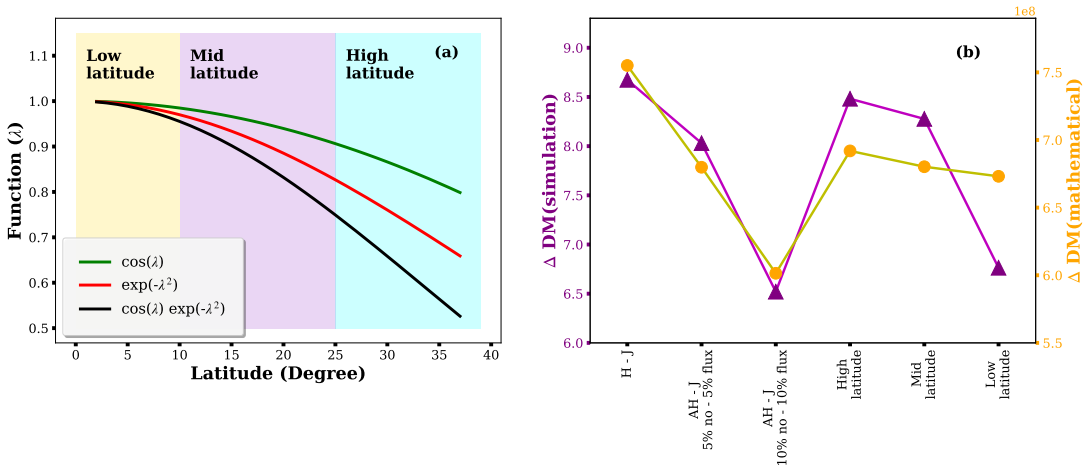


Figure 4.8: Qualitative comparison of net change in solar dipole moment in our SFT simulation with the mathematical approximations. *Panel (a):* depicts the latitudinal ($\lambda$) dependency of different analytical functions contributing to the ultimate dipole moment. High, mid and low latitudinal regions are denoted by cyan, violet and yellow. *Panel (b):* change in dipole moment ($\Delta$ DM) of our simulations(violet traingles) are compared with the mathematically derived approximated values (orange circles) for six different cases labelled on the horizontal axis.

## 4.5 Concluding Discussions

Emergence of active regions and transport of the associated magnetic flux on the solar surface primarily determines the Sun's polar field and dipole moment build-up. The global dipolar field acts as the seed which modulate the amplitude of the future sunspot cycle underscoring its importance. In this study, we focus on the orientation of the active regions and investigate their impacts on the large-scale magnetic field of the Sun, especially, the dipole moment and hemispheric polar field. We keep the flux transport parameters and some BMR properties like the separation, area, latitudinal and longitudinal position fixed, eliminating variations originating from these properties. This enables us to segregate contributions from "anomalous sunspot regions" in the creation of irregularities in the solar cycle. It is to be noted that "rogue" regions (Nagy et al., 2017) with very high tilt angle or high magnetic flux (or a combination of both) are a subset of anomalous sunspots according to our classification. How a few rogue or highly tilted active regions can significantly impact the dipole moment evolution has been studied earlier (Jiang et al., 2014; Nagy et al., 2017). In comparison, our focus is not on rogue regions specifically but on a more comprehensive study of the impact of diverse classes of anomalous regions with

varying numbers, flux content emergence timing and location.

We consider all active regions as bipolar sunspots (i.e., $\beta$-spots) and do not consider any regions with complex morphology (e.g., $\delta$-spots). By performing multiple SFT simulations we find that a fraction of the total sunspot number emerging as anomalous regions can significantly influence the large-scale magnetic field evolution during the solar cycle. The appearance of AH-J/H-AJ regions changes the polarity reversal timing and eventually suppresses the axial dipole moment at the end of the solar cycle – in conformity with the findings of (Jiang et al., 2015; Nagy et al., 2017).

In this work, we establish a crucial point through SFT simulations: the AH-J and H-AJ regions contribute almost identically in the dipole moment evolution, polar field build-up and their reversal epoch; this is because over a few rotational timescales the Sun's differential rotation makes their orientation similar. In addition, AH-AJ active regions behave similarly to H-J regions in their long-term evolution. We perform an analysis which shows that our simulation results are consistent with the algebraic formulation motivated from mathematical theory (see section 4.4).

Based on our findings we conclude that in the context of the the long-term evolution of the Sun's large-scale magnetic field, the sunspots' orientation can be grouped into two classes: 1) Those that contribute positively to the dipole moment – Hale-Joy sunspots (H-J) and 2) Which contribute negatively – Anti Hale-Joy sunspots (AH-J). These two distinct classes of active region configurations also exhibit characteristically distinct dynamics over shorter time scales leading to disparate interactions with the local magnetic field distribution.

Our analyses demonstrate that the amount of flux and the number density of anomalous regions play an essential role in the dynamics of surface magnetic field evolution. Although not always, we notice that in some cases a large population of anomalous sunspots can impact the ultimate dipole moment more than a small population carrying the same amount of flux. Therefore we speculate that sometimes a larger group of anomalous spots can cumulatively be more influential than a single large rogue region due to their latitudinal and phase distribution diversity.

It is known that the total amount of unsigned polar flux is of the order of the unsigned flux contained in a single but very large active region. A similar amount of net flux dis-

tributed over a fraction of sunspots of the anomalous class of regions appearing at distinct phases and latitudes will affect the cycle differently. Our simulations show that AH-J regions near the equator have the highest impact on the ultimate dipole moment strength, whereas their appearance during the mid-phase of the solar cycle has the highest impact on the reversal timing. Near-equatorial emergence is understood to be more influential in general. This carries over to the case of anomalous regions. The leading polarity of AH-J/H-AJ regions is opposite to the sign of the new polar field (that is being imparted) in the opposite hemisphere. Thus upon appear near the equator and diffusing to the other hemisphere, it may reduce the strength of the new polar field of the opposite hemisphere (and the ultimate dipole moment) during the descending phase of the solar cycle. In sharp contrast, at high latitudes, the initial phase population of anomalous regions hardly influences the overall magnetic cycle evolution and its inherent dynamics. We believe that along with the diverse phase and latitudinal distributions, the hemispheric asymmetry in the distribution of AH-J/H-AJ regions may translate to the asymmetry seen in the polar field weakening.

The result from different scenarios based on different synthetic sunspot distributions is described in section 4.3 and tabulated in Table 4.1. Note that the statistics reported correspond to one random realization of each scenario. Although these values may differ from one random realization to the other, the qualitative behaviour of the global magnetic field evolution under different possible scenarios still have a resemblance to the observed Sun.

In summary, our simulations provide insight on how the interplay of anomalous and regular active regions modulate the solar dipole moment evolution. Given that the dipole moment at the minima of a cycle is the most important factor determining the strength of the future sunspot cycle, these insights are important in the context of solar cycle predictions. In order to constrain polar field evolution and dynamics it would be important to extract the combined data of AH-J, H-AJ and AH-AJ regions (with their precise number, flux content and the emergence phase-latitude information) along with the H-J regions from observation. Such an exercise will provide the necessary observational constraints for driving more precise predictive models of surface flux transport evolution and illuminate the fine subtleties of the Babcock-Leighton mechanism for solar polar field production.

# Chapter 5

# Investigating the Drivers of Extreme Variability in Solar Activity Over Cycle 19-20

*"Over the past century, the Sun's activity – which exhibits significant variations – went through a phase known as the Modern Maximum. Notably, the strongest sunspot cycle on record during this period, and indeed since direct sunspot observations began, was cycle 19; this was followed by a significantly weaker cycle 20. Understanding and reconstructing this extreme variability has remained elusive. Utilizing data-driven, coupled models of magnetic field evolution on the Sun's surface and within its convection zone, here we show that random deviations in the tilt angle and polarity orientation of bipolar sunspot pairs is sufficient to explain these observed, extreme fluctuations during the modern maximum in solar activity. Our results support the theory that perturbation in the poloidal field source of the dynamo mechanism – mediated via the emergence of anomalously tilted solar active regions - is the primary driver of extreme variations in the Sun's activity. This study has implications for understanding how the Sun may switch from a phase of extreme activity to quiescent, low activity phases – such as the Maunder Minimum.* [1] "

## 5.1 Introduction

The sunspot cycle – characterized by an approximately 11-year quasi-periodic rise and fall in solar activity – is a striking manifestation of the Sun's magnetic behavior (Charbonneau, 2020; Usoskin, 2023). However, the strength of the Sun's activity cycle is not uniform and varies from one cycle to another, resulting in a variable forcing of the heliosphere that

[1] This chapter is based on Pal and Nandy (2025).

seamlessly bridges physical phenomena originating in our host star's interior to planetary impacts (Daglis et al., 2021). Observational evidence has uncovered that over the past century, the Sun has exhibited a prolonged period of unusually high activity known as the *Modern Maximum* (Solanki et al., 2004). The strongest cycle during this phase – in fact over the past four centuries since direct sunspot cycle observations began with Galileo Galilei and his contemporaries – was sunspot cycle 19 peaking around 1957; this was followed by an unexpectedly weak sunspot cycle 20. Understanding and reconstructing this extreme solar activity fluctuation over cycles 19-20 through physics-based models has remained an outstanding challenge (Cameron et al., 2010; Jiang et al., 2013; Bhowmik and Nandy, 2018; Virtanen et al., 2022; Pal and Nandy, 2024a; Yeates et al., 2025).

It is understood that nonlinearities inherent in the magnetohydrodynamic solar dynamo mechanism and stochastic perturbations in the dynamo source terms can lead to amplitude fluctuations from one solar cycle to another (Charbonneau and Dikpati, 2000; Saha et al., 2025). The Sun's large-scale dipolar field – the poloidal component (of which the polar field is a proxy) – is inducted by solar differential rotation within the Sun's convection zone to produce the toroidal magnetic field component of the following sunspot cycle (Parker, 1955). Magnetic (Lorentz) feedback of strong toroidal flux tubes on the Sun's differential rotation can, in principle, result in amplitude modulation; however, observations show that inter-cycle variations (known as torsional oscillations) in the solar differential rotation which acts as the source of the Sun's toroidal field – is quite small $\leq 5\%$ (Mahajan et al., 2024).

Strong toroidal fields are unstable to magnetic buoyancy and rise up to emerge through the solar surface giving rise to bipolar sunspot pairs — which are observed to be systematically tilted relative to the local latitude (due to the action of the Coriolis force on rising flux tubes). Observations (Dasi-Espuig et al., 2010; Muñoz-Jaramillo et al., 2012), theoretical considerations (Cameron and Schüssler, 2015) as well as data-driven, physical models of the long-term evolution of solar magnetic fields – such as solar surface flux transport (SFT) models and dynamo models (Bhowmik and Nandy, 2018) – have suggested that the dispersal of the magnetic flux of these tilted bipolar sunspots (mediated by plasma flows) is the primary mechanism for recreation of the Sun's large scale dipolar field; the latter mechanism is known as the Babcock-Leighton (BL) mechanism (Babcock, 1961;

Leighton, 1969). As magnetic flux tubes rise through the solar convection zone, they are buffeted by vigorous turbulence, generating an observed scatter in the tilt angles around the mean (Joy's law tilt) expected from Coriolis force (Cheung and Isobe, 2014). The amplitude of this scatter is observed to be much more than the mean tilt angle, which acts as a significant source of perturbation on the poloidal field source (Jiang et al., 2014; Nagy et al., 2017). Anti-Hale active regions (ARs) – bipolar sunspot pairs whose polarity orientation does not conform to the conventional solar cycle trend – are an additional source of perturbation (Nagy et al., 2017; Pal et al., 2023). Other mechanisms, such as tilt quenching and latitudinal quenching, are also known to act as amplitude-limiting mechanisms for the BL poloidal field generation mechanism (Jiao et al., 2021; Yeates et al., 2025).

Although the interplay of these nonlinearities and stochastic forcing are theorized to drive solar activity fluctuations, capturing the extreme variation between cycles 19-20 has remained elusive. Here we address the outstanding question whether solar cycles 19 and 20 can be accurately reconstructed using known physics and physical models of solar magnetic field evolution.

## 5.2 Numerical Model Description

### 5.2.1 Data-driven SPhoTraM Simulation

**Model Equation:**

The CESSI Photospheric-Flux Transport Model (SPhoTraM) is a newly developed two-dimensional numerical model designed to simulate the solar surface magnetic flux transport processes. It solves the radial component of the magnetic induction equation in the spatial domain in the presence of diffusion $\eta$ (mimicking the effect of super-granular flows) and transport profiles like meridional circulation $v(\theta)$ and differential rotation $\omega(\theta)$. SPhoTraM employs various finite difference schemes combined with flux limiter algorithms to numerically solve the magnetic induction equation with improved accuracy. In general, the surface flux transport model is the replication of the well-known BL mecha-

nism, which can be expressed by the following mathematical equation:

$$\frac{\partial B_r}{\partial t} = -\omega(\theta)\frac{\partial B_r}{\partial \phi} - \frac{1}{\mathrm{R}_\odot \sin\theta}\frac{\partial}{\partial \theta}\left(v(\theta)B_r \sin\theta\right) + \frac{\eta}{{\mathrm{R}_\odot}^2}\left[\frac{1}{\sin\theta}\frac{\partial}{\partial\theta}\left(\sin\theta\frac{\partial B_r}{\partial\theta}\right) + \frac{1}{\sin^2\theta}\frac{\partial^2 B_r}{\partial\phi^2}\right] + S(\theta,\phi,t). \tag{5.1}$$

In our model, the advective terms, $v(\theta)$ follow an axisymmetric profile, peaking at mid-latitudes with a velocity of 15 m/s and going to zero beyond $\pm 75^\circ$, while $\omega(\theta)$ is derived from helioseismic observations, with the profile following Bhowmik and Nandy (2018); Pal et al. (2023). We set $\eta$ to 250 $\mathrm{Km}^2/\mathrm{s}$. Another important term in our model is $S(\theta,\phi,t)$, which is the source term for magnetic flux emergence, accounting for contributions from newly formed sunspot regions based on observational or theoretical input. This term is modeled as an ideal bipolar magnetic region, following the mathematical profile outlined in previous works (Bhowmik and Nandy, 2018; Pal et al., 2023).

**Model Source Term:**

To generate the source term, we require information on the emergence time, heliographic latitudinal and longitudinal positions, and area of active regions for each solar cycle, all of which are taken from the observational database provided by RGO/USAF/NOAA Data Centre (2023). We record the emergence information for each sunspot when it reaches its maximum area. After 1976, the sunspot records transitioned from the RGO database to the USAF/NOAA database. To ensure consistency between the two datasets, we apply a cross-calibration by multiplying a correction factor of 1.4 to all areas less than 206 micro-hemispheres for active regions appearing post-1976 (Bhowmik and Nandy, 2018). Other quantities, such as the magnetic flux associated with a sunspot, tilt angle, sunspot group radius, and the separation between the two polarities of a sunspot pair, are derived from the observational data using empirical and mathematical relationships. The magnetic flux ($\Phi$) of each active region is calculated using the relation: $\Phi(\mathrm{A}) = 3.5 \times 10^{19} \times \mathrm{A}$, where A is the sunspot area in microhemispheres, and $\Phi$ is the total magnetic flux in Maxwells, whic is assumed to be equally distributed in the two polarities. We estimate the radius of the sunspot from the area information and consider that the radial separation between two polarities of a sunspot pair is proportional to the radius of the sunspot. We compute the

standard tilt angle using the square root relation, $\gamma = C T_n \sqrt{\lambda}$ to incorporate Joy's tilt law in a sunspot pair. Here, $\gamma$ is the tilt angle, $\lambda$ is the latitudinal position of the centroid of the AR and $T_n$ is the tilt coefficient for $n^{th}$ solar cycle. The variation in tilt angles with solar cycle strength (known as tilt quenching) is modeled through $T_n = 1.73 - 0.0035\,S_n$, as derived from Jiang et al. (2011), where $S_n$ denotes the solar cycle strength. The constant factor C is set to 0.7, accounting for the reduction in tilt angles caused by near-surface localized inflows (Jiang et al., 2014).

**Introducing Stochaticity in the Source Term:**

To introduce tilt scatter, we adopt a methodology commonly used in previous studies (Jiang et al., 2014; Jiao et al., 2021). These studies show that the tilt angles of the sunspots deviate from Joy's Law in a manner consistent with a Gaussian distribution. This distribution has a zero mean value, indicating no systematic bias, while its standard deviation ($\sigma$) depends on the sunspot area (A) according to the empirical relation: $\sigma = -11 \times \log(A) + 35$ (For a detailed illustration, see the Appendix section in Lemerle et al. (2015)). For each sunspot group, we randomly sample a tilt scatter value ($\varepsilon$) from this Gaussian distribution (having zero mean and $\sigma$ standard deviation) which is determined by that sunspot group's area obtained from the observed database. The resulting tilt angle is then given by $\gamma = C T_n \sqrt{\lambda} + \varepsilon$. In our simulations, incorporation of random tilt-angle scatter gives rise to anomalous sunspots, including anti-Joy regions (specially those which carry opposite tilt orientations to standard Joy ARs) and ARs with unusually large tilt angles. We also consider the anti-Hale ARs are distributed randomly all over the cycle phase, emergence latititude and two hemispheres. These anti-Hale sunspot distributions are generated from independent random realizations following the methodology described by Pal et al. (2023). In Figure 5.1, such anomalous AR distributions (Latitudinal and flux distribution) for solar cycle 18 and 19 are shown.

To quantify the contribution from stochasticity, we calculate the flux-weighted tilt coefficient, $T_A = (\frac{\sum_i \gamma_i \times \phi_i}{\sum_i \phi_i |\lambda_i|})$, where $\gamma_i$, $\phi_i$, and $|\lambda_i|$ represent the tilt angle, flux content, and the absolute latitude of the $i^{th}$ sunspot. When this coefficient is multiplied by the signed total flux emergence during that cycle this generates $\Phi T_A$ – which provides physical insight into the average contribution of tilted sunspots to the resulting polar flux at the end of that

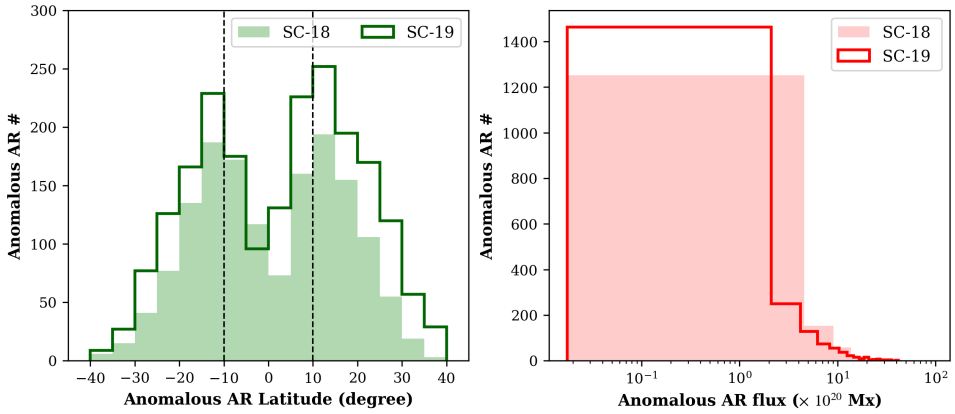


Figure 5.1: The top panel illustrates the latitudinal distribution of anomalous ARs (both anti-Hale and anti-Joy regions) for solar cycle 18 (filled histogram) and solar cycle 19 (solid histogram). The bottom panel displays the flux distribution of anomalous sunspots, with red filled and solid histograms representing the flux throughout the sunspot cycles 18 and 19, respectively. For clarity and better visualization, the x-axis in this panel is on a logarithmic scale.

cycle (Dasi-Espuig et al., 2010; Jiao et al., 2021).

**Estimation of Large-Scale Magnetic Fields:**

We calculate the axial dipole moment and polar flux using the photospheric map generated by the SPhoTraM simulations utilizing the following relations.

$$\mathrm{DM}(t) = \frac{3}{4\pi R_\odot^2} \int_{\phi=0}^{2\pi} \int_{\lambda=-\pi/2}^{\pi/2} B_r(\lambda,\phi,t)\, \sin\lambda\, \cos\lambda\, d\lambda\, d\phi, \tag{5.2}$$

$$\Phi_{N/S}(t) = \int_{\phi=0}^{2\pi} \int_{\lambda_{N/S}} R_\odot^2\, B_r(\lambda_{N/S},\phi,t)\, \cos\lambda_{N/S}\, d\lambda_{N/S}\, d\phi \tag{5.3}$$

Here $\lambda$ and $\phi$ represent latitude and longitude, respectively. $R_\odot$ is the solar radius. $\Phi_{N/S}$(t) denotes the polar flux in the northern and southern hemispheres, respectively, and DM(t) is the global axial dipole moment. The polar field is calculated based on the surface magnetic field distribution only in the polar cap region ($\pm 70^\circ$ to $\pm 90^\circ$), whereas the axial dipole moment corresponds to the entire photospheric magnetic field.

**Optimization of the Polar Flux:**

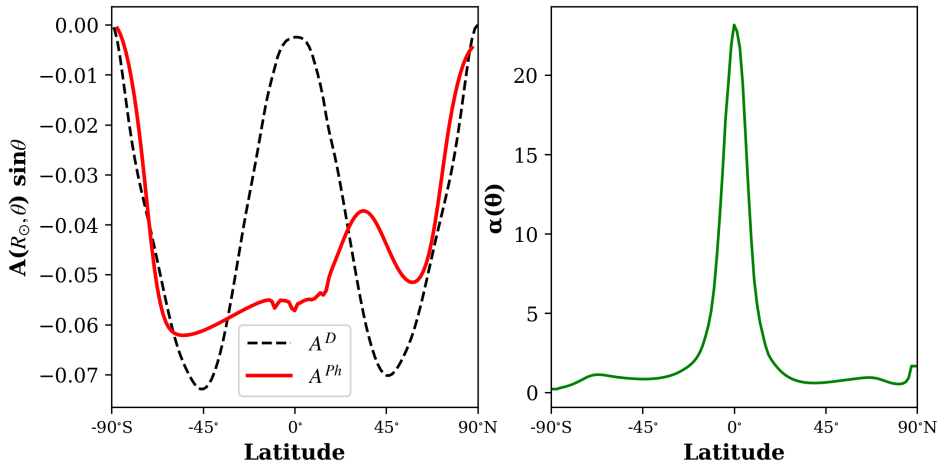


Figure 5.2: The left panel presents surface vector potential at the minima of solar cycle 16 (begining of cycle 17) from SPhoTraM simulation ($A^{Ph}$ denoted by red curve) and from dynamo run ($A^{D}$ denoted by black dashed line). The right panel shows the latitudinal correction function $\alpha(\theta)$.

The observational magnetograms and polar field measurements are only available from 1974 onward. To bridge this gap, we use polar flux estimates derived from Mount Wilson Observatory calibrated polar faculae data, which extend back to 1906 (Muñoz-Jaramillo et al., 2012). We first generate multiple ensembles of AR input source terms for each solar cycle for Monte Carlo (MC) SPhoTraM simulation. In each ensemble of this MC simulation, our methodology automatically introduces stochastic variation in the tilt angles and in the distribution of anti-Hale regions in terms of flux content, emergence locations, and phase of appearance. Then we compare the SFT simulated polar flux generated from each ensemble run with observed polar flux values and select a set which satisfies both of the following criteria: (1) the simulated polar flux reversal timing must be within $\pm 1$ year of the observed reversal time and (2) the simulated polar flux at the end of each solar cycle must lie within a $\pm 20\%$ range of the observed polar flux value. For each sunspot cycle, we identify the optimal solution from the reduced ensembles by selecting the one that best matches the observed polar flux at the cycle minimum. This is how we optimize the simulated polar flux for our study.

### 5.2.2 Dynamo Simulation

**Model Equation:**

To generate solar cycles, we utilize the two-dimensional kinematic axisymmetric dynamo model that solves the toroidal (B) and poloidal component ($B_P$) of the magnetic induction equation in presence of source terms for sustaining the dynamo mechanism (Nandy, 2002; Chatterjee et al., 2004). Inducing a toroidal field from the poloidal field, followed by the regeneration of the poloidal field from the toroidal field, lies at the heart of the dynamo cycle. In this axisymmetric model, the temporal evolution of the vector potential for the poloidal component $A^D(r, \theta)$ and the toroidal component of the magnetic field $B(r, \theta)$ are described by the following equations:

$$\begin{aligned} \frac{\partial A^D}{\partial t} + \frac{1}{s}\left[\mathbf{v_p}\cdot\nabla(sA^D)\right] &= \eta_p\left(\nabla^2 - \frac{1}{s^2}\right)A^D + \alpha B \\ \frac{\partial B}{\partial t} + s\left[\mathbf{v_p}\cdot\nabla\left(\frac{B}{s}\right)\right] + (\nabla\cdot\mathbf{v_p})B &= \eta_t\left(\nabla^2 - \frac{1}{s^2}\right)B \\ +s\left(\left[\nabla\times(A^D\hat{\mathbf{e}}_\phi)\right]\cdot\nabla\Omega\right) &+ \frac{1}{s}\frac{\partial(sB)}{\partial r}\frac{\partial\eta_t}{\partial r} \end{aligned} \tag{5.4}$$

where, s = r $\sin\theta$. In this equation, $v_p$ represents the poloidal velocity in the meridional plane (or meridional circulation) that causes advection and distortions in the magnetic field. We utilize a single-cell flow in each hemisphere, threading the convection zone. The terms involving $\eta_P$ and $\eta_t$ correspond to the diffusion of poloidal and toroidal magnetic fields, respectively.

Source terms in a dynamo model are crucial to compensate for the dissipation of magnetic fields within the convection zone. The internal rotational shear, as determined from helioseismic observations, acts as a source for generating toroidal fields. We adopt the analytical advective and diffusive flow profiles from Passos et al. (2014) for this study. In our simulation, the generation of the poloidal field from the toroidal component is represented by two distinct mechanisms which are thought to operate within the Sun's interior. The first one is the BL Mechanism introduced confined in the near-surface layers. The second mechanism, the mean-field $\alpha$-effect due to helical turbulent convection, operates on relatively weaker toroidal field in the bulk of the solar convection zone. These two terms

are incorporated in the equation as a single source term $\alpha$. The mathematical profile with appropriate quenching of these source terms is included following Passos et al. (2014). In each ensemble of MC simulation, our methodology automatically introduces variation in the tilt angles and in the distribution of anti-Hale regions in terms of flux content, emergence locations, and phase of appearance.

**SFT Maps Coupled with Dynamo Framework:**

We follow the methodology described in Bhowmik and Nandy (2018) to couple the dynamo model with SFT simulations. We emphasize that our model does not incorporate any intrinsic amplitude fluctuation of the $\alpha$ mechanism over time. Instead, the variability in the poloidal field source term is introduced exclusively by integrating the SPhoTraM generated surface magnetic map at every cycle minimum (Bhowmik and Nandy, 2018). Our SPhoTraM model generates the radial magnetic field $B_r^{Ph}(R_\odot, \theta, t_m)$ which is related to the magnetic vector potential $A^{Ph}(R_\odot, \theta, t_m)$ through the relation $B = \nabla \times A$, which reduces to:

$$B_r^{Ph}(R_\odot, \theta, t_m) = \frac{1}{R_\odot \sin\theta} \frac{\partial}{\partial \theta} [\sin\theta A^{Ph}(R_\odot, \theta, t_m)] \tag{5.5}$$

From this equation, we compute the surface vector potential $A^{Ph}$ by integrated $B_r^{Ph}(R_\odot, \theta, t_m)$ separately for the two hemispheres. The governing equations are:

$$A^{Ph}(R_\odot, \theta, t_m) \sin\theta = \begin{cases} For\ 0 < \theta < \pi/2, \\ \int_0^\theta B_r(R_\odot, \theta', t_m) \quad \sin\theta' d\theta' \\ \\ For\ \pi/2 < \theta < \pi, \\ \int_\theta^\pi B_r(R_\odot, \theta', t_m) \quad \sin\theta' d\theta' \end{cases} \tag{5.6}$$

It is noted that, here, $B_r^{Ph}(R_\odot, \theta, t_m)$ is calculated by longitudinally averaging the surface magnetic field during solar minima ($t = t_m$).

After calculating the vector potential from SPhoTraM run, denoted as $A^{Ph}$, it is fed into the dynamo model after proper calibration, which replaces the dynamo-generated vector

potential $A^D$ (see left panel of Figure 5.2 for an example). To calibrate $A^D$ at solar minima against $A^{Ph}$, we scale their amplitudes on the solar surface by a constant factor ($k$), which is determined at the minimum of solar cycle 16 and kept fixed throughout the simulation. Thus we use $A^D = k \times A^{Ph}$.

After this amplitude calibration, although the amplitudes of $A^D$ and $A^{Ph}$ are aligned, their latitudinal distributions, specifically $A^D(R_\odot, \theta, t_m)\sin\theta$ and $A^{Ph}(R\odot, \theta, t_m)\sin\theta$ still differ significantly. To reconcile this, $A^D$ at each solar minimum is further corrected by a latitudinal function $\alpha(\theta)$, such that the product $\alpha(\theta) \times A^D(R\odot, \theta, t_m)\sin\theta$ matches $A^{Ph}(R\odot, \theta, t_m)\sin\theta$ at the solar surface (see right panel of Figure 5.2 for an example). We assume that the correction to the dynamo's poloidal field – arising from the BL mechanism – is confined to the radial range between $0.8R\odot$ and $R\odot$. This assimilation is implemented sequentially at each cycle minima and forces the dynamo generation of the toroidal component of the magnetic field which acts as the source of the sunspot cycle. To elaborate, at each solar minimum, the dynamo simulation is paused, and $A^D(r, \theta, t_m)\sin\theta$ is multiplied by $k\alpha(\theta)$ at all grid points within this mentioned radial layer (remember $k$ is fixed but $\alpha(\theta)$ changes for each cycle). Once $A^D$ has been updated to reflect the SPhoTraM-generated vector potential $A^{Ph}$, the dynamo simulation resumes and continues its evolution. It is to be noted that all the other plasma parameters in the dynamo model are kept fixed for each solar cycle simulation.

This iterative approach enables us to produce a sunspot number time series driven by the SPhoTraM model, thereby providing a physics-based reconstruction of solar cycles over an extended period, including the extreme variations.

## 5.3 Results and Discussions

We first reconstruct century-scale solar polar field variations using an SFT model. These models are driven by incorporating as input the emergence profile and statistics of bipolar sunspot pairs. We prepare the synthetic input of ARs using observed sunspot emergence statistics derived from the RGO/USAF/NOAA Data Centre (2023) database – which provides details on the area, emergence time, and location of sunspots. These information are used to drive the SPhoTraM model (a brief description of which is available in subsection 5.2.1). Past work has shown that long-term simulations using this database fail to

reproduce variations across all solar cycles, including extreme solar cycles (Bhowmik and Nandy, 2018; Pal and Nandy, 2024a). This limitation arises because this database lacks two crucial information necessary for precise modeling. The first is the tilt angle information of ARs, which significantly influences polar field generation, is unavailable. Although models often assume that tilt angles follow the mean Joy's law tilt expected from Coriolis force, scatter around the mean tilt is crucial for capturing polar field variations (Jiang et al., 2014; Nagy et al., 2017). The second limitation is the lack of observational constraints on the polarity orientation of sunspots which results in an inability to account for the impact of anomalous ARs (anti-Hale configurations). These anomalous sunspots can significantly reduce the polar field and the overall solar cycle strength (Pal et al., 2023). To overcome these limitations, we incorporate these two properties of ARs into our SPhoTraM simulations.

We begin our simulation in 1902, at the beginning of solar cycle 14, initializing it with a dipolar magnetic field configuration. First, we generate the ensembles of sunspot input sources for a single solar cycle. Each ensemble introduces random scatter into the standard empirically calculated tilt angles; for technical details, see subsection 5.2.1. Additionally, we distribute approximately 8% - 8.4% of the total ARs of that cycle as anti-Hale regions – which we note is consistent with the observed range gleaned from the most recent solar cycles for which polarity information exists (Li, 2018). Accounting for tilt scatter and anti-Hale active region distribution in this manner, we generate multiple input sources for solar cycles 14 to 23 and perform Monte Carlo (MC) SPhoTraM simulations. From these ensembles, we choose the optimal solution for each solar cycle, which minimizes the difference between the simulated and observed polar field at cycle minima (for detailed methodology of optimizing, see subsection 5.2.1)

Figure 5.3 (top panel) shows the optimized simulated polar flux variations for the northern and southern hemispheres (solid red and blue, respectively) compared with the observed polar flux (dashed curves). This figure demonstrates that by accounting for tilt angle scatter and anti-Hale sunspots, we are able to successfully reproduce the polar field evolution of solar cycles 18 and 19 (which serve as sources for sunspot cycles 19 and 20, respectively), along with other cycles over century-scale. The butterfly diagram (Figure 5.3 bottom panel) depicts the time-latitude evolution of the longitudinally averaged

radial magnetic field ($B_r$). The diagram shows the surface field dynamics associated with polar field reversal and build-up in our optimized simulation. Additionally, the magnetic flux surges toward the poles, representing both positive and negative polarity contributions, including perturbation due to anomalous ARs are clearly discernible. These surges play a crucial role in determining polar field amplitude.

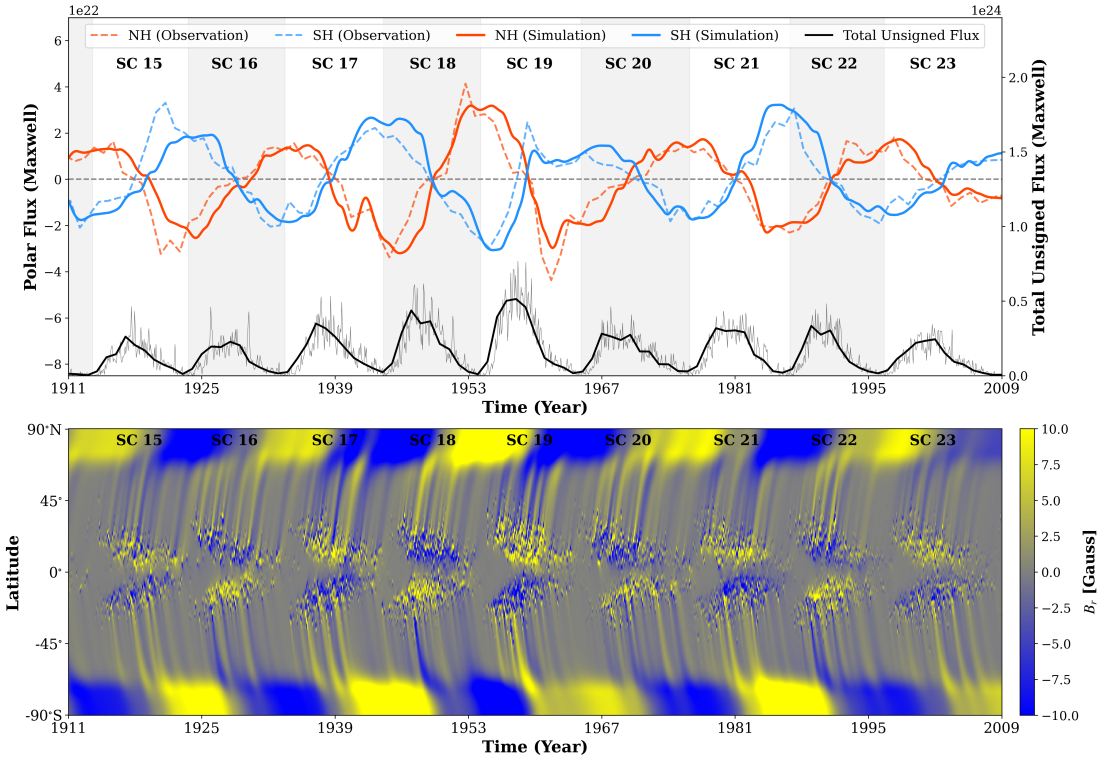


Figure 5.3: The top panel illustrates the variations in the optimized simulated polar flux (solid curves) alongside the observed polar flux obtained from the MWO polar faculae database (dashed curves) for solar cycles 15 to 23. The red and blue curves represent the Northern and Southern hemispheres, respectively. Additionally, the black/grey curve in the same panel depicts the total yearly/monthly averaged unsigned sunspot flux, derived from the RGO/USAF/NOAA database. The bottom panel presents the time-latitudinal distribution of the radial magnetic field ($B_r$) based on the optimized simulation. Here, yellow and blue shades indicate magnetic fields of positive and negative polarity, respectively.

In the next stage, we employ a two-dimensional (axisymmetric) kinematic dynamo model (for model details see subsection 5.2.2) to reconstruct the solar cycle time series over a century covering the Modern Maximum phase. In this approach, we assimilate the longitudinally averaged surface magnetic field from the optimized SFT simulation as the source of the poloidal field into the dynamo model at the end of each solar cycle (see subsection 5.2.2 for a more detailed methodology). Our solar dynamo model integrates a

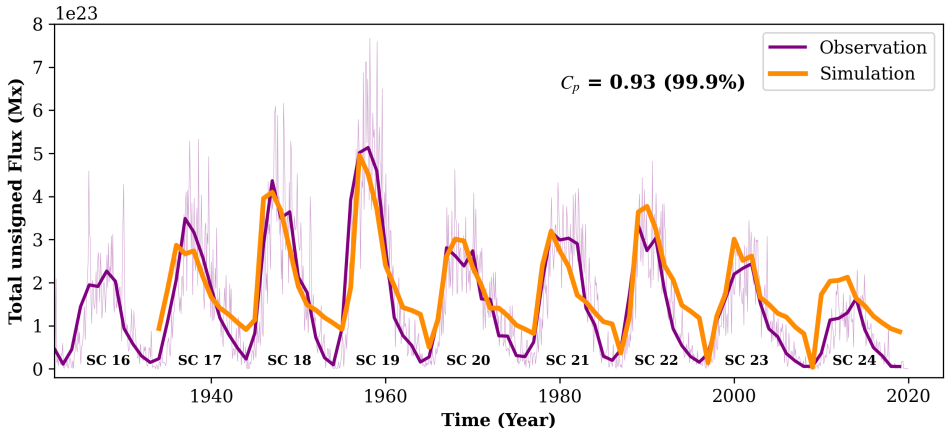


Figure 5.4: The violet curve represents the total yearly averaged unsigned sunspot flux from solar cycle 16 to 24, derived from the USAF/RGO/NOAA database. The orange curve indicates the total unsigned flux simulated using the dynamo model (refer 5.2.2), driven by the poloidal field generated by the SPhoTraM model. A Pearson correlation coefficient of 0.93, calculated with a 99% confidence level, highlights the strong agreement between the observed and simulated flux strengths at cycle maxima.

buoyancy algorithm to simulate sunspot emergence as eruptions of the toroidal field when it exceeds a specified threshold magnetic field strength. These toroidal field eruptions are then used as a proxy for the total sunspot flux that has erupted during the cycle. The simulated magnetic flux from these sunspot eruptions is compared with the observed unsigned sunspot flux, which represents the total unsigned flux derived from sunspot emergence data in the RGO/USAF/NOAA database. The result is depicted in Figure 5.4. It is noted that the simulated magnetic flux does not reach the observed low value at minima. This is a general issue in diverse dynamo models due to cycle overlap (Hazra and Nandy, 2016; Kumar et al., 2019). This can be by fine-tuning the meridional flow from cycle to cycle, which we do not consider here (Hazra and Choudhuri, 2017). Our results show that the SPhoTraM generated poloidal field successfully reproduces the cycle strength of solar cycles 19 and 20, while capturing the overall trend of other cycles over the century scale. This outcome highlights the importance of properly accounting for tilt angle scatter and anomalous regions in governing extreme variations in solar activity.

To deconstruct the physics of extreme solar variability over sunspot cycles 19-20, we study the mean flux-weighted tilt angle distribution of sunspots in the simulation runs that successfully reproduce the polar flux for solar cycles 18 and 19 (which subsequently act as seeds of sunspot cycles 19 and 20, respectively). If no stochasticity is included in tilt-angle

variations, the values of flux-weighted tilt coefficient, i.e. $\Phi T_A$ remain nearly identical for cycles 18 and 19, as shown in the top panel of Figure 5.5.

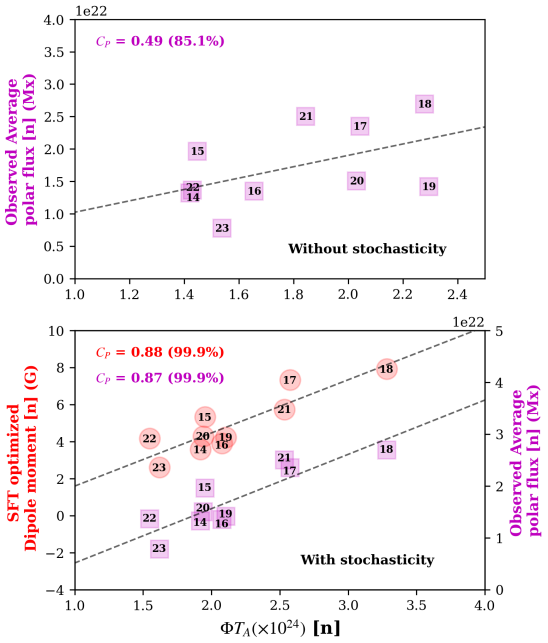


Figure 5.5: Top panel denotes correlation between the flux-weighted tilt coefficient multiplied by total flux ($\Phi T_A$) for the n$^{th}$ solar cycle and the observed average polar flux at the end of the same cycle. This correlation is estimated using the sunspot database without incorporating stochasticity. Bottom panel illustrates correlation between the $\Phi T_A$ and two quantities at the end of the same solar cycle (n): (i) the dipole moment simulated by SPhoTraM simulation (left $x$-axis, red circles), and (ii) the observed average polar flux (right $x$-axis, magenta squares). These correlations are estimated after incorporating stochasticity in the sunspot emergence statistics. The grey dashed lines in both panels represent the best-fit linear regressions.

However, upon incorporating tilt-angle fluctuations, $\Phi T_A$ increases substantially for cycle 18, while it decreases for cycle 19. Moreover, the correlation between $\Phi T_A$ of the n$^{th}$ solar cycle and the observed average polar flux at the end of the same cycle improves significantly when stochasticity is incorporated into the sunspot emergence statistics (compare the magenta squares in the top and bottom panels of Figure 5.5). Similarly, we observe a strong positive correlation ($r = 0.88$, with 99.9% confidence) between $\Phi T_A$ of the n$^{th}$ cycle and the dipole moment at the end of the same cycle, as generated by the optimized SFT simulation (see the red circles in the bottom panel of Figure 5.5). This result suggests that solar cycle 18, with its higher $\Phi T_A$ leads to a stronger dipole moment at the end of the cycle which seeds the extreme sunspot cycle 19. This is because, when the tilt angle of a sunspot pair is high, the latitudinal separation between opposite polarities increases due

to plasma flows, avoiding intra-active region flux cancellation and allowing transport of significant amount of flux efficiently toward the poles. A stronger polar field enhances the seed poloidal field for the following cycle, which explains the exceptionally strong solar cycle 19. The highest value of $\Phi T_A$ further indicates that cycle 18 had ARs with very high tilt-angle scatter – or, equivalently, the highest degree of stochasticity – accounting for its exceptionally high amplitude.

On the other hand, the sudden drop in $\Phi T_A$ observed for solar cycle 19 offers a contrasting and compelling explanation for the weak amplitude of solar cycle 20. When the tilt angle of a sunspot pair is small, a larger portion of magnetic flux cancels internally within the active region itself, thereby reducing the efficiency of poleward flux transport. This diminished transport of magnetic flux weakens the buildup of the polar field, which in turn contributes to a weaker subsequent solar cycle – as observed in cycle 20. Additionally, the $\Phi T_A$ parameter accounts for the influence of anomalous sunspots, including anti-Hale ARs, which possess reversed polarities relative to standard sunspots. Being a stronger cycle, solar cycle 19 exhibits a higher number of such anomalous ARs compared to cycle 18, as shown in the Figure 5.1 in subsection 5.2.1. These anomalous ARs contribute a greater amount of opposite – polarity flux toward the poles, ultimately diminishing the net polar field strength by the end of cycle 19. Consequently, anti-Hale ARs play a crucial role in generating extreme solar cycle variability – where a high-amplitude cycle culminates in a weak polar field, leading to a subdued following cycle.

We note that it is challenging to separately assess the effects of anti-Joy and anti-Hale regions across solar cycles 18 and 19 due to several factors which influence their contributions. The most important factor, elaborated in detail in Pal et al. (2023), is that an anti-Joy region with a tilt angle opposite to that expected from Joy's Law evolves into an anti-Hale region (due to the action of differential rotation) within a rotational timescale – far shorter than solar cycle timescales – and thus their contributions are nearly similar. Therefore, from the physical perspective, it is a better strategy to group these types of ARs within the general framework of anomalous ARs.

## 5.4 Summary

Solar cycle 19 stands out as exceptionally strong, yet the polar field build-up at its end is surprisingly weak, leading to a weaker subsequent solar cycle 20. Such variations in solar cycles can arise from multiple factors, including the non-linear mechanisms and external stochastic mechanisms involved in magnetic field generation and transport. The lack of long-term observations makes it challenging to constrain these processes. In this study, we employ a novel ensemble run methodology applied on a coupled, data-driven solar surface flux transport model and dynamo model to reconstruct the past ten solar cycles. We specifically focus on understanding the extreme variation from sunspot cycle 19 to 20.

Our results reinforce the hypothesis that one of the key factors – if not the most important one – driving cycle-to-cycle variations is the random scattering in sunspot tilt angles. More importantly, our simulations show that reasonable fluctuations in the tilt angle of ARs – within the observed range of variabilities – is able to recover the significant variation in polar field at the end of cycles 18 and 19 that act as seeds for historically strong sunspot cycle 19 and the much weaker cycle 20. Our results imply that no exotic new physics need to be invoked to explain the extreme fluctuations observed during the Modern maximum in solar activity. Our data-driven, observationally constrained physics-based simulations lend further credence to the emerging understanding that stochastic perturbations – and not non-linear quenching – is the primary driver of centennial-scale solar variability.

Building upon our findings, we may surmise that such random (stochastic) fluctuations, manifest in solar ARs with highly anomalous tilt (and sometimes with large flux) may indeed result in a catastrophic reduction in the value of the polar field – precipitating a Maunder-like grand minimum. This possibility, already alluded to in Nagy et al. (2017), appears to be a distinct possibility based on this work which recovers the extreme fall in amplitude from sunspot cycle 19 to 20. While Nagy et al. (2017) suggest a "rogue" or extreme anomalous AR may achieve this, a number of anomalous ARs – realizing which is more probable – may achieve an analogous effect in precipitating grand minima episodes. Our work motivates further investigations into intriguing possibilities.

# Chapter 6

# Comparative Analysis of Polar Precursors for Solar Cycle Prediction: Global Dipole Moment versus Hemispheric Polar Flux

*"Accurate forecasting of future solar cycle amplitudes is crucial because solar activity modulates the near-Earth space environment, yet such predictions remain a long-standing challenge in solar physics. Observations indicate a correlation between the polar field strength at a solar cycle minimum and the subsequent sunspot cycle amplitude – which has been widely relied upon for solar activity predictions. However, it remains an open question which polar precursor – polar field strength or axial dipole moment – serves as the more robust predictor of future solar activity. In this study, we employ an observationally constrained, data-driven surface flux transport model to reconstruct century-scale variations in both the polar flux and the axial dipole moment evolution and perform a comprehensive assessment of their predictive capabilities. Our analysis demonstrates that the axial dipole moment exhibits a stronger, more strong correlation with the amplitude of the subsequent sunspot cycle than the polar field. This provides new physical evidence supporting the axial dipole moment as the primary magnetic precursor for solar cycle prediction within the framework of the Babcock–Leighton dynamo mechanism.* [1] "

[1] This chapter is based on a submitted research work

## 6.1 Introduction

Solar magnetic activity – manifested through magnetic cycles – plays a pivotal role in influencing space weather, satellite operations, and even Earth's climate system (Solanki, 2002; Airapetian et al., 2020; Temmer, 2021; Nandy et al., 2021, 2023). One of the most prominent features of solar magnetism is the appearance of dark, strongly magnetized sunspots on the solar surface with an approximate 11-year periodicity, known as the solar cycle (Hale, 1908; Hathaway, 2015; Norton et al., 2023; Usoskin, 2023). These sunspots have been observed continuously for centuries, from early pioneering observations with the newly invented telescope in the early $17^{th}$ century (Vaquero, 2007; Clette et al., 2015; Pevtsov, Alexei A. et al., 2019).

The origin of the solar cycle lies in the complex, nonlinear interactions between magnetic fields and plasma flows in the solar convection zone (Cameron and Schüssler, 2015; Charbonneau, 2020; Hazra et al., 2023). The turbulent nature of the Sun's convection zone gives rise to fluctuations that leave their imprint on the generation of the magnetic field in the solar interior leading to cycle-to-cycle variations (Charbonneau, 2020; Brun, 2020; Choudhuri, 2018; Pal and Nandy, 2024a, 2025; Saha et al., 2025). The inherent stochastic nature and non-linear feedback of the solar dynamo mechanism, coupled with the lack of clear periodic patterns in sunspot records, make solar cycle prediction highly challenging (Petrovay et al., 2020; Nandy et al., 2021). As a result, precursor methods – where indicators from the declining phase or solar minimum are used to forecast the upcoming cycle's strength – have gained traction in both empirical and physics-based modeling approaches (Upton and Hathaway, 2014; Bhowmik and Nandy, 2018; Jiang et al., 2023; Pal and Nandy, 2024a; Jaswal et al., 2024; Jha and Upton, 2024; Jouve et al., 2025).

Among these, polar precursor methods – first proposed by Schatten et al. (1978) – stand out due to their strong physical basis. Observations consistently suggest a positive correlation between the amplitude of the Sun's polar magnetic field (the radial component of the poloidal field) at solar minimum and the strength of the subsequent sunspot cycle (Schatten et al., 1978; Yeates et al., 2008; Muñoz-Jaramillo et al., 2012; Petrovay et al., 2020; Nandy et al., 2023). This connection arises naturally within the Babcock–Leighton (BL) dynamo framework, where the polar poloidal field is transported to the tachocline

and converted into toroidal field, which seeds the sunspots of the next cycle.

Polar precursors generally fall into two categories based on large-scale solar magnetic field indicators: (1) the polar field or polar flux, and (2) the global axial dipole moment. Other proxies, such as polar filament statistics and geomagnetic indices, have also been explored to enable earlier cycle forecasts (Nandy, 2021; Routh et al., 2025). Recent efforts have investigated how early a reliable prediction can be made before the onset of a new solar cycle. For instance, Kumar et al. (2021) demonstrate that polar precursors may be useful as early as 2–3 years before the solar minimum.

However, the limited availability of long-term polar field and dipole moment observations constrains the robustness of empirical predictions and makes it difficult to determine the most effective precursor. In this letter, we address this fundamental question: Which polar precursor – hemispheric polar flux or global dipole moment – offers better predictive capability for future solar cycles? To answer this, we utilize a data-driven, optimized solar Surface Flux Transport (SFT) model and reconstruct century-scale datasets of polar field and dipole moment evolution. We analyze these simulated solar cycles alongside available observations to reassess the polar precursor approach. Furthermore, we propose an alternative precursor that can potentially allow solar cycle prediction well before the minimum. Our results demonstrate that the global dipole moment provides a more accurate and physically justified basis for solar cycle prediction than the hemispheric polar flux, making it a valuable tool for long-term space weather forecasting.

## 6.2 Data and Methodology

We utilize the RGO/NOAA database to obtain the sunspot area (SSA) time series, which provides measurements for the monthly averaged northern hemisphere (NH SSA), southern hemisphere (SH SSA), and the total SSA (see blue, grey and orange filled curve in three consecutive panels of Figure 6.1). As polar precursors, we primarily focus on two key physical quantities: (1) the hemispheric polar flux and (2) the axial dipole moment. For hemispheric polar flux, we utilize polar faculae observations spanning solar cycles 14 to 23, which are widely regarded as the most reliable photospheric proxy for reconstructing the Sun's polar magnetic flux (see maroon and purple dashed curve in first two panels of Figure 6.1). However, direct observational data for the global dipole moment

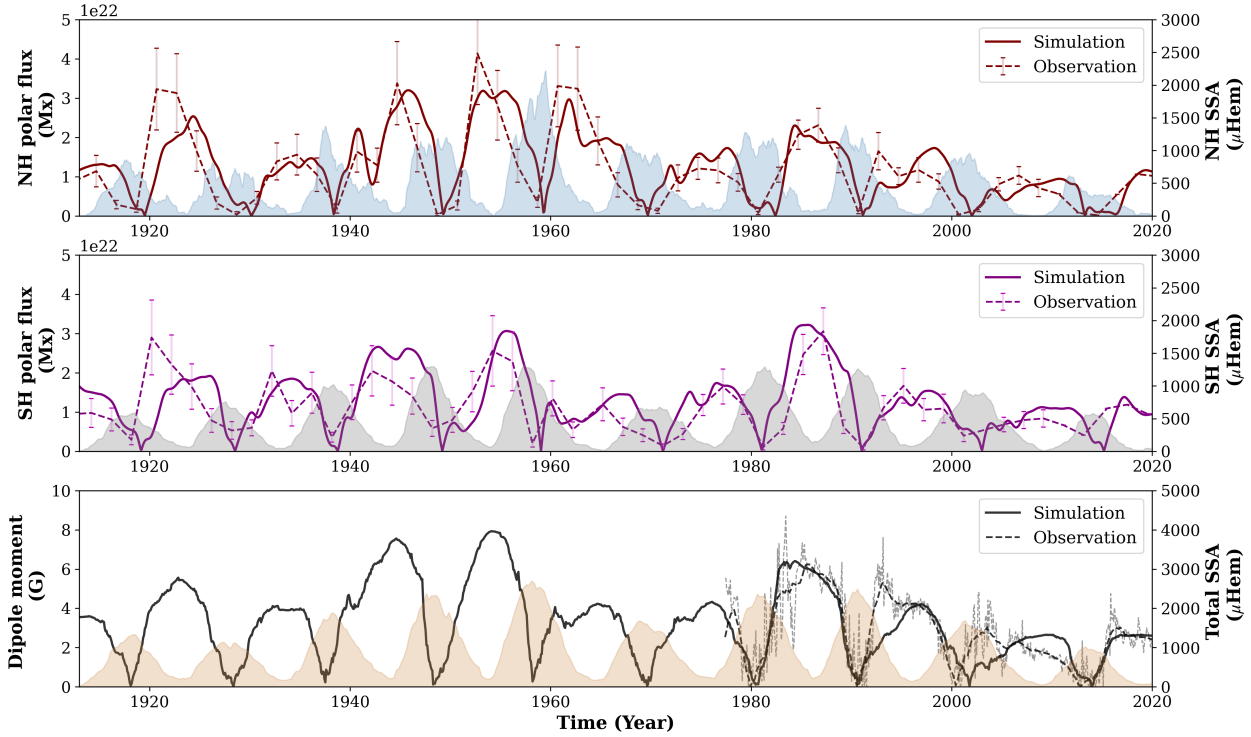


Figure 6.1: Time evolution of the Northern Hemisphere (NH) polar flux and NH sunspot area (top), Southern Hemisphere (SH) polar flux and SH sunspot area (middle), and the axial dipole moment and total sunspot area (bottom) from solar cycles 15 to 24. The filled curves denote the sunspot area (SSA) in each panel, while the solid and dashed lines represent the simulated and observed polar flux or dipole moment, respectively.

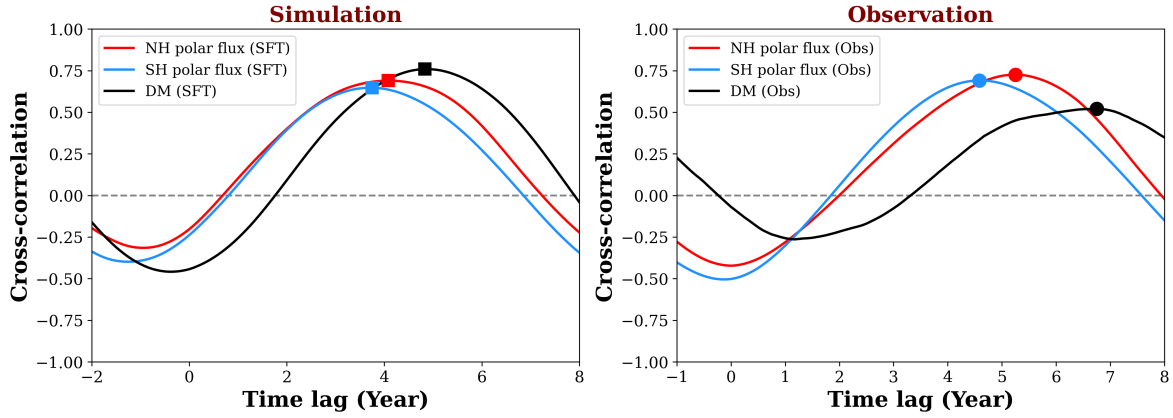


Figure 6.2: Cross-correlation r($\tau$) between the poloidal field and sunspot area (SSA) time series. The left and right panels correspond to the simulation and observation, respectively. Red, blue, and black curves represent the Northern Hemisphere polar flux, Southern Hemisphere polar flux, and the axial dipole moment. The maximum absolute values of r are indicated by boxes (simulation) and circles (observation).

are only available for solar cycles 21 to 24, taken from WSO database. To overcome this limitation, surface flux transport (SFT) models provide a powerful means to reconstruct the Sun's surface magnetic field for earlier cycles, thereby enabling the study of dipole moment variations over an extended period.

In this study, we employ a data-driven, optimized SFT model – SPhoTraM – to reconstruct both polar flux and axial dipole moment over the past century (Pal and Nandy, 2025). This model ingests active region properties such as latitude, longitude, and magnetic flux from the RGO/NOAA sunspot database. To account for tilt angle scatter and anomalous active region emergence, we follow the treatment described in Pal et al. (2023); Pal and Nandy (2025). Using this observational input, we simulate the solar surface magnetic field evolution for decadal-scale solar cycles, optimizing the simulated polar flux to match the observed polar faculae-based polar flux measurements. For a detailed description of the modeling framework and methodology, readers are referred to Pal and Nandy (2025). With this simulated dipole moment reconstruction, we extend our analysis from the four observed cycles to ten cycles spanning the past century. This uniform framework allows us to systematically compare the two polar precursors in terms of their correlation with the peak sunspot area of subsequent cycles.

It is important to note that we treat the polar flux separately for the northern and southern hemispheres, and likewise consider the sunspot area (SSA) independently for the northern hemisphere (NH) and southern hemisphere (SH). However, when analyzing the relationship between the axial dipole moment time series and the SSA time series, we use the total SSA.

## 6.3 Results and Discussions

### 6.3.1 Analysis of Time Lags Between Different Time Series

To determine the time lags between any two time series, we use cross-correlation analysis, a statistical method that quantifies the similarity between two time series as a function of time lag, using the entire signal duration. Let $x(t)$ and $y(t)$ be two discrete time series of length $N$, sampled at uniform intervals. The cross-correlation coefficient $r(\tau)$ where the latter signal is lagged by, $\tau$ is defined as:

$$r(\tau) = \frac{\sum_{j=1}^{N} (x(t_j) - \bar{x}) \times (y(t_j + \tau) - \bar{y})}{\sqrt{\sum_{j=1}^{N} (x(t_j) - \bar{x})^2 \times \sum_{j=1}^{N} (y(t_j + \tau) - \bar{y})^2}}, \tag{6.1}$$

Here $\bar{x}$ and $\bar{y}$ are the mean values of the $x(t)$ and $y(t)$ time series, respectively. The cross-correlation coefficient $r(\tau)$ ranges between $-1$ and $+1$.

In Figure 6.3, we present the cross-correlation analysis between the NH polar flux and NH SSA (red curve), the SH polar flux and SH SSA (blue curve), and the global dipole moment and total SSA (black curve). All polar components are obtained from the SFT simulation described in section 6.2. We find that the NH and SH polar fluxes lead their respective hemisphere's SSA by approximately 4.1 and 3.7 years, respectively, while the dipole moment leads the total SSA by about 4.8 years – indicating that the dipole moment tends to peak a few months earlier than the polar flux. These lead values are determined based on the location of maximum $r(\tau)$, and the corresponding coefficients indicate a strong and statistically significant correlation (99.9% confidence level), with a peak value of 0.76 for the dipole moment and SSA, and 0.65–0.68 for the polar flux and SSA. A similar analysis using observational datasets, as detailed in section 6.2, is shown in Figure 6.3 (right panel). Observational results agree well with the simulation, except for the dipole moment series – likely due to limitations in the statistical robustness of the available observational dataset.

In the next step, we apply wavelet coherence analysis, which extends traditional correlation techniques by capturing localized relationships between two time series in both time and frequency domains. For this, we employ the MATLAB wavelet-coherence package based on the algorithm developed by Grinsted et al. (2004). The second panels of Figure 6.3(a-c) reveal a statistically significant coherence concentrated around the 11-year period band throughout the full duration of the time series. Within this band, the phase arrows predominantly point leftward and upward, indicating a near anti-phase relationship and that the polar flux and dipole moment series lead the SSA time series. This phase behavior suggests a precursor relationship between polar field proxies and SSA. To quantify this, we extract the phase angles and compute corresponding time lags at the 11-year period. As shown in the third and fourth panels of Figure 6.3(a–c), the results indicate

that the NH polar flux leads NH SSA by 4.3 years with a phase of 133°, the SH polar flux leads SH SSA by 4.4 years with a phase of 137°, and the global dipole moment leads total SSA by 5.4 years with a phase of 166°, on average. Based on these results, we find that the dipole moment of a cycle reaches its peak approximately 1 year earlier than the polar flux. This temporal lead makes the dipole moment a potentially earlier and more effective precursor for forecasting the amplitude of the upcoming sunspot cycle.

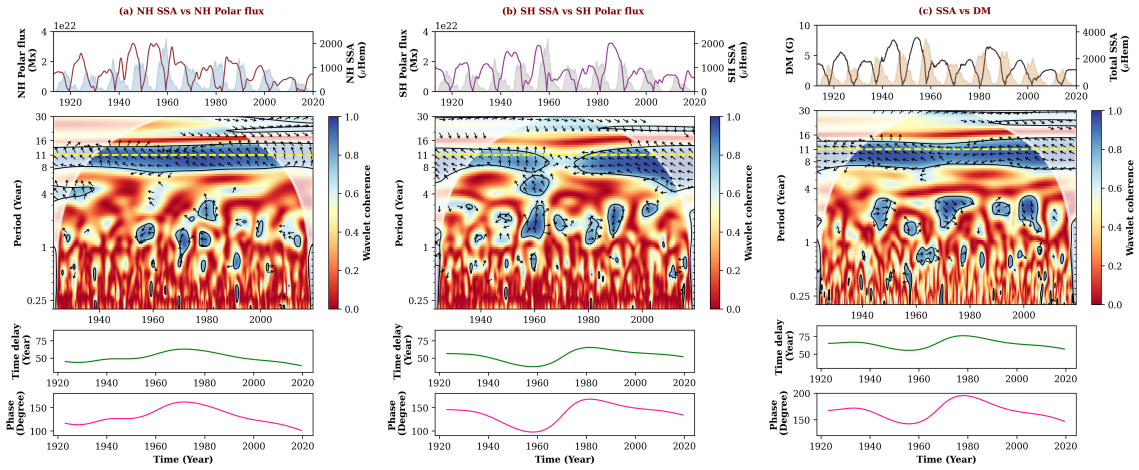


Figure 6.3: Wavelet coherence analysis between the sunspot area (SSA) and the Northern Hemisphere polar flux (panel a), Southern Hemisphere polar flux (panel b), and axial dipole moment (panel c). The first row shows the simulated and observed time series, identical to those in Figure 6.1. The second row presents the wavelet coherence between each pair of series, where color indicates the coherence strength (see color bar), arrows represent the phase relationship, and the white-shaded region marks the cone of influence. Black contours enclose regions of statistically significant coherence ($p < 0.01$). The yellow dashed line denotes the 11-year periodicity. The third and fourth rows show the temporal evolution of the time lag and phase relationship, respectively.

### 6.3.2 The Polar precursor methods for Solar Cycle Prediction

**Over the years, several precursor techniques have been proposed and successfully applied to predict the amplitude and timing of future solar cycles. Among the most widely accepted is the correlation between the polar field strength at the end of a cycle and the amplitude of the following cycle, first introduced by Schatten et al. (1978). Subsequent studies, such as Kumar et al. (2021), have further demonstrated that the rate of polar field/dipole moment growth during the declining phase of a cycle is also linked to the amplitude of the next one. More recently, Jaswal et al. (2024) identified a predictive relationship connecting the decay rate of the dipole moment in cycle**

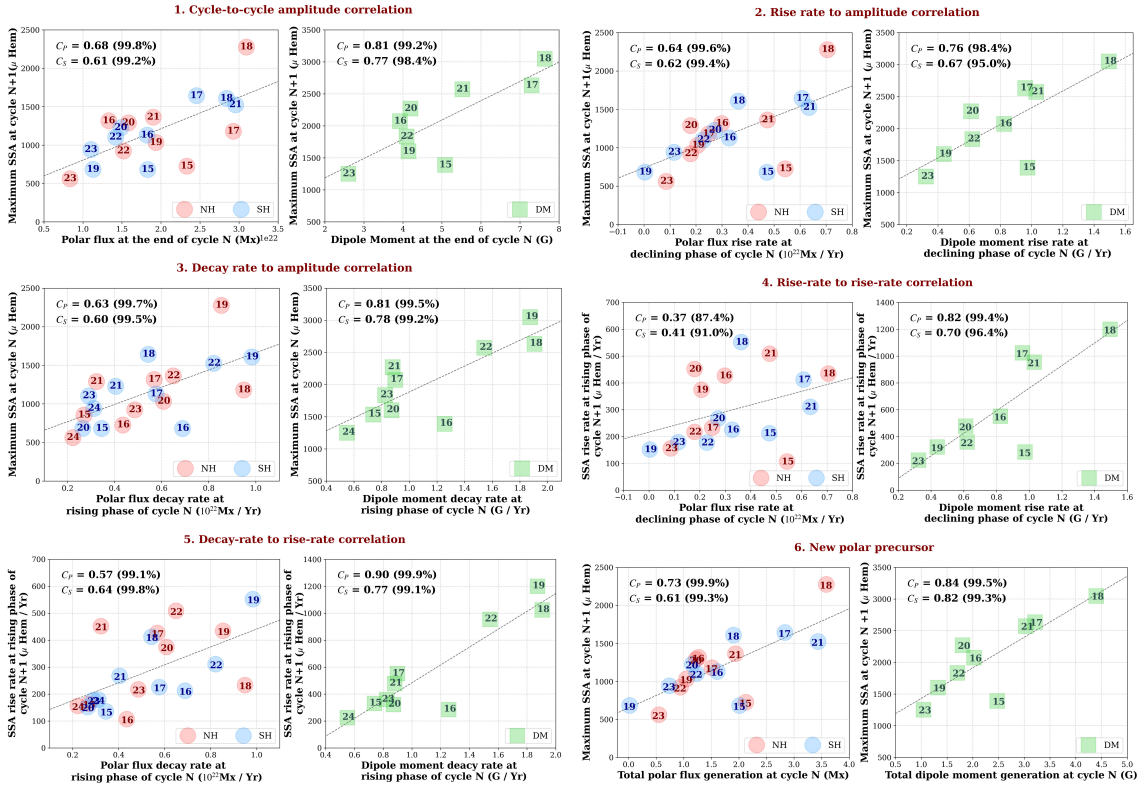


Figure 6.4: Pearson and Spearman correlation coefficients between different polar precursors (hemispheric polar flux and axial dipole moment) and the corresponding sunspot area (SSA) time series. Each panel represents a specific precursor relationship described in subsection 6.3.2 (see text for details).

**N with the rise rate of sunspot activity in cycle N+1. In this section, we independently examine and validate these well-established relationships between the polar field proxies derived from our SFT model output and the SSA time series through a comprehensive statistical correlation analysis.**

First, we assess the predictive relationship between various polar precursors – namely, the NH polar flux, SH polar flux, and the axial dipole moment – and the amplitude of the subsequent solar cycle. The first three sets of correlations (1, 2, and 3) are performed for the following variables listed below. Second, we examine whether polar precursors can predict not just the amplitude but also the timing (rise rate) of solar activity. Two additional correlation analyses are conducted for this (4 and 5):

1. **Cycle-to-cycle amplitude correlation:** Between the amplitude of each polar precursor (NH polar flux, SH polar flux and axial DM) at the end of cycle N-1 and the peak SSA (NH, SH, and total) of the subsequent cycle N.

2. **Rise rate to amplitude correlation:** Between the rise rate of each polar precursor during the declining phase of cycle N-1 and the peak SSA of cycle N.

3. **Decay rate correlation:** Between the decay rate of each polar precursor during the rising phase of cycle N and the peak SSA of the same cycle.

4. **Rise-rate to rise-rate correlation:** Between the rise rate of each polar precursor during the declining phase of cycle N-1 and the rise rate of SSA in cycle N.

5. **Decay-rate to rise-rate correlation:** Between the decay rate of each polar precursor during the rising phase of cycle N and the rise rate of SSA in the same cycle.

We find that all correlation coefficients range between 0.6 and 0.8, with statistical significance within confidence level, with the exception of the correlation between the polar flux decay rate during the rising phase of cycle n and the SSA amplitude of that same cycle. These results are summarized in Figure 6.4 and Table 6.3.2.

### 6.3.3 An Alternative Polar precursor for Solar Cycle Prediction

Until now, our analysis shows that the amplitude of the polar flux or dipole moment at the end of a solar cycle serves as a robust predictor for the strength of the following cycle (see Table 6.3.2). However, such cycle-to-cycle amplitude correlation can only be utilized after the cycle minimum, limiting its utility for early prediction. To overcome this, we introduce an alternative polar precursor that enables earlier estimation of the upcoming cycle strength—well before the minimum, based on the polar component amplitude. Specifically, we define a proxy based on the product of the rise rate of the polar flux or dipole moment and the total cycle length, which serves as an approximation of the net polar field or dipole moment generated during a solar cycle under the assumption of linear growth. This approach allows us to quantify the cumulative polar field buildup over the cycle phase and test its correlation with the next cycle's strength. We find that this proxy correlates strongly with the peak SSA of the subsequent cycle, as demonstrated in Figure 6.4 and summarized in Table 6.3.2, suggesting its potential as an early polar precursor for solar cycle forecasting.

All together, we find that the dipole moment yields stronger and more statistically

| x | y | Correlation coefficient (Simulation) | Correlation coefficient (Observation) |
|---|---|---|---|
| **1. Cycle-to-cycle amplitude correlation:** | | | |
| DM at the end of cycle N | Maximum SSA at cycle N+1 | $C_P$ = 0.83 (99.7%) $C_S$ = 0.77 (99.1%) | $C_P$ = 0.98 (98.1%) $C_S$ = 0.99 (99.9%) |
| PF at the end of cycle N | Maximum SSA at cycle N+1 | $C_P$ = 0.69 (99.9%) $C_S$ = 0.61 (99.5%) | $C_P$ = 0.64 (99.7%) $C_S$ = 0.63 (99.7%) |
| **2. Rise rate to amplitude correlation:** | | | |
| DM rise rate at DP of cycle N | Maximum SSA at cycle N+1 | $C_P$ = 0.76 (98.4%) $C_S$ = 0.67 (95.0%) | $C_P$ = 0.90 (90.0%) $C_S$ = 0.79 (80.0%) |
| PF rise rate at DP of cycle N | Maximum SSA at cycle N+1 | $C_P$ = 0.64 (99.6%) $C_S$ = 0.62 (99.4%) | $C_P$ = 0.84 (99.9%) $C_S$ = 0.73 (99.9%) |
| **3. Decay rate to amplitude correlation:** | | | |
| DM decay rate at RP of cycle N | Maximum SSA at cycle N | $C_P$ = 0.81 (99.5%) $C_S$ = 0.78 (99.2%) | $C_P$ = 0.91 (91.9%) $C_S$ = 0.79 (80.0%) |
| PF decay rate at RP of cycle N | Maximum SSA at cycle N | $C_P$ = 0.63 (99.7%) $C_S$ = 0.60 (99.5%) | $C_P$ = 0.64 (99.7%) $C_S$ = 0.63 (99.7%) |
| **4. Rise-rate to rise-rate correlation:** | | | |
| DM rise rate at DP of cycle N | SSA rise rate at RP of cycle N+1 | $C_P$ = 0.82 (99.4%) $C_S$ = 0.70 (96.4%) | $C_P$ = 0.98 (90.6%) $C_S$ = 0.99 (99.9%) |
| PF rise rate at DP of cycle N | SSA rise rate at RP of cycle N+1 | $C_P$ = 0.37 (87.4%) $C_S$ = 0.41 (91.0%) | $C_P$ = 0.49 ( 96.1%) $C_S$ = 0.52 (97.3%) |
| **5. Decay-rate to rise-rate correlation:** | | | |
| DM decay rate at RP of cycle N | SSA rise rate at RP of cycle N | $C_P$ = 0.90 (99.9%) $C_S$ = 0.77 (99.1%) | $C_P$ = 0.79 (79.1%) $C_S$ = 0.79 (80.0%) |
| PF decay rate at RP of cycle N | SSA rise rate at RP of cycle N | $C_P$ = 0.57 (99.1%) $C_S$ = 0.64 (99.8%) | $C_P$ = 0.45 (95.3%) $C_S$ = 0.58 (99.3%) |
| **6. An alternative Polar Precursor:** | | | |
| Total DM generation at cycle N | Maximum SSA at cycle N+1 | $C_P$ = 0.84 (99.5%) $C_S$ = 0.82 (99.3%) | $C_P$ = 0.93 (93.6%) $C_S$ = 0.79 (80.0%) |
| Total PF generation at cycle N | Maximum SSA at cycle N+1 | $C_P$ = 0.73 (99.9%) $C_S$ = 0.61 (99.3%) | $C_P$ = 0.75 (99.9%) $C_S$ = 0.83 (99.9%) |

Table 6.1: Correlation of different polar precursors with Sunspot area (SSA) time series. RP and DP denote rising phase and declining phase, respectively.

significant correlations compared to the polar flux across all correlation analyses (1–6) discussed in subsection 6.3.2, subsection 6.3.3, and as summarized in Table 6.3.2.

### 6.3.4 Understanding the Physical Connection Between Polar Precursors and Solar Cycle Evolution

The reason behind the strong correlations found between polar precursors (like NH/SH polar flux and axial dipole moment) and next-cycle SSA amplitude and rise rate is grounded in solar dynamo theory and surface flux transport physics. The Babcock–Leighton mechanism describes how the Sun regenerates its poloidal magnetic field from the decay of sunspots, thereby sustaining the solar magnetic cycle. Deep within the convection zone, the Sun's differential rotation stretches the existing poloidal field lines into a strong toroidal field. When this toroidal field becomes sufficiently intense, it rises buoyantly to the solar surface, forming bipolar sunspot pairs. These pairs exhibit a systematic tilt with respect to the equator due to the Coriolis force, known as Joy's law, where the leading sunspot (in the direction of rotation) lies closer to the equator than the trailing one. Now the surface transport processes – primarily meridional flow and supergranular diffusion – carry the trailing polarity flux toward the poles, where it cancels the existing polar field. Meanwhile, leading-polarity flux tends to cancel across the equator with opposite-polarity flux from the other hemisphere due to differential rotation and diffusion. The net effect is the accumulation of trailing-polarity flux at the poles, which eventually cancels the pre-existing polar field and regenerates the Sun's new polar field. This newly formed poloidal field then sinks beneath the surface, where it is sheared again by differential rotation to produce a new toroidal field, completing the cycle and setting the stage for the next sunspot emergence.

The intensity of cancellation and accumulation of opposite-polarity flux at the poles determines the polar field strength at minimum. A stronger, well-formed polar field at cycle N minimum reflects efficient transport of flux to the convection zone, which in turn sets the stage for strong toroidal field generation (via differential rotation) in the next cycle N+1.

Similarly, the polar field rise-rate during the declining phase of cycle N indicates how quickly the following-polarity flux transports towards the pole, i.e., how rapidly polar field

reversal and build-up happen. A fast, coherent build-up of polar field or dipole moment implies an intense poloidal field/ dipole moment at the end, which translates into a stronger subsequent cycle N+1. These causal relationship supports the well-known Waldmeier effect, where the rise rate of the sunspot cycle correlates with the same sunspot cycle amplitude as suggested by Kumar et al. (2022). Additionally, a rapid build-up of the polar field or dipole moment during solar cycle N indicates a faster growth of the subsequent solar cycle N + 1, suggesting its potential as a predictor of the sunspot peak timing.

Decay rate during rising phase of cycle N reflects how rapidly the polar field is being eroded by incoming new cycle active regions. This may also signal how strong and quickly the new cycle ramps up, though this process is more complex due to ongoing flux emergence and active region overlap between cycles. A faster decay of the polar flux/ dipole moment implies stronger or more frequent emergence of sunspots, thus a stronger cycle peak, another version of the Waldmeier effect as suggested by Jaswal et al. (2024). Furthermore, a faster decay of the polar field or dipole moment during solar cycle N is found to be associated with a more rapid rise of the same solar cycle N, implying its potential utility in predicting the timing of the sunspot maximum.

In the Babcock-Leighton dynamo context, the polar flux takes longer to build up because the magnetic flux must physically reach the poles from low to mid latitudes, which takes approximately 3-5 years. However, the dipole moment is observed to decay more rapidly and undergo polarity reversal nearly a year before the polar flux, reinforcing its utility in early solar cycle prediction, both the timing and strength of the upcoming solar cycle peak.

## 6.4 Conclusions

In this work, we have addressed the long-standing question of which polar magnetic field precursor – the hemispheric polar flux or the global axial dipole moment – serves as a more reliable indicator of future solar cycle strength. By employing a century-scale reconstruction of the Sun's surface magnetic field using a data-driven, optimized surface flux transport model, we systematically analyze both quantities and their relationship with the subsequent cycle's sunspot activity.

Our findings show that the axial dipole moment exhibits consistently stronger and

more statistically significant correlations with the amplitude and rise rate of the subsequent sunspot cycle compared to the hemispheric polar flux. The dipole moment not only peaks earlier than the polar flux by nearly a year but also reflects a more global measure of the Sun's poloidal field, encompassing both high- and low-latitude magnetic flux contributions. This makes it a physically superior and temporally earlier precursor for solar cycle forecasting.

We further introduce an alternative early-cycle precursor, defined as the product of the polar field (or dipole moment) rise rate and cycle length, which correlates well with the amplitude of the next cycle, providing a promising pathway for earlier solar cycle prediction – well before solar minimum using the dipole moment contribution. Additionally, we identify that a faster buildup of the polar field or dipole moment during a cycle correlates with a faster rise and larger amplitude of the subsequent cycle, implying potential for predicting not only the strength but also the timing of solar maxima. In predicting the timing of the sunspot peak, the axial dipole moment also serves as a better indicator than the hemispheric polar flux.

Taken together, these results provide compelling observational and theoretical evidence supporting the axial dipole moment as the primary magnetic precursor of the solar cycle within the Babcock–Leighton dynamo framework. This study strengthens the physical foundation for solar activity forecasts and contributes toward the development of reliable, physics-based space weather prediction tools.

# Chapter 7

# Polar Filaments as a Solar Cycle Precursor: A Babcock–Leighton Dynamo Model Perspective

*"The Sun's polar magnetic fields at cycle minima are among the most reliable indicators of future solar activity. However, direct measurements of these high-latitude fields remain challenging from near-Earth vantage points. In addition to the polar field itself, high-latitude structures such as polar filaments – which form along polarity inversion lines – may serve as valuable indirect probes of the evolving polar field. In this study, we investigate this possibility using data-driven surface flux transport simulations in conjunction with long-term filament observations from the Meudon Observatory (data reduction is done by Srinjana Routh and Subhamoy Chatterjee; see Routh et al. 2025). Our analysis establishes a physical link between filament formation and the Babcock–Leighton mechanism responsible for the Sun's polar field reversal. We find that the residual polar filament area at the end of a solar cycle correlates strongly with the polar flux build-up, identifying it as a promising early precursor for solar cycle forecasting. These results suggest that polar filaments captures the magnetic coupling between consecutive cycles, thereby providing clues to the origin of future solar activity.* [1] *"*

[1] This chapter is based on a collaborative research work recently accepted for publication in The Astrophysical Journal Letters (Routh et al., 2025). The content presented here focuses solely on the research work that forms an integral part of this thesis — specifically, the data-driven Surface Flux Transport (SFT) simulations and the subsequent correlation analyses conducted to examine whether polar filaments can serve as reliable proxies for the buildup of polar magnetic flux.

## 7.1 Introduction

Solar filaments are elongated, thread-like structures of cool, dense plasma suspended in the Sun's magnetized corona (McIntosh, 1972). They appear as dark, ribbon-like features in H$\alpha$ observations because their temperature is much lower than that of the surrounding corona. Filaments form along polarity inversion lines (PILs) – regions where the magnetic polarity of the photosphere changes sign – and their shape and stability are governed by the underlying magnetic field configuration (Martin, 1998). Based on their location and magnetic environment, filaments are classified into three main types: active region filaments, which appear within magnetically complex sunspot regions; quiescent filaments, which form in quiet Sun areas and are typically long-lived; and polar filaments, which emerge at high latitudes near the edges of global magnetic flux systems (Tlatov et al., 2016; Xu et al., 2021).

Among these, polar filaments are of particular importance because their formation and migration are closely linked to the large-scale solar magnetic field evolution. The poleward movement of polar filaments – known as the rush-to-the-pole – coincides with the reversal of the Sun's polar magnetic fields, marking a critical phase of the solar cycle as suggested by Cliver (2014); Mazumder et al. (2021).

In this work, our particular interest lies in studying polar filaments, which emerge at high latitudes near the boundary of decaying and newly transported magnetic flux. These filaments often appear during the rising phase of the solar cycle and vanish following polar field reversal, making them valuable indicators of the large-scale surface magnetic field evolution. Their formation depends on magnetic flux cancellation and is closely tied to the global dipole field, coronal structure, and solar dynamo processes (Mackay et al., 2010; Jaswal et al., 2024). In this study, we combine observational data of polar filaments with surface flux transport (SFT) simulations to show that polar filaments effectively trace the polar field reversal process governed by the Babcock–Leighton mechanism. We also reveal a strong correlation between polar filament patterns with the ultimate polar field/dipole moment build-up, offering a promising predictive tool for solar activity forecasting. For other details, please refer to Routh et al. (2025).

## 7.2 Methods

### 7.2.1 Observational Data

In this study, we use the area and length of polar filaments detected from the Meudon Synoptic Maps. Our analysis is restricted to Solar Cycles 16 through 21, as Meudon data is not available beyond this period, and incorporating other data sources may introduce calibration inconsistencies. We consider those polar filaments which are located at $|\theta| \geq 50^{\circ}$ latitudes. To study the corresponding hemispheric sunspot activity, we use the daily cross-calibrated sunspot area dataset from 1874 onward, compiled by Mandal et al. (2020). For observational polar magnetic field data, we utilize the Mount Wilson Observatory (MWO) polar faculae time series from Muñoz-Jaramillo et al. (2012). For further details on the filament tracking methodology and the calculation of their geometric properties, which was performed by Srinjana Routh and Subhamoy Chatterjee, we refer the reader to Routh et al. (2025).

### 7.2.2 Reconstruction of Solar Surface Magnetic Fields for Sunspot Cycles 16–21

We employ an observationally constrained, data-driven Surface Flux Transport (SFT) model, SPhoTraM (Pal and Nandy, 2025), to reconstruct the evolution of the solar surface magnetic field over sunspot cycles 16–21. The model is driven by observed properties of sunspot emergences – including latitude, longitude, area, and timing – sourced from the Royal Greenwich Observatory (RGO) database (RGO/USAF/NOAA Data Centre, 2023). The statistical distributions of sunspot tilt angles and magnetic polarity orientations are incorporated through a Monte Carlo ensemble approach, from which the optimal realization is selected by maximizing consistency with available observational constraints. From the simulated photospheric magnetic field maps generated by SPhoTraM, we calculate the hemispheric polar flux using the mathematical formulations described below.

$$\Phi_{N/S}(t) = \int_{\phi=0}^{2\pi} \int_{\lambda_{N/S}} R_{\odot}^{2}\, B_r(\lambda_{N/S}, \phi, t)\, \cos\lambda_{N/S}\, d\lambda_{N/S}\, d\phi \tag{7.1}$$

Here, $\lambda$ and $\phi$ denote the heliographic latitude and longitude, respectively, and $R_\odot$ is the solar radius. $B_r$ is the radial magnetic field generated from the simulation. $\Phi_{N/S}(t)$ represents the polar flux in the northern and southern hemispheres, respectively. The polar flux is calculated using the surface magnetic field confined to the polar caps (within $\pm 70^\circ$ to $\pm 90^\circ$ latitude).

The simulated polar flux time series are shown in the first panel of Figure 7.1. The SFT outputs are optimized by calibrating the resulting polar flux against observed polar faculae counts (see Pal and Nandy (2025) for methodological details and results). Importantly, this data-driven simulation framework enables the reconstruction of butterfly diagrams during periods lacking direct observations – illustrated in the second panel of the same figure Figure 7.1 – thereby offering a window into the historical evolution of solar magnetism.

## 7.3 Results: Polar Filaments as Diagnostics of the Babcock-Leighton Mechanism and Precursor of Solar Cycle Strength

The Babcock–Leighton (BL) mechanism forms the cornerstone of our understanding of how the Sun regenerates its magnetic field from one solar cycle to the next. In this framework, the large-scale poloidal magnetic field arises from the decay and dispersal of tilted bipolar sunspot regions that emerge from the toroidal magnetic field generated deep within the solar interior. Once these sunspots appear on the surface, convective flows, differential rotation, and meridional circulation act to redistribute their magnetic flux. The magnetic flux of the leading polarity tends to cancel across the equator, while the following polarity flux is carried poleward by meridional circulation. Over time, this accumulation and interaction of flux near the poles reverses the existing polar fields and builds up new ones of opposite polarity. Through this gradual but cyclic process of emergence, decay, transport, and reversal, the Sun's magnetic field regenerates — capturing the essence of the Babcock–Leighton dynamo mechanism that links the surface manifestations of solar activity to the deeper magnetic engine driving the solar cycle (Babcock, 1961; Leighton, 1969; Cameron and Schüssler, 2015; Bhowmik and Nandy, 2018; Charbonneau, 2020; Pal et al., 2023; Pal and Nandy, 2024a).

7.3. Results: Polar Filaments as Diagnostics of the Babcock-Leighton Mechanism and Precursor of Solar Cycle Strength

The large-scale redistribution of magnetic flux across the solar surface, governed by plasma motions such as differential rotation, meridional flow, and turbulent diffusion, can be effectively captured through Surface Flux Transport (SFT) modeling (Jiang et al., 2014; Bhowmik and Nandy, 2018; Pal et al., 2023; Yeates et al., 2023; Pal and Nandy, 2024a, 2025). In this study, we utilize the data-driven SFT model SPhoTraM to simulate the evolution of the surface magnetic field and polar flux. The simulated spatio-temporal magnetic field maps allow us to investigate how variations in polar filament area correspond to changes in the large-scale magnetic field configuration – thereby assessing whether these filaments can serve as surface tracers of the Sun's global magnetic evolution.

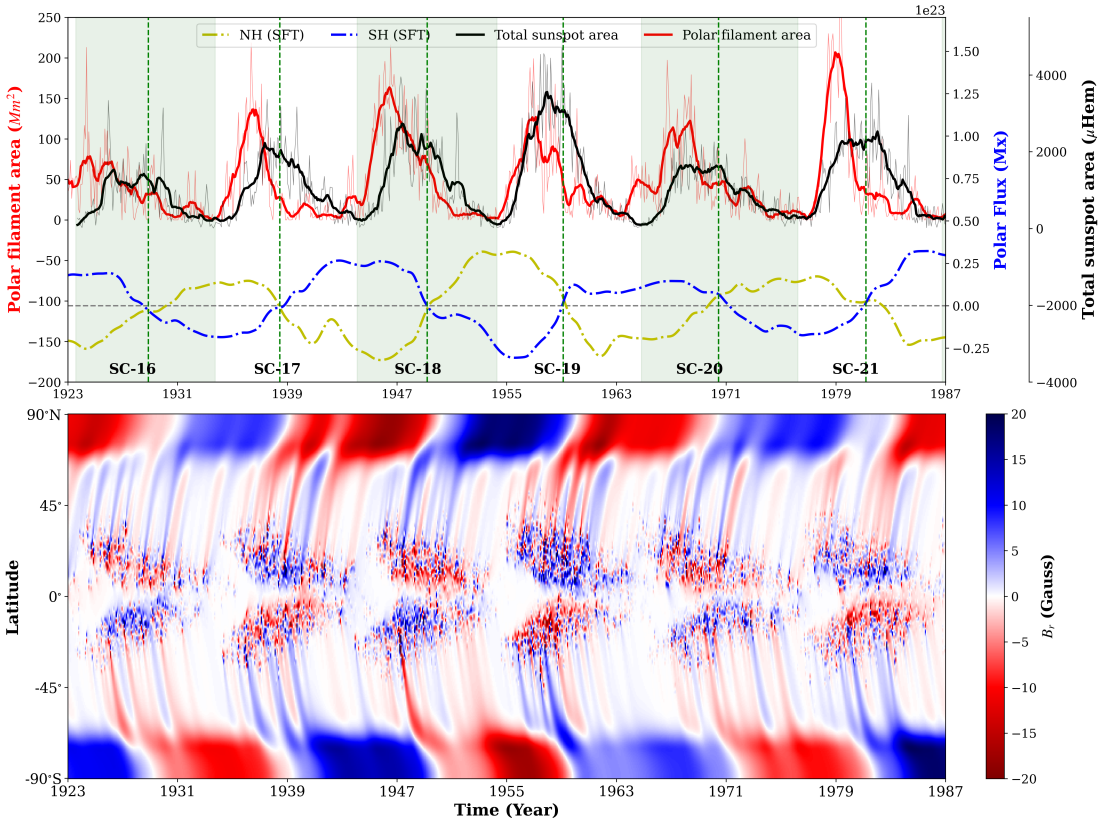


Figure 7.1: Top panel: The red curve shows the total polar filament area over solar cycles 16–21, and the black curve represents the corresponding sunspot area (Mandal et al., 2020). Light red and black lines denote Carrington-rotation and monthly averages, while darker lines indicate 13-month running means. The yellow and blue dotted-dashed curve shows the northern and southern polar flux from the data-driven optimized SFT model. Green dashed lines mark polar field reversals. Bottom panel: Spatio-temporal evolution of the radial magnetic field ($B_r$) from solar cycles 16–21, generated using the data-driven optimized SFT model (Pal and Nandy, 2025). Blue and red indicate positive and negative polarities, respectively. (This figure is adapted from Routh et al. (2025). Observational data reduction is performed by Srinjana Routh and Subhamoy Chatterjee and the simulations are by Shaonwita Pal)

The evolution of polar filaments follows a rhythm deeply tied to the solar magnetic cycle, as illustrated in Figure 7.1. As shown in the upper panel of Figure 7.1, the total polar filament area typically reaches its peak before the sunspot number maximum – well ahead of the global magnetic field reversal. This timing reveals that filament formation is most vigorous during the early and mid-rising phases of a solar cycle, when the magnetic flux emerging from new active regions begins to interact with the remnants of the previous cycle's field. These encounters between opposite polarities lead to magnetic cancellation near the poles, gradually setting the stage for the Sun's magnetic polarity reversal. Once the reversal has taken place, the freshly formed polar fields grow stronger through the declining phase, and the polar environment becomes more magnetically stable. The continuous poleward transport of flux now reinforces the existing field rather than disturbing it, leading to a marked reduction in filament formation. Consequently, the total filament area diminishes rapidly after solar maximum. Occasionally, isolated filaments still appear late in the cycle – these are often linked to the emergence of anomalous or anti-Hale active regions, whose opposite polarity orientation briefly disrupts the otherwise stable magnetic configuration (Pal et al., 2023). Thus, the waxing and waning of polar filaments encapsulate the magnetic conversation between successive solar cycles, acting as subtle messengers of the Sun's evolving magnetism.

The lower panel depicts the time–latitude map of the longitudinally averaged radial magnetic field ($B_r$) derived from our optimized Surface Flux Transport (SFT) simulations for solar cycles 16–21 (Pal and Nandy, 2025). The simulation captures the gradual poleward transport of magnetic flux that originates from the decay of bipolar active regions. As the following-polarity flux from mid-latitudes drifts toward the poles, it encounters and cancels the pre-existing polar magnetic field of opposite polarity. This flux cancellation process, central to the Babcock–Leighton (BL) dynamo mechanism, ultimately leads to the reversal and regeneration of the Sun's polar fields. If polar filaments form along polarity inversion lines (PILs) where these opposing flux systems interact, their emergence and evolution should naturally trace the timing and spatial structure of the global magnetic field reversal. Our analysis demonstrates that the observed patterns of polar filament formation indeed mirror this magnetic evolution, highlighting their potential as diagnostic markers of the Sun's surface magnetic dynamics.

We next explore whether polar filaments can serve as early indicators of the Sun's polar field build-up at the end of a sunspot cycle – and thereby act as potential precursors of the strength of the upcoming solar cycle. Because these filaments form through the interaction of opposite magnetic polarities migrating toward the poles, their evolution naturally reflects the dynamics of flux transport on the solar surface. Consequently, the statistical properties of polar filaments may encode key signatures of the large-scale magnetic processes that regulate the solar dynamo and drive the cyclic regeneration of the Sun's magnetic field.

To examine this possibility, we first quantify the physical characteristics of the polar filaments – specifically their average area, $\langle A \rangle$, and average length, $\langle L \rangle$—for each solar cycle. These averages are obtained by integrating the total filament area and length over a given cycle and dividing by the cycle's duration. The differences between consecutive cycles, expressed as

$$\Delta\langle A_N \rangle = \langle A_N \rangle - \langle A_{N-1} \rangle, \quad \Delta\langle L_N \rangle = \langle L_N \rangle - \langle L_{N-1} \rangle, \tag{7.2}$$

represent how the filament characteristics evolve from one cycle to the next and are referred to as the *remnant filament parameters*.

We then compare these remnant filament quantities with the polar magnetic flux amplitude at the end of each solar cycle, using both observed polar faculae data (Muñoz-Jaramillo et al., 2012) and simulated results from the SPhoTraM model (Pal and Nandy, 2025). A clear and statistically significant positive correlation emerges between the change in average filament area, $\Delta\langle A_N \rangle$, and the amplitude of the polar flux, as shown in the first column of Figure 7.2. A similar but slightly weaker trend is observed for the filament length difference, $\Delta\langle L_N \rangle$, as seen in the second column of Figure 7.2.

This result suggests that cycles with larger polar filament coverage tend to culminate in stronger polar fields. Physically, this can be understood by recognizing that polar filaments form along polarity inversion lines where opposite magnetic fluxes meet and cancel. When greater flux is transported poleward during a cycle, more extensive and complex filament structures appear at high latitudes, reflecting stronger magnetic activity and higher residual flux. As the cycle progresses toward its end, this accumulated flux contributes to rebuilding the polar magnetic field, setting the stage for the next cycle's amplitude.

Thus, polar filaments not only trace the magnetic evolution of the solar poles but may

also serve as valuable proxies for the Sun's magnetic memory. Their behavior encodes signatures of flux transport and accumulation that underpin the Babcock–Leighton mechanism – offering a new observational perspective to anticipate the strength of future solar cycles.

## 7.4 Concluding Remarks

In this study, we have demonstrated that polar filaments – dark, elongated structures observed at high solar latitudes – serve as effective surface tracers of the evolution and reversal of the Sun's polar magnetic fields. Through a combination of observational data from Meudon Synoptic Maps and data-driven Surface Flux Transport (SFT) simulations, we have shown that the emergence and evolution of polar filaments are intimately linked to the Babcock–Leighton mechanism of poloidal field generation.

Our analysis reveals that polar filament formation peaks during the rising phase of each solar cycle and declines after the polar field reversal near solar maximum. This behavior reflects the underlying process of poleward flux transport and interaction between decaying old-cycle flux and newly emerged trailing polarity flux. We also find that anomalous active regions, particularly anti-Hale BMRs, can generate high-latitude opposite-polarity surges during the declining phase, contributing to the presence of polar filaments beyond the expected window.

A key result of this study is the discovery of a statistically significant correlation between the remnant polar filament area and the polar flux amplitude at the end of a solar cycle. This suggests that polar filaments can serve not only as indicators of polar field evolution but also as potential *precursors of the next solar cycle's strength*, given the established role of the polar field as a solar cycle predictor. Constraining the Sun's polar magnetic landscape remains an outstanding challenge, deemed the last great frontier of the Sun (Nandy et al., 2023). In this context, our findings provide an observational pathway for diagnostics of the high latitude polar field dynamics, and utilizing this to predict the following sunspot cycle strength.

These findings open up several avenues for future research. Extending the filament database beyond Solar Cycle 21 using other observatories (e.g., Kanzelhöhe Solar Observatory, Kodaikanal Solar Observatory (KSO), Big Bear Solar Observatory (BBSO)) with

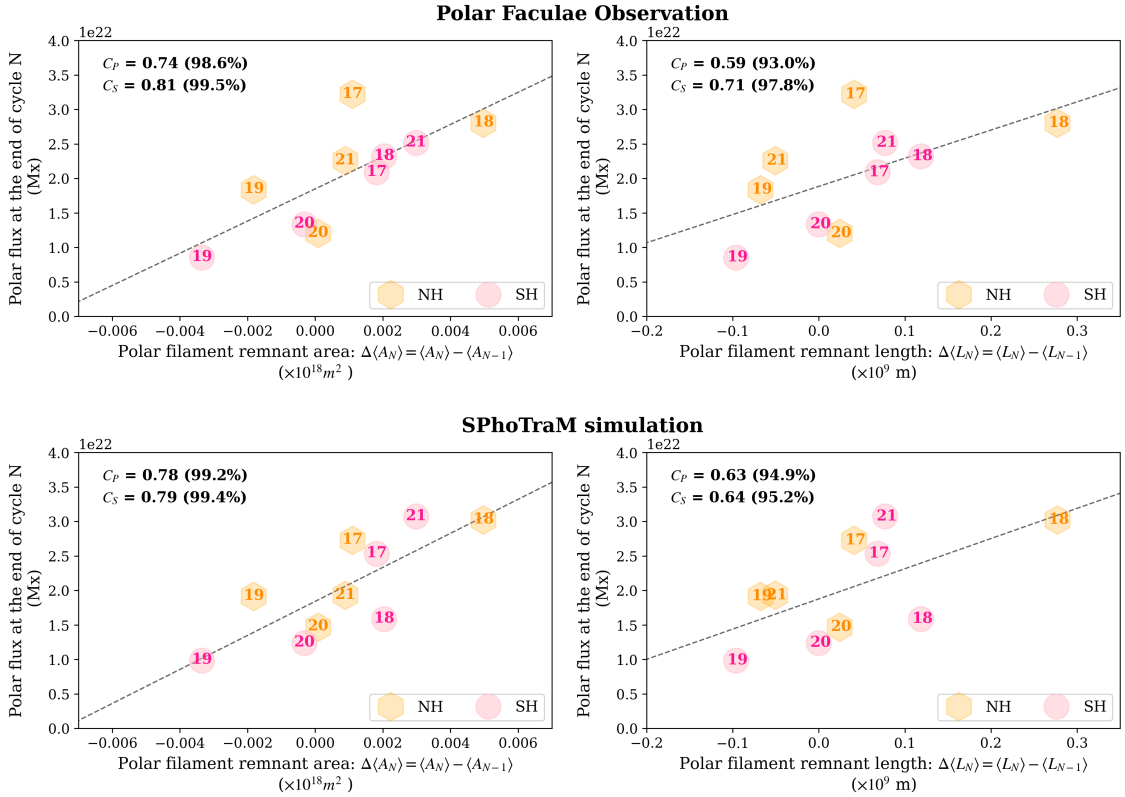


Figure 7.2: The left panel presents the correlation between the remnant average polar filament area, $\Delta\langle A_N\rangle$, and the polar flux amplitude at the end of solar cycle N. The right panel shows the corresponding correlation between the remnant filament length, $\Delta\langle L_N\rangle$, and the polar flux strength at the same epoch. Orange hexagons and Pink circles denote data points from the northern and southern hemispheres, respectively, with the cycle number N labeled inside each point. The black dashed lines indicate the best-fit linear regressions. The analysis is performed using both observed polar faculae data (top panel) and simulated results from the SPhoTraM (SFT) model (bottom panel). (This figure is adapted from Routh et al. (2025). Observational data reduction is performed by Srinjana Routh and Subhamoy Chatterjee and the simulations are by Shaonwita Pal)

proper calibration could further strengthen the statistical basis of this correlation. Additionally, the application of automated filament detection techniques, such as deep learning and temporal tracking algorithms, can enhance consistency across datasets. On the modeling front, Surface Flux Transport (SFT) simulations can be used to identify polarity inversion lines (PILs) on the simulated solar surface and to quantify their total length and area. Since filaments form along these PILs, such modeling offers a powerful way to infer the distribution and evolution of solar filaments, even for historical solar cycles where direct observations are unavailable. By comparing the simulated PIL characteristics with observed filament properties in more recent cycles, we can gain valuable insights into the long-term behavior of solar filaments and their link to the Sun's global magnetic evolution.

Finally, given their visibility in H$\alpha$ and strong coupling to surface magnetic field evolution, polar filaments offer a promising, independent, and observationally accessible proxy for understanding and forecasting solar magnetic cycles. As we approach Solar Cycle 26, continued monitoring and modeling of polar filaments may provide valuable insight into the build-up of magnetic memory in the solar dynamo and its role in modulating future solar activity. Thus, the filament-based metrics provide a physically motivated, observable quantity that complements traditional proxies like polar faculae and axial dipole moments.

# Chapter 8

# The Sun's Large-Scale Corona has a Dynamical Memory of Magnetism: Insights from Predicting the 08 April 2024 Total Solar Eclipse

*"Stellar coronal magnetic fields heat the outer atmosphere of stars to a million degrees, drives stellar winds and spawns dynamic events such as flares and coronal mass ejections. Cumulatively, these phenomena associated with coronal magnetism govern (exo)planetary space environments. Yet, observing and constraining the magnetic structure of stellar coronae have proved to be remarkably difficult, even for our nearest star – the Sun. Models of coronal magnetism fills this important gap by providing a physical basis for understanding and predicting solar and stellar coronae. Total solar eclipses are a rare opportunity to test such theoretical models. Utilizing a coupled solar surface flux transport model and a magnetohydrodynamic coronal field model, we reproduce the observed coronal structure of the 08 April 2024 total solar eclipse – which occurred near the maximum of sunspot cycle 25 – when coronal structuring is at its most complex. Surprisingly, we uncover that the Sun's large-scale corona has a magnetic memory persisting up to solar rotational timescale (i.e., a month) even during this active phase of the Sun. This memory emerges from the slow evolution of the photospheric magnetic field and may provide the physical basis for longer-term forecasts of the Sun's large-scale coronal structure, solar wind and heliospheric open flux.*[1] *"*

[1]This chapter is based on Pal et al. (2024) which is already submitted.

## 8.1 Introduction

The solar corona, the outermost layer of the Sun's atmosphere, is a highly structured and magnetized plasma whose influence encompasses interplanetary space and extends to the end of the heliosphere where the our local plasma bubble meets the interstellar medium. Coronal magnetic fields and their dynamics heats the atmosphere of stars to a million degrees, drives energetic phenomena such as flares and coronal mass ejections and spawns supersonic stellar winds. Cumulatively, these stellar phenomena, determine (exo)planetary space environments and solar system space weather. Despite reaching temperatures of more than a million degrees, the corona of our nearest star, the Sun, is very faint in visible light due to its low density compared to the photosphere (Aschwanden et al., 2001; Walsh and Ireland, 2003; Cranmer and Winebarger, 2019). Consequently, the white-light corona is usually obscured by the intense brightness of the solar disk making observations of its structure difficult. The underlying magnetic field that governs the corona is even more challenging to observe and constraint despite their immense importance to astrophysics and solar-terrestrial physics (Yang et al., 2020, 2024).

The Sun's corona can only be observed under special circumstances, such as during rare natural events such as total solar eclipses or with the aid of artificial coronagraphs (MacQueen et al., 1974). Total solar eclipses remain uniquely valuable for studying the large-scale structure of the corona as they provide opportunities to directly observe the Sun's outer atmosphere (Blackwell and Petford, 1966; Druckmüller et al., 2006; Pasachoff, 2017; Caspi et al., 2020; Rušin et al., 2020). During a total eclipse, the Moon blocks the Sun's photosphere and reveals the faint, glowing structures of the corona. On April 8, 2024, a total solar eclipse swept across Mexico, the United States, and Canada, offering both a spectacular observational opportunity and a valuable test case for predictive models of the solar corona. Notably, this event occurred near the maximum phase of solar cycle 25 – when the Sun was very active with multiple sunspots or active regions emerging frequently on the solar surface. Eclipses during solar maximum are particularly important because they allow us to examine how dynamic processes shape the global corona under conditions of strong magnetic activity and to test predictive models of coronal magnetism when they are most difficult to predict.

Several space-based coronagraphs, such as those onboard European Space Agency's (ESA) SOHO and National Aeronautics and Space Administration (NASA) STEREO missions and the recently launched NASA PUNCH and ESA PROBA-3 missions, are providing routine observations of the outer corona. However, we note that all of these instruments lack the capability to directly capture the coronal magnetic field (Yashiro et al., 2004; Howard et al., 2011; Antonucci et al., 2020; Lamy and Gilardy, 2022). Therefore, physics-based coronal field models remain the most viable option to explore and predict coronal magnetic fields.

Many predictive models of the solar corona have been developed in recent years. Traditional approaches, such as Potential Field Source Surface (PFSS) models, provide an efficient approximation of the global coronal magnetic field configuration (Nandy et al., 2018; Dash et al., 2020). However, by assuming a current-free corona, they neglect plasma dynamics, reconnection, and non-potential magnetic stresses, which become especially important during solar maximum. Full magnetohydrodynamic (MHD) models include plasma flows, pressure gradients, and Lorentz forces and thus offer a more realistic description of the corona (Mikić et al., 1999; Lionello et al., 2009; van der Holst et al., 2010; Mikić et al., 2018; Boe et al., 2020; Hazra et al., 2021). Yet, their predictive skill depends critically on reliable photospheric boundary conditions (Riley et al., 2006; Lionello et al., 2009). Time-dependent assimilation models have advanced this field by reproducing evolving coronal structures (Downs et al., 2025).

The Sun's corona is governed by the magnetic field distribution at its lower boundary, i.e, the Sun's surface (photosphere). All models of coronal magnetism therefore utlize the photospheric magnetic field distribution as input. Global coronal structures are shaped not only by newly emerging active regions but also by the cumulative history of past magnetic activity (Nandy et al., 2018). A central challenge in modeling the corona lies in disentangling how much of its large-scale morphology is controlled by short-term flux emergence versus the persistent influence of long-term magnetic evolution. We refer to this persistence as the dynamic "memory" of the solar corona.

Photospheric flux transport processes – such as differential rotation, meridional circulation, and turbulent diffusion – operate on timescales of weeks to years, imprinting the photospheric magnetic field with the memory of past flux emergence and transport (Upton

and Hathaway, 2014; Petrie, 2015; Bhowmik and Nandy, 2018; Pal et al., 2023). This memory effect may be compromised during solar maximum, when frequent magnetic flux emergence in the form of sunspots interacts with long-lived polar and low-latitude fields to produce a corona shaped by both current and past magnetic conditions. From the physical perspective, the coronal configuration (e.g., that observed during an eclipse) is not solely determined by the active regions present at that moment, but also by the accumulated magnetic flux reconfigured over preceding rotations. Studying the dynamic memory of the corona is therefore of fundamental importance for assessing what imbibes predictability in models of coronal magnetism and how far in advance predictions of coronal magnetic field and associated phenomena may be made.

Against this backdrop, Surface Flux Transport (SFT)-driven coronal models have emerged as a promising pathway for predictive capability. By simulating the advection, diffusion, and shearing of magnetic flux on the photosphere through processes such as differential rotation, meridional circulation, and supergranular diffusion (Upton and Hathaway, 2014; Jiang et al., 2014; Bhowmik and Nandy, 2018; Yeates et al., 2023), SFT models capture how magnetic imprints from earlier active regions persist and interact with newly emerged flux on the Sun's surface to determine the global magnetic field distribution on the Sun's surface; since the latter in turn govern the coronal magnetic field, SFT models coupled to coronal field models are central to exploring the dynamical memory of the corona,

In this work, we employ a newly developed Solar Photospheric-flux Transport Model (SPhoTraM) (Pal and Nandy, 2025), which has been calibrated with long-term solar activity observation to provide robust forecasts of the surface magnetic field. Using SPhoTraM and a full MHD coronal model within the Space Weather Modeling Framework (SWMF) (Gombosi et al., 2021), we predict the Sun's coronal structure on 08 April 2024 and show that our coupled modelling framework captures the observed large-scale coronal structure on the day of the total solar eclipse. We explore how much of the corona's structure can be explained by its "memory" of past magnetic activity, even during times of strong and rapid changes, i.e., at this maximum phase of sunspot cycle 25. Surprisingly, we find that the large-scale memory of the corona persists even during this strong phase of solar activity. Our findings provide a physical foundation for forecasting coronal fields and associated drivers of the heliospheric space environment – such as the large-scale structure of the

solar wind, open flux and cosmic ray flux – at all phases of the solar cycle.

## 8.2 Numerical Model Description

In this section, we describe the two primary physics-based models used in this study for solar eclipse prediction: (i) a data-driven Surface Flux Transport (SFT) model and (ii) a full three-dimensional magnetohydrodynamic (MHD) coronal magnetic field model. The data-driven SFT model evolves the observed photospheric magnetic field by incorporating flux emergence, differential rotation, meridional flow, and supergranular diffusion, thereby providing a realistic description of the large-scale surface magnetic field distribution. The resulting surface magnetic field is then used as the lower boundary condition for the full 3D MHD coronal model. By driving the coronal simulation with this realistic magnetic boundary, we generate synthetic coronal structures and eclipse images that can be directly compared with observations.

### 8.2.1 Solar Photospheric-flux Transport Model (SPhoTraM)

The SPhoTraM model is a class of SFT models that simulate the evolution of the magnetic field of the photosphere in response to large-scale flows (e.g., meridional flow and differential rotation) and supergranular diffusion, with no back reaction on these flows (Leighton, 1964; Pal and Nandy, 2025). It solves the radial component of magnetic induction equation as follows:

$$\begin{aligned}\frac{\partial B_r}{\partial t} &= -\omega(\theta)\frac{\partial B_r}{\partial \phi} - \frac{1}{\mathrm{R}_\odot \sin\theta}\frac{\partial}{\partial \theta}\left(v(\theta)B_r \sin\theta\right) \\ &+ \frac{\eta}{{\mathrm{R}_\odot}^2}\left[\frac{1}{\sin\theta}\frac{\partial}{\partial\theta}\left(\sin\theta\frac{\partial B_r}{\partial\theta}\right) + \frac{1}{\sin^2\theta}\frac{\partial^2 B_r}{\partial\phi^2}\right] \\ &+ S(\theta,\phi,t),\end{aligned} \tag{8.1}$$

where the source term $S(\theta,\phi,t)$ models the observed sunspots utilizing their properties, including their emergence latitude, longitude, and area from the historical sunspot data from (RGO/USAF/NOAA Data Centre, 2023) to synthetically model bipolar active regions as input sources. The tilt angle $\alpha$ of the BMR is assigned according to the following expression: $\alpha = g\,T_n\sqrt{|\lambda|}$, where $\lambda$ is the heliographic latitude of the BMR centroid. The

factor $T_n$ accounts for the dependence of tilt angle on the solar cycle strength (Jiang et al., 2014). The constant $g$ is set at 0.7, which incorporates the effect of localized inflows toward active regions, which ultimately reduces the tilt angle. We estimate the radius of each polarity region (denoted as $R_{\rm spot}$) from the total sunspot area $A$. The radial separation $d$ between the centroids of the leading and following spots is considered proportional to $R_{\rm spot}$ in our model. Ultimately, we calculate the magnetic flux associated with a Bipolar Magnetic Region using the empirical relationship: $\Phi(A) = 7.0 \times 10^{19} \cdot A$ [Mx]. This total flux is assumed to be equally distributed between the leading and following polarities of the BMR. With these calculations, we synthetically model symmetric bipolar sunspots following van Ballegooijen et al. (1998) and insert them at appropriate phases of the sunspot cycle. These serve as the source term in the SFT model. For more details, see Bhowmik and Nandy (2018); Pal et al. (2023).

We simulate the evolution of the photospheric magnetic field over multiple solar cycle timescales, covering solar cycles 15 through 25 up to March 4, 2024 using the RGO/NOAA database. Beyond this date, we use sunspot properties derived from the Helioseismic and Magnetic Imager (HMI) database to drive the SFT model and extend the simulation up to April 1, 2024. It is known that sunspot areas reported by HMI are systematically larger than those in the RGO–NOAA/USAF dataset. Since our SFT simulations are calibrated using over a century of RGO–NOAA/USAF data (starting from 1913), we apply a scaling factor of 2.3 to the HMI recorded area to ensure consistency in the large-scale magnetic field evolution. For more details, readers can refer Nandy et al. (2018); Dash et al. (2020). Such long-term SFT simulations enable more accurate estimation of the polar magnetic flux, overcoming the limitations of observed magnetograms, which often are recorded near the visible solar disk and suffer from projection effects near the solar limb and high latitude. Accurate computation of the polar flux is essential for predicting the large-scale structure of the coronal magnetic field, as it plays a crucial role in determining the orientation and tilt of coronal streamers.

### 8.2.2 The Alfvén Wave Solar Model (AWSoM)

The coronal magnetic field and plasma evolution in this study are simulated using the Alfvén Wave Solar Model (AWSoM), a comprehensive three-dimensional magnetohydro-

dynamic (MHD) model developed at the University of Michigan (Sokolov et al., 2013; van der Holst et al., 2014; Gombosi et al., 2021). AWSoM solves the full set of nonideal MHD equations in conservative form, namely, the mass continuity, momentum, magnetic field, and total energy equations, while also accounting for additional thermodynamic processes such as coronal heating, radiative cooling, and thermal conduction. In addition to these standard MHD equations, the model incorporates two additional transport equations that describe the propagation, reflection, and dissipation of Alfvén wave energy – one for waves traveling parallel to the magnetic field and another for waves propagating in the opposite direction.

The nonlinear interaction between these counter-propagating Alfvén waves drives a turbulent cascade, which acts as a fundamental mechanism for converting wave energy into thermal energy, thereby heating the corona and accelerating the solar wind (Tu and Marsch, 1993, 1995; Chandran et al., 2009; Réville et al., 2020). This model also includes key thermodynamic processes such as anisotropic thermal conduction along magnetic field lines and optically thin radiative cooling, enabling a realistic representation of coronal plasma behavior. To efficiently handle the steep temperature and density gradients in the transition region and lower corona, we adopt the Threaded Field Line Model (TFLM) formulation introduced by Sokolov et al. (2021). This approach captures the essential thermodynamic coupling between the chromosphere and corona without requiring extremely fine spatial resolution, thereby significantly reducing computational cost. The AWSoM model has been rigorously validated against a wide range of solar and heliospheric observations (Sachdeva et al., 2019; Henadhira Arachchige et al., 2022) and has been successfully applied in diverse contexts, including solar and stellar wind modeling as well as wind–magnetosphere interaction studies (Garraffo et al., 2022; Hazra et al., 2022; Chebly et al., 2022; Hazra et al., 2025).

The inner boundary of the simulation domain is specified using the photospheric magnetic field map generated by the SPhoTraM model. This map provides the radial component of the magnetic field at the solar surface, which serves as the lower boundary condition for the coronal MHD solution. At this boundary, we assume a uniform plasma density of n=2 $\times 10^7\, cm^{-3}$ and a temperature of T=50,000 K, values that represent typical chromospheric and low-coronal conditions. These parameters ensure a physically consis-

tent transition between the dense, cool photosphere and the overlying hot corona. At the outer boundary, located at a heliocentric distance of $24\,R_{\odot}$, an outflow condition with a zero-gradient constraint is applied. This allows plasma and magnetic field structures, including the solar wind, to leave the simulation domain freely without artificial reflection or numerical buildup. Within this framework, two key input parameters play a particularly important role in determining the coronal and solar wind properties. The first is the outward-propagating Poynting flux parameter, which defines the ratio of the Poynting flux to the magnetic field strength at the inner boundary and governs the amount of Alfvén wave energy injected into the corona. The second is the correlation length of Alfvén wave dissipation, which characterizes the spatial scale of nonlinear interactions between counter-propagating waves and thereby controls the rate at which turbulent energy is converted into heat. Using these boundary conditions, the prescribed magnetic field distribution, and the relevant physical parameters, the model is advanced in time until it reaches a steady-state solution that self-consistently describes the coronal magnetic field, plasma properties, and solar wind flow throughout the computational domain. The AWSoM simulation using the SFT-generated magnetic field boundary condition computes a self-consistent, steady-state solution of the solar corona.

## 8.3 Results and Discussions

Solar surface magnetic field distribution – which changes frequently during solar maxima – dictates Sun's coronal magnetic field configuration. To predict the large-scale coronal magnetic fields and compare our predicted maps to direct observations, we chose the total solar eclipse of 2024. In order to study the large-scale magnetic memory of Sun's corona we first generate the predicted surface map and then utilize it to model large-scale coronal magnetic fields.

### 8.3.1 Prediction of surface magnetic field on the day of eclipse

We employ the observational data-driven surface flux transport model to predict the Sun's photospheric magnetic field for April 8, 2024 – the day of the total solar eclipse. Long-term simulations with such models self-consistently preserves the memory of the Sun's surface

magnetic field evolution over solar cycle timescales, allowing for reliable predictions of the photospheric magnetic field distribution Bhowmik and Nandy (2018). To predict the solar photospheric magnetic field on the eclipse day, our model incorporates the last observed solar active region as of April 1, 2024. The model is then run forward in time without introducing any new sunspot emergence until April 8, 2024, providing a forecast of the photospheric field leading up to the eclipse date (described in subsection 8.2.1).

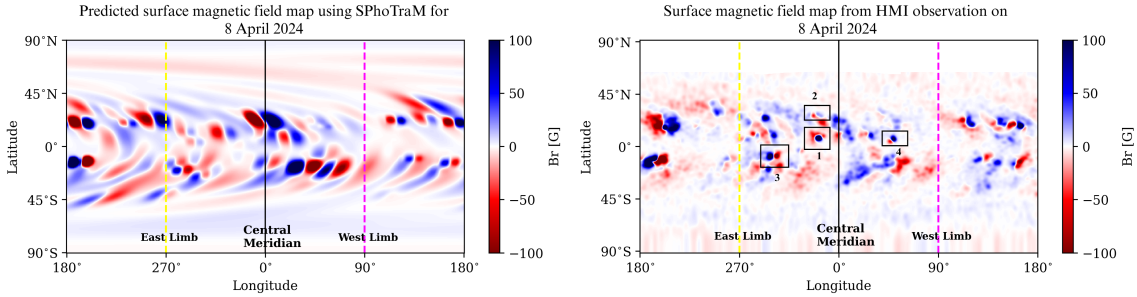


Figure 8.1: The first panel shows the SPhoTraM-simulated photospheric magnetic field map for the solar eclipse of 08 April 2024. The last active region included in the simulation was inserted on 01 April 2024, one week prior to the eclipse, making this a forward prediction. The second panel presents the HMI synoptic map observed on the actual eclipse day, 08 April 2024. In both panels, red and blue correspond to negative and positive polarities, respectively. The solid black dashed line denotes the central meridian, and the yellow/magenta dashed lines indicate the Sun's visible east/west limb, respectively. In the HMI map (second panel), the boxed regions highlight newly emerged active regions that were absent in the SPhoTraM prediction due to the earlier prediction. For instance, boxes 1–4 correspond to new sunspots NOAA 13628, 13632, 13633, and 13627. Both these maps are correctly aligned to fix the center at observed central meridian longitude for better comparison.

In Figure 8.1, the left panel shows the predicted photospheric magnetic field map on April 8, 2024. Our predicted map indicates that the Sun's photosphere is clustered by numerous active regions near low latitudes, while the polar regions exhibit weak magnetic fields – both clear signatures that the Sun is currently near the maximum phase of solar cycle 25 and in the process of reversing its magnetic polarity. Similarly, we also show the near-real-time daily updated Helioseismic Magnetic Imager (HMI) synoptic map on the right in Figure 8.1. When compared to our prediction, this observed map shows a strong similarity in terms of the large-scale magnetic structures. During solar maximum, we expect to have frequent new sunspot emergence, which is also highlighted in the right panel by black squares. However, these highlighted regions contribute minimally to the global coronal configuration due to their emergence location. It is also clear that near-real-time observations tend to miss observations in the polar region due to projection effects,

which we capture in the predicted surface map well.

Overall, Our result demonstrates that the data-driven SPhoTraM simulations is capable of accurately capturing the large-scale features of the solar photospheric magnetic field in advance, even during periods of high solar activity.

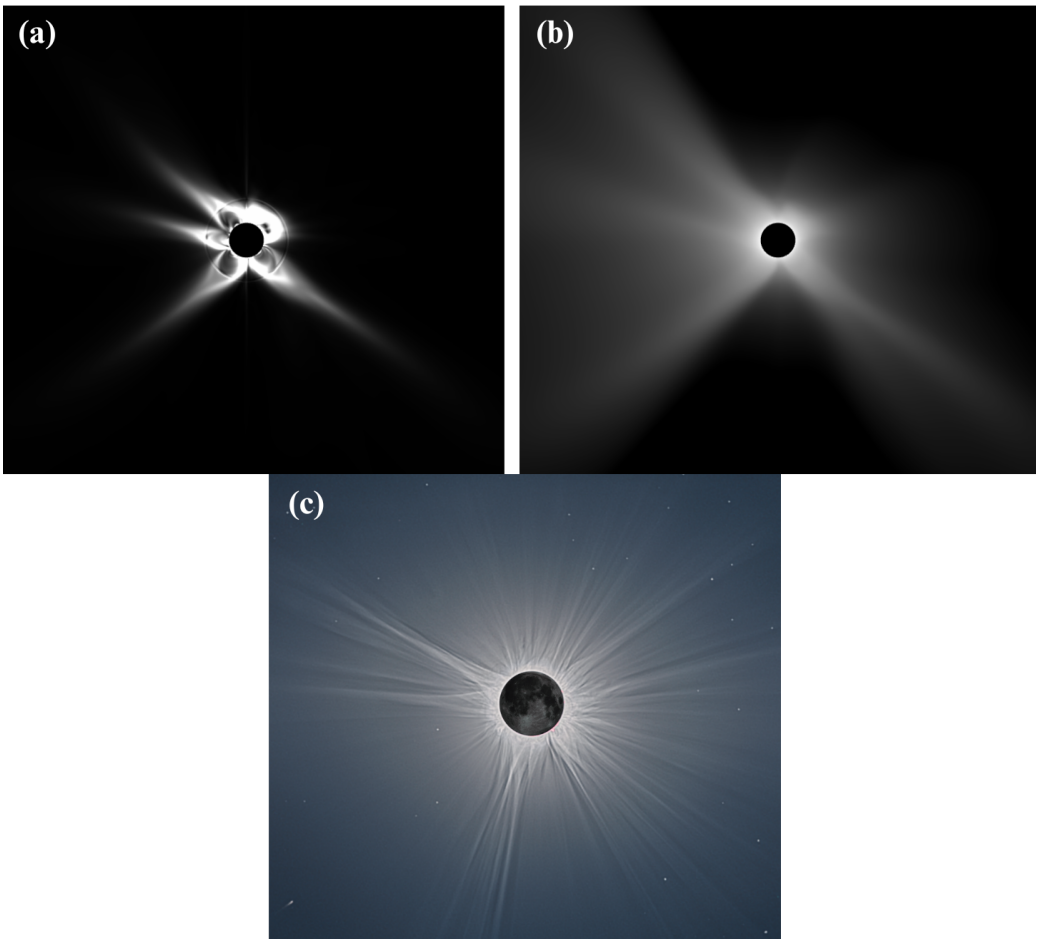


Figure 8.2: Panel (a) and (b) illustrates the simulated coronal number density distribution and the current density distribution from the surface flux transport coupled coronal magnetic model (SPhoTraM-AWSoM). Panel (c) represents the white light eclipse image taken by Petr Horalek, from Durango Mexico. To ensure proper alignment, all of these images are rotated to present the solar north-up view.

### 8.3.2 Comparison between coronal model predictions and eclipse observations

We utilize the SPhoTraM-generated predicted surface map as the lower boundary condition within the three-dimensional Alfvén Wave Solar Model (AWSoM) to predict how the magnetic field and plasma are distributed throughout the solar corona (see section 9.2 for

more details). The AWSoM simulation using the SFT-generated magnetic field boundary condition computes self-consistent, steady-state solution of the solar corona. From this equilibrium steady state solution, we can extract various coronal plasma properties, such as number density, current density and temperature. These quantities, in turn, provide the basis for generating synthetic observations of the corona. Figure 8.2(a) and (b) show the predicted structure of the current density magnitude and electron number density distribution in the solar corona, which is compared with a white light eclipse image taken by Petr Horalek in Durango, Mexico (Figure 8.2(c)).

Our model results reveal multiple elongated, petal-like structures known as streamers in the corona during the total solar eclipse day. Since the Sun is close to the solar magneic cycle maximum, we expect the sunspot emergences to be highest as compared to solar cycle minimum phase; such a dynamic global corona is expected. Our coupled SPhoTraM–AWSoM simulation successfully reproduces many of the large-scale streamer features visible during the eclipse, particularly along the north-east, east, and south-east limbs. The south-west streamers are also reasonably well captured, although those in the north-west appear less pronounced in our simulation compared to observations. This discrepancy highlights some limitations of our surface magnetic field modeling approach. First, the bottom boundary condition – our predicted photospheric magnetic map – may introduce uncertainties. Because our forecast does not include sunspot emergence after April 1, 2024, any active regions that appeared in the week leading up to the eclipse day are missing from the input, and these can influence the coronal structure, especially near the solar maximum. Second, the MHD model depends on several parameters that are not directly constrained by observations, such as those governing Alfvén wave turbulence-driven coronal heating. Small changes in these parameters may alter the predicted streamer brightness or location. Finally, transient solar events, such as magnetic storms or coronal mass ejections (CMEs), which occur more frequently during solar maximum, can significantly distort the corona on short timescales. Since our model evolves toward a steady state, it does not capture such rapid changes.

Despite these limitations, the simulation captures the essential global features of the corona remarkably well. The broad streamer belt and the large-scale distribution of structures align with the eclipse observations, demonstrating the ability of our SPhoTraM–AWSoM

framework to provide reliable predictions of the global coronal configuration. This predictive capability is particularly valuable for planning eclipse observations and for improving our broader understanding of how solar magnetic activity shapes the corona.

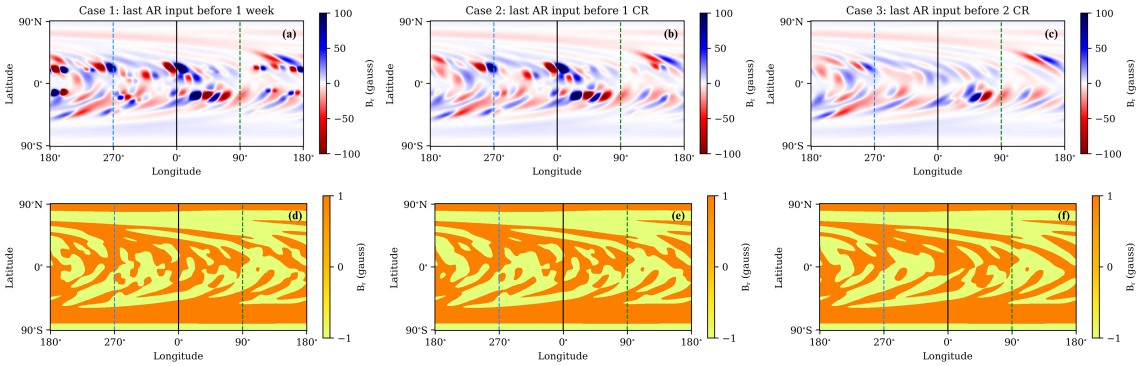


Figure 8.3: The top panel illustrates the SPhoTraM-simulated surface magnetic field map on the day of the eclipse. Panel (a) corresponds to the scenario where the last active region (AR) is inserted one week prior to the eclipse, followed by emergence-free SFT evolution until the eclipse day. Panels (b) and (c) depict similar simulations, but with the last AR introduced one Carrington rotation (CR) and two CRs before the eclipse, respectively. The bottom panel—panels (d), (e), and (f)—shows the corresponding polarity distributions on the solar surface for the same three cases: with the last AR inserted one week before, one CR before, and two CRs before the eclipse day, respectively. All of these panels, red and blue, denote negative and positive polarities.

### 8.3.3 Does large-scale magnetic memory exist in solar corona?

By combining surface magnetic field predictions from SFT model with coronal magnetic structure reconstruction from full MHD models, and validating both against observations, we are now well positioned to address the key question: does the solar corona retain a memory of large-scale magnetism as hypothesied by Nandy et al. (2018). Here, we investigate whether the solar corona retains a dynamical memory of past surface magnetic field evolution during the solar maximum phase. During maximum, the absence or presence of even a single large active region can dramatically reshape coronal structures. Thus, this is an ideal time to test whether the corona still retains memory of past magnetic field evolution, or whether new emergence completely erases it.

To investigate the extent to which the solar corona retains memory, we therefore design three case studies, each differing in how far back the last assimilated AR was inserted into the SPhoTraM model before the day of eclipse:

**Case 1:** The last AR is introduced one week prior to the eclipse, and the SFT simulation

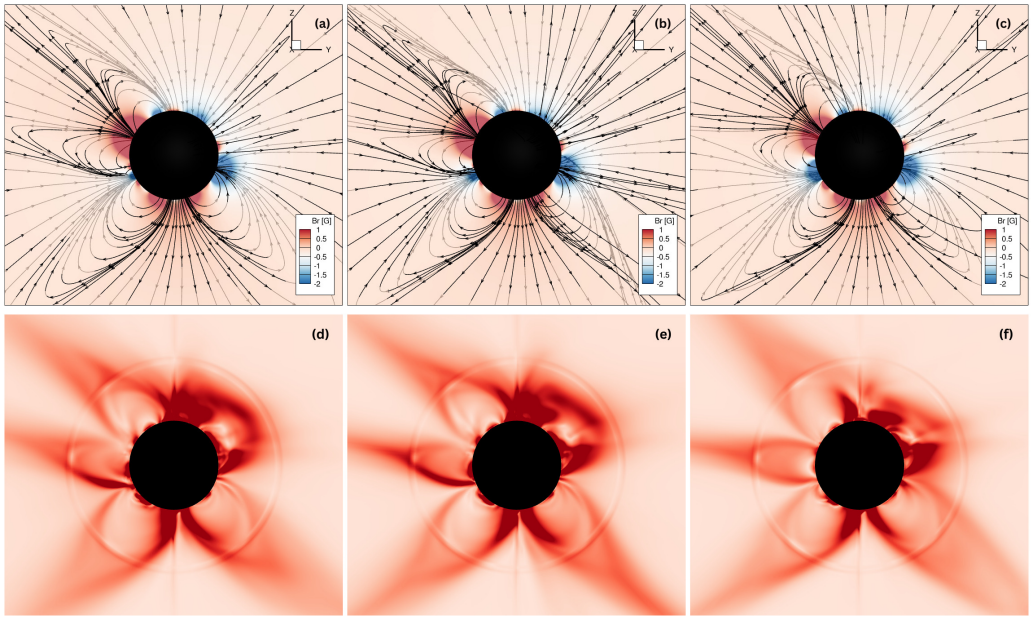


Figure 8.4: The top panel illustrates the reconstructed coronal magnetic field line structures in the solar corona on the day of the eclipse with the background color representing the radial magnetic field amplitude ($B_r$) in the plane of the sky. Panel (a) corresponds to the scenario where the last active region (AR) is inserted one week prior to the eclipse, followed by emergence-free SFT evolution until the eclipse day. Panels (b) and (c) depict similar simulations, but with the last AR introduced one Carrington rotation (CR) and two CRs before the eclipse, respectively. The bottom panel – panels (d), (e), and (f) – shows the corresponding unsigned current density distributions ($|J|$) on the solar corona for the same three cases: with the last AR inserted one week before, one CR before, and two CRs before the eclipse day, respectively.

is then extended forward by one week (seven days) without any new sunspot emergence.

**Case 2:** The last AR is introduced one Carrington rotations ($\sim$ 27 days) prior to the eclipse day, and the SFT simulation is then extended forward by one CR without any new sunspot emergence.

**Case 3:** The last AR is introduced two CRs ($\sim$ 54 days) prior to the eclipse day, and the SFT simulation is then extended forward by two CRs without any new sunspot emergence.

The resulting solar surface magnetic maps (top panels) and polarity separation distributions (bottom panels) for these three cases are shown in Figure 8.3. As expected, the longer the forward run without assimilation of new emergences, the more ARs are missing. In particular, Cases 2 and 3 fail to capture several major ARs that actually appeared on the Sun before the eclipse. However, a closer inspection of Figure 8.3(d) and (e) shows that the polarity separation maps appear nearly identical. In contrast, panel (f) reveals localized differences in connectivity between opposite polarities. This result indicates that by two CRs the memory of the true AR distribution is already lost.

To capture how these surface map changes affect the coronal magnetic field structures, we use each surface map as the bottom boundary condition to drive the 3D full MHD AWSoM model and perform three separate simulations. Large-scale Magnetic field configuration from these simulations are presented in Figure 8.4. Remarkably, the global structure of the steady-state corona remains largely unchanged in the first two cases, despite the absence of several ARs in Case 2. The large-scale streamer belt and overall topology are preserved, with only modest changes such as differences in the tilt angles of streamers and subtle shifts in field-line connectivity. In contrast, the third case (Figure 8.4(c) and (f)) shows clear differences in both the magnetic field structure and the current density compared to the first two cases. The absence of nearly two months of AR emergence significantly alters the global configuration, consistent with the differences seen in the surface polarity distributions in Figure 8.3(f).

These results indicate that the solar corona possesses a dynamical memory with a timescale of approximately one solar rotation, even during solar maximum, but that beyond a rotational timescale, this memory starts degrading precluding longer-range predictions of associated heliospheric forcing parameters.

## 8.4 Discussions

Accurate predictions of the Sun's coronal field is one of the outstanding challenges in solar and stellar physics, given the role that coronal magnetism plays in heating of the million degree outer corona of stars, in driving energetic phenomena such as flares and CMEs and in governing planetary space environments through modulation of solar wind, open magnetic flux and cosmic ray flux. Total solar eclipses provide a rare opportunity to test and constrain physical models of coronal magnetism. Such complex, predictive coronal models are difficult to develop, but are now reaching increasing levels of sophistication and success in predictions (Downs et al., 2025; Shi et al., 2025; Liu et al., 2025).

In this study, we employ a (long-term calibrated) data-driven surface flux transport model coupled to a physics-based magnetohydrodynamic model of the solar corona to explore the underlying basis of coronal field predictability. This predictability is endowed by two primary pathways. The first important ingredient is an accurate determination of the surface or photospheric magnetic field distribution which acts as the bottom boundary based on which coronal magnetic fields are estimated. The second ingredient being an accurate coronal field estimation model which imbibes the physics of the solar corona.

We find that our forward-modeled prediction of the large-scale coronal structure of the 08 April 2024 total solar eclipse compares favourably with the eclipse observations. More importantly we demonstrate that the evolution of the global photospheric magnetic field distribution, governed by relatively slow near-surface plasma flux transport processes, imbibes a memory in the Sun's large-scale coronal field structure, which unexpectedly persists up to a rotational timescale (i.e., approximately a month) even during solar maximum. This leads to the surprising conclusion that the solar corona has a dynamical 'memory' of large-scale magnetism not just during solar minimum as hypothesized earlier, but at all phases of the sunspot cycle – irrespective of activity levels.

The solar corona, therefore, exhibits a dual character: it can rapidly respond to local-scale restructuring while retaining global memory over longer timescales. Based on our findings, we propose that although transient events, such as flares and CMEs can reorganize coronal magnetic field structures on Alfvénic timescales – typically in minutes to hours depending on the length of the magnetic structure – the large-scale coronal field

relaxes back to its original, surface magnetic field governed configuration following such perturbations. In hindsight, this explains why simpler coronal field extrapolation models (e.g., the Potential Field Source Surface Model) – which lack some of the sophisticated physics of full-scale magnetohydrodynamic models but rely on surface magnetic field distribution as inputs – still manage to capture some important aspects of global coronal field connectivity, solar wind and open flux reconstructions reasonably well (Yardley et al., 2024; Wilkins et al., 2025).

Our findings have important implications for space weather forecasting and predicting the solar wind, solar open flux and cosmic ray flux at Earth. These are critical physical parameters that modulate the state of the heliosphere and the planetary space environments. Our work demonstrates the fundamental physics that allows for early predictions of coronal magnetism and thus motivates the development of physics-based coronal and heliospheric models that can take advantage of this underlying memory that seamlessly connects magnetic fields from the solar interior to the heliosphere.

# Chapter 9

# Reconstructing Long-Term Open Solar Flux Variations

*"The interplanetary magnetic field (IMF), carried by the solar wind into the heliosphere, plays a critical role in space weather by interacting with Earth's magnetosphere and modulating geomagnetic storms, auroral activity, and cosmic ray transport. The IMF is directly linked to the Sun's open magnetic flux (OSF), which originates from the large-scale structure of the solar corona. Here, we reconstruct century-scale variations in the OSF using a physics-based, data-driven modeling framework that couples optimized surface flux transport simulations with dynamic coronal magnetic field extrapolations. We introduce stochastic variability in active region emergence to simulate the Sun's surface magnetic field over the past 100 years and utilizing these photospheric maps we simulate solar corona. By allowing the source surface height to vary with solar activity, we establish a robust empirical relationship between the surface magnetic field strength and coronal topology. Our results reveal long-term evolution in the source surface height and solar open flux, including a contraction of the solar corona after Cycle 21, indicating the end of the Modern Grand Maximum. Our independent approach offers a new pathway for reconstructing historical heliospheric conditions and provides improved constraints for space climate studies and solar wind forecasting.* [1] *"*

## 9.1 Introduction

In recent years, there has been significant interest – both observational and theoretical – in understanding the origin and evolution of the Sun's open magnetic flux, also known as the Interplanetary Magnetic Field (IMF). The open magnetic flux represents a component of the Sun's large-scale magnetic field that originates in coronal holes, typically rooted

[1] This chapter is based on research work which is under preparation (Pal and Nandy, 2024b).

in the solar surface, and extends outward into interplanetary space, carried by the solar wind (Lockwood, 2013; Frost et al., 2022). This outward-flowing field becomes the IMF, which surrounds the Earth and interacts with the Earth's magnetosphere in complex ways, modulating the ambient magnetic conditions of the heliosphere. Understanding variations in the IMF or open solar flux (OSF) is therefore essential, as it not only influences the geomagnetic environment but also affects cosmic ray modulation and variations in the total solar irradiance (Lean et al., 2002; Lockwood, 2002; Nandy et al., 2023; Dash et al., 2023). The strength and structure of the IMF usually vary over the course of the 11-year solar cycle, highlighting the need to investigate its origin and temporal evolution in conjunction with changes in the Sun's surface magnetic field throughout the solar cycle.

However, direct near-Earth measurements of the IMF have been available only for the past few decades (see black curves in both panel of Figure 9.1), primarily through NASA's Goddard Space Flight Center via the Space Physics Data Facility, which compiles data into the OMNI and OMNI2 databases dating back to the early 1960s – the start of the space age (King and Papitashvili, 2005; Lockwood et al., 2009a; SPDF OMNIWeb database, 2025). The absence of earlier IMF observations presents a significant gap in our understanding of the Sun's long-term magnetic variability, underscoring the importance of reconstructing the IMF to develop a comprehensive view of solar magnetic behavior over extended timescales. To address this, earlier studies have reconstructed the historical OSF using a variety of approaches, including geomagnetic indices (such as the aa index, IDV index), cosmogenic isotope records, and physics-based models involving surface flux transport and coronal magnetic field modeling (Pulkkinen et al., 2001; Rouillard et al., 2010; Svalgaard and Cliver, 2010; Jiang et al., 2011; Lockwood, 2013; Wang and Lean, 2021).

Despite this progress, a persistent discrepancy exists between OSF values derived from physics-based models and those inferred from in situ spacecraft measurements – a challenge widely referred to as the 'Open Solar Flux Problem' (Wallace et al., 2019; Linker et al., 2021; Arge et al., 2024). This mismatch has become a central concern within the heliophysics community, prompting significant efforts to understand and resolve it. Several factors likely contribute to this discrepancy. Firstly, the major challenges come from the photospheric magnetic field as they may underestimate the magnetic flux, specifically

from the unobserved solar poles (Linker et al., 2017). Additionally, inter-calibration issues between different magnetograph instruments exacerbate this problem, causing inconsistencies in studying the long-term evolution of the Sun's magnetic field (Wang et al., 2022). Secondly, Limitations of In Situ Measurements: The reliability of in situ measurements as indicators of the global open flux remains a critical question. Lastly, numerical model Assumptions. Finally, coronal magnetic field models often rely on assumptions and free parameters that may be oversimplified or poorly constrained, and which may vary with solar activity – further affecting the accuracy of OSF estimates (Lee et al., 2011; Arden et al., 2014).

In this study, we address the OSF problem by beginning with a surface flux transport model that is optimized using observed polar flux. We investigate how a key parameter of the coronal magnetic field model – the source surface height – varies across different phases of solar activity. By incorporating these variations, we optimize the simulated OSF against in situ observations and reconstruct its century-scale evolution. As a key contributor to the interplanetary magnetic field (IMF), understanding OSF variability is essential, and our approach offers a novel, physics-based framework for its reconstruction using magnetic field evolution models.

## 9.2 Data and Methods

The emergence and evolution of sunspot magnetic flux on the solar surface govern the structure of the large-scale coronal magnetic field, which extends into the heliosphere as open solar flux (OSF), also known as the Interplanetary Magnetic Field (IMF) (Mackay and Yeates, 2012). The initial phase of these solar magnetic processes can be physically modeled using the Surface Flux Transport (SFT) model, which describes the evolution of surface magnetic fields under the influence of large-scale plasma flows such as meridional advection, differential rotation, and turbulent supergranular diffusion (Bhowmik and Nandy, 2018; Yeates et al., 2023; Pal et al., 2023). The second phase, which governs the evolution of the large-scale structure of the global coronal magnetic field, can be modeled using the Potential Field Source Surface (PFSS) model (Wiegelmann et al., 2017). This model operates under the assumption that the region between the solar surface ($R_\odot$) and the source surface (typically located at $2.5R_\odot$) is current-free. Beyond the source surface,

the magnetic field is dominated by the solar wind and is carried outward along a spiral trajectory, known as the Parker spiral. While this assumption neglects electric currents below the source surface region, it does not significantly affect the representation of the global magnetic field's large-scale features.

We utilize our newly developed SFT model, 'SPhoTraM' (Pal and Nandy, 2025), incorporating active region statistics from the RGO/USAF/NOAA Data Centre (2023) as input sources of the model to simulate the evolution of the solar surface magnetic field over the past century. In this simulation, the polar flux for each sunspot cycle is optimized against observational estimates derived from polar faculae measurements (find more technical details in Pal and Nandy (2025)). An important aspect of this type of optimized SFT simulation is ensuring an accurate representation of the polar field in the surface magnetic map. This is crucial for addressing the open solar flux problem, which often arises from the underestimation of high-latitude magnetic flux (Linker et al., 2017). The surface magnetic maps generated in Pal and Nandy (2025) are used as the lower boundary condition for modeling the global coronal magnetic field structure through the PFSS extrapolation. We use the PFSS code from Yeates (2018) for our study. The PFSS model computes the coronal magnetic field extending from the solar surface ($R_\odot$) up to the source surface (SS), typically situated at $2.5R_\odot$. The SS height represents a hypothetical boundary beyond which magnetic field lines are assumed to become purely radial – that is, they are considered open – and thus contribute to the OSF. The choice of the SS height has a significant impact on the estimation of OSF (Lee et al., 2011; Arden et al., 2014). A lower SS height allows more magnetic closed loops to penetrate the SS, causing them to be classified as open field lines and thus increasing the calculated open flux. In contrast, a higher SS height reduces the number of field lines that extend beyond the SS, resulting in a lower estimate of OSF.

To analyze the long-term variation in the heliospheric magnetic field (HMF), we utilize hourly magnetic field measurements collected from various space-based instruments in geocentric or L1 (Lagrange point) orbits since the 1960. These data are compiled in the SPDF OMNIWeb database (2025) and standardized to 1 AU ($R_E$) after proper cross-calibration. Our understanding of the Sun's open flux is primarily motivated by key observations from the Ulysses mission, which traversed a wide range of heliographic latitudes.

The mission revealed that the HMF flux density remains remarkably uniform across latitudes (Balogh et al., 1995). This finding allows the total open solar flux to be estimated from interplanetary magnetic field measurements taken at a single point in the heliosphere (typically at 1 AU), by simply multiplying the measured flux density by the surface area of a sphere at that distance.

For this study, we use the 27-day averaged interplanetary magnetic field magnitude, corresponding to one solar rotation (a Carrington period of approximately 27.3 days), to capture the long-term trends in the heliospheric magnetic field. The total unsigned magnetic flux is calculated using the expression following Lockwood and Owens (2009); Wallace et al. (2019): $\Phi_{obs}(t) = \pi R_E^2 |B_r|$, where, $\Phi_{obs}$ denotes the total open solar flux estimated from the in situ observation. $|B_r|$ is the unsigned radial component of the heliospheric magnetic field. $R_E$ is the Earth's radius and set to 1 AU. Ultimately, we use the observed open flux, $\Phi_{obs}$, smoothed using a running mean with a temporal window of three solar rotations to reduce short-term fluctuations and highlight long-term trends. The black curve in both panels of Figure 9.1 represents $\Phi_{obs}$, derived from in situ observations.

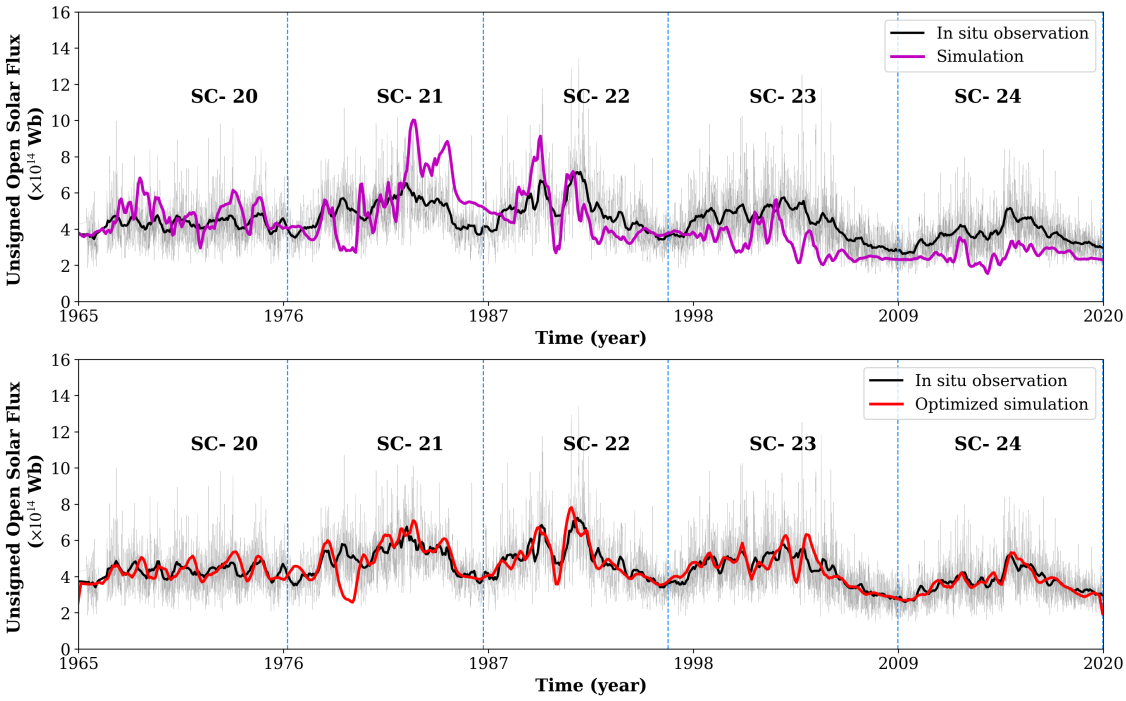


Figure 9.1: OSF variations. Black and red curve denotes in situ observation and SFT-PFSS simulated OSF (for a fixed SS), respectively. Optimized OSF variations from solar cyle 20 to 24 and compared with in situ observation.

## 9.3 Results and Discussions

Since in situ observations are available starting from solar cycle 20, we first use the surface magnetic maps generated by the SFT model for solar cycles 20 to 24 as the bottom boundary condition for the PFSS model. This enables the extrapolation of the coronal magnetic field up to the source surface height, which is set at $R_s = 2.2, R_\odot$ in our study. We calculate the temporal variation of the OSF ($\Phi_{\rm sim}(t)$) by integrating the radial component of the magnetic field ($B_r(R_s, \theta, \phi, t)$) at that height, according to the following expression:

$$\Phi_{sim}(t) = R_s^2 \int B_r(R_s, \theta, \phi, t)\, sin\theta\, d\theta\, d\phi \tag{9.1}$$

The magenta curve in Figure 9.1 (top panel) shows the simulated time evolution of the unsigned OSF from sunspot cycles 20 to 24. However, a noticeable discrepancy arises when this simulated OSF is compared with in situ observational data, depicted by the black curve in the same panel. For instance, during certain phases of the solar cycle, the simulated OSF underestimates the observed values (for example, in solar cycles 23 and 24), while in other phases, it overestimates them (for example, in the declining phase of solar cycle 21). This phase-dependent mismatch indicates that a simple multiplicative scaling factor is insufficient to resolve the discrepancy between the simulated and observed OSF, which corresponds to the Open Solar Flux problem, as discussed in the introduction (section 9.1). This observed mismatch suggests that the assumption of a fixed SS height in the PFSS model may fail to adequately capture the dynamic nature of the Sun's magnetic environment, which can be one potential candidate for causing open solar flux problems. Instead, allowing the SS height to vary over the solar cycle phases could better reflect the evolving conditions of the Sun's large-scale magnetic field.

We divide each sunspot cycle into fifteen equal phases to account for variations in the SS height throughout the solar cycle. The first two phases represent the Starting phase, phases three through nine correspond to the Rising and Maximum phases, and the final six phases represent the Declining and End phases. The left panel of Figure 9.2 shows one such division for solar cycle 22. For a given phase, we systematically vary the SS height from $1.2R_\odot$ to $3.5R_\odot$, calculate the OSF from simulations, and determine the root mean

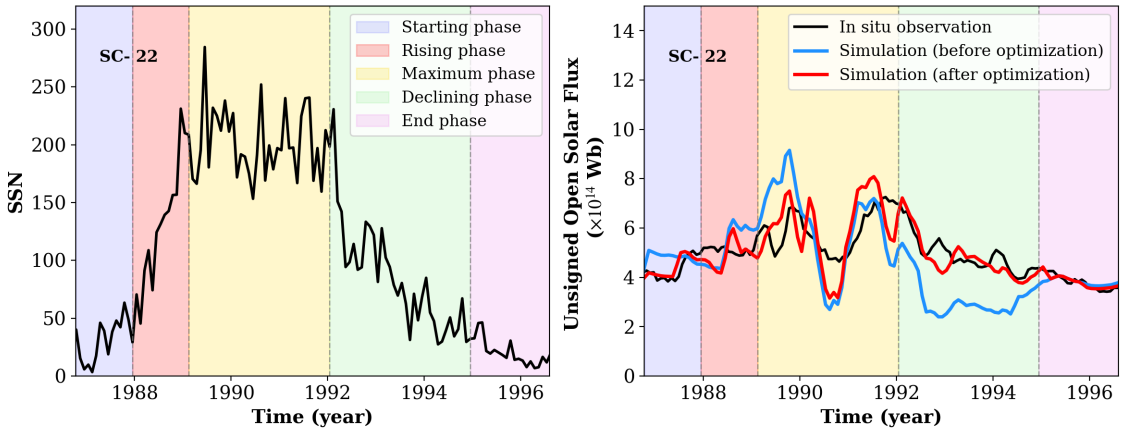


Figure 9.2: First panel denotes 5 different phases of solar cycle through which SS height is optimized. Second panel denotes the optimization of OSF for solar cycle 22. Details are described in the main text.

squared difference (RMSD) between the simulated and in situ observed OSF. We calculate RMSD by the expression: RMSD $= \sqrt{\frac{1}{N}\sum_{i=1}^{N}(\Phi^{i}_{obs} - \Phi^{i}_{sim})^2}$, where N is number of data points in a particular phase. This iterative process is repeated until we achieve a closer match between the modeled and observed OSF. The SS height value corresponding to the minimum RMSD is then selected for that phase. This type of optimization is known as the RMSD-based model optimization method. In the right panel of Figure 9.2, the blue curve represents the OSF before optimization, while the red curve represents the OSF after optimization for solar cycle 22. We extend this analysis across solar cycles 20 to 24 to obtain the optimized unsigned OSF variation over multiple cycles. The final result is shown in the bottom panel of Figure 9.1 where the red curve (modeled OSF), closely align with the black curve (in situ observation), confirming that allowing the SS height to vary yields a much better match between simulation and observed data.

We investigate the phase-wise variations in the SS height throughout each solar cycle over the past five cycles, aiming to identify any specific trends or dependencies of the OSF on the SS height model parameter. Panel a of Figure 9.3 represents the time series of SS height variations from solar cycle 20 to 24. We calculate the average SS height for each solar cycle and find a strong correlation between the average SS height and the total magnetic flux content of these cycles. Interestingly, a notable and abrupt reduction in the average SS height is observed from cycle 21 through 24, suggesting that as solar magnetic

activity declines, the SS height also decreases. This correlation indicates a trend where the average SS height during the active phases of a cycle is linked to the overall strength of that cycle.

Figure 9.3b illustrates the SS height variations across 15 phases for each solar cycle from cycle 20 to 24. The black curve in the same panel represents the average SS height variation over the solar cycle phases, obtained by averaging the SS heights across all five cycles. Notably, at the starting and ending phases of the solar cycle – corresponding to solar minima – the average SS height is higher. This behavior is consistent with the understanding that the OSF is generally lower during solar minima. If the SS height were kept lower during these phases, it would erroneously include more open field lines, thus increasing the open flux. Therefore, the SS height increases during solar minima to more accurately represent the reduced levels of open solar flux. We observe a strong correlation between the average polar flux at the final phase of a solar cycle and the SS height at the same phase. Furthermore, the average polar flux at the end of the cycle correlates with the SS height at the starting phase of the subsequent cycle. During the solar cycle minimum, particularly at the starting or ending phase of the cycle, the polar flux (high latitudinal field) generally dominates the global magnetic field due to the minimal emergence of sunspots during this period. As a result, most of the open solar flux is contributed by the polar flux. If the polar flux at the end of the cycle is high, the open solar flux would also be expected to be high. However, this is not typically observed at the cycle minimum, as the open solar flux should decrease. To achieve this reduction in open solar flux, the source surface height needs to be adjusted (increased) based on the average polar flux during these phases. This is because the average polar flux at the end of the cycle influences the source surface height during both this phase and subsequent phases. However, the behavior of SS height during the active phases of the cycle remains less clear from this plot.

We employ three key correlations to reconstruct the SS height variations for past solar cycles: (1) the correlation between the average SS height of a sunspot cycle and the total magnetic flux content of that cycle; (2) the correlation between the average polar flux at the end of a cycle and the SS height during the final phase of that cycle; and (3) the correlation between the average polar flux at the end of a cycle and the SS height at the beginning phase of the subsequent cycle. Using the fitted linear relationships from these three correlation

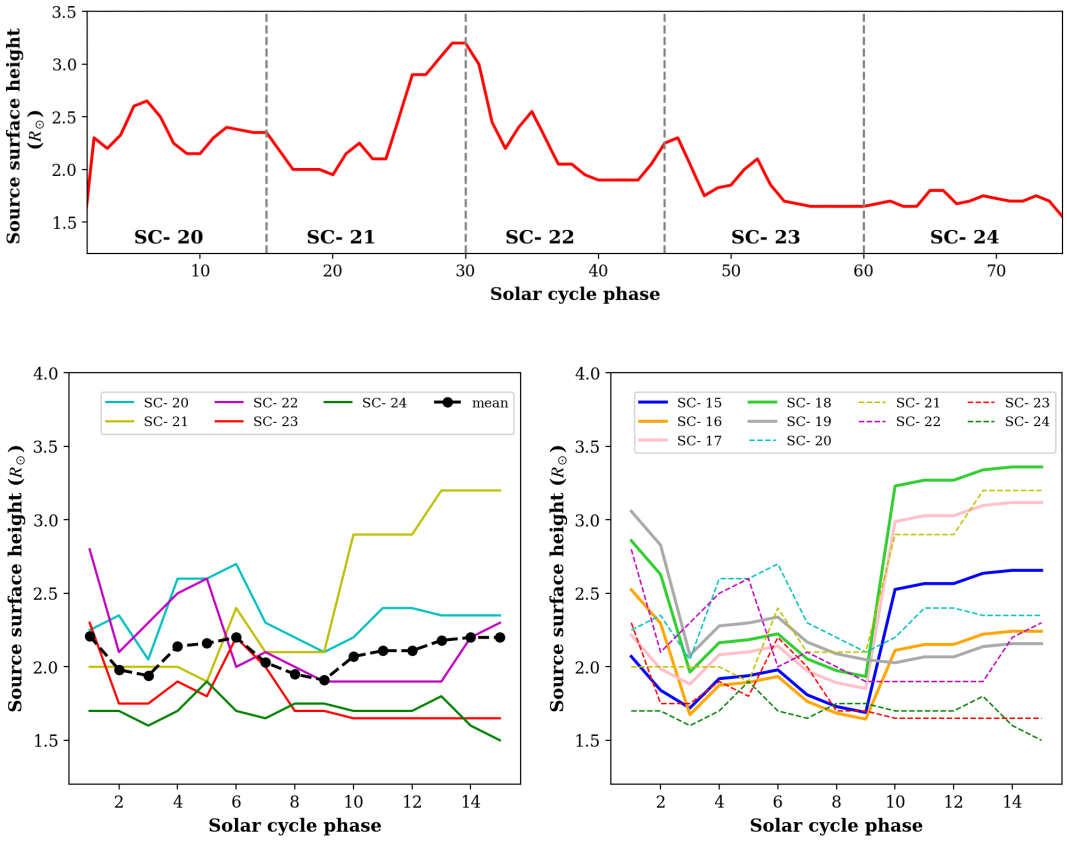


Figure 9.3: SS height variations over different phases of solar cycle 20 to 24 (first panel) and cycle 15 to 24 (second panel). Other details are described in the main text. Certain decrease in source surface height from solar cycle 21 ro 24.

analyses, we adjust the SS height relative to the black curve and reconstruct the dynamic average SS height variations for solar cycles 15 to 19 across each phase of the cycle (see panel c of Figure 9.3). Now, utilizing the SFT-generated surface magnetic maps along

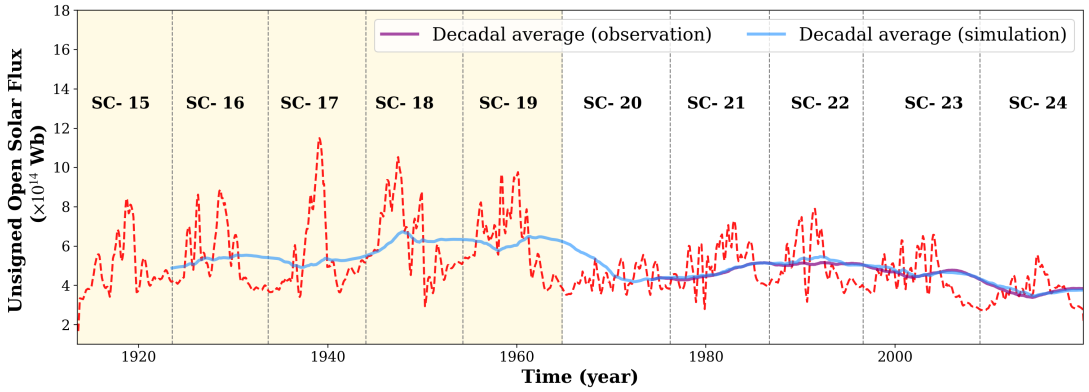


Figure 9.4: Century scale reconstructed OSF. Highlighted region denotes the reconstruction. Decadal average variations of reconstructed OSF.

with dynamically varying SS heights across different phases of the solar cycle in the PFSS model, we calculate the unsigned OSF for past sunspot cycles (cycle 15-19). The reconstruction is shown in Figure 9.4, with the highlighted region representing the reconstructed OSF for solar cycles 15 to 19. The reconstructed OSF exhibits long-term variations that follow a solar cycle-like behavior. Furthermore, when examining the decadal averages, a distinct trend emerges: the OSF gradually increases by approximately 33% between 1920 and 1970. However, following 1970, the OSF began to decline, showing a decrease of nearly 23% up to the present (see Figure 9.4). These findings provide valuable insights into the historical evolution of the Sun's magnetic environment and its connection to solar activity over the past century.

## 9.4 Concluding Remarks

In this study, we present a novel, physics-based approach to reconstruct the long-term evolution of the Sun's open magnetic flux (OSF), a key component of the interplanetary magnetic field (IMF), by coupling data-driven optimized SFT simulations with dynamic PFSS extrapolations. A central advancement of our work lies in demonstrating that allowing the source surface (SS) height to vary with the solar cycle phase significantly improves the

agreement between simulated and observed OSF, effectively addressing the longstanding Open Solar Flux Problem. This phase-dependent optimization captures the Sun's dynamic corona more realistically than models that assume a fixed SS height.

Our results show that the SS height correlates strongly with both the polar flux and the total magnetic flux content of the cycle, revealing a physical connection between the large-scale surface field and the global topology of the coronal field. Notably, we find evidence that the solar corona began a gradual contraction after Solar Cycle 21 (post-1987), coinciding with the decline in solar cycle amplitude and indicating the termination of the Modern Grand Maximum period, which is also noted in Virtanen et al. (2020). Using these correlations, we reconstructed century-scale variations of OSF for solar cycles 15–24. The reconstruction exhibits a solar-cycle-like trend with a long-term modulation of approximately 50 years.

This work opens several directions for future studies and insights into studying solar corona and solar wind. First, the use of idealized PFSS models, which assume a current-free corona, limits the accuracy of open flux estimates –especially during solar maximum, when non-potential magnetic structures become important. Incorporating more realistic, time-dependent models such as magneto-frictional or full magnetohydrodynamic (MHD) frameworks could address this limitation. Second, the empirical constraints we derive on the source surface height offer a useful proxy for estimating the Alfvén surface, which is expected to be directly probed by upcoming missions like PUNCH (Polarimeter to Unify the Corona and Heliosphere).

In summary, our framework provides a reliable and adaptable method for advancing heliospheric reconstructions and space weather modeling. It also leads to predicting future solar wind conditions and open solar flux variations, with potential applications in space climate analysis and operational space weather forecasting.

# Chapter 10

# Concluding Summary and Future Work

In this thesis, we investigate the physics governing the variability of the Sun's magnetic field, from the photosphere to the outer solar atmosphere – the corona and heliosphere. A central focus of our work is the development of a data-driven Surface Flux Transport model, **SPhoTraM**, which we use to study the long-term evolution of the solar surface magnetic field. In addition, we employ various coronal magnetic field models to predict the short-term dynamics of the solar corona and to reconstruct the long-term evolution of the open magnetic flux that extends to Earth. We investigate the underlying causes of solar cycle irregularities observed in sunspot records using solar flux transport dynamo models and explore how other solar features – such as polar filaments – can serve as proxies for polar field build-up. Furthermore, we demonstrate that the solar axial dipole moment acts as the most reliable predictor of future solar cycle strength from both observational and Babcock–Leighton dynamo perspectives. A key objective of this thesis is to understand the fundamental role of the Babcock–Leighton mechanism in governing polar field dynamics through analytical theory, numerical modeling, and observational analysis.

Here, we briefly summarize the content of each chapter in this thesis. Chapter 1 presents the introduction, providing the conceptual foundation and motivation that guide the subsequent chapters. The remaining chapters (Chapters 2 to 9) are outlined as follows:

**Chapter 2: First-principle based Numerical Models**

This chapter presents a comprehensive study of first-principles-based numerical models used to investigate the Sun's magnetic field evolution from its surface to the solar corona. We have newly developed a data-driven Surface Flux Transport (SFT) model called SPho-

TraM, which evolves the solar surface magnetic field by solving the radial magnetic induction equation. Through systematic parameter studies, we find that the emergence latitude plays the most dominant role in determining the evolution of the polar flux, while variations in tilt angle, flux content, and polarity separation also influence the polar field build-up. We have also studied the effect of meridional circulation and diffusion in large-scale polar field build-up through a rigorous parameter space study. To model the solar corona, we implement two types of extrapolation: the Potential Field Source Surface (PFSS) model, which assumes a current-free corona, and the Alfvén Wave Solar-atmosphere Model (AWSoM), a full MHD model that accounts for Alfvén wave-driven heating and wind acceleration. Additionally, we use the SURYA solar dynamo model to simulate solar cycle evolution based on the Babcock–Leighton mechanism.

**Chapter 3: Algebraic Quantification of the Sun's Dipole Moment**

In this chapter, we apply a simplified analytic method to estimate the Sun's axial dipole moment at solar minima by using the observed properties of bipolar magnetic regions (BMRs). This method bypasses complex numerical simulations and instead quantifies individual active regions' contributions to the global dipole field. We apply this approach to historical sunspot data spanning solar cycles 14 to 24, validate our estimates against multiple polar field proxies, and establish strong correlations. Using this method, we reconstruct a century-scale dipole moment time series and find that it strongly correlates with the strength of the subsequent solar cycles, confirming the dipole moment as a robust precursor. Our prediction for Solar Cycle 25 suggests a moderate peak sunspot number of 127, consistent with cycle amplitudes between cycles 20 and 24. We further analyze how dipole moment build-up depends on BMR characteristics such as latitude, tilt, and flux. While the method works well overall, it struggles with anomalous cycles like Solar Cycle 19 due to the sheer number and flux of sunspots.

**Chapter 4: Solar Cycle Fluctuations: Impact of Anomalous Sunspots**

In this chapter, we investigate how anomalous active regions – sunspots that deviate from Hale's polarity law and Joy's tilt law – affect the long-term evolution of the Sun's large-scale magnetic field, particularly the axial dipole moment and polar flux. Using a surface

flux transport (SFT) model, we simulate the magnetic evolution driven by both typical and anomalous bipolar magnetic regions (BMRs). The study reveals that even a small percentage of such anomalous regions (e.g., Anti-Hale or Anti-Joy configurations) can substantially weaken the solar dipole moment and delay its polarity reversal, impacting the strength and duration of the next solar cycle. We explore how these effects depend on the emergence time, latitude, flux content, and number of anomalous BMRs. Interestingly, the impact from Anti-Hale and Anti-Joy regions appears similar due to differential rotation, which makes their orientation dynamically equivalent over time. We also find that low-latitude and mid-phase emergences have the strongest influence. A theoretical framework described in Chapter 3 supports these numerical results, confirming that the latitudinal position and orientation of active regions are crucial in determining their contribution to the dipole moment.

**Chapter 5: Investigating the Drivers of Extreme Variability in Solar Activity Over Cycle 19-20**

In this chapter, we explore the drivers behind extreme variations in solar activity over the past century, focusing on the transition from the historically strong Solar Cycle 19 to the weaker Cycle 20. We develop and use a coupled, data-driven surface flux transport model (SPhoTraM) and a solar dynamo model to simulate the Sun's magnetic field evolution. By incorporating tilt-angle scatter and anti-Hale sunspot emergences into our Monte Carlo ensemble simulations, we accurately reproduce observed polar flux and dipole moment variations across multiple solar cycles. Our results highlight the crucial role of stochastic perturbations – especially variations in sunspot tilt angles and polarity orientations – in shaping solar cycle amplitudes. We show that these stochastic effects are more influential than nonlinear feedback processes in generating extreme solar variability. By quantifying active region anomalies using the ARDoR metric, we find that cycles like 18, 19, and 20 require a significant degree of randomness to explain their behavior. Our findings suggest that such randomness can account for grand transitions in solar activity, including the possibility of entering grand minima episodes like the Maunder Minimum.

**Chapter 6: Comparative Analysis of Polar Precursors for Solar Cycle Prediction: Global Dipole Moment versus Hemispheric Polar Flux**

This chapter focuses on identifying the more effective polar magnetic precursor for solar cycle prediction. Using century-long reconstructions, it demonstrates that the axial dipole moment shows a stronger and earlier correlation with the amplitude and timing of the next solar cycle than hemispheric polar flux. It also introduces an alternative early-cycle precursor, based on the rise rate of the dipole moment and the solar cycle length, which can enable forecasts several years before solar minimum.

**Chapter 7: Polar Filaments as a Solar Cycle Precursor: A Babcock–Leighton Dynamo Model Perspective**

In this chapter, we explore the potential of polar filaments – long, cool plasma structures visible in H$\alpha$ – as indicators of the Sun's polar magnetic field evolution and their value in forecasting solar cycle strength. These filaments, especially those near the solar poles, form along polarity inversion lines during magnetic field interactions and show a strong connection with the Babcock–Leighton mechanism responsible for poloidal field generation. Using observational data from Meudon Synoptic Maps (Cycles 16–21) and surface flux transport simulations (SPhoTraM), the chapter demonstrates that polar filaments peak during the rising phase of the solar cycle, decline post-polar field reversal, and are closely tied to the buildup of polar magnetic flux. A key finding is the statistically significant correlation between the remnant polar filament area or length and the strength of the polar magnetic field at the cycle's end. This positions polar filaments as reliable, independent proxies for understanding and predicting solar magnetic activity.

**Chapter 8: The Sun's Large-Scale Corona has a Dynamical Memory of Magnetism: Insights from Predicting the 08 April 2024 Total Solar Eclipse**

In this chapter, we predict total solar eclipses to study the Sun's corona, especially during solar maximum, utilizing physics-based solar magnetic field evolution models. We use our calibrated Solar Photospheric-flux Transport Model (SPhoTraM) and its role in predicting the Sun's surface magnetic field one week prior to the 2024 eclipse. Coupled with a full MHD coronal model (AWSoM), this prediction allows us to compare our prediction with

solar eclipse observations to test how accurate these physical models are. We have also studied whether the large-scale corona carries a 'magnetic memory' even during highly dynamic solar maximum conditions.

**Chapter 9: Reconstructing Long-Term Open Solar Flux Variations**

In this chapter, we investigate the long-term evolution of the Sun's open magnetic flux (OSF), a key contributor to the interplanetary magnetic field (IMF), by coupling a physics-based surface flux transport (SFT) model with potential field source surface (PFSS) extrapolations. Using a data-driven approach, we simulate the Sun's surface magnetic field over the last century and dynamically adjust the source surface (SS) height across different phases of the solar cycle to address the long-standing open solar flux problem. We show that allowing the SS height to vary significantly improves the match between simulated and observed OSF. Our study finds strong correlations between the SS height and the surface magnetic field's polar and total flux, revealing how the surface field governs the corona's global topology. We reconstruct century-scale OSF variations for solar cycles 15–24 and discover a long-term modulation, including a decline in SS height and OSF after Cycle 21, indicating the end of the Modern Grand Maximum.

## 10.1 Future Work

One of the most important aspects of this thesis has been the reconstruction of the observationally optimized surface magnetic field evolution over the past century using our newly developed Surface Flux Transport (SFT) model. This effort provides century-scale surface magnetic maps of the Sun, offering a powerful resource for investigating the long-term magnetic and dynamical behavior of the solar surface. For instance, using these reconstructed maps, we have already addressed the long-standing open solar flux problem by reproducing its century-scale variations. As a future extension, this dataset can be utilized to explore other long-term solar variability phenomena and their connection with observational records—such as total solar irradiance, modulation potential, heliospheric current sheet tilt variations, and galactic cosmic ray flux. These studies will help establish a more comprehensive picture of how surface magnetic field evolution influences the broader heliospheric environment.

From a more fundamental perspective, the reconstructed dataset also enables us to investigate the interplay between nonlinearity and stochasticity in the SFT processes that govern polar field evolution, and thereby the amplitude of subsequent sunspot cycles. This aspect can also be further explored using the simplified algebraic prescription introduced in Chapter 3 of this thesis.

By coupling the SFT models with the coronal magnetic field evolution models, we are also now well placed to perform the data driven simulations of the solar corona and device methodologies to move from global structures to exploring eruptive structures which may give rise to flares and CMEs. Our data-driven coronal magnetic field models can be further calibrated using direct observations, providing valuable context for upcoming initiatives in coronal magnetometry. These efforts will help bridge the gap between model-based and observational constraints, enabling more accurate reconstruction of the coronal magnetic field. For example, forward modeling of polarization signatures – such as Stokes parameters and white-light polarization – can be performed using the magnetic and plasma parameters derived from our coronal model. The resulting synthetic polarization maps can then be compared with observations from existing instruments such as MLSO/CoMP and future missions like DKIST and PUNCH. Such comparisons will be instrumental in validating and refining both the coronal magnetic field models and the next generation of coronal magnetometry techniques.

Moreover, solar wind forecasting schemes can be developed by coupling our data-driven SFT models with magnetohydrodynamic (MHD) models of the solar corona and solar wind, such as HUXt. These coupled models can be calibrated using in-situ measurements from the OMNI database, thereby enabling both solar wind and space weather predictions. The predictive framework established through this work is also of particular relevance in the context of recently launched and upcoming space missions aimed at exploring the solar corona – such as NASA's PUNCH mission, ISRO's Aditya-L1 mission, and ESA's Proba-3 mission – which together will provide valuable observational inputs to validate and advance such data-driven modeling efforts.

# Bibliography


Abbo, L., Ofman, L., Antiochos, S. K., Hansteen, V. H., Harra, L., Ko, Y. K., Lapenta, G., Li, B., Riley, P., Strachan, L., von Steiger, R., and Wang, Y. M. (2016). Slow Solar Wind: Observations and Modeling. *Space Science Reviews*, 201(1-4):55–108.

Airapetian, V. S., Barnes, R., Cohen, O., Collinson, G. A., Danchi, W. C., Dong, C. F., Del Genio, A. D., France, K., Garcia-Sage, K., Glocer, A., and et al. (2020). Impact of space weather on climate and habitability of terrestrial-type exoplanets. *International Journal of Astrobiology*, 19(2):136–194.

Antonucci, E., Harra, L., Susino, R., and Telloni, D. (2020). Observations of the Solar Corona from Space. *Space Science Reviews*, 216(8):117.

Arden, W. M., Norton, A. A., and Sun, X. (2014). A "breathing" source surface for cycles 23 and 24. *Journal of Geophysical Research (Space Physics)*, 119(3):1476–1485.

Arge, C. N., Leisner, A., Antiochos, S. K., Wallace, S., and Henney, C. J. (2024). Proposed Resolution to the Solar Open Magnetic Flux Problem. *The Astrophysical Journal*, 964(2):115.

Aschwanden, M. J., Poland, A. I., and Rabin, D. M. (2001). The New Solar Corona. *Annual Review of Astronomy and Astrophysics*, 39:175–210.

Aschwanden, M. J., Winebarger, A., Tsiklauri, D., and Peter, H. (2007). The Coronal Heating Paradox. *The Astrophysical Journal*, 659(2):1673–1681.

Axford, W. I. (1985). The Solar Wind. *Solar Physics*, 100:575.

Babcock, H. W. (1961). The Topology of the Sun's Magnetic Field and the 22-YEAR Cycle. *The Astrophysical Journal*, 133:572.

Balbus, S. A. and Latter, H. N. (2010). The tachocline and differential rotation in the Sun. *Monthly Notices in Royal Astronomical Society*, 407(4):2565–2574.

Balogh, A., Smith, E. J., Tsurutani, B. T., Southwood, D. J., Forsyth, R. J., and Horbury, T. S. (1995). The Heliospheric Magnetic Field Over the South Polar Region of the Sun. *Science*, 268(5213):1007–1010.

Basu, S. and Antia, H. M. (2008). Helioseismology and solar abundances. *Physics Reports*, 457(5-6):217–283.

Baumann, I., Schmitt, D., Schüssler, M., and Solanki, S. K. (2004). Evolution of the large-scale magnetic field on the solar surface: A parameter study. *Astronomy and Astrophysics*, 426:1075–1091.

Bhowmik, P. (2019). Polar flux imbalance at the sunspot cycle minimum governs hemispheric asymmetry in the following cycle. *Astronomy and Astrophysics*, 632:A117.

Bhowmik, P., Jiang, J., Upton, L., Lemerle, A., and Nandy, D. (2023). Physical Models for Solar Cycle Predictions. *Space Science Reviews*, 219(5):40.

Bhowmik, P. and Nandy, D. (2018). Prediction of the strength and timing of sunspot cycle 25 reveal decadal-scale space environmental conditions. *Nature Communications*, 9:5209.

Blackwell, D. E. and Petford, A. D. (1966). Observations of the 1963 July 20 solar eclipse. I Spectroscopic separation of the F K components of the solar corona at large distances from the Sun. *Monthly Notices in Royal Astronomical Society*, 131:383.

Blazek, J. (2005). *Computational Fluid Dynamics: Principles and Applications*. Elsevier.

Boe, B., Habbal, S., and Druckmüller, M. (2020). Coronal Magnetic Field Topology from Total Solar Eclipse Observations. *The Astrophysical Journal*, 895(2):123.

Brett, L. (1988). Methods of Spherical Harmonic Analysis. *Quarterly Journal of the Royal Astronomical Society*, 29:129.

Broiles, T. W., Desai, M. I., and McComas, D. J. (2012). Formation, shape, and evolution of magnetic structures in CIRs at 1 AU. *Journal of Geophysical Research (Space Physics)*, 117(A3):A03102.

Brueckner, G. E., Howard, R. A., Koomen, M. J., Korendyke, C. M., Michels, D. J., Moses, J. D., Socker, D. G., Dere, K. P., Lamy, P. L., Llebaria, A., Bout, M. V., Schwenn, R., Simnett, G. M., Bedford, D. K., and Eyles, C. J. (1995). The Large Angle Spectroscopic Coronagraph (LASCO). *Solar Physics*, 162(1-2):357–402.

Brun, A. (2020). *On Solar and Solar-Like Stars Convection, Rotation and Magnetism*, pages 75–89.

Cameron, R. and Schüssler, M. (2015). The crucial role of surface magnetic fields for the solar dynamo. *Science*, 347(6228):1333–1335.

Cameron, R. H., Jiang, J., Schmitt, D., and Schüssler, M. (2010). Surface Flux Transport Modeling for Solar Cycles 15-21: Effects of Cycle-Dependent Tilt Angles of Sunspot Groups. *The Astrophysical Journal*, 719(1):264–270.

Cameron, R. H. and Schüssler, M. (2017). An update of Leighton's solar dynamo model. *Astronomy and Astrophysics*, 599:A52.

Carrington, R. C. (1858). On the Distribution of the Solar Spots in Latitude since the Beginning of the Year 1854; with a Map. *Monthly Notices of the Royal Astronomical Society*, 19(1):1–3.

Caspi, A., Seaton, D. B., Tsang, C. C. C., DeForest, C. E., Bryans, P., DeLuca, E. E., Tomczyk, S., Burkepile, J. T., Casey, T. T., Collier, J., Darrow, D. D., Del Rosso, D., Durda, D. D., Gallagher, P. T., Golub, L., Jacyna, M., Johnson, D. D., Judge, P. G., Klemm, C. D., Laurent, G. T., Lewis, J., Mallini, C. J., Parent, T. D., Propp, T., Steffl, A. J., Warner, J., West, M. J., Wiseman, J., Yates, M., Zhukov, A. N., and NASA WB-57 2017 Eclipse Observing Team (2020). A New Facility for Airborne Solar Astronomy: NASA's WB-57 at the 2017 Total Solar Eclipse. *The Astrophysical Journal*, 895(2):131.

Chandran, B. D. G., Quataert, E., Howes, G. G., Xia, Q., and Pongkitiwanichakul, P. (2009). Constraining Low-Frequency Alfvénic Turbulence in the Solar Wind Using Density-Fluctuation Measurements. *The Astrophysical Journal*, 707(2):1668–1675.

Charbonneau, P. (2007). Babcock–leighton models of the solar cycle: Questions and issues. *Advances in Space Research*, 39(11):1661–1669.

Charbonneau, P. (2020). Dynamo models of the solar cycle. *Living Reviews in Solar Physics*, 17(1):4.

Charbonneau, P., Christensen-Dalsgaard, J., Henning, R., Larsen, R. M., Schou, J., Thompson, M. J., and Tomczyk, S. (1999). Helioseismic Constraints on the Structure of the Solar Tachocline. *The Astrophysical Journal*, 527(1):445–460.

Charbonneau, P. and Dikpati, M. (2000). Stochastic Fluctuations in a Babcock-Leighton Model of the Solar Cycle. *The Astrophysical Journal*, 543(2):1027–1043.

Chatterjee, P., Nandy, D., and Choudhuri, A. R. (2004). Full-sphere simulations of a circulation-dominated solar dynamo: Exploring the parity issue. *Astronomy and Astrophysics*, 427:1019–1030.

Chebly, J. J., Alvarado-Gómez, J. D., and Poppenhaeger, K. (2022). Destination exoplanet: Habitability conditions influenced by stellar winds properties. *Astronomische Nachrichten*, 343(4):e10093.

Chen, R. and Zhao, J. (2017). A Comprehensive Method to Measure Solar Meridional Circulation and the Center-to-limb Effect Using Time-Distance Helioseismology. *The Astrophysical Journal*, 849(2):144.

Cheung, M. C. M. and Isobe, H. (2014). Flux Emergence (Theory). *Living Reviews in Solar Physics*, 11(1):3.

Choudhuri, A. R. (1998). *The Physics of Fluids and Plasmas: An Introduction for Astrophysicists*.

Choudhuri, A. R. (2000). The Current Status of Kinematic Solar Dynamo Models. *Journal of Astrophysics and Astronomy*, 21(3-4):373–377.

Choudhuri, A. R. (2018). Flux transport dynamo: From modelling irregularities to making predictions. *Journal of Atmospheric and Solar-Terrestrial Physics*, 176:5–9.

Choudhuri, A. R. and Gilman, P. A. (1987). The Influence of the Coriolis Force on Flux Tubes Rising through the Solar Convection Zone. *The Astrophysical Journal*, 316:788.

Choudhuri, A. R., Schussler, M., and Dikpati, M. (1995). The solar dynamo with meridional circulation. *Astronomy and Astrophysics*, 303:L29.

Christensen-Dalsgaard, J. (2002). Helioseismology. *Reviews of Modern Physics*, 74(4):1073–1129.

Ciecholewski, M. (2015). Automated coronal hole segmentation from solar euv images using the watershed transform. *Journal of Visual Communication and Image Representation*, 33:203–218.

Clark, D. H. and Stephenson, F. R. (1978). An Interpretation of the Pre-Telescopic Sunspot Records from the Orient. *Quarterly Journal of the Royal Astronomical Society*, 19:387.

Clette, F., Cliver, E., Lefèvre, L., Svalgaard, L., and Vaquero, J. (2015). Revision of the sunspot number(s). *Space Weather*, 13.

Cliver, E. W. (2014). The Extended Cycle of Solar Activity and the Sun's 22-Year Magnetic Cycle. *Space Science Reviews*, 186(1-4):169–189.

Cranmer, S. R. (2009). Coronal Holes. *Living Reviews in Solar Physics*, 6(1):3.

Cranmer, S. R. and Winebarger, A. R. (2019). The Properties of the Solar Corona and Its Connection to the Solar Wind. *Annual Review of Astronomy and Astrophysics*, 57:157–187.

Daglis, I. A., Chang, L. C., Dasso, S., Gopalswamy, N., Khabarova, O. V., Kilpua, E., Lopez, R., Marsh, D., Matthes, K., Nandy, D., Seppälä, A., Shiokawa, K., Thiéblemont, R., and Zong, Q. (2021). Predictability of variable solar-terrestrial coupling. *Annales Geophysicae*, 39(6):1013–1035.

Dalal, S., Haywood, R. D., Mortier, A., Chaplin, W. J., and Meunier, N. (2023). Predicting convective blueshift and radial-velocity dispersion due to granulation for FGK stars. *Monthly Notices in Royal Astronomical Society*, 525(3):3344–3353.

Darwish, M. and Moukalled, F. (2003). Tvd schemes for unstructured grids. *International Journal of Heat and Mass Transfer*, 46(4):599–611.

Dash, S., Bhowmik, P., S, A. B., Ghosh, N., and Nandy, D. (2020). Prediction of the sun's coronal magnetic field and forward-modeled polarization characteristics for the 2019 july 2 total solar eclipse. *The Astrophysical Journal*, 890(1):37.

Dash, S., Nandy, D., and Pal, S. (2020). Dynamics of the Sun's Polar Field: Possible Insights from Out of the Ecliptic Observations. In *AGU Fall Meeting Abstracts*, volume 2020, pages SH014–06.

Dash, S., Nandy, D., and Usoskin, I. (2023). Long-term forcing of the Sun's coronal field, open flux, and cosmic ray modulation potential during grand minima, maxima, and regular activity phases by the solar dynamo mechanism. *Monthly Notices in Royal Astronomical Society*, 525(4):4801–4814.

Dasi-Espuig, M., Solanki, S. K., Krivova, N. A., Cameron, R., and Peñuela, T. (2010). Sunspot group tilt angles and the strength of the solar cycle. *Astronomy and Astrophysics*, 518:A7.

De Moortel, I. and Browning, P. (2015). Recent advances in coronal heating. *Philosophical Transactions of the Royal Society of London Series A*, 373(2042):20140269–20140269.

Deforest, C., Killough, R., Gibson, S., Henry, A., Case, T., Beasley, M., Laurent, G., Colaninno, R., Waltham, N., and Punch Science Team (2022). Polarimeter to UNify the Corona and Heliosphere (PUNCH): Science, Status, and Path to Flight. In *2022 IEEE Aerospace Conference*, pages 1–11.

Dikpati, M., de Toma, G., and Gilman, P. A. (2006). Predicting the strength of solar cycle 24 using a flux-transport dynamo-based tool. *Geophysical Research Letters*, 33(5).

Dikpati, M., Gilman, P. A., and de Toma, G. (2008). The waldmeier effect: An artifact of the definition of wolf sunspot number? *The Astrophysical Journal*, 673(1):L99–L101.

Domingo, V., Fleck, B., and Poland, A. I. (1995). SOHO: The Solar and Heliospheric Observatory. *Space Science Reviews*, 72(1-2):81–84.

Downs, C., Linker, J. A., Caplan, R. M., Mason, E. I., Riley, P., Davidson, R., Reyes, A., Palmerio, E., Lionello, R., Turtle, J., Ben-Nun, M., Stulajter, M. M., Titov, V. S., Török, T., Upton, L. A., Attie, R., Jha, B. K., Arge, C. N., Henney, C. J., Valori, G., Strecker, H., Calchetti, D., Germerott, D., Hirzberger, J., Suárez, D. O., Rodríguez, J. B., Solanki, S. K., Cheng, X., and Wu, S. (2025). A near-real-time data-assimilative model of the solar corona. *Science*, 388(6753):1306–1310.

Druckmüller, M., Rušin, V., and Minarovjech, M. (2006). A new numerical method of total solar eclipse photography processing. *Contributions of the Astronomical Observatory Skalnate Pleso*, 36(3):131–148.

D'Silva, S. and Choudhuri, A. R. (1993). A theoretical model for tilts of bipolar magnetic regions. *Astronomy and Astrophysics*, 272:621.

Durney, B. (1974). On the sun's differential rotation. *Solar Physics*, 38.

Durrant, C. J., Turner, J. P. R., and Wilson, P. R. (2004). The Mechanism involved in the Reversals of the Sun's Polar Magnetic Fields. *Solar Physics*, 222(2):345–362.

Duvall, Jr., T. L. (1979). Large-scale solar velocity fields. *Solar Physics*, 63(1):3–15.

Eddington, A. S. (1925). Circulating currents in rotating stars. *The Observatory*, 48:73–75.

Fan, Y. (2021). Magnetic fields in the solar convection zone. *Living Reviews in Solar Physics*, 18(1):5.

Feldman, U., Landi, E., and Schwadron, N. A. (2005). On the sources of fast and slow solar wind. *Journal of Geophysical Research (Space Physics)*, 110(A7):A07109.

Fisher, G. H., Fan, Y., and Howard, R. F. (1995). Comparisons between Theory and Observation of Active Region Tilts. *The Astrophysical Journal*, 438:463.

Fisk, L. A. and Schwadron, N. A. (2001). Origin of the Solar Wind: Theory. *Space Science Reviews*, 97:21–33.

Frost, A. M., Owens, M., Macneil, A., and Lockwood, M. (2022). Estimating the Open Solar Flux from In-Situ Measurements. *Solar Physics*, 297(7):82.

Garraffo, C., Alvarado-Gómez, J. D., Cohen, O., and Drake, J. J. (2022). Revisiting the Space Weather Environment of Proxima Centauri b. *The Astrophysical Journal Letters*, 941(1):L8.

Gary, G. A. (2001). Plasma Beta above a Solar Active Region: Rethinking the Paradigm. *Solar Physics*, 203(1):71–86.

Gilman, P. A. (2018). Magnetic Buoyancy and Rotational Instabilities in the Tachocline. *The Astrophysical Journal*, 853(1):65.

Gizon, L., Cameron, R. H., Pourabdian, M., Liang, Z.-C., Fournier, D., Birch, A. C., and Hanson, C. S. (2020). Meridional flow in the Sun's convection zone is a single cell in each hemisphere. *Science*, 368(6498):1469–1472.

Golub, L. and Pasachoff, J. M. (2009). *The Solar Corona*.

Gombosi, T. I., Chen, Y., Glocer, A., Huang, Z., Jia, X., Liemohn, M. W., Manchester, W. B., Pulkkinen, T., Sachdeva, N., Al Shidi, Q., Sokolov, I. V., Szente, J., Tenishev, V., Toth, G., van der Holst, B., Welling, D. T., Zhao, L., and Zou, S. (2021). What sustained multi-disciplinary research can achieve: The space weather modeling framework. *Journal of Space Weather and Space Climate*, 11:42.

Grinsted, A., Moore, J. C., and Jevrejeva, S. (2004). Application of the cross wavelet transform and wavelet coherence to geophysical time series. *Nonlinear Processes in Geophysics*, 11(5/6):561–566.

Guo, Y., Xia, C., and Keppens, R. (2016). Magneto-frictional Modeling of Coronal Nonlinear Force-free Fields. II. Application to Observations. *The Astrophysical Journal*, 828(2):83.

Hale, G. E. (1908). On the Probable Existence of a Magnetic Field in Sun-Spots. *The Astrophysical Journal*, 28:315.

Hale, G. E., Ellerman, F., Nicholson, S. B., and Joy, A. H. (1919). The Magnetic Polarity of Sun-Spots. *The Astrophysical Journal*, 49:153.

Hale, G. E. and Nicholson, S. B. (1925). The Law of Sun-Spot Polarity. *The Astrophysical Journal*, 62:270.

Hanasoge, S. M. (2022). Surface and interior meridional circulation in the Sun. *Living Reviews in Solar Physics*, 19(1):3.

Hanasoge, S. M. and Sreenivasan, K. R. (2014). The Quest to Understand Supergranulation and Large-Scale Convection in the Sun. *Solar Physics*, 289(9):3403–3419.

Harvey, J. W. and Sheeley, Jr., N. R. (1979). Coronal Holes and Solar Magnetic Fields (Article published in the special issues: Proceedings of the Symposium on Solar Terrestrial Physics held in Innsbruck, May- June 1978. (pp. 137-538)). *Space Science Reviews*, 23(2):139–158.

Hathaway, D. H. (1993). Doppler Measurement of the Solar Meridional Circulation. In Brown, T. M., editor, *GONG 1992. Seismic Investigation of the Sun and Stars*, volume 42 of *Astronomical Society of the Pacific Conference Series*, page 265.

Hathaway, D. H. (2010a). The Solar Cycle. *Living Reviews in Solar Physics*, 7(1):1.

Hathaway, D. H. (2010b). The Solar Cycle. *Living Reviews in Solar Physics*, 7(1):1.

Hathaway, D. H. (2012). Supergranules as Probes of the Sun's Meridional Circulation. *The Astrophysical Journal*, 760(1):84.

Hathaway, D. H. (2015). The solar cycle. *Living Reviews in Solar Physics*, 12(1):4.

Hazra, G. and Choudhuri, A. R. (2017). A theoretical model of the variation of the meridional circulation with the solar cycle. *Monthly Notices in Royal Astronomical Society*, 472(3):2728–2741.

Hazra, G., Nandy, D., Kitchatinov, L., and Choudhuri, A. R. (2023). Mean Field Models of Flux Transport Dynamo and Meridional Circulation in the Sun and Stars. *Space Science Reviews*, 219(5):39.

Hazra, S., Cohen, O., and Sokolov, I. V. (2022). Exoplanet Radio Transits as a Probe for Exoplanetary Magnetic Fields-Time-dependent MHD Simulations. *The Astrophysical Journal*, 936(2):144.

Hazra, S., Cohen, O., and Sokolov, I. V. (2025). An MHD simulation of the possible modulations of stellar CMEs radio observations by an exoplanetary magnetosphere. *New Astronomy*, 119:102420.

Hazra, S. and Nandy, D. (2016). A Proposed Paradigm for Solar Cycle Dynamics Mediated via Turbulent Pumping of Magnetic Flux in Babcock-Leighton-type Solar Dynamos. *The Astrophysical Journal*, 832(1):9.

Hazra, S. and Nandy, D. (2019). The origin of parity changes in the solar cycle. *Monthly Notices of the Royal Astronomical Society*, 489(3):4329–4337.

Hazra, S., Passos, D., and Nandy, D. (2014). A Stochastically Forced Time Delay Solar Dynamo Model: Self-consistent Recovery from a Maunder-like Grand Minimum Necessitates a Mean-field Alpha Effect. *The Astrophysical Journal*, 789(1):5.

Hazra, S., Réville, V., Perri, B., Strugarek, A., Brun, A. S., and Buchlin, E. (2021). Modeling Solar Wind Variations over an 11 Year Cycle with Alfvén Wave Dissipation: A Parameter Study. *The Astrophysical Journal*, 910(2):90.

Henadhira Arachchige, K., Cohen, O., Munoz-Jaramillo, A., and Yeates, A. R. (2022). Comparing the Performance of a Solar Wind Model from the Sun to 1 au Using Real and Synthetic Magnetograms. *The Astrophysical Journal*, 938(1):39.

Higginson, A. K., Antiochos, S. K., DeVore, C. R., Wyper, P. F., and Zurbuchen, T. H. (2017). Dynamics of Coronal Hole Boundaries. *The Astrophysical Journal*, 837(2):113.

Hoeksema, J. T. (1984). *Structure and Evolution of the Large Scale Solar and Heliospheric Magnetic Fields.* PhD thesis, Stanford University, California.

Hotta, H., Bekki, Y., Gizon, L., Noraz, Q., and Rast, M. (2023). Dynamics of Large-Scale Solar Flows. *Space Science Reviews*, 219(8):77.

Howard, R. (1979). Evidence for large-scale velocity features on the sun. *The Astrophysical Journal Letters*, 228:L45–L50.

Howard, R. A., Thernisien, A. F., Vourlidas, A., Plunkett, S. P., Korendyke, C. M., Sheeley, N. R., Morrill, J. S., Socker, D. G., Linton, M. G., Liewer, P. C., De Jong, E. M., Velli, M. M., Mikic, Z., Bothmer, V., and Lamy, P. L. (2011). Observations of the White Light Corona from Solar Orbiter and Solar Probe Plus. In *AGU Fall Meeting Abstracts*, volume 2011, pages SH43F–06.

Huang, Z., Tóth, G., Sachdeva, N., Zhao, L., van der Holst, B., Sokolov, I., Manchester, W. B., and Gombosi, T. I. (2023). Modeling the Solar Wind during Different Phases of the Last Solar Cycle. *The Astrophysical Journal Letters*, 946(2):L47.

Iijima, H., Hotta, H., Imada, S., Kusano, K., and Shiota, D. (2017). Improvement of solar-cycle prediction: Plateau of solar axial dipole moment. *Astronomy and Astrophysics*, 607:L2.

Ivanov, V. G. and Miletsky, E. V. (2014). Spörer's law and relationship between the latitude and amplitude parameters of solar activity. *Geomagnetism and Aeronomy*, 54(7):907–914.

Jaswal, P., Saha, C., and Nandy, D. (2024). Discovery of a relation between the decay rate of the Sun's magnetic dipole and the growth rate of the following sunspot cycle: a new precursor for solar cycle prediction. *Monthly Notices in Royal Astronomical Society*, 528(1):L27–L32.

Jha, B. K. and Upton, L. A. (2024). Predicting the Timing of the Solar Cycle 25 Polar Field Reversal. *The Astrophysical Journal Letters*, 962(1):L15.

Jiang, J. (2020). Nonlinear Mechanisms that Regulate the Solar Cycle Amplitude. *The Astrophysical Journal*, 900(1):19.

Jiang, J., Cameron, R. H., Schmitt, D., and Işık, E. (2013). Modeling solar cycles 15 to 21 using a flux transport dynamo. *Astronomy and Astrophysics*, 553:A128.

Jiang, J., Cameron, R. H., Schmitt, D., and Schüssler, M. (2011). The solar magnetic field since 1700. I. Characteristics of sunspot group emergence and reconstruction of the butterfly diagram. *Astronomy and Astrophysics*, 528:A82.

Jiang, J., Cameron, R. H., and Schüssler, M. (2015). The Cause of the Weak Solar Cycle 24. *The Astrophysical Journal Letters*, 808(1):L28.

Jiang, J., Cameron, R. H., and Schüssler, M. (2014). EFFECTS OF THE SCATTER IN SUNSPOT GROUP TILT ANGLES ON THE LARGE-SCALE MAGNETIC FIELD AT THE SOLAR SURFACE. *The Astrophysical Journal*, 791(1):5.

Jiang, J., Chatterjee, P., and Choudhuri, A. R. (2007). Solar activity forecast with a dynamo model. *Monthly Notices in Royal Astronomical Society*, 381(4):1527–1542.

Jiang, J., Hathaway, D. H., Cameron, R. H., Solanki, S. K., Gizon, L., and Upton, L. (2014). Magnetic Flux Transport at the Solar Surface. *Space Science Reviews*, 186(1-4):491–523.

Jiang, J., Song, Q., Wang, J.-X., and Baranyi, T. (2019). Different Contributions to Space Weather and Space Climate from Different Big Solar Active Regions. *The Astrophysical Journal*, 871(1):16.

Jiang, J., Zhang, Z., and Petrovay, K. (2023). Comparison of physics-based prediction models of solar cycle 25. *Journal of Atmospheric and Solar-Terrestrial Physics*, 243:106018.

Jiao, Q., Jiang, J., and Wang, Z.-F. (2021). Sunspot tilt angles revisited: Dependence on the solar cycle strength. *Astronomy and Astrophysics*, 653:A27.

Jouve, L., Hung, C. P., Brun, A. S., Hazra, S., Fournier, A., Talagrand, O., Perri, B., and Strugarek, A. (2025). Forecasting the solar cycle using variational data assimilation: Validation on cycles 22 to 25. *Astronomy and Astrophysics*, 699:A30.

Karadimou, D. P. and Markatos, N.-C. (2018). Study of the numerical diffusion in computational calculations. In Rao, S. P., editor, *Numerical Simulations in Engineering and Science*, chapter 4. IntechOpen, Rijeka.

Karak, B. B. (2023). Models for the long-term variations of solar activity. *Living Reviews in Solar Physics*, 20(1):3.

Karak, B. B. and Choudhuri, A. R. (2011). The Waldmeier effect and the flux transport solar dynamo. *Monthly Notices of the Royal Astronomical Society*, 410(3):1503–1512.

Karak, B. B., Jiang, J., Miesch, M. S., Charbonneau, P., and Choudhuri, A. R. (2014). Flux Transport Dynamos: From Kinematics to Dynamics. *Space Science Reviews*, 186(1-4):561–602.

Kichatinov, L. L. (1990). Origin of the sun's differential rotation. In Stenflo, J. O., editor, *Solar Photosphere: Structure, Convection, and Magnetic Fields*, pages 297–307, Dordrecht. Springer Netherlands.

King, J. H. and Papitashvili, N. E. (2005). Solar wind spatial scales in and comparisons of hourly Wind and ACE plasma and magnetic field data. *Journal of Geophysical Research (Space Physics)*, 110(A2):A02104.

Kitchatinov, L. L. (2011). Solar differential rotation: origin, models and implications for dynamo. In *Astronomical Society of India Conference Series*, volume 2 of *Astronomical Society of India Conference Series*, pages 71–80.

Kitchatinov, L. L. and Olemskoy, S. V. (2011). Does the Babcock-Leighton mechanism operate on the Sun? *Astronomy Letters*, 37(9):656–658.

Kleeorin, N., Safiullin, N., Kuzanyan, K., Rogachevskii, I., Tlatov, A., and Porshnev, S. (2020). The mean tilt of sunspot bipolar regions: theory, simulations and comparison with observations. *Monthly Notices of the Royal Astronomical Society*, 495(1):238–248.

Kleimann, J., Dialynas, K., Fraternale, F., Galli, A., Heerikhuisen, J., Izmodenov, V., Kornbleuth, M., Opher, M., and Pogorelov, N. (2022). The Structure of the Large-Scale Heliosphere as Seen by Current Models. *Space Science Reviews*, 218(4):36.

Klimchuk, J. A. (2006). On Solving the Coronal Heating Problem. *Solar Physics*, 234(1):41–77.

Knizhnik, K. J., Linton, M. G., and DeVore, C. R. (2018). The Role of Twist in Kinked Flux Rope Emergence and Delta-spot Formation. *The Astrophysical Journal*, 864(1):89.

Kojima, M., Breen, A. R., Fujiki, K., Hayashi, K., Ohmi, T., and Tokumaru, M. (2004). Fast solar wind after the rapid acceleration. *Journal of Geophysical Research (Space Physics)*, 109(A4):A04103.

Komm, R. W., Howard, R. F., and Harvey, J. W. (1993). Meridional Flow of Small Photospheric Magnetic Features. *Solar Physics*, 147(2):207–223.

Kosovichev, A. and Korzennik, S. (2023). Helioseismic Observations of Solar Torsional Oscillations for Two Solar Cycles. In *American Astronomical Society Meeting Abstracts*, volume 241 of *American Astronomical Society Meeting Abstracts*, page 226.01.

Kosugi, T., Matsuzaki, K., Sakao, T., Shimizu, T., Sone, Y., Tachikawa, S., Hashimoto, T., Minesugi, K., Ohnishi, A., Yamada, T., Tsuneta, S., Hara, H., Ichimoto, K., Suematsu, Y., Shimojo, M., Watanabe, T., Shimada, S., Davis, J. M., Hill, L. D., Owens, J. K., Title, A. M., Culhane, J. L., Harra, L. K., Doschek, G. A., and Golub, L. (2007). The Hinode (Solar-B) Mission: An Overview. *Solar Physics*, 243(1):3–17.

Koutchmy, S. and Livshits, M. (1992). Coronal Streamers. *Space Science Reviews*, 61(3-4):393–417.

Kumar, P., Biswas, A., and Karak, B. B. (2022). Physical link of the polar field buildup with the Waldmeier effect broadens the scope of early solar cycle prediction: Cycle 25 is likely to be slightly stronger than Cycle 24. *Monthly Notices in Royal Astronomical Society*, 513(1):L112–L116.

Kumar, P., Nagy, M., Lemerle, A., Karak, B. B., and Petrovay, K. (2021). The Polar Precursor Method for Solar Cycle Prediction: Comparison of Predictors and Their Temporal Range. *The Astrophysical Journal*, 909(1):87.

Kumar, R., Jouve, L., and Nandy, D. (2019). A 3D kinematic Babcock Leighton solar dynamo model sustained by dynamic magnetic buoyancy and flux transport processes. *Astronomy and Astrophysics*, 623:A54.

Kutiev, Ivan, Tsagouri, Ioanna, Perrone, Loredana, Pancheva, Dora, Mukhtarov, Plamen, Mikhailov, Andrei, Lastovicka, Jan, Jakowski, Norbert, Buresova, Dalia, Blanch, Estefania, Andonov, Borislav, Altadill, David, Magdaleno, Sergio, Parisi, Mario, and Miquel Torta, Joan (2013). Solar activity impact on the earth´s upper atmosphere. *J. Space Weather Space Clim.*, 3:A06.

Lamy, P. and Gilardy, H. (2022). The State of the White-Light Corona over the Minimum and Ascending Phases of Solar Cycle 25 - Comparison with Past Cycles. *Solar Physics*, 297(10):140.

Lavraud, B., Fargette, N., Réville, V., Szabo, A., Huang, J., Rouillard, A. P., Viall, N., Phan, T. D., Kasper, J. C., Bale, S. D., Berthomier, M., Bonnell, J. W., Case, A. W., Dudok de Wit, T., Eastwood, J. P., Génot, V., Goetz, K., Griton, L. S., Halekas, J. S., Harvey, P., Kieokaew, R., Klein, K. G., Korreck, K. E., Kouloumvakos, A., Larson, D. E., Lavarra, M., Livi, R., Louarn, P., MacDowall, R. J., Maksimovic, M., Malaspina, D., Nieves-Chinchilla, T., Pinto, R. F., Poirier, N., Pulupa, M., Raouafi, N. E., Stevens, M. L., Toledo-Redondo, S., and Whittlesey, P. L. (2020). The Heliospheric Current Sheet and Plasma Sheet during Parker Solar Probe's First Orbit. *The Astrophysical Journal Letters*, 894(2):L19.

Lax, P. (2006). Gibbs phenomena. *J. Sci. Comput.*, 28:445–449.

Lean, J. L., Wang, Y. M., and Sheeley, N. R. (2002). The effect of increasing solar activity on the Sun's total and open magnetic flux during multiple cycles: Implications for solar forcing of climate. *Geophysical Research Letters*, 29(24):2224.

Lee, C. O., Luhmann, J. G., Hoeksema, J. T., Sun, X., Arge, C. N., and de Pater, I. (2011). Coronal Field Opens at Lower Height During the Solar Cycles 22 and 23 Minimum Periods: IMF Comparison Suggests the Source Surface Should Be Lowered. *Solar Physics*, 269(2):367–388.

Leighton, R. B. (1964). Transport of Magnetic Fields on the Sun. *The Astrophysical Journal*, 140:1547.

Leighton, R. B. (1969). A Magneto-Kinematic Model of the Solar Cycle. *The Astrophysical Journal*, 156:1.

Lemerle, A. and Charbonneau, P. (2017). A Coupled 2 × 2D Babcock-Leighton Solar Dynamo Model. II. Reference Dynamo Solutions. *The Astrophysical Journal*, 834(2):133.

Lemerle, A., Charbonneau, P., and Carignan-Dugas, A. (2015). A Coupled 2 × 2D Babcock-Leighton Solar Dynamo Model. I. Surface Magnetic Flux Evolution. *The Astrophysical Journal*, 810(1):78.

Levine, R. H. (1982). Open Magnetic Fields and the Solar Cycle - Part One - Photospheric Sources of Open Magnetic Flux. *Solar Physics*, 79(2):203–230.

Levy, E. H. (1976). The interplanetary magnetic field structure. *Nature*, 261(5559):394–395.

Li, J. (2018). A systematic study of hale and anti-hale sunspot physical parameters. *The Astrophysical Journal*, 867(2):89.

Libbrecht, K. G. and Woodard, M. F. (1991). Advances in Helioseismology. *Science*, 253(5016):152–157.

Linker, J. A., Caplan, R. M., Downs, C., Riley, P., Mikic, Z., Lionello, R., Henney, C. J., Arge, C. N., Liu, Y., Derosa, M. L., Yeates, A., and Owens, M. J. (2017). The Open Flux Problem. *The Astrophysical Journal*, 848(1):70.

Linker, J. A., Heinemann, S. G., Temmer, M., Owens, M. J., Caplan, R. M., Arge, C. N., Asvestari, E., Delouille, V., Downs, C., Hofmeister, S. J., Jebaraj, I. C., Madjarska, M. S., Pinto, R. F., Pomoell, J., Samara, E., Scolini, C., and Vršnak, B. (2021). Coronal Hole Detection and Open Magnetic Flux. *The Astrophysical Journal*, 918(1):21.

Lionello, R., Linker, J. A., and Mikić, Z. (2009). Multispectral Emission of the Sun During the First Whole Sun Month: Magnetohydrodynamic Simulations. *The Astrophysical Journal*, 690(1):902–912.

Liu, X., Liu, W., Manchester, IV, W. B., Welling, D. T., Tóth, G., Gombosi, T. I., DeRosa, M. L., Bertello, L., Pevtsov, A. A., Pevtsov, A. A., Reardon, K., Wilbanks, K., Rewoldt, A., and Zhao, L. (2025). Forecasting the 8 April 2024 Total Solar Eclipse with Multiple Solar Photospheric Magnetograms. *The Astrophysical Journal*, page arXiv:2503.10974.

Llorente, J. S., Agenjo, A., Carrascosa, C., de Negueruela, C., Mestreau-Garreau, A., Cropp, A., and Santovincenzo, A. (2013). PROBA-3: Precise formation flying demonstration mission. *Acta Astronautica*, 82(1):38–46.

Lockwood, M. (2002). An evaluation of the correlation between open solar flux and total solar irradiance. *Astronomy and Astrophysics*, 382:678–687.

Lockwood, M. (2013). Reconstruction and Prediction of Variations in the Open Solar Magnetic Flux and Interplanetary Conditions. *Living Reviews in Solar Physics*, 10(1):4.

Lockwood, M. and Owens, M. (2009). The Accuracy of Using the Ulysses Result of the Spatial Invariance of the Radial Heliospheric Field to Compute the Open Solar Flux. *The Astrophysical Journal*, 701(2):964–973.

Lockwood, M., Owens, M., and Rouillard, A. P. (2009a). Excess open solar magnetic flux from satellite data: 2. A survey of kinematic effects. *Journal of Geophysical Research (Space Physics)*, 114(A11):A11104.

Lockwood, M., Rouillard, A. P., and Finch, I. D. (2009b). The Rise and Fall of Open Solar Flux During the Current Grand Solar Maximum. *The Astrophysical Journal*, 700(2):937–944.

Low, B. C. and Lou, Y. Q. (1990). Modeling Solar Force-free Magnetic Fields. *The Astrophysical Journal*, 352:343.

Lowder, C., Qiu, J., and Leamon, R. (2017). Coronal Holes and Open Magnetic Flux over Cycles 23 and 24. *Solar Physics*, 292(1):18.

MacGregor, K. B. and Charbonneau, P. (1997). Solar Interface Dynamos. I. Linear, Kinematic Models in Cartesian Geometry. *The Astrophysical Journal*, 486(1):484–501.

Mackay, D. H., Karpen, J. T., Ballester, J. L., Schmieder, B., and Aulanier, G. (2010). Physics of Solar Prominences: II—Magnetic Structure and Dynamics. *Space Science Reviews*, 151(4):333–399.

Mackay, D. H. and Yeates, A. R. (2012). The Sun's Global Photospheric and Coronal Magnetic Fields: Observations and Models. *Living Reviews in Solar Physics*, 9(1):6.

MacQueen, R. M., Gosling, J. T., Hildner, E., Munro, R. H., Poland, A. I., and Ross, C. L. (1974). The High Altitude Observatory white light coronagraph. In Menzel, D. H., Larmore, L., and Crawford, D., editors, *Instrumentation in Astronomy II*, volume 44 of *Society of Photo-Optical Instrumentation Engineers (SPIE) Conference Series*, pages 207–212.

Mahajan, S. S., Hathaway, D. H., Muñoz-Jaramillo, A., and Martens, P. C. (2021). Improved measurements of the sun's meridional flow and torsional oscillation from correlation tracking on MDI and HMI magnetograms. *The Astrophysical Journal*, 917(2):100.

Mahajan, S. S., Upton, L. A., Antia, H. M., Basu, S., DeRosa, M. L., Hess Webber, S. A., Hoeksema, J. T., Jain, K., Komm, R. W., Larson, T., Nagovitsyn, Y. A., Pevtsov, A. A., Roudier, T., Tripathy, S. C., Ulrich, R. K., and Zhao, J. (2024). The Sun's Large-Scale Flows I: Measurements of Differential Rotation & Torsional Oscillation. *Solar Physics*, 299(3):38.

Makarov, V. I., Tlatov, A. G., Callebaut, D. K., Obridko, V. N., and Shelting, B. D. (2001). Large-Scale Magnetic Field and Sunspot Cycles. *Solar Physics*, 198(2):409–421.

Mandal, S., Krivova, N. A., Solanki, S. K., Sinha, N., and Banerjee, D. (2020). Sunspot area catalog revisited: Daily cross-calibrated areas since 1874. *Astronomy and Astrophysics*, 640:A78.

Martin, S. F. (1998). Conditions for the Formation and Maintenance of Filaments (Invited Review). *Solar Physics*, 182(1):107–137.

Mazumder, R., Chatterjee, S., Nandy, D., and Banerjee, D. (2021). Solar Cycle Evolution of Filaments over a Century: Investigations with the Meudon and McIntosh Hand-drawn Archives. *The Astrophysical Journal*, 919(2):125.

McClintock, B. H. and Norton, A. A. (2013). Recovering Joy's Law as a Function of Solar Cycle, Hemisphere, and Longitude. *Solar Physics*, 287(1-2):215–227.

McClintock, B. H., Norton, A. A., and Li, J. (2014). RE-EXAMINING SUNSPOT TILT ANGLE TO INCLUDE ANTI-HALE STATISTICS. *The Astrophysical Journal*, 797(2):130.

McIntosh, P. S. (1972). Solar magnetic fields derived from hydrogen alpha filtergrams. *Reviews of Geophysics and Space Physics*, 10:837–846.

Miesch, M. S., Brun, A. S., and Toomre, J. (2006). Solar Differential Rotation Influenced by Latitudinal Entropy Variations in the Tachocline. *The Astrophysical Journal*, 641(1):618–625.

Mikić, Z., Downs, C., Linker, J. A., Caplan, R. M., Mackay, D. H., Upton, L. A., Riley, P., Lionello, R., Török, T., Titov, V. S., Wijaya, J., Druckmüller, M., Pasachoff, J. M., and Carlos, W. (2018). Predicting the corona for the 21 August 2017 total solar eclipse. *Nature Astronomy*, 2:913–921.

Mikić, Z., Linker, J. A., Schnack, D. D., Lionello, R., and Tarditi, A. (1999). Magnetohydrodynamic modeling of the global solar corona. *Physics of Plasmas*, 6(5):2217–2224.

Muñoz-Jaramillo, A., Dasi-Espuig, M., Balmaceda, L. A., and DeLuca, E. E. (2013). Solar Cycle Propagation, Memory, and Prediction: Insights from a Century of Magnetic Proxies. *The Astrophysical Journal Letters*, 767(2):L25.

Muñoz-Jaramillo, A., Nandy, D., and Martens, P. C. H. (2009). Helioseismic Data Inclusion in Solar Dynamo Models. *The Astrophysical Journal*, 698(1):461–478.

Muñoz-Jaramillo, A., Navarrete, B., and Campusano, L. E. (2021). Solar Anti-Hale Bipolar Magnetic Regions: A Distinct Population with Systematic Properties. *The Astrophysical Journal*, 920(1):31.

Muñoz-Jaramillo, A., Senkpeil, R. R., Windmueller, J. C., Amouzou, E. C., Longcope, D. W., Tlatov, A. G., Nagovitsyn, Y. A., Pevtsov, A. A., Chapman, G. A., Cookson, A. M., Yeates, A. R., Watson, F. T., Balmaceda, L. A., DeLuca, E. E., and Martens, P. C. H. (2015). Small-scale and Global Dynamos and the Area and Flux Distributions of Active Regions, Sunspot Groups, and Sunspots: A Multi-database Study. *The Astrophysical Journal*, 800(1):48.

Muñoz-Jaramillo, A., Sheeley, N. R., Zhang, J., and DeLuca, E. E. (2012). Calibrating 100 Years of Polar Faculae Measurements: Implications for the Evolution of the Heliospheric Magnetic Field. *The Astrophysical Journal*, 753(2):146.

Muñoz-Jaramillo, A., Nandy, D., Martens, P. C. H., and Yeates, A. R. (2010). A double-ring algorithm for modeling solar active regions: Unifying kinematic dynamo models and surface flux-transport simulations. *The Astrophysical Journal Letters*, 720(1):L20.

Nagy, M., Lemerle, A., and Charbonneau, P. (2019). Impact of rogue active regions on hemispheric asymmetry. *Advances in Space Research*, 63(4):1425–1433.

Nagy, M., Lemerle, A., Labonville, F., Petrovay, K., and Charbonneau, P. (2017). The Effect of "Rogue" Active Regions on the Solar Cycle. *Solar Physics*, 292(11):167.

Nagy, M., Petrovay, K., Lemerle, A., and Charbonneau, P. (2020). Towards an algebraic method of solar cycle prediction. II. Reducing the need for detailed input data with ARDoR. *Journal of Space Weather and Space Climate*, 10:46.

Nandy, D. (2002). Constraints on the Solar Internal Magnetic Field from a Buoyancy Driven Solar Dynamo. *Astrophysics and Space Science*, 282(1):209–219.

Nandy, D. (2004). Exploring Magnetic Activity from The Sun to the Stars. *Solar Physics*, 224(1-2):161–169.

Nandy, D. (2006). Magnetic helicity and flux tube dynamics in the solar convection zone: Comparisons between observation and theory. *Journal of Geophysical Research: Space Physics*, 111(A12).

Nandy, D. (2021). Progress in Solar Cycle Predictions: Sunspot Cycles 24-25 in Perspective. *Solar Physics*, 296(3):54.

Nandy, D., Banerjee, D., Bhowmik, P., Brun, A. S., Cameron, R. H., Gibson, S. E., Hanasoge, S., Harra, L., Hassler, D. M., Jain, R., Jiang, J., Jouve, L., Mackay, D. H., Mahajan, S. S., Mandrini, C. H., Owens, M., Pal, S., Pinto, R. F., Saha, C., Sun, X., Tripathi, D., and Usoskin, I. G. (2023). Exploring the solar poles: The last great frontier of the sun. *Bulletin of the American Astronomical Society*.

Nandy, D., Baruah, Y., Bhowmik, P., Dash, S., Gupta, S., Hazra, S., Lekshmi, B., Pal, S., Pal, S., Roy, S., Saha, C., and Sinha, S. (2023). Causality in heliophysics: Magnetic fields as a bridge between the Sun's interior and the Earth's space environment. *Journal of Atmospheric and Solar-Terrestrial Physics*, 248:106081.

Nandy, D., Bhowmik, P., Yeates, A. R., Panda, S., Tarafder, R., and Dash, S. (2018). The Large-scale Coronal Structure of the 2017 August 21 Great American Eclipse: An Assessment of Solar Surface Flux Transport Model Enabled Predictions and Observations. *The Astrophysical Journal*, 853(1):72.

Nandy, D. and Choudhuri, A. R. (2001). Toward a mean field formulation of the babcock-leighton type solar dynamo. i. -coefficient versus durney's double-ring approach. *The Astrophysical Journal*, 551(1):576.

Nandy, D. and Martens, P. (2007). Space climate and the solar–stellar connection: What can we learn from the stars about long-term solar variability? *Advances in Space Research*, 40:891–898.

Nandy, D., Martens, P. C. H., Obridko, V., Dash, S., and Georgieva, K. (2021). Solar evolution and extrema: current state of understanding of long-term solar variability and its planetary impacts. *Progress in Earth and Planetary Science*, 8(1):40.

Norton, A., Howe, R., Upton, L., and Usoskin, I. (2023). Solar Cycle Observations. *Space Science Reviews*, 219(8):64.

Owens, M. J. and Forsyth, R. J. (2013). The Heliospheric Magnetic Field. *Living Reviews in Solar Physics*, 10(1):5.

Pal, S., Bhowmik, P., Mahajan, S. S., and Nandy, D. (2023). Impact of Anomalous Active Regions on the Large-scale Magnetic Field of the Sun. *The Astrophysical Journal*, 953(1):51.

Pal, S., Dash, S., Hazra, S., and Nandy, D. (2024). Insights from the April 8 Great American Eclipse: Dynamical Memory of the Sun's Corona during Solar Maximum. In *AGU Fall Meeting Abstracts*, volume 2024 of *AGU Fall Meeting Abstracts*, pages SH01–05.

Pal, S., Dash, S., and Nandy, D. (2020). Flux Erosion of Magnetic Clouds by Reconnection With the Sun's Open Flux. *Geophysical Research Letters*, 47(8):e86372.

Pal, S. and Nandy, D. (2024a). Algebraic quantification of the contribution of active regions to the Sun's dipole moment: applications to century-scale polar field estimates and solar cycle forecasting. *Monthly Notices in Royal Astronomical Society*, 531(1):1546–1553.

Pal, S. and Nandy, D. (2024b). Reconstruction of Interplanetary Magnetic Field by Optimizing the Sun's Source Surface as a Function of Magnetic Activity. In *AGU Fall Meeting Abstracts*, volume 2024 of *AGU Fall Meeting Abstracts*, pages SH01–06.

Pal, S. and Nandy, D. (2025). Extreme fluctuations in the Sun's activity over the Modern Maximum: Understanding the enigmatic solar cycles 19-20. *Astronomy and Astrophysics*, 700:L15.

Panasenco, O., Velli, M., D'Amicis, R., Shi, C., Réville, V., Bale, S. D., Badman, S. T., Kasper, J., Korreck, K., Bonnell, J. W., Wit, D. d. T., Goetz, K., Harvey, P. R., MacDowall, R. J., Malaspina, D. M., Pulupa, M., Case, A. W., Larson, D., Livi, R., Stevens, M., and Whittlesey, P. (2020). Exploring Solar Wind Origins and Connecting Plasma Flows from the Parker Solar Probe to 1 au: Nonspherical Source Surface and Alfvénic Fluctuations. *The Astrophysical Journal Supplement Series*, 246(2):54.

Parker, E. (1959). Extension of the Solar Corona into Interplanetary Space. *Journal of Geophysical Research*, 64(11):1675–1681.

Parker, E. N. (1955). Hydromagnetic Dynamo Models. *The Astrophysical Journal*, 122:293.

Parker, E. N. (1958). Dynamics of the Interplanetary Gas and Magnetic Fields. *The Astrophysical Journal*, 128:664.

Parker, E. N. (1965). Dynamical Theory of the Solar Wind. *Space Science Reviews*, 4(5-6):666–708.

Parker, E. N. (1988). Nanoflares and the Solar X-Ray Corona. *The Astrophysical Journal*, 330:474.

Pasachoff, J. M. (2017). Heliophysics at total solar eclipses. *Nature Astronomy*, 1:0190.

Passos, D., Nandy, D., Hazra, S., and Lopes, I. (2014). A solar dynamo model driven by mean-field alpha and Babcock-Leighton sources: fluctuations, grand-minima-maxima, and hemispheric asymmetry in sunspot cycles. *Astronomy and Astrophysics*, 563:A18.

Paternò, L. (2010). The solar differential rotation: a historical view. *Astrophysics and Space Science*, 328(1-2):269–277.

Pesnell, W. D., Thompson, B. J., and Chamberlin, P. C. (2012). The Solar Dynamics Observatory (SDO). *Solar Physics*, 275(1-2):3–15.

Petrie, G. J. D. (2015). Solar Magnetism in the Polar Regions. *Living Reviews in Solar Physics*, 12(1):5.

Petrovay, K. (2020). Solar cycle prediction. *Living Reviews in Solar Physics*, 17(1):2.

Petrovay, K., Nagy, M., and Yeates, A. R. (2020). Towards an algebraic method of solar cycle prediction. I. Calculating the ultimate dipole contributions of individual active regions. *Journal of Space Weather and Space Climate*, 10:50.

Pevtsov, Alexei A., Tlatova, Kseniya A., Pevtsov, Alexander A., Heikkinen, Elina, Virtanen, Ilpo, Karachik, Nina V., Bertello, Luca, Tlatov, Andrey G., Ulrich, Roger, and Mursula, Kalevi (2019). Reconstructing solar magnetic fields from historical observations - v. sunspot magnetic field measurements at mount wilson observatory. *Astronomy and Astrophysics*, 628:A103.

Piddington, J. H. (1972). Solar Dynamo Theory and the Models of Babcock and Leighton. *Solar Physics*, 22(1):3–19.

Press, W. H., Teukolsky, S. A., Vetterling, W. T., and Flannery, B. P. (1992). *Numerical recipes in FORTRAN. The art of scientific computing*.

Pulkkinen, T. I., Nevanlinna, H., Pulkkinen, P. J., and Lockwood, M. (2001). The Sun-Earth Connection in Time Scales from Years to Decades and Centuries. *Space Science Reviews*, 95:625–637.

Rajaguru, S. P. and Antia, H. M. (2020). Time-Distance Helioseismology of Deep Meridional Circulation. In Monteiro, M. J. P. F. G., García, R. A., Christensen-Dalsgaard, J., and McIntosh, S. W., editors, *Dynamics of the Sun and Stars; Honoring the Life and Work of Michael J. Thompson*, volume 57 of *Astrophysics and Space Science Proceedings*, pages 107–113.

Rempel, M. (2005). Solar Differential Rotation and Meridional Flow: The Role of a Subadiabatic Tachocline for the Taylor-Proudman Balance. *The Astrophysical Journal*, 622(2):1320–1332.

Réville, V., Velli, M., Panasenco, O., Tenerani, A., Shi, C., Badman, S. T., Bale, S. D., Kasper, J. C., Stevens, M. L., Korreck, K. E., Bonnell, J. W., Case, A. W., de Wit, T. D., Goetz, K., Harvey, P. R., Larson, D. E., Livi, R., Malaspina, D. M., MacDowall, R. J., Pulupa, M., and Whittlesey, P. L. (2020). The Role of Alfvén Wave Dynamics on the Large-scale Properties of the Solar Wind: Comparing an MHD Simulation with Parker Solar Probe E1 Data. *The Astrophysical Journal Supplement Series*, 246(2):24.

RGO/USAF/NOAA Data Centre (1874-2023). RGO/USAF/NOAA Data Centre Sunspot Data. *https://solarscience.msfc.nasa.gov/greenwch.shtml*.

Rieutord, M. and Rincon, F. (2010). The Sun's Supergranulation. *Living Reviews in Solar Physics*, 7(1):2.

Riley, P., Linker, J. A., Mikić, Z., Lionello, R., Ledvina, S. A., and Luhmann, J. G. (2006). A Comparison between Global Solar Magnetohydrodynamic and Potential Field Source Surface Model Results. *The Astrophysical Journal*, 653(2):1510–1516.

Rimmele, T. R., Warner, M., Keil, S. L., Goode, P. R., Knölker, M., Kuhn, J. R., Rosner, R. R., McMullin, J. P., Casini, R., Lin, H., Wöger, F., von der Lühe, O., Tritschler, A., Davey, A., de Wijn, A., Elmore, D. F., Fehlmann, A., Harrington, D. M., Jaeggli, S. A., Rast, M. P., Schad, T. A., Schmidt, W., Mathioudakis, M., Mickey, D. L., Anan,

T., Beck, C., Marshall, H. K., Jeffers, P. F., Oschmann, J. M., Beard, A., Berst, D. C., Cowan, B. A., Craig, S. C., Cross, E., Cummings, B. K., Donnelly, C., de Vanssay, J.-B., Eigenbrot, A. D., Ferayorni, A., Foster, C., Galapon, C. A., Gedrites, C., Gonzales, K., Goodrich, B. D., Gregory, B. S., Guzman, S. S., Guzzo, S., Hegwer, S., Hubbard, R. P., Hubbard, J. R., Johansson, E. M., Johnson, L. C., Liang, C., Liang, M., McQuillen, I., Mayer, C., Newman, K., Onodera, B., Phelps, L., Puentes, M. M., Richards, C., Rimmele, L. M., Sekulic, P., Shimko, S. R., Simison, B. E., Smith, B., Starman, E., Sueoka, S. R., Summers, R. T., Szabo, A., Szabo, L., Wampler, S. B., Williams, T. R., and White, C. (2020). The Daniel K. Inouye Solar Telescope - Observatory Overview. *Solar Physics*, 295(12):172.

Roberts, P. H. (1972). Kinematic Dynamo Models. *Philosophical Transactions of the Royal Society of London Series A*, 272(1230):663–698.

Rouillard, A. P., Davies, J. A., Lavraud, B., Forsyth, R. J., Savani, N. P., Bewsher, D., Brown, D. S., Sheeley, N. R., Davis, C. J., Harrison, R. A., Howard, R. A., Vourlidas, A., Lockwood, M., Crothers, S. R., and Eyles, C. J. (2010). Intermittent release of transients in the slow solar wind: 1. Remote sensing observations. *Journal of Geophysical Research (Space Physics)*, 115(A4):A04103.

Routh, S., Pal, S., Nandy, D., Chatterjee, S., Banerjee, D., and Saleem Khan, M. (2025). Polar Filaments Capture High Latitude Solar Poloidal Field Interactions and can Foretell the Future Sunspot Cycle Amplitude before Polar Field Precursors. *arXiv e-prints*, page arXiv:2510.12142.

Rušin, V., Prikryl, P., and Prikryl, E. A. (2020). White-light solar corona structure observed by naked eye and processed images. *Monthly Notices in Royal Astronomical Society*, 495(2):2170–2178.

Sachdeva, N., van der Holst, B., Manchester, W. B., Tóth, G., Chen, Y., Lloveras, D. G., Vásquez, A. M., Lamy, P., Wojak, J., Jackson, B. V., Yu, H.-S., and Henney, C. J. (2019). Validation of the Alfvén Wave Solar Atmosphere Model (AWSoM) with Observations from the Low Corona to 1 au. *The Astrophysical Journal*, 887(1):83.

Saha, C., Chandra, S., and Nandy, D. (2022). Evidence of persistence of weak magnetic cycles driven by meridional plasma flows during solar grand minima phases. *Monthly Notices of the Royal Astronomical Society: Letters*, 517(1):L36–L40.

Saha, C., Mukhopadhyay, S., and Nandy, D. (2025). On the Origin of Long-term Modulation in the Sun's Magnetic Activity Cycle. *The Astrophysical Journal Letters*, 984(1):L5.

Sanchez, S., Fournier, A., and Aubert, J. (2014). The Predictability of Advection-dominated Flux-transport Solar Dynamo Models. *The Astrophysical Journal*, 781(1):8.

Schatten, K. (2003). Solar activity and the solar cycle. *Advances in Space Research*, 32(4):451–460. Heliosphere at Solar Maximum.

Schatten, K. H., Scherrer, P. H., Svalgaard, L., and Wilcox, J. M. (1978). Using Dynamo Theory to predict the sunspot number during Solar Cycle 21. *Geophysical Research Letters*, 5(5):411–414.

Schatten, K. H., Wilcox, J. M., and Ness, N. F. (1969). A model of interplanetary and coronal magnetic fields. *Solar Physics*, 6(3):442–455.

Schmidt, H. U. (1968). Magnetohydrodynamics of an Active Region. In Kiepenheuer, K. O., editor, *Structure and Development of Solar Active Regions*, volume 35, page 95.

Schou, J., Antia, H. M., Basu, S., Bogart, R. S., Bush, R. I., Chitre, S. M., Christensen-Dalsgaard, J., Di Mauro, M. P., Dziembowski, W. A., Eff-Darwich, A., Gough, D. O., Haber, D. A., Hoeksema, J. T., Howe, R., Korzennik, S. G., Kosovichev, A. G., Larsen, R. M., Pijpers, F. P., Scherrer, P. H., Sekii, T., Tarbell, T. D., Title, A. M., Thompson, M. J., and Toomre, J. (1998). Helioseismic Studies of Differential Rotation in the Solar Envelope by the Solar Oscillations Investigation Using the Michelson Doppler Imager. *The Astrophysical Journal*, 505(1):390–417.

Schrijver, C. J. and De Rosa, M. L. (2003). Photospheric and heliospheric magnetic fields. *Solar Physics*, 212(1):165–200.

Schrijver, C. J., Kauristie, K., Aylward, A. D., Denardini, C. M., Gibson, S. E., Glover, A., Gopalswamy, N., Grande, M., Hapgood, M., Heynderickx, D., Jakowski, N., Kalegaev, V. V., Lapenta, G., Linker, J. A., Liu, S., Mandrini, C. H., Mann, I. R., Nagatsuma, T., Nandy, D., Obara, T., Paul O'Brien, T., Onsager, T., Opgenoorth, H. J., Terkildsen, M., Valladares, C. E., and Vilmer, N. (2015). Understanding space weather to shield society: A global road map for 2015-2025 commissioned by COSPAR and ILWS. *Advances in Space Research*, 55(12):2745–2807.

Schrijver, C. J. and Title, A. M. (2001). On the Formation of Polar Spots in Sun-like Stars. *The Astrophysical Journal*, 551(2):1099–1106.

Schrijver, C. J. and Zwaan, C. (2000). *Solar and Stellar Magnetic Activity*.

Schwabe, H. (1844). Sonnenbeobachtungen im Jahre 1843. Von Herrn Hofrath Schwabe in Dessau. *Astronomische Nachrichten*, 21(15):233.

Scott, R. B., Pontin, D. I., Antiochos, S. K., DeVore, C. R., and Wyper, P. F. (2021). The Dynamic Formation of Pseudostreamers. *The Astrophysical Journal*, 913(1):64.

Shi, G., Shan, J., Feng, L., Chen, J., and Gan, W. (2025). The Role of Farside Magnetic Structures in Modeling the 2024 Solar Eclipse. *The Astrophysical Journal*, 992(1):89.

Shi, T., Manchester, W., Landi, E., van der Holst, B., Szente, J., Chen, Y., Tóth, G., Bertello, L., and Pevtsov, A. (2024). AWSoM Magnetohydrodynamic Simulation of a Solar Active Region. II. Statistical Analysis of Alfvén Wave Dissipation and Reflection, Scaling Laws, and Energy Budget on Coronal Loops. *The Astrophysical Journal*, 961(1):60.

SILSO World Data Center (1700-2019). The International Sunspot Number. *http://www.sidc.be/silso/*.

Smith, E. J. (2001). The heliospheric current sheet. *Journal of Geophysical Research*, 106(A8):15819–15832.

Snodgrass, H. B. (1983). Magnetic rotation of the solar photosphere. *The Astrophysical Journal*, 270:288–299.

Snodgrass, H. B. (1987). Torsional Oscillations and the Solar Cycle. *Solar Physics*, 110(1):35–49.

Snodgrass, H. B. and Ulrich, R. K. (1990). Rotation of Doppler Features in the Solar Photosphere. *The Astrophysical Journal*, 351:309.

Sokoloff, D., Khlystova, A., and Abramenko, V. (2015). Solar small-scale dynamo and polarity of sunspot groups. *Monthly Notices in Royal Astronomical Society*, 451(2):1522–1527.

Sokolov, I. V., Holst, B. v. d., Manchester, W. B., Su Ozturk, D. C., Szente, J., Taktakishvili, A., Tóth, G., Jin, M., and Gombosi, T. I. (2021). Threaded-field-line Model for the Low Solar Corona Powered by the Alfvén Wave Turbulence. *The Astrophysical Journal*, 908(2):172.

Sokolov, I. V., van der Holst, B., Oran, R., Downs, C., Roussev, I. I., Jin, M., Manchester, IV, W. B., Evans, R. M., and Gombosi, T. I. (2013). Magnetohydrodynamic Waves and Coronal Heating: Unifying Empirical and MHD Turbulence Models. *The Astrophysical Journal*, 764(1):23.

Solanki, S. K. (1993). Smallscale Solar Magnetic Fields - an Overview. *Space Science Reviews*, 63(1-2):1–188.

Solanki, S. K. (2002). Solar variability and climate change: is there a link? *Astronomy Geophysics*, 43(5):5.9–5.13.

Solanki, S. K., Usoskin, I. G., Kromer, B., Schüssler, M., and Beer, J. (2004). Unusual activity of the Sun during recent decades compared to the previous 11,000 years. *Nature*, 431(7012):1084–1087.

SPDF OMNIWeb database (1963-2025). SPDF OMNIWeb database. *https://omniweb.gsfc.nasa.gov/form/dx1.html*.

Stenflo, J. O. and Kosovichev, A. G. (2012). BIPOLAR MAGNETIC REGIONS ON THE SUN: GLOBAL ANALYSIS OF THESOHO/MDI DATA SET. *The Astrophysical Journal*, 745(2):129.

Svalgaard, L. and Cliver, E. W. (2010). Heliospheric magnetic field 1835-2009. *Journal of Geophysical Research (Space Physics)*, 115(A9):A09111.

Szabo, A., Larson, D., Whittlesey, P., Stevens, M., Jones, S., Koval, A., Pulupa, M., Livi, R., Kasper, J., and Bale, S. (2022). The Heliospheric Current Sheet Observed by Parker Solar Probe. In *44th COSPAR Scientific Assembly. Held 16-24 July*, volume 44, page 1470.

Szente, J., Landi, E., Manchester, IV, W. B., Toth, G., van der Holst, B., and Gombosi, T. I. (2019). SPECTRUM: Synthetic Spectral Calculations for Global Space Plasma Modeling. *The Astrophysical Journal Supplement Series*, 242(1):1.

Temmer, M. (2021). Space weather: the solar perspective. *Living Reviews in Solar Physics*, 18(1):4.

Thomson, D. J., Lanzerotti, L. J., and Maclennan, C. G. (2001). Interplanetary magnetic field: Statistical properties and discrete modes. *Journal of Geophysical Research*, 106(A8):15941–15962.

Tlatov, A. G., Kuzanyan, K. M., and Vasil'yeva, V. V. (2016). Tilt Angles of Quiescent Filaments and Filaments of Active Regions. In Dorotovic, I., Fischer, C. E., and Temmer, M., editors, *Coimbra Solar Physics Meeting: Ground-based Solar Observations in the Space Instrumentation Era*, volume 504 of *Astronomical Society of the Pacific Conference Series*, page 241.

Tu, C. Y. and Marsch, E. (1993). A model of solar wind fluctuations with two components: Alfvén waves and convective structures. *Journal of Geophysical Research*, 98(A2):1257–1276.

Tu, C. Y. and Marsch, E. (1995). Magnetohydrodynamic Structures Waves and Turbulence in the Solar Wind - Observations and Theories. *Space Science Reviews*, 73(1-2):1–210.

Upton, L. and Hathaway, D. H. (2013). PREDICTING THE SUN's POLAR MAGNETIC FIELDS WITH a SURFACE FLUX TRANSPORT MODEL. *The Astrophysical Journal*, 780(1):5.

Upton, L. and Hathaway, D. H. (2014). Predicting the Sun's Polar Magnetic Fields with a Surface Flux Transport Model. *The Astrophysical Journal*, 780(1):5.

Upton, L. A. and Hathaway, D. H. (2018). An Updated Solar Cycle 25 Prediction With AFT: The Modern Minimum. *Geophysical Research Letters*, 45(16):8091–8095.

Usoskin, I. G. (2023). A history of solar activity over millennia. *Living Reviews in Solar Physics*, 20(1):2.

van Ballegooijen, A. A., Cartledge, N. P., and Priest, E. R. (1998). Magnetic flux transport and the formation of filament channels on the sun. *The Astrophysical Journal*, 501(2):866–881.

van Ballegooijen, A. A. and Mackay, D. H. (2007). Model for the Coupled Evolution of Subsurface and Coronal Magnetic Fields in Solar Active Regions. *The Astrophysical Journal*, 659(2):1713–1725.

van der Holst, B., Huang, J., Sachdeva, N., Kasper, J. C., Manchester, IV, W. B., Borovikov, D., Chandran, B. D. G., Case, A. W., Korreck, K. E., Larson, D., Livi, R., Stevens, M., Whittlesey, P., Bale, S. D., Pulupa, M., Malaspina, D. M., Bonnell, J. W., Harvey, P. R., Goetz, K., and MacDowall, R. J. (2022). Improving the Alfvén Wave Solar Atmosphere Model Based on Parker Solar Probe Data. *The Astrophysical Journal*, 925(2):146.

van der Holst, B., Manchester, IV, W. B., Frazin, R. A., Vásquez, A. M., Tóth, G., and Gombosi, T. I. (2010). A Data-driven, Two-temperature Solar Wind Model with Alfvén Waves. *The Astrophysical Journal*, 725(1):1373–1383.

van der Holst, B., Sokolov, I. V., Meng, X., Jin, M., Manchester, IV, W. B., Tóth, G., and Gombosi, T. I. (2014). Alfvén Wave Solar Model (AWSoM): Coronal Heating. *The Astrophysical Journal*, 782(2):81.

Vaquero, J. (2007). Historical sunspot observations: A review. *Advances in Space Research*, 40(7):929–941.

Vidotto, A. A. (2021). The evolution of the solar wind. *Living Reviews in Solar Physics*, 18(1):3.

Virtanen, I. I., Koskela, J. S., and Mursula, K. (2020). Abrupt Shrinking of Solar Corona in the Late 1990s. *The Astrophysical Journal Letters*, 889(2):L28.

Virtanen, I. O. I., Pevtsov, A. A., Bertello, L., and Mursula, K. (2022). Reconstructing solar magnetic fields from historical observations. IX. The photospheric magnetic field from 1915 to 1985. *Astronomy and Astrophysics*, 667:A168.

Virtanen, I. O. I., Virtanen, I. I., Pevtsov, A. A., and Mursula, K. (2019). Reconstructing solar magnetic fields from historical observations. VI. Axial dipole moments of solar active regions in cycles 21-24. *Astronomy and Astrophysics*, 632:A39.

von Kusserow, U. and Marsch, E. (2025). *The Solar Wind in Space*, pages 91–148. Springer Berlin Heidelberg, Berlin, Heidelberg.

Waldmeier, M. (1935). Neue eigenschaften der sonnenfleckenkurve. *Astronomische Mitteilungen der Eidgenössischen Sternwarte Zurich*, 14:105–136.

Wallace, S., Arge, C. N., Pattichis, M., Hock-Mysliwiec, R. A., and Henney, C. J. (2019). Estimating Total Open Heliospheric Magnetic Flux. *Solar Physics*, 294(2):19.

Walsh, R. W. and Ireland, J. (2003). The heating of the solar corona. , 12(1):1–41.

Wang, Y.-M., Hawley, S. H., and Sheeley, Jr., N. R. (1996). The Magnetic Nature of Coronal Holes. *Science*, 271(5248):464–469.

Wang, Y. M., Lean, J., and Sheeley, N. R., J. (2002). Role of a Variable Meridional Flow in the Secular Evolution of the Sun's Polar Fields and Open Flux. *The Astrophysical Journal Letters*, 577(1):L53–L57.

Wang, Y. M. and Lean, J. L. (2021). A New Reconstruction of the Sun's Magnetic Field and Total Irradiance since 1700. *The Astrophysical Journal*, 920(2):100.

Wang, Y. M., Nash, A. G., and Sheeley, Jr., N. R. (1989). Magnetic Flux Transport on the Sun. *Science*, 245(4919):712–718.

Wang, Y. M., Sheeley, N. R., J., and Nash, A. G. (1991). A New Solar Cycle Model Including Meridional Circulation. *The Astrophysical Journal*, 383:431.

Wang, Y. M. and Sheeley, Jr., N. R. (1994). The Rotation of Photospheric Magnetic Fields: A Random Walk Transport Model. *The Astrophysical Journal*, 430:399.

Wang, Y. M., Ulrich, R. K., and Harvey, J. W. (2022). Magnetograph Saturation and the Open Flux Problem. *The Astrophysical Journal*, 926(2):113.

Wang, Z.-F., Jiang, J., and Wang, J.-X. (2021). Algebraic quantification of an active region contribution to the solar cycle. *Astronomy and Astrophysics*, 650:A87.

Weber, M. A., Fan, Y., and Miesch, M. S. (2013). Comparing Simulations of Rising Flux Tubes Through the Solar Convection Zone with Observations of Solar Active Regions: Constraining the Dynamo Field Strength. *Solar Physics*, 287(1-2):239–263.

Wiegelmann, T., Petrie, G. J. D., and Riley, P. (2017). Coronal Magnetic Field Models. *Space Science Reviews*, 210(1-4):249–274.

Wilkins, C. P., Pontin, D. I., Yeates, A. R., Antiochos, S. K., Schunker, H., and Lamichhane, B. (2025). The Sun's Open–Closed Flux Boundary and the Origin of the Slow Solar Wind. *The Astrophysical Journal*, 985(2):190.

Worden, J. and Harvey, J. (2000). An Evolving Synoptic Magnetic Flux map and Implications for the Distribution of Photospheric Magnetic Flux. *Solar Physics*, 195(2):247–268.

WSO Data Centre (1976-2023). WSO Polar Field Observations. http://wso.stanford.edu/Polar.html.

Xu, Y., Banerjee, D., Chatterjee, S., Pötzi, W., Wang, Z., Ruan, X., Jing, J., and Wang, H. (2021). Migration of Solar Polar Crown Filaments in the Past 100 Years. *The Astrophysical Journal*, 909(1):86.

Yang, Z., Bethge, C., Tian, H., Tomczyk, S., Morton, R., Del Zanna, G., McIntosh, S. W., Karak, B. B., Gibson, S., Samanta, T., He, J., Chen, Y., and Wang, L. (2020). Global maps of the magnetic field in the solar corona. *Science*, 369(6504):694–697.

Yang, Z., Tian, H., Tomczyk, S., Liu, X., Gibson, S., Morton, R. J., and Downs, C. (2024). Observing the evolution of the Sun's global coronal magnetic field over 8 months. *Science*, 386(6717):76–82.

Yardley, S. L., Brooks, D. H., D'Amicis, R., Owen, C. J., Long, D. M., Baker, D., Démoulin, P., Owens, M. J., Lockwood, M., Mihailescu, T., Coburn, J. T., Dewey, R. M., Müller, D., Suen, G. H. H., Ngampoopun, N., Louarn, P., Livi, S., Lepri, S., Fludra, A., Haberreiter, M., and Schühle, U. (2024). Multi-source connectivity as the driver of solar wind variability in the heliosphere. *Nature Astronomy*, 8:953–963.

Yashiro, S., Gopalswamy, N., Michalek, G., St. Cyr, O. C., Plunkett, S. P., Rich, N. B., and Howard, R. A. (2004). A catalog of white light coronal mass ejections observed by the SOHO spacecraft. *Journal of Geophysical Research (Space Physics)*, 109(A7):A07105.

Yeates, A. (2018). antyeates1983/pfss: First release of pfss code.

Yeates, A. R. (2020). How Good Is the Bipolar Approximation of Active Regions for Surface Flux Transport? *Solar Physics*, 295(9):119.

Yeates, A. R., Attrill, G. D. R., Nandy, D., Mackay, D. H., Martens, P. C. H., and van Ballegooijen, A. A. (2010). Comparison of a Global Magnetic Evolution Model with Observations of Coronal Mass Ejections. *The Astrophysical Journal*, 709(2):1238–1248.

Yeates, A. R., Baker, D., and van Driel-Gesztelyi, L. (2015). Source of a Prominent Poleward Surge During Solar Cycle 24. *Solar Physics*, 290(11):3189–3201.

Yeates, A. R., Bertello, L., Pevtsov, A. A., and Pevtsov, A. A. (2025). Latitude Quenching Nonlinearity in the Solar Dynamo. *The Astrophysical Journal*, 978(2):147.

Yeates, A. R., Cheung, M. C. M., Jiang, J., Petrovay, K., and Wang, Y.-M. (2023). Surface Flux Transport on the Sun. *Space Science Reviews*, 219(4):31.

Yeates, A. R., Nandy, D., and Mackay, D. H. (2008). Exploring the Physical Basis of Solar Cycle Predictions: Flux Transport Dynamics and Persistence of Memory in Advection- versus Diffusion-dominated Solar Convection Zones. *The Astrophysical Journal*, 673(1):544–556.

Zhang, D., Jiang, C., Liang, D., and Cheng, L. (2015). A review on tvd schemes and a refined flux-limiter for steady-state calculations. *Journal of Computational Physics*, 302:114–154.

Zhao, J., Bogart, R. S., Kosovichev, A. G., Duvall, Jr., T. L., and Hartlep, T. (2013). Detection of Equatorward Meridional Flow and Evidence of Double-cell Meridional Circulation inside the Sun. *The Astrophysical Journal Letters*, 774(2):L29.

Zhao, J., Hartlep, T., Kosovichev, A. G., and Mansour, N. N. (2009). Imaging the Solar Tachocline by Time-Distance Helioseismology. *The Astrophysical Journal*, 702(2):1150–1156.

Zhukova, A., Khlystova, A., Abramenko, V., and Sokoloff, D. (2020). A Catalog of Bipolar Active Regions Violating the Hale Polarity Law, 1989 - 2018. *Solar Physics*, 295(12):165.